THÈSE POUR OBTENIR LE GRADE DE DOCTEUR DE L'UNIVERSITE DE MONTPELLIER

En Mathématiques et Modélisation

École doctorale : Information, Structures, Systèmes

Unité de recherche : Institut Montpelliérain Alexander Grothendieck

Simulation de l'hémodynamique intracardiaque

Présentée par SALOMÉ BRU

Le 02/12/2025

Sous la direction de FRANCK NICOUD

Devant le jury composé de

Franck NICOUD	Professeur, Université de Montpellier	Directeur
Carine GUIVIER-CURIEN	Professeure, Polytech Marseille	Rapporteure
Morgane EVIN	Chargée de recherche, Université Gustave Eiffel	Rapporteure
Damien GARCIA	Directeur de recherche, Université de Lyon	Examinateur
Rodrigo MENDEZ ROJANO	Ingénieur, FineHeart	Examinateur
Simon MENDEZ	Chargé de recherche, Université de Montpellier	Examinateur

UNIVERSITÉ DE MONTPELLIER

Abstract

This thesis investigates left heart hemodynamics with a particular focus on how the mitral valve shapes intraventricular flow, energetic costs, and mixing, and on the specific energetic penalty introduced by mitral regurgitation. The aim is to separate the influence of global determinants (such as heart rate and geometric scale) from local determinants related to mitral valve morphology, and to quantify how these factors impact pumping efficiency and transport within the left ventricle.

An image-based, high-fidelity simulation framework was developed with the YALES2BIO solver. The computations rely on a moving-domain finite-volume formulation with pressure projection and explicit turbulence modeling. A parametric mitral valve model, developed in this thesis, controls leaflet asymmetry and ensures smooth, continuous opening and closing kinematics throughout the cardiac cycle. A patient-specific geometry of the left atrium and left ventricle is driven by prescribed wall motion. On this basis, a kinetic energy budget is established for the moving ventricular domain, enabling the analysis of viscous dissipation and myocardial power to assess cardiac pumping efficiency. Apical blood renewal is also investigated using a passive scalar approach.

Three main findings emerge. First, global variations in size and rate predominantly act as changes of scale: once signals are expressed in nondimensional form, velocities and normalized vortex dimensions are similar across cases, giving the reference configuration predictive value within the explored range. Second, mitral valve morphology is a first-order organizer of the diastolic jet and vortical topology; even small geometric changes can produce large alterations in intraventricular flow, yet viscous dissipation remains a small fraction of myocardial work in all cases. Third, in controlled mitral regurgitation, the energetic penalty is governed primarily by regurgitant volume rather than lesion mechanism, and intraventricular viscous dissipation stays near healthy levels while the efficiency penalty is dominated by retrograde loss at the mitral plane during systole.

Keywords: left heart hemodynamics; mitral valve; mitral regurgitation; kinetic energy budget; viscous dissipation.

Résumé

Cette thèse étudie l'hémodynamique du coeur gauche en mettant l'accent sur la façon dont la valve mitrale façonne l'écoulement intraventriculaire, les coûts énergétiques et le mélange, ainsi que sur la pénalité énergétique spécifique introduite par la régurgitation mitrale. L'objectif est de dissocier l'influence des déterminants globaux (tels que la fréquence cardiaque et l'échelle géométrique) de celle des déterminants locaux liés à la morphologie de la valve mitrale, et de quantifier l'impact de ces facteurs sur le rendement de pompage et le transport au sein du ventricule gauche.

Un cadre de simulation à haute fidélité fondé sur l'imagerie a été développé avec le solveur YALES2BIO. Les calculs reposent sur une formulation en volumes finis sur domaine mobile avec projection de pression et une modélisation de la turbulence. La valve mitrale est décrite par un modèle paramétrique, proposé dans cette thèse, qui contrôle l'asymétrie des feuillets et impose des cinématiques d'ouverture/fermeture continues sur tout le cycle cardiaque. Une géométrie spécifique au patient du ventricule gauche (avec mouvement des parois imposé) sert de base aux simulations. Sur cette base, un bilan d'énergie cinétique est établi dans le domaine mobile pour analyser la dissipation visqueuse et la puissance myocardique, et ainsi évaluer le rendement de pompage du coeur. Le renouvellement sanguin apical est également étudié au moyen d'une approche par scalaire passif.

Trois principaux constats se dégagent. Premièrement, les variations globales de taille et de fréquence agissent principalement comme un changement d'échelle : une fois les signaux exprimés sous forme adimensionnelle, les vitesses et les dimensions normalisées des tourbillons sont similaires d'un cas à l'autre, ce qui confère au cas de référence un pouvoir prédictif dans l'intervalle exploré. Deuxièmement, la morphologie de la valve mitrale est un organisateur de premier ordre du jet diastolique et de la topologie tourbillonnaire: de petites modifications géométriques peuvent produire de fortes altérations de l'écoulement intraventriculaire, tout en maintenant une dissipation visqueuse qui demeure une faible fraction du travail myocardique dans tous les cas. Troisièmement, dans une régurgitation mitrale contrôlée, la pénalité énergétique est gouvernée principalement par le volume régurgité plutôt que par le mécanisme lésionnel. La dissipation visqueuse intraventriculaire reste proche du niveau sain, tandis que la perte d'efficacité est dominée par la perte rétrograde au plan mitral pendant la systole.

Mots-clés : hémodynamique du cœur gauche ; valve mitrale ; régurgitation mitrale ; bilan d'énergie cinétique ; dissipation visqueuse.

Remerciements

Au terme de ces années de thèse, je voudrais exprimer ma gratitude à celles et ceux qui ont contribué à la réalisation de ce travail. Leur soutien, leurs conseils et leur confiance ont joué un rôle essentiel.

Je tiens tout d'abord à remercier chaleureusement mes directeurs de thèse, Franck Nicoud et Simon Mendez, pour la qualité de l'encadrement dont j'ai bénéficié durant ces années. Merci à Simon pour ses conseils précieux, en particulier lors de ma prise en main du code et de la mise en place du cadre numérique en début de thèse. Merci à Franck de m'avoir proposé ce sujet de thèse et d'avoir toujours su se rendre disponible, que ce soit pour discuter des aspects scientifiques les plus techniques ou pour m'accompagner dans mes moments de doute et de remise en question sur mes travaux. Vos conseils, votre exigence et votre confiance m'ont permis de progresser et de mener à bien cette thèse.

Je remercie également Morgane Evin et Carine Guivier-Curien d'avoir accepté de rapporter ce travail, ainsi que Damien Garcia et Rodrigo Mendez Rojano pour leur participation au jury. Je leur suis reconnaissante du temps qu'ils ont consacré à l'évaluation de cette thèse.

Mes remerciements vont également au personnel de l'université qui m'a accompagnée au cours de ces années. Merci à l'ensemble des membres de l'équipe de l'IMAG pour leur accueil et leur disponibilité. J'adresse aussi un mot particulier au personnel du restaurant administratif, dont la gentillesse et la bonne humeur ont rendu mes journées un peu plus agréables.

Vient maintenant le moment de remercier toutes les personnes de l'IMAG. Avant d'entrer dans les détails, un grand merci à vous tous. L'ambiance du labo a énormément compté pour moi, et vous avez rendu ces années de thèse beaucoup moins solitaires et surtout bien plus agréables. Merci à Morgane pour son accueil au sein de l'équipe à un moment où mon état mental n'était pas idéal, ainsi que pour ses conseils toujours précieux. Merci à Tanguy et Aurélio pour votre présence pendant mon stage, et à Aurélio tout particulièrement pour les soirées pâtes chez toi (et désolé de ne jamais avoir réussi à accrocher à Munchkin). Merci à Tom pour ton accueil à une période où j'étais enfin prête à reparler aux gens : tu ne t'en souviens probablement pas, mais ta gentillesse lors de cette soirée a eu un

rôle décisif. Merci aussi à Pablo d'être venu me parler le lendemain, officialisant ainsi le renouement avec les autres. Et merci de m'avoir montré que je n'étais pas la seule à me remettre en question à longueur de temps (et quelque chose me dit que nos remises en question communes ne sont pas encore terminées). Merci à toutes les personnes de l'équipe sang qui m'ont permis de me sentir moins seule dans mon travail : Pierre, Junyi, Inès, Ozy, Francisco, Pierre-Louis. Merci tout particulièrement à Bart', qui a eu le chic pour apparaître (sans même s'en rendre compte) pile aux moments où j'en avais le plus besoin, et à Corentin qui, en plus d'avoir répondu à beaucoup de mes questions, a été un cobureau formidable. Et comme les cobureaux, c'est important : merci à Zaineb d'avoir été la première à discuter avec moi. Merci à Sofian pour ton bref passage (et, même si ça n'a rien à voir, bravo pour ton énième victoire au ping-pong contre Baptiste), ainsi qu'à Guillaume pour ton passage encore plus court. Merci enfin à Nicolas, dernier arrivé au bureau, dont ta présence et ton implication (y compris dans les décorations) sont très appréciées. En dehors des cobureaux, merci aux autres doctorants du laboratoire qui font vivre ces couloirs. Merci Pierrick pour ton far, qui a fait très plaisir sur la fin du manuscrit. Merci Guillaume de m'avoir accueillie un temps dans ton bureau, et de m'avoir expliqué avec passion ta manière de voir les maths. Merci à Victor, Yefei, Marwa, Christelle, Christina, Joris, Adam, Hugo, Antoine, Alexandre, Anne, Arax, et à tous et toutes les autres avec qui je n'ai pas vraiment eu l'occasion d'échanger. Merci également à Gabriele, pour ton accent chantant, et à Fabien, pour les randonnées. Merci Orlane pour tes conseils à la patinoire. Merci Thibault pour Taz. Merci Nathan pour ton goût pour le bon vin et tes talents en mixologie. Merci Hermès pour ton rire qu'on entend à l'autre bout du couloir. Merci Raph' et Marien d'avoir réussi à rester au moins une fois au bureau encore plus tard que Thiziri. Un grand merci à Thiziri pour ta gentillesse, qui a vraiment compté. Merci Chloé de m'avoir fait rencontrer Mochi (<3). Merci à Amélie pour tes talents impressionnants aux mots fléchés, et pour avoir permis de lancer les soirées Twilight. Merci Antoine d'être un vampire végétarien, et merci de rire à mes blagues comme si j'étais la personne la plus drôle sur cette planète. Promis, j'essaie de pas trop te traumatiser à notre prochain bivouac. Merci Nikola pour ta bonne humeur constante et pour ne jamais te plaindre. Et surtout, merci pour ton absence de filtre, qui me fait toujours rire. Merci à Baptiste de sauver des lions avec moi, et à Ulysse d'avoir été un partenaire parfait pour démasquer un meurtrier. Merci Greg pour ta patience aux jeux, et merci de toujours me laisser gagner. Merci à Pierre d'avoir rejoint le groupe de Magic. Un grand merci enfin à Luca, pour avoir supporté mes innombrables discussions sur Baldur's Gate 3 (petit moment pub pour ce jeu formidable), pour m'avoir initiée à D&D et à Magic : je ne suis pas prête de m'ennuyer.

Je ne vous ai évidemment pas oubliés, mais je n'aurais jamais réussi à résumer en une seule phrase tout ce que vous m'avez apporté. Alors voici un petit paragraphe pour vous.

Merci Chloé pour ta bienveillance. Merci de me pousser à exprimer ce que je ressens quand ça ne va pas, et d'être toujours là pour m'écouter. Merci pour

ta franchise et ta manière de dire les choses. Merci aussi d'être beaucoup trop investie dans n'importe quel jeu, et de réussir à faire peur aux gens. Et surtout, merci pour la personne que tu es. Courage pour ta fin de thèse, j'ai entièrement confiance en toi. À nos prochains bivouacs, où je finirai sûrement en PLS parce qu'on a pas du tout les mêmes capacités.

Merci à Julien pour tout ce que tu m'as apporté. Merci pour nos nombreuses discussions, pour m'avoir supportée même (surtout) quand ça n'allait pas. Merci pour ta manière de voir les choses. Et surtout, merci pour tes merveilleux goûts musicaux (si rares à l'IMAG), pour ton humour incroyable et tes jeux de mots, toujours très qualitatifs. Merci pour le bout de chemin qu'on a fait ensemble.

Pour finir, je voudrais remercier particulièrement la meilleure cobureau qu'on puisse avoir. Merci Juliette d'avoir apporté autant de bonne humeur et de vie chaque jour dans ce bureau, et d'en avoir fait un endroit aussi agréable. Merci pour ton soutien au fil des années, pour les brunchs, les décos, les discussions, et pour toutes ces petites attentions (y compris me forcer à boire de l'eau) qui ont clairement contribué à ma survie au labo. Merci aussi pour ton énergie absolument inépuisable, et pour m'en avoir transmis un peu quand j'en avais besoin. Merci de toujours croire en moi, dans tous les domaines (RIP mes bleus à la pole quand tu refusais de me laisser lâcher). J'ai eu une vraie chance de te rencontrer à l'IMAG.

En dehors de l'IMAG, je voudrais remercier les personnes du LIRMM avec qui j'ai eu l'occasion de discuter et de passer des soirées. Merci à Paul, Thibaut, Elena et Sarah. Merci à Jacques de supporter Quentin toute la journée dans ton bureau et de discuter autant ensembles. Merci aussi à Hypolite, qui maintenant doit les supporter tous les deux. Et merci à Pierre de m'avoir convaincue de terminer cette thèse.

Et puisqu'il n'y a pas qu'au travail que j'ai vécu de bons moments, je voudrais aussi remercier Maugan pour ces trois années de MI. Morgane, merci pour ton humour, ta manière de penser, et tout ce que tu m'as apporté. Et désolée de ne pas avoir mieux su garder le contact.

Merci également à mes vieux copains de PEIP. Merci Marlène, Manon et Sébastien pour nos soirées, rares mais précieuses, qui me permettent de respirer et de retrouver l'insouciance (et peut-être un peu l'immaturité) de nos débuts.

Merci à la famille de Quentin d'avoir su m'accueillir comme vous l'avez fait. Les moments passés en Aveyron sont toujours un plaisir (et pas seulement parce que c'est le meilleur département de France). Merci à Denis, à Bernadette, et à Noémi. Merci également à Guy et Christiane pour leur gentillesse au fil des années. Merci aussi aux copains d'Aveyron de savoir si bien me recevoir. Merci Émilien de me faire relativiser à chaque fois sur l'état des voitures de Quentin - finalement, et même si ça me semblait impossible, ça pourrait être pire. Merci Tanguy pour tes reels parfois... discutables que je me retrouve obligée de regarder, et merci

Hugo pour être une oreille attentive. Merci Léa.

Merci enfin à ma famille au grand complet. Votre présence et votre soutien ont toujours compté. Merci de m'avoir fait grandir dans un environnement chaleureux et bienveillant, et de faire de chacune de nos retrouvailles un moment réellement précieux. Merci Papi et Mamie, merci Papi et Francine. Merci à mes oncles, mes tantes, et à tous mes cousins. Merci Mathieu pour le frère que tu es, et pour tous les moments qu'on a partagés en grandissant. Et merci pour toutes nos parties ensemble (même si, malgré tous mes efforts, c'est toi qui a toujours gagné). Merci Lauren, pour ta gentillesse et ton soutien. Merci Papa pour tout ce que tu m'as apporté. Et merci de m'avoir appris, dès mes 3 ans, cette grande leçon que je m'efforce toujours d'appliquer quand je joue : l'important n'est pas de gagner, mais de massacrer son adversaire. Merci Maman, pour nos discussions, pour ton amour, et pour toujours prendre soin de moi - et désolée de t'inquiéter parfois. J'ai énormément de chance de vous avoir. Je vous aime.

Hello toi. Je ne trouverai jamais vraiment les mots pour dire ce que ta présence a représenté durant ces années. Merci pour le calme que tu as mis dans ma vie, et pour cette façon que tu as de rendre les choses plus simples juste en étant là. Merci de toujours croire en moi, comme si c'était évident, et merci de réussir à m'en convaincre parfois. Merci d'être celui auprès de qui je peux toujours me sentir bien, où que j'en sois dans ma vie.

Et merci de toujours faire battre mon coeur un peu plus fort. D'ailleurs, pour ceux que le fonctionnement d'un coeur intrigue, les 130 pages qui suivent en dévoilent un peu la mécanique.

Contents

Contents **xii**

Chapter 1 Introduction **3**
1.1 Motivation . . . 4
1.2 Cardiac function and anatomy . . . 4
1.2.1 The circulatory loop . . . 4
1.2.2 Anatomy of the left heart . . . 6
1.2.3 The cardiac cycle . . . 7
1.3 Studies of the cardiovascular system . . . 10
1.3.1 Medical imaging . . . 10
1.3.2 Experimental studies . . . 12
1.3.3 Numerical simulations . . . 13
1.4 Thesis objectives and overview . . . 29
1.4.1 Objectives . . . 29
1.4.2 Thesis overview . . . 29

Chapter 2 Complex hemodynamic simulations: the YALES2BIO solver **31**
2.1 The YALES2BIO solver . . . 32
2.2 Blood flow modeling . . . 32
2.2.1 Governing equations . . . 32
2.2.2 Initial and boundary conditions . . . 33
2.3 Arbitrary Lagrangian-Eulerian (ALE) formulation . . . 34
2.3.1 Governing equations in ALE form . . . 34
2.3.2 Integral formulation . . . 35
2.3.3 Finite-volume discretization and control volumes . . . 35
2.3.4 Low-storage Runge-Kutta time advancement . . . 36
2.3.5 Pressure projection method . . . 38
2.3.6 Turbulence modeling . . . 38
2.4 Valve modeling . . . 40
2.4.1 Legacy immersed-boundary valve model . . . 40
2.4.2 Limitations and motivation for an updated model . . . 41
2.4.3 Improved mitral valve model (present work) . . . 42
2.4.4 Assessment of the proposed model . . . 45

Chapter 3 Intraventricular hemodynamics **51**
3.1 Description of the model . . . 52
3.1.1 Image-based left heart geometry . . . 52
3.1.2 Boundary conditions . . . 53
3.1.3 Numerical solver and mesh . . . 55
3.1.4 Valve model . . . 57
3.1.5 Leakage verification and parameter selection . . . 58
3.2 Hemodynamics over one cardiac cycle . . . 59
3.2.1 Qualitative description . . . 60
3.2.2 Atrial inflow and pre-filling vortex seeding . . . 62
3.2.3 Ventricular filling . . . 62
3.2.4 Systolic ejection . . . 65
3.2.5 Conclusion . . . 67

Chapter 4 Parametric Study **69**
4.1 Effect of heart rate and volume variations . . . 70
4.1.1 Numerical setup . . . 70
4.1.2 Reference configuration . . . 70
4.1.3 Parametric study . . . 71
4.1.4 Results . . . 71
4.1.5 Conclusion and limitations . . . 75
4.2 Effect of the mitral valve on intraventricular hemodynamics . . . 78
4.2.1 Materials and methods . . . 79
4.2.2 Results . . . 81
4.3 Overall conclusion . . . 85

Chapter 5 Advanced hemodynamic analysis **87**
5.1 Introduction . . . 88
5.2 Materials and methods . . . 88
5.3 Kinetic energy budget . . . 89
5.3.1 Methodology . . . 89
5.3.2 Results . . . 93
5.3.3 Discussion . . . 98
5.4 Mixing in the left ventricle . . . 99
5.5 Overall conclusion . . . 102

Chapter 6 Study of mitral regurgitation **105**
6.1 Mitral regurgitation: definition . . . 106
6.1.1 Clinical presentation and classification . . . 106
6.1.2 State of the art: approaches for studying mitral regurgitation 108
6.2 Methodology . . . 109
6.3 Reference case for regurgitation: analysis . . . 112
6.4 Analysis of the effect of regurgitant volume on energy loss . . . 115
6.5 Analysis of the MR mechanism on energy loss . . . 119
6.6 Overall conclusion . . . 121

Chapter 7 Main results, discussion & perspectives **125**
7.1 Main results 126
7.1.1 Image-based framework and valve modeling 126
7.1.2 Global scaling vs. local valvular effects 126
7.1.3 Energetic analysis and mixing without regurgitation 126
7.1.4 Energetic cost of mitral regurgitation 126
7.2 Discussion of modeling choices and consequences 127
7.2.1 Prescribed kinematics on an image-based domain 127
7.2.2 Mitral valve representation 127
7.2.3 Geometric precision 127
7.2.4 Turbulence modeling and resolution 128
7.2.5 Mixing metric 128
7.3 Perspectives: from washout to thrombosis risk in the apex 128

Chapter 8 Appendix **133**
8.1 Physics-Guided Neural Networks for Intraventricular Vector Flow Mapping 133
8.2 Critical evaluation of kinetic schemes for coagulation 146

List of Figures **163**

List of Tables **167**

Bibliography **169**

List of Abbreviations

ALE = Arbitrary Lagrangian–Eulerian

Ao = Aorta

AV = Aortic Valve

CFD = Computational Fluid Dynamics

CMR = Cardiac Magnetic Resonance

CO = Cardiac Output

CT = Chordae Tendineae

DNS = Direct Numerical Simulation

EDV = End Diastolic Volume

EF = Ejection Fraction

EFSI = Electro Fluid–Structure Interaction

EL = Energy Loss

EPIV = Echocardiographic Particle Image Velocimetry

ESV = End Systolic Volume

FSI = Fluid–Structure Interaction

IBM = Immersed Boundary Method

KE = Kinetic Energy

LA = Left Atrium

LES = Large Eddy Simulation

LH = Left Heart

LV = Left Ventricle

MCL = Mock Circulatory Loops

MR = Mitral Regurgitation

MRI = Magnetic Resonance Imaging

MV = Mitral Valve

NS = Navier-Stokes

PM = Papillary Muscles

PV = Pulmonary Veins

Re = Reynolds number

RIIS = Resistive Immersed Implicit Surface

RK4 = 4th-order Runge–Kutta

RV = Regurgitant Volume

RF = Regurgitant Fraction

SV = Stroke Volume

TKE = Turbulent Kinetic Energy

TEE = Transesophageal Echocardiography

TTE = Transthoracic Echocardiography

VFM = Vector Flow Mapping

WSS = Wall Shear Stress

Chapter 1

Introduction

Chapter contents

1.1 Motivation 4
1.2 Cardiac function and anatomy 4
1.2.1 The circulatory loop 4
1.2.2 Anatomy of the left heart 6
1.2.3 The cardiac cycle 7
1.3 Studies of the cardiovascular system 10
1.3.1 Medical imaging 10
1.3.2 Experimental studies 12
1.3.3 Numerical simulations 13
1.4 Thesis objectives and overview 29
1.4.1 Objectives 29
1.4.2 Thesis overview 29

This introductory chapter outlines the motivations of this thesis. It begins with a general overview of cardiac function and anatomy, followed by a review of previous research based on medical imaging and numerical simulations. The chapter concludes with a statement of the thesis objectives and an overview of its structure.

1.1 Motivation

According to the World Health Organization, cardiovascular diseases accounted for approximately 32% of global deaths in 2019, making them the leading cause of mortality worldwide [1]. This statistic underscores the pressing need for improved diagnostic tools and therapeutic strategies to combat these conditions effectively. In this context, studying intracardiac flow dynamics is crucial for several reasons:

- **Understanding Pathophysiology**: Intracardiac flow patterns can reveal underlying pathophysiological mechanisms. Abnormal flow, such as regurgitation or stenosis, may indicate structural anomalies, valvular dysfunctions, or regions of myocardial impairment.
- **Early Diagnosis**: Subtle changes in hemodynamics often precede clinical symptoms. For instance, abnormal vortex patterns or increased shear stress can be early indicators of conditions like heart failure or mitral regurgitation. Early detection enabled by flow analysis could improve patient outcomes.
- **Personalized Treatment**: Patient-specific flow modeling can inform therapeutic decisions. For example, detailed knowledge of how blood interacts with a prosthetic valve can guide surgical planning or optimize the design of medical devices.
- **Prognostic Value**: Key flow parameters, such as turbulence intensity or shear stress distributions, have been linked to the progression of heart disease. Quantifying these parameters enables clinicians to classify patients according to risk and monitor disease progression over time.
- **Innovation in Biomarkers**: Developing effective biomarkers based on flow dynamics can enhance the accuracy of diagnosing and monitoring cardiomyopathies. These quantitative markers can complement traditional diagnostic methods, providing a more comprehensive view of cardiac health.

The ultimate objective is to advance the understanding of cardiac pathologies and improve patient outcomes through personalized treatment strategies. Section 1.2 provides an overview of the cardiovascular system, while Section 1.3 reviews current research on intracardiac flow dynamics.

1.2 Cardiac function and anatomy

1.2.1 The circulatory loop

The cardiovascular system is a closed-loop network consisting of the heart and an extensive network of blood vessels, including arteries, capillaries, and veins. Its primary role is to transport oxygen and nutrients efficiently throughout the body

via the bloodstream. At the center of this system lies the heart, functioning as a pump.

This circulatory loop is divided into two circuits: the pulmonary and systemic circuits (illustrated in Fig. 1.1). In the pulmonary circuit, deoxygenated blood (represented in blue in the figure) is directed into the right side of the heart, transported to the lungs for oxygenation, and subsequently returned to the left side of the heart. The systemic circuit then takes over, where oxygen-rich blood is pumped from the left heart through the aorta, delivering oxygen and nutrients to tissues and organs across the body. The blood, now deoxygenated, completes the loop by returning to the right side of the heart, ready to restart the cycle.

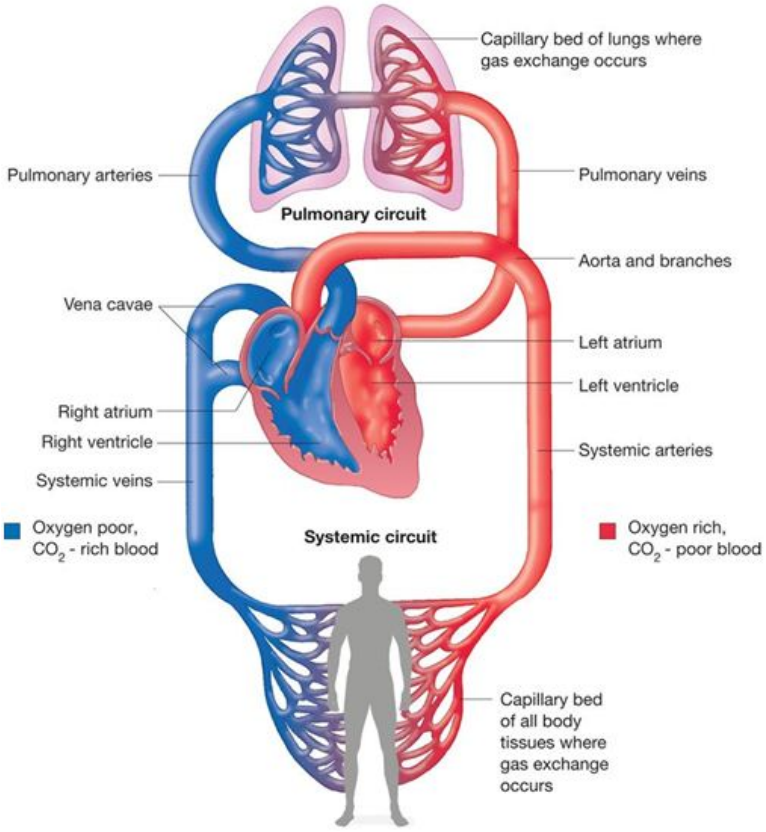


Figure 1.1: Circulatory loop diagram. Extracted from [2].

These two circuits operate simultaneously, completing a full cycle in approximately one second. On average, the human heart beats 60 to 80 times per minute, transporting around 5 liters of blood during this period.

The heart itself is divided into two anatomically and functionally distinct halves: the right and left sides. The right side is responsible for pumping blood exclusively to the lungs, while the left side propels blood to the entire body. To meet the higher demands of systemic circulation, the pressure generated in the left ventricle is approximately five times higher than that in the right ventricle. Consequently, any issues with the heart's functionality are more likely to manifest in the left ventricular flow than in the right one. Given the clinical

and physiological significance of the left heart, this thesis focuses on examining the flow within the left ventricle, and the discussion will primarily revolve around the left side of the heart.

1.2.2 Anatomy of the left heart

1.2.2.1 External features

The human heart comprises four chambers: the left and the right side each have one atrium and one ventricle. The atria, located in the upper part of the heart, act as receiving chambers and contract to push blood into the ventricles. The ventricles, situated in the lower part of the heart, serve as the primary pumping chambers, propelling blood either to the lungs (right ventricle) or to the rest of the body (left ventricle).

The heart wall consists of three distinct layers, illustrated Fig. 1.2:

- The epicardium, which forms the protective outer layer of the heart.
- The myocardium, the thick muscular layer responsible for contraction.
- The endocardium, the thin inner layer in contact with the blood.

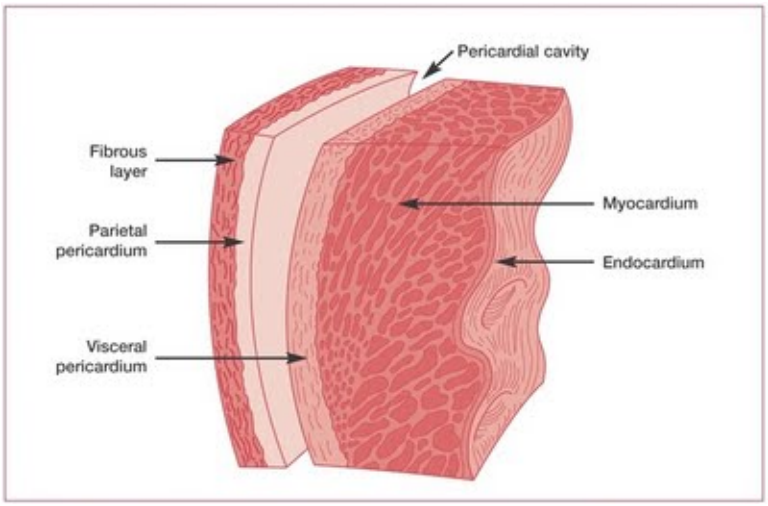


Figure 1.2: Heart layers.

The apex of the heart is the inferior tip of the left ventricle. This region is a common access point for left ventricular interventions, including valvular therapies [3]. However, the relatively thin myocardium at the apex (a few millimeters) makes this area vulnerable to perforation during surgical procedures.

1.2.2.2 Valves

The left heart contains two valves: the mitral valve and the aortic valve (see Fig. 1.3). These valves ensure unidirectional blood flow and play distinct roles in cardiac function.

The aortic valve is located between the left ventricle and the aorta. It consists of three cusps (designated as the right, left, and posterior cusps) whose edges are attached to the walls of the outflow vessel. This attachment occurs in slightly dilated regions known as sinuses. During the onset of diastole, a small amount of blood flows back toward the heart, filling these sinuses. This process brings the cusps together, effectively closing the valve to prevent regurgitation into the left ventricle. While the aortic valve plays a critical role in regulating aortic flow, its influence on intraventricular flow dynamics is limited.

The mitral valve, on the other hand, significantly affects left ventricular flow, as it separates the atrium and the ventricle. It consists of two asymmetric leaflets, with the anterior leaflet being approximately twice the size of the posterior one and positioned toward the aorta. The mitral valve leaflets are supported by fibrous cords known as chordae tendineae, which attach to the free edges of the leaflets and connect them to papillary muscles (see Fig. 1.3b). These muscles, located within the left ventricular wall, contract during systole to prevent the leaflets from prolapsing into the atrium. The chordae tendineae act as tension regulators:

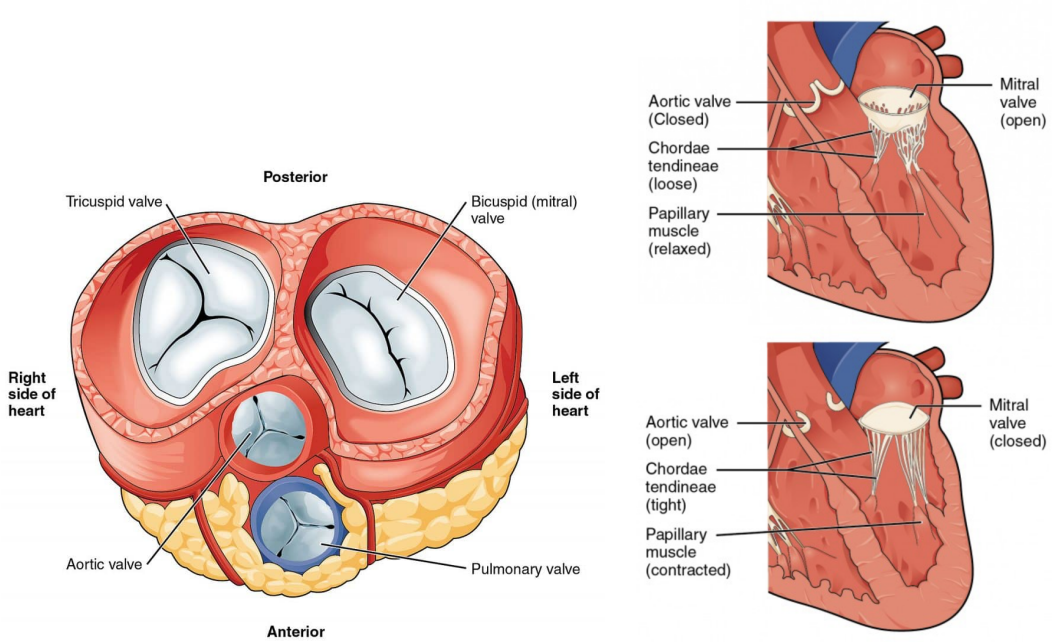
- During diastole, they remain loose, allowing the valve to open fully.
- During systole, they tighten, ensuring the valve remains closed and prevents regurgitation.

The left ventricle contains two papillary muscles supporting the mitral valve, while the right ventricle has three papillary muscles associated with the tricuspid valve. This system of chordae and muscles ensures proper valve function and maintains the integrity of unidirectional blood flow.

1.2.3 The cardiac cycle

The cardiac cycle refers to a complete heartbeat, encompassing all events from the entry of blood into the heart to its ejection into the body. It consists of distinct phases that occur in a coordinated sequence, as illustrated in Fig. 1.4.

During a cardiac cycle, each cavity (atrium or ventricle) undergoes two phases: diastole (filling and relaxation) and systole (ejection and contraction). The movements of both sides of the heart are synchronized. Unless otherwise specified, diastole and systole generally refer to the ventricle. While the description below focuses on the left side of the heart, the mechanism is identical on the right side.



(a) (b)

Figure 1.3: (a) The four valves of the heart, with the atria and great vessels removed. All valves are shown in the closed position. Extracted from [2]. (b) Left atrium and left ventricle with the papillary muscles and the chordae tendineae. Top: diastole, bottom: systole.

1.2.3.1 Diastole: Ventricular relaxation and filling

At the beginning of the cardiac cycle (see Fig. 1.4) both the atrium and ventricle are relaxed. Blood flows into the left atrium from the four pulmonary veins. The diastole of the ventricle is divided into two phases:

1. Isovolumic relaxation: During this early stage of diastole, the mitral valve remains closed. As the myocardium relaxes, the pressure within the ventricle drops without any change in volume. This is referred to as the isovolumic relaxation phase.

2. Ventricular filling: As relaxation progresses, ventricular pressure decreases further. Once it drops below the atrial pressure, the mitral valve opens, allowing blood to flow from the atrium into the ventricle. Both chambers are in diastole, the mitral valve is open, and the aortic valve remains closed, preventing backflow of blood into the ventricle from the aorta. At rest, most filling (approximately 70-80%) occurs passively during early rapid filling and diastasis; atrial contraction contributes the remaining 20-30% (the "atrial kick"). By the end of diastole, the left ventricle contains approximately 130 mL of blood, referred to as the end-diastolic volume (EDV).

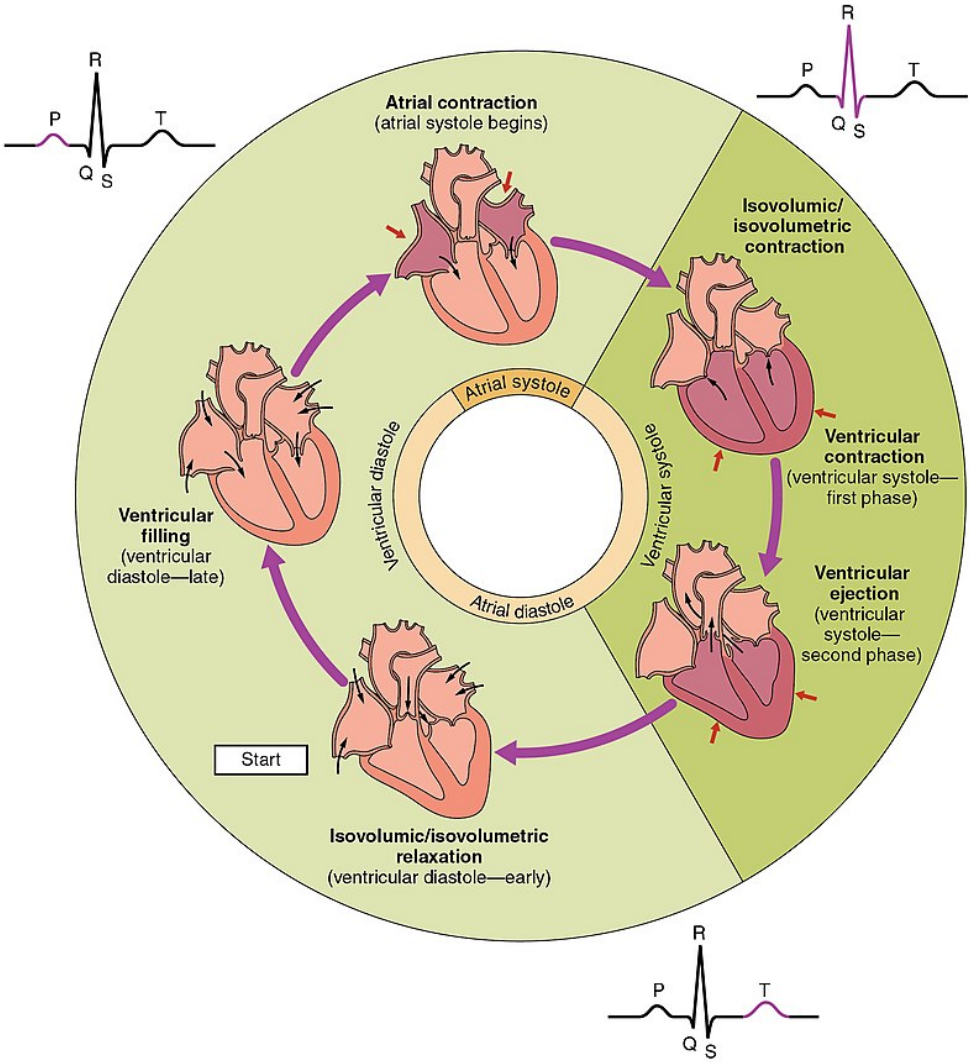


Figure 1.4: Diagram depicting the various phases of the cardiac cycle. Extracted from [2].

1.2.3.2 Systole: Ventricular contraction and ejection

Ventricular systole begins with the contraction of the myocardium. It is divided into two phases:

1. Isovolumic contraction: During the early phase of systole, the rising pressure in the ventricle exceeds that of the relaxed atrium, causing the mitral valve to close. However, the pressure has not yet reached the threshold required to open the aortic valve. Since no blood is ejected during this phase, the ventricular volume remains constant, hence the term isovolumic contraction phase.

2. Ventricular ejection: As the contraction continues, the pressure in the ventricle exceeds that in the aorta, causing the aortic valve to open. Blood is ejected from the ventricle into the aorta. The amount of blood ejected is the stroke volume (SV), typically 70–80 mL in a healthy adult. After ejection, approximately

50–60 mL of blood remains in the ventricle, referred to as the end-systolic volume (ESV).

Considering an EDV of 130 mL and an ESV of 50–60 mL, the stroke volume represents the difference between these values.

1.3 Studies of the cardiovascular system

Measuring intracardiac blood flow is challenging, and several complementary approaches are used. This section reviews three families of methods: in vivo medical imaging (Section 1.3.1), in vitro and ex vivo experimental models (Section 1.3.2), and in silico numerical simulations (Section 1.3.3).

1.3.1 Medical imaging

Imaging-based assessment provides in vivo measurements to characterize intracardiac flow under physiological operating conditions. Numerous surveys detail the scope of these methods and their flow-derived metrics (e.g., velocity fields, vorticity, kinetic energy, relative-pressure surrogates), as well as emerging AI-driven pipelines for dealiasing and inference [4–9]. Two modalities dominate clinical and research use: ultrasound-based echocardiography and 4D Flow MRI (phase-contrast MRI).

1.3.1.1 Ultrasound-based modalities

Echocardiography uses high-frequency ultrasound emitted by a transthoracic transducer; echoes from cardiac structures are received and reconstructed into real-time images. Doppler echocardiography analyzes frequency shifts to estimate the direction and magnitude of blood velocity, complementing anatomical views with functional flow information. Being noninvasive and fast, echocardiography is the most widely used modality for intracardiac flow evaluation.

In typical transthoracic studies, spatial resolution is millimetric (0.5–1.5 mm), frame rates are high (on the order of 50–200 Hz in 2D), and examinations take on the order of 10–30 min. These characteristics make echocardiography well suited to quantify inflow timing and orientation, jet onset and evolution, and overall energetic trends.

The use of echocardiography in the analysis of left ventricular dynamics has led to significant advancements in the understanding of blood flow patterns and their impact on cardiac function. Beyond imaging anatomical structures, modern techniques such as Doppler Vortography, vector flow mapping (VFM), and echocardiographic particle image velocimetry (EPIV) provide detailed insights into the velocity fields and energy dissipation within the heart [10–13]. These techniques have supported studies of vortex organization, kinetic energy, and energy loss (EL) metrics across conditions: higher EL with prosthetic valves and near-normal patterns after repair [14, 15], ongoing debate about the functional

role of diastolic vortices in efficient filling and energy storage [16, 17], and disease-related alterations in vortex timing/persistence with changes in EL and wall stress [11, 18]. Taken together, ultrasound-derived flow maps provide a practical, noninvasive window on flow organization and energetic penalties.

Building on a numerical database generated during this thesis, Hang Jung *et al.* synthesized color Doppler sequences and applied physics-guided machine learning for intracardiac vector flow mapping (iVFM) to reconstruct intraventricular vector fields; reconstructions were benchmarked against the numerical results and further assessed on in vivo apical three-chamber cine-loops using physics-constrained labels. This contribution underpins the published method (see Appendix 8.1 and [19]) and illustrates how physics-based simulation can supply quantitative labels while remaining compatible with clinical ultrasound.

Despite its wide availability and high temporal resolution, echocardiography has well-known limitations: angle dependence and aliasing in Doppler measurements; out-of-plane motion and restricted acoustic windows for advanced reconstructions; and dependence on imaging view and operator, which reduces reproducibility and complicates fully volumetric quantification. These constraints motivate the use of complementary modalities such as MRI, which offers volumetric coverage and standardized flow metrics at the cost of lower temporal resolution and longer acquisitions.

1.3.1.2 Magnetic resonance imaging (MRI)

Phase-contrast MRI (4D Flow MRI) encodes all three velocity components in a 3D volume over the cardiac cycle, yielding chamber-wide flow maps under in vivo conditions. Beyond anatomic imaging, these data enable the computation of flow-derived metrics such as kinetic energy, viscous energy loss, vorticity, hemodynamic forces, and relative-pressure estimates, thereby complementing Doppler-based assessments with volumetric coverage and through-plane velocities [20–22].

In typical whole-heart acquisitions, spatial resolution is millimetric and temporal resolution is on the order of tens of milliseconds, with scan times of 30-60 minutes depending on the strategy. Post-processing (background-phase correction, dealiasing, segmentation) is often required before deriving Kinetic Energy (KE)/energy loss fields or pressure. These characteristics make 4D flow MRI well suited to quantify chamber-wide energetics and topology.

Applications span physiology and disease: altered diastolic vortex organization has been linked to increased EL [21], alterations in the magnitude and timing of left ventricular KE have been observed after myocardial infarction and with aging [23, 24], and rate-dependent changes in intraventricular energetics have been characterized in relation to leaflet kinematics [25]. Resolution-oriented studies further indicate that key diastolic features (e.g., the mitral vortex ring) are captured reliably under current protocols, whereas mid-scale structures remain more challenging [22].

Despite its volumetric coverage and reduced angle sensitivity, 4D Flow MRI has limitations: lower temporal resolution than echocardiography; spatial smooth-

ing and partial-volume effects that can under-resolve peak jets; and sensitivity to acquisition parameters and post-processing choices. While clinical imaging provides patient-specific flow fields, it is constrained by spatial/temporal resolution and acquisition artifacts. To probe mechanisms under controlled conditions and to generate quantitative benchmarks, in vitro experimental models have been developed (Section 1.3.2).

1.3.2 Experimental studies

Experimental investigations of cardiac hemodynamics use Mock Circulatory Loops (MCL) connected to compliant or optically clear left-heart phantoms. These closed circuits reproduce physiological pressure and flow and allow repeatable measurements. They complement in vivo imaging by providing quantitative ground truth for studying mechanisms and for validating reconstruction methods and CFD [26, 27]. Broad reviews summarize bench models for valve mechanics and repair, including mitral-specific test rigs [28], and describe how MCLs are used for fundamental left-heart hemodynamics, for testing cardiovascular devices (for example prosthetic and transcatheter valves or ventricular assist devices), and for clinical training (such as rehearsal of catheter-based deployments and echo/CMR acquisition on phantoms) [27, 29–31]. Modern experimental platforms measure time-resolved velocity fields (using planar or tomographic PIV, or particle tracking) while recording pressure and, when available, MRI or ultrasound on the same heartbeat [32–34]. This multi-modal acquisition reveals the main flow structures during filling and ejection, enables relative-pressure reconstruction and compact descriptions of the dynamics, and provides reference datasets for validating numerical solvers [33, 34]. Although these models simplify blood rheology and wall mechanics, they offer strict control of boundary conditions (stroke volume, heart rate, and valve motion) and high repeatability, which are essential for systematic studies [26].

Within this general framework, a large body of work has focused on the mitral valve as a primary driver of intraventricular flow organization. Orientation and annular tilt steer the diastolic jet, set the topology of the LV vortex system, and modulate transport and dissipation. In vitro studies in LV phantoms show that rotating mechanical valves or increasing annular angle reorients the inflow jet, alters vortex-ring formation and wall impingement, and impacts washout and turbulence metrics [35, 36]. Systematic in vitro measurements have also quantified effective orifice area, transvalvular pressure gradients, and Doppler-based diagnostics for prosthetic valves, providing reference datasets for assessing function and malfunction [37, 38]. Beyond orientation, valve type and apparatus (biological vs. mechanical designs, single vs. double orifice, chordal support) influence vortex cores and turbulent kinetic energy, as captured by tomographic PIV in anatomically inspired models [32].

Experimental platforms also probe interventions and pathologies. Edge-to-edge repair splits the mitral inflow into paired jets and vortex rings, with measurable

changes in intraventricular energy loss relative to single-orifice or healthy-like inflow [39]. Models of mitral regurgitation quantify altered vortex formation, separation, and viscous energy dissipation, supporting energy-based metrics for MR stratification [40]. Valve-in-valve configurations have been assessed in vitro to characterize transvalvular gradients and flow organization, informing device selection and implantation strategy [41]. Finally, multi-modal phantoms facilitate cross-validation against clinical imaging (e.g. 4D flow MRI, vector ultrasound), tightening the link between bench measurements and in vivo reconstructions [33].

In vitro measurements provide controlled boundary conditions and high-fidelity validation data, but they remain constrained by setup idealizations and limited access to wall mechanics. These aspects can be partly overcome with numerical simulations.

1.3.3 Numerical simulations

Together with imaging and in vitro data, numerical simulations complete the analysis by providing full-field, time-resolved quantities and by enabling controlled parameter studies. These simulations enable the investigation of complex flow patterns and their interactions with cardiac structures under diverse conditions, from normal physiology to severe pathologies. Numerous models have been developed over the years to simulate blood flow in the heart [42–44].

Across the literature, four main classes of models can be identified. In computational fluid dynamics (CFD) with prescribed kinematics, blood flow is solved while wall or leaflet motion is imposed either from medical imaging data [45–53] or from idealized kinematic laws [54, 55]. This strategy avoids direct coupling between fluid and solid domains, making it computationally efficient while still capturing key aspects of intracardiac flow. While classical CFD models do not account for the mechanical response of cardiac tissues, a more physically consistent alternative is fluid-structure interaction (FSI). FSI models solve the fluid and solid domains in a bidirectionally coupled manner, enabling the feedback of fluid loads on leaflet or wall motion [56, 57]. They are particularly relevant for simulating valve dynamics, but require higher computational cost and additional constitutive or activation assumptions [56–59]. Electromechanical models focus on electrical activation and myocardial mechanics; they are often employed to generate physiologic ventricular kinematics or to study sensitivity to material and activation parameters, with or without detailed hemodynamics [60–64]. Finally, Electro-Fluid–Structure Interaction (EFSI) frameworks couple activation, deformation, and flow in a unified description, offering in principle the most physiologically faithful simulations [58, 65]. However, this comes at the price of the largest computational and data demands, which often limit their practical use.

Across all these approaches, different degrees of fidelity have been adopted, depending on the aims of each study. Simplifications may concern the overall geometry, for example, whether the atria and aorta are omitted altogether [54, 60, 64, 66], represented by tubular extensions [49, 55, 56, 67–69], or reconstructed in

detail from patient-specific imaging [46, 47, 70–72]. The level of ventricular wall detail may also vary, from smooth surfaces [45, 47, 54, 68] to anatomically enriched geometries including trabeculae and papillary muscles [70, 73, 74]. Among these structural choices, the representation of the mitral valve is often the most critical factor for intraventricular flow. Depending on the study, the valve may be omitted entirely [53, 60, 66, 75], represented with a simplified geometry [46, 54, 70], or reconstructed from patient-specific data [72, 74]. Its motion can be modeled as an instantaneous switch between open and closed states [70, 72, 73], as a continuous prescribed kinematic law [45, 68], or as the result of a fully coupled FSI simulation [56, 57]. These varying levels of simplification and detail directly affect the realism of the simulated flow patterns, as well as the associated computational cost.

Altogether, these approaches illustrate the wide spectrum of strategies found in the literature, ranging from highly simplified conceptual models to detailed patient-specific simulations. A comparison of these strategies is presented in Table 1.1.

Year, Ref	Cardiac Compartments				Valves			Subvalvular and Internal Structures		
	LV	**LA**	**PV**	**Ao**	**MV Geom**	**MV Method**	**AV**	**CT**	**PM**	**Trab.**
2008, Watanabe et al. [75]	1	0	0	1 (tube)	None	Inflow modulation to mimic valve effect	0	0	0	0
2012, Le and Sotiropoulos [66]	PS (MRI)	0	0	0	0	-	0	0	0	0
2013, Seo and Mittal [67]	1 (CT-scan)	1 (tube)	0	1 (tube)	0	-	0	0	0	0
2014, Baillargeon et al. [61]	Zygote (adapted)	Zygote (adapted)	Zygote (adapted)	Zygote (adapted)	Simulated via viscous resistance	0	Simulated via viscous resistance	0	0	0
2014, Seo et al. [45]	1 (CT-scan)	1 (tube)	0	1	1 (generic based on healthy cohort)	Kinematics prescribed from echo, IBM Mittal et al. [76]	0	0	0	0
2015, Domenichini and Pedrizzetti [54]	1	0	0	0	1	IBM	0	0	0	0
2015, Vedula et al. [46]	PS (CT-scan)	PS (CT-scan)	PS	PS (CT-scan)	1 (from Seo et al. [45])	-	0	0	0	1
2016, Vedula et al. [50]	PS (CT-scan)	1 (tube)	0	0	1 (from Seo et al. [45])	-	0	0	1	1
2016, Lantz et al. [53]	PS (Geom and prescribed motion from CT-scan)	1	1	1	0	Velocity profile imposed	0	0	1	1

(Table continued on next page.) *Legend:* LV = Left Ventricle, LA = Left Atrium, PV = Pulmonary Veins, Ao = Aorta, MV = Mitral Valve, AV = Aortic Valve, CT = Chordae Tendineae, PM = Papillary Muscles, Trab. = Trabeculae. MV Method = Modeling strategy for the MV (e.g., FSI, IBM, on/off, porous disk...). 0 = not modeled, 1 = generic model, PS = patient-specific.

Year, Ref	Cardiac Compartments				Valves			Subvalvular and Internal Structures		
	LV	**LA**	**PV**	**Ao**	**MV Geom**	**MV Method**	**AV**	**CT**	**PM**	**Trab.**
2016, Seo et al. [77]	1 (CT-scan)	1 (tube)	0	1 (tube)	1 (from Seo et al. [45])	-	0	0	0	0
2016, Su et al. [68]	PS (MRI)	1 (tube)	0	1 (tube)	1 (ideal Geom)	MRI-based motion	0	0	0	0
2017, Gao et al. [56]	1 (MRI)	1 (tube)	0	1 (tube)	1 (MRI)	FSI	open/closed switching	0 (attachment points only)	positions only (no geometry)	0
2017, Khodaei et al. [78]	PS (Geom and prescribed motion from MRI)	0	0	1	1 (Geom from anatomical data)	FSI	0	1	0	0
2017, Pedrizzetti et al. [79]	1 (MRI)	0	0	0	0	-	0	0	0	0
2017, Spandan et al. [55]	1	1 (tube)	0	1 (tube)	1	FSI (mechanical and natural)	0	0	0	0
2018, Caballero et al. [74]	PS (CT-scan)	PS (CT-scan)	0	PS (CT-scan)	PS (CT-scan) with varying thickness	FSI	PS (CT-scan)	1 (point-source insertion to model the effects)	1	1
2018, Govindarajan et al. [80]	1	1 (tube)	0	0	1 (PS Geom)	FSI	0	0	0	0
2018, Meschini et al. [69]	1 (as in Meschini et al. [81])	1 (tube)	0	1 (tube)	1	IBM	1 (porous disk)	1 (direct-forcing)	0	0

(Table continued on next page.) *Legend:* LV = Left Ventricle, LA = Left Atrium, PV = Pulmonary Veins, Ao = Aorta, MV = Mitral Valve, AV = Aortic Valve, CT = Chordae Tendineae, PM = Papillary Muscles, Trab. = Trabeculae. MV Method = Modeling strategy for the MV (e.g., FSI, IBM, on/off, porous disk...). 0 = not modeled, 1 = generic model, PS = patient-specific.

Year, Ref	Cardiac Compartments				Valves			Subvalvular and Internal Structures		
	LV	LA	PV	Ao	MV Geom	MV Method	AV	CT	PM	Trab.
2018, Meschini et al. [81]	1 (ideal adult model)	1 (tube)	0	1 (tube)	1	IBM	1 (porous disk)	0	0	0
2019, Celotto et al. [49]	PS (MRI)	1 (tube)	0	1 (tube)	1 (from Domenichini and Pedrizzetti [54])	1 (from Domenichini and Pedrizzetti [54])	plane open/closed	0	0	0
2019, Chan et al. [82]	1	0	0	0	0	-	0	0	0	0
2019, Collia et al. [83]	1 (MRI)	0	0	0	1 (CT + echo)	IBM	simple open/close (no leaflets)	0	0	0
2019, Collia et al. [84]	1	0	0	0	1 (improved from Domenichini and Pedrizzetti [54])	1 (improved from Domenichini and Pedrizzetti [54])	same as Collia et al. [83]	0	0	0
2019, Feng et al. [57]	0	PS (CT-scan)	0	0	PS (MRI)	FSI	0	1	0	0
2019, Le et al. [22]	PS (MRI)	0	0	0	0 (inlet only from MRI)	-	0	0	0	0
2019, Meschini et al. [85]	1 (as in Meschini et al. [81])	1 (tube)	0	1 (tube)	1	IBM	1 (porous disk)	0	0	0
2019, Su et al. [86]	PS (MRI)	1	1	1	PS (MRI)	-	1	0	0	0
2020, Fumagalli et al. [51]	PS (Geom + Def)	0	0	PS	PS (from MRI + Zygote)	-	0	0	0	0

(Table continued on next page.) *Legend:* LV = Left Ventricle, LA = Left Atrium, PV = Pulmonary Veins, Ao = Aorta, MV = Mitral Valve, AV = Aortic Valve, CT = Chordae Tendineae, PM = Papillary Muscles, Trab. = Trabeculae. MV Method = Modeling strategy for the MV (e.g., FSI, IBM, on/off, porous disk...). 0 = not modeled, 1 = generic model, PS = patient-specific.

Year, Ref	Cardiac Compartments				Valves			Subvalvular and Internal Structures		
	LV	**LA**	**PV**	**Ao**	**MV Geom**	**MV Method**	**AV**	**CT**	**PM**	**Trab.**
2020, Levrero-Florencio et al. [60]	1 (ellipsoid truncated, electromechanical)	0	0	0	0	-	0	0	0	0
2020, Meschini et al. [25]	1	1 (tube)	0	1 (tube)	1	FSI	0	0	0	0
2020, Viola et al. [65]	1 (EFSI)	1 (simplified)	inflow with 4 directions	1	1	FSI	1 (true Geom)	0	0	0
2021, Collia et al. [87]	1	0	0	0	1 (FSI, same as Meschini et al. [81])	-	0	0	0	0
2021, Collia [88]	1	0	0	0	1 (FSI, same as Meschini et al. [81])	-	0	0	0	0
2021, Lantz et al. [73]	PS (Geom and prescribed motion from CT-scan)	1	1	1	1 (native and prosthetic)	open/closed, IBM	1 (open/closed)	0	1	1
2021, Meschini et al. [89]	1 (as in Meschini et al. [81])	1 (tube)	0	1 (tube)	1	IBM	1 (porous disk)	same as Meschini et al. [69]	0	0

(Table continued on next page.) *Legend:* LV = Left Ventricle, LA = Left Atrium, PV = Pulmonary Veins, Ao = Aorta, MV = Mitral Valve, AV = Aortic Valve, CT = Chordae Tendineae, PM = Papillary Muscles, Trab. = Trabeculae. MV Method = Modeling strategy for the MV (e.g., FSI, IBM, on/off, porous disk...). 0 = not modeled, 1 = generic model, PS = patient-specific.

Year, Ref	Cardiac Compartments				Valves			Subvalvular and Internal Structures		
	LV	LA	PV	Ao	MV Geom	MV Method	AV	CT	PM	Trab.
2021, Salvador et al. [63]	PS (MRI), Def from electrome-chanical	0	0	0	0	0D flow-rate model	0 (0D flow-rate model)	0	0	0
2022, Chang et al. [90]	PS (Geom from CT), FSI	0	0	1 (tube)	0	-	0	0	0	0
2022, Collia and Pedrizzetti [91]	PS (Geom + Def from 3D echo)	0	0	0	1 (as in Domeni-chini and Pedrizzetti [54])	(as in Domenichini and Pedrizzetti [54])	open when MV closes	0	0	0
2022, Ghodrati et al. [71]	PS (CT-scan)	PS (CT-scan)	PS (CT-scan)	PS (CT-scan)	1 (tube)	-	0	0	0	0
2022, Goubergrits et al. [52]	PS (CT-scan)	1	1	1	1	2D-planar modeling	2D-planar modeling	1	0	0
2022, Obermeier et al. [48]	PS (CT-scan)	1	1	1	1	2D-planar modeling	2D-planar modeling	1	0	0
2022, Salvador et al. [64]	PS (MRI), Def from electrome-chanical	0	0	0	0	0D model to mimic flow rate	0 (0D model to mimic flow rate)	0	0	0
2022, Zingaro et al. [58]	1 (Zygote, EFSI)	1 (Zygote, RIIS)	1 (Zygote, EFSI)	1 (Zygote, EFSI)	1 (Zygote)	RIIS	1 (Zygote, RIIS)	0	0	0
2023, Bennati et al. [72]	PS (Domain + Def, MRI)	PS	PS	PS	PS	(inst. open/close)	PS	0	0	0

(Table continued on next page.) *Legend:* LV = Left Ventricle, LA = Left Atrium, PV = Pulmonary Veins, Ao = Aorta, MV = Mitral Valve, AV = Aortic Valve, CT = Chordae Tendineae, PM = Papillary Muscles, Trab. = Trabeculae. MV Method = Modeling strategy for the MV (e.g., FSI, IBM, on/off, porous disk...). 0 = not modeled, 1 = generic model, PS = patient-specific.

Year, Ref	Cardiac Compartments				Valves			Subvalvular and Internal Structures		
	LV	**LA**	**PV**	**Ao**	**MV Geom**	**MV Method**	**AV**	**CT**	**PM**	**Trab.**
2023, Bennati et al. [59]	PS (Domain + Def)	PS	PS	PS	PS	(inst. open/close)	PS	0	0	0

Legend: LV = Left Ventricle, LA = Left Atrium, PV = Pulmonary Veins, Ao = Aorta, MV = Mitral Valve, AV = Aortic Valve, CT = Chordae Tendineae, PM = Papillary Muscles, Trab. = Trabeculae. MV Method = Modeling strategy for the MV (e.g., FSI, IBM, on/off, porous disk...). 0 = not modeled, 1 = generic model, PS = patient-specific.

Table 1.1: Overview of numerical simulations and their levels of modeling.

Building on the degrees of fidelity summarized in Table 1.1, the different modeling classes have also been used as controlled experiments to isolate the contribution of specific anatomical structures to intraventricular flow. Several studies have targeted the mitral valve, chordae tendineae, papillary muscles, and atria to quantify their respective roles. The MV shapes the diastolic vortex ring and, more broadly, the intraventricular flow topology [45, 68, 81]. Atrial contraction modifies inflow direction and timing at the mitral orifice and can substantially reshape intraventricular patterns and energetics [71, 86]. Papillary muscles and trabeculae can interact strongly with the flow, disrupting developing vortices and enhancing apical washout [50, 53]. The chordae tendineae alter near-valvular velocity profiles and the spatial distribution of kinetic energy, with noticeable apical differences when they are omitted [69]. Taken together, these studies support the view that, in principle, adding anatomical detail and applying careful numerical treatment (e.g., boundary conditions, mesh resolution, discretization, solver settings) tends to improve model–data agreement; in practice, carefully calibrated simplified models (with kinematics, boundary conditions, and resolution chosen consistently) can reproduce the dominant intraventricular features and energetics with high fidelity [22, 45, 67, 81].

A complementary line of work has examined intraventricular energetics across physiological and pathological states. Early analyses linked inflow orientation and E/A ratio to mixing and residence times, with only a limited direct effect on pumping power [67]; comparative studies characterized the partitioning of KE, TKE, and dissipation over the cardiac cycle [87]. Imaging-based resolution analyses showed that high-resolution image-based simulations reproduce key diastolic features (mitral vortex ring and energetics), whereas intermediate-scale vortices remain challenging [22]; intraventricular energetics also varies with heart rate via concomitant changes in leaflet kinematics [25].

Because the mitral valve governs jet formation within the left ventricle, its representation is one of the most influential modeling choices for intraventricular flow and energetics. Valve-centered modeling has quantified how MV stenosis severity affects KE, WSS, and transvalvular pressure drops [85], how leaflet elasticity feeds back on opening and gradients [49], and how MR alters turbulence, dissipation, mixing, and near-leaflet WSS [48, 59, 72, 83]; prosthetic orientation also reshapes topology and losses [73, 81]. Beyond valves, chamber-scale pathologies (post-infarction remodeling, aneurysm, hypokinesis) disrupt washout and KE levels, creating stasis-prone regions [48, 52, 82]; impaired active relaxation requires higher diastolic filling pressures to maintain output [56].

Taken together, these results show that in silico analyses, ranging from prescribed-kinematics CFD to fully coupled FSI/EFSI and electromechanical digital twins, can disentangle flow organization and energetics in a task-dependent manner, with accuracy governed as much by realistic kinematics and inflow conditions as by geometric complexity. This motivates selecting the lightest modeling formulation that still resolves the target observables (e.g., prescribed-motion CFD or reduced-order couplings for chamber-scale energetics and vortex organization),

while reserving added subvalvular detail and fully coupled FSI/EFSI for questions that hinge on leaflet mechanics, wall-resolved stresses, or mechano-electric feedback. In parallel, the rise of cardiac digital twins illustrates the potential of personalized models to test therapeutic strategies and optimize patient outcomes [92], even though practical deployment still faces non-trivial challenges in computation time, uncertainty quantification, and integration of patient-specific data. The main findings surveyed here are synthesized in Table 1.2, with corresponding modeling choices in Table 1.1.

Year, Ref	Quantities	Purpose	Key Findings
2008, Watanabe et al. [75]	• Vortex • Dissip • Mixing	Study the importance of flow patterns on efficiency of the heart.	Physiological flow path: • does not have an energy saving effect ($\frac{dissip}{\mathcal{P}_{muscle}}$ negligible). • avoids any mixing of blood.
2012, Le and Sotiropoulos [66]	Vortex	Study of the vortex during cardiac cycle.	Information on vortex.
2013, Seo and Mittal [67]	• KE • TKE • Vortex • Dissip • Mixing	Delineate the effect of flow patterns on ventricular performance. Study the effect of the orientation of the jet coming at the MV level, and different E/A ratio.	• The effect of intraventricular blood flow pattern on the pumping power is physiologically insignificant ($\frac{dissip}{\mathcal{P}_{muscle}}$ negligible). • Diastolic flow patterns significantly affect both mixing and residence time of blood cells.
2014, Baillargeon et al. [61]		Present a model.	• Reproduces physiological pressure-volume curves. • Consistent results with experimental and clinical data.
2014, Seo et al. [45]	• Mixing • Flow Patterns	Study the influence of the MV leaflets on diastolic flow patterns.	• A normal physiological MV promotes the formation of a circulatory flow pattern in the LV • The MV leaflets increase the strength of the apical flow, enhancing apical washout and mixing of ventricular blood.
2015, Domenichini and Pedrizzetti [54]	Vortex (VFT)	Proposes a geometric model of the mitral valve.	MV geometry has a strong influence on flow.
2015, Vedula et al. [46]	Vortex	Study if modeling of the LA is important for the flow patterns.	The simulations indicate that the complex flow features in the atrium have an insignificant impact on the ventricular filling.
2016, Vedula et al. [50]	• KE • Vortex • Dissip • Mixing	Study the effects of trabeculae and papillary muscles (PM) on the hemodynamics of the LV.	• Trabeculae and PM significantly disrupt the vortices that develop during early filling. • Trabeculae enhance the apical washout. • Trabeculae enhance viscous dissipation rate of the ventricular flow (but this effect is not significant in the overall power budget).

Table - Continued on next page

Year, Ref	Quantities	Purpose	Key Findings
2016, Lantz et al. [53]	• Vortex • Mixing	Compare model with PM and trabeculae and without.	PM and trabeculae strongly interact with the blood.
2016, Seo et al. [77]	Thrombosis formation	Using a (simplified) coagulation cascade model, study the effect of 3 different degrees of apex aneurysm and different EF on thrombosis formation.	Low flow strength or flow stasis in the apical region lead to thrombus formation.
2016, Su et al. [68]	Vortex (VFT)	Study the influence of the MV on hemodynamics.	• MV plays an important role in the generation of vortex ring. • The asymmetric bileaflet MV directed the transmitral jet towards the apex.
2017, Gao et al. [56]	Pressure	Investigate how myocardial active relaxation function affects the LV pump function.	Diastolic filling pressure increases significantly with impaired myocardial active relaxation to maintain the normal cardiac output.
2017, Khodaei et al. [78]	Pressure (stress on MV leaflets)	Study the effect of CT on MV prolapse.	• Leaflet stress increases during prolapse. • CT forces higher and non-uniformly distributed.
2017, Pedrizzetti et al. [79]	HDF	Estimate HDF. Comparison between HDF from MRI and from model.	-
2017, Spandan et al. [55]	Flow Patterns	Study deformation of the LV depending on the MV model (natural or mechanical). Compare with experimental results.	For the mechanical valve, higher vorticity regions in the wake of the valve. This results in the mitral jet not reaching the bottom of the ventricle. Overall, mechanical MVs adversely affect LV hemodynamics.
2018, Caballero et al. [74]	• LV efficiency • Flow pattern in LA • Stress on MV leaflets	Study of the impact of chordae rupture on the left heart dynamic and severity of MR.	• MR due to ruptured chordae causes a reduction of the LV pump performance, from 75% in healthy case to 23% in severe MR. • Different flow pattern in the LA.
2018, Govindarajan et al. [80]	Vortex	Study how the MV moves, and its influence on vortex formation.	• Anterior leaflet opens more than posterior leaflet. • Vortex helps pumping efficiency.

Table - Continued on next page

Year, Ref	Quantities	Purpose	Key Findings
2018, Meschini et al. [69]	• KE • Flow patterns	Study of the effect of chordae tendineae on flow.	• KE higher when no chordae. • Chordae induce notable differences in the flow structure. Velocity lower in the apex without chordae. • Different LV deformation.
2018, Meschini et al. [81]	• KE • Flow patterns	Study of the flow and KE depending on the MV (natural, biological and mechanical prosthetic) and on the EF.	• When EF physiological, no flow stagnation in the apex (for all MV). • For pathological EF (<40%), bileaflets mechanical valve induces a reduction of the recirculation in the apex. • Biological prosthetic seems better than mechanical one to reproduce physiological flow and KE (even if KE higher).
2019, Celotto et al. [49]	Pressure	Study influence of MV elasticity in flow.	• The elasticity of the valve influences the amplitude of the mitral opening. • The timings of opening/closure are driven by the transmitral blood flow due to the ventricular dynamics. • The increase of stiffness increases the transvalvular pressure gradients.
2019, Chan et al. [82]	• KE • Vortex • Dissip	Investigate the correlation between four myocardial infarction parameters with intraventricular vortex and flow energetics.	In essence, they observed KE during diastole and systole and linked its increase and decrease to the four factors.
2019, Collia et al. [83]	Volume of regurgitation	Study MR depending on the LV (healthy or dilated) on the MV (healthy and pathological, different degrees of prolapse).	• Physiological flow path: Regurgitating volume is found to be proportional to the effective orifice area, with the limited dependence of the LV geometry and type of prolapse. • May be associated with thrombogenic risk.
2019, Collia et al. [84]	Flow patterns	Study of flow depending on the viscosity at the IB. Comparison with a FSI solution. Study of the influence of MV modeling.	"This model of valvular dynamics corresponds to an asymptotic description of leaflet motion when information about tissue properties are not available or cannot be extrapolated"
2019, Feng et al. [57]	• KE • Dissip	Study effect of pathological conditions and geometric and structural variations.	MR results in higher LA pressure and dissip, but reduce fluid residence time.

Table - Continued on next page

Year, Ref	Quantities	Purpose	Key Findings
2019, Le et al. [22]	KE	Study of different mesh size on the flow and correlate with MRI results.	• Suggests that it is feasible for CFD to replicate important features of the diastolic flow including the mitral vortex ring and its energetics (LV KE). • Other features such as the mid-level vortex cannot be retrieved from the CFD under current simulation assumptions.
2019, Meschini et al. [85]	• KE • Mixing • WSS	Study of MV stenosis, with 4 different severity levels.	• The mitral jet shrink and strengthen when the stenosis gets more severe. • With stenosis severity, the KE of the flow, the tissues shear stresses, the transvalvular pressure drop and MR increase.
2019, Su et al. [86]	• KE • Vortex	Study of the effect of the atrium and MV. Studied four models: with/without the atrium and with/without the mitral valve (MV) each time.	• The atrium significantly altered the way fluid arrived (compared to modeling just a tube) • The influence of the MV is not negligible. KE much lower when no MV.
2020, Fumagalli et al. [51]	• Pressure • WSS	Study of different severity degrees of SAM.	The subaortic stenosis due to the combination of HOCM and SAM yields a jet-like flow through the LVOT, with sensible pressure jumps and localized high WSS in the ascending aorta.
2020, Levrero-Florencio et al. [60]		Present an electromechanical model, do a sensitivity analysis.	Some mechanical biomarkers are dominated by sensitivity parameters.
2020, Meschini et al. [25]	• KE • Pressure • WSS	Study effect of Heart Rate (HR) on flow and KE.	• As the number of bpm increases, the KE also rises. • Regarding the FSI of the leaflets, they do not open at the same time nor in the same way depending on the bpm.
2020, Viola et al. [65]	• KE • WSS	Present an EFSI model.	To present the model.
2021, Collia et al. [87]	• KE • TKE • Dissip	Study energetics in LV and RV, and compare them.	-
2021, Collia [88]	Mixing	Study of MV asymmetry and regurgitation.	Optimal valve asymmetry was found at 0.25, with a favorable range between 0.2 and 0.4.

Table - Continued on next page

Year, Ref	Quantities	Purpose	Key Findings
2021, Lantz et al. [73]	• Vortex • Dissip • Mixing • Flow Patterns	Investigate the effect of prosthetic valve orientation on LV flow patterns (1 native valve and prosthetic valve with 4 angles).	• Blood goes deeper to the apex when native valve. • Much more dissipation when prosthetic valve (but the same for the 4 angles).
2021, Meschini et al. [89]	Pressure	Study of hypertrophy of MV leaflets and their link to SAM. Test for different hypertrophy, leaflet size and EF.	SAM occurs when elongated leaflets, hypertrophic ventricles and strong ejection fraction are present at the same time.
2021, Salvador et al. [63]		Present a complete electromechanical digital twin.	Shown that it can be used to simulate therapies and predict the effect of patient-specific parameters.
2022, Chang et al. [90]		Propose a scalable parallel algorithm for simulating the cardiac (FSI) of a patient-specific human left ventricle.	Present their model.
2022, Collia and Pedrizzetti [91]	• KE • TKE • Vortex (VFT) • HDF	Study the effect of MV asymmetry.	• Optimal asymmetry: 0.2. • When the asymmetry was reversed (PL > AL), more dissipation and KE.
2022, Ghodrati et al. [71]	• Vortex (VFT) • Flow patterns	Study the importance of the atrium. Test with physiological atrium and tube.	Atrium is important to achieve the correct flow (arrival angle) at the MV level.
2022, Goubergrits et al. [52]	• KE • Mixing • Pressure • Dissip	Investigate the effect of aneurysms, MR, hypokinetic LVs on KE, dissip, washout.	• Disturbed washout in aneurysmal cases. • Diastolic jet less coherent when higher MR.
2022, Obermeier et al. [48]	• KE • Dissip	Four patients with and without LV aneurysm and with severe and no MR. All selected LVs are dilated and characterized by a reduced EF.	• KE higher when aneurysm, and lower when MR. • Dissip higher when aneurysm and when MR too.
2022, Salvador et al. [64]		Study the role of mecha-electric feedback and hemodynamic coupling in ventricular tachycardia related to a scar.	Mecha-electric feedback influences the duration and stability of tachycardias.

Table - Continued on next page

Year, Ref	Quantities	Purpose	Key Findings
2022, Zingaro et al. [58]	• Vortex • Flow patterns • Pressure	3D cardiac electromechanical model of the left ventricle coupled to a lumped-parameter (0D) closed-loop model.	Present their model.
2023, Bennati et al. [72]	• Pressure • WSS	Compare healthy and different regurgitant scenarios (with change in HR or LV volume when MR).	• Same LV pressure for all the cases. • Higher WSS on MV leaflets in MR.
2023, Bennati et al.[59]	• TKE • Mixing • Pressure • WSS	Investigate and compare between different subjects the occurrence of turbulence and the risk of hemolysis and of thrombi formation.	• There is less risk of thrombus formation in the atrium and ventricle in the case of MR, but more turbulence occurs. • More thrombi risk when no MR.

Table 1.2: Overview of numerical simulations and their investigated quantities.

Most simulation studies have quantified energy loss primarily as viscous dissipation in simplified or idealized left heart geometries, often omitting the left atrium and pulmonary veins and adopting instantaneous valve switching. In contrast, this thesis employs an image-based, patient-specific left heart that includes the left atrium and pulmonary veins, together with a mitral valve whose opening and closure are prescribed as smooth, time-continuous kinematics. On this basis, we establish a closed kinetic energy budget on the moving ventricular domain, not limited to dissipation alone, which permits a quantitative assessment of pumping efficiency and of the influence of mitral valve geometry and kinematics on that efficiency. The same budget is then applied to mitral regurgitation to separate intraventricular viscous dissipation from the additional retrograde loss across the mitral plane induced by the regurgitant jet, thereby quantifying their respective contributions to the overall efficiency penalty.

1.4 Thesis objectives and overview

1.4.1 Objectives

The goal of this work is to quantify how global and local determinants shape left heart hemodynamics, with a particular focus on the role of mitral valve geometry on intraventricular flow organization, energetic costs, and mixing, and the specific energetic penalty introduced by mitral regurgitation. To this end, the thesis pursues the following objectives:

1. Develop a high-fidelity, image-based computational framework for left heart flows (YALES2BIO, ALE finite-volume formulation), including an improved parametric MV model.

2. Distinguish between global scaling effects (heart rate/size) and local valvular effects (leaflet orientation and opening area) on intraventricular flow organization.

3. Establish a kinetic-energy budget on the ventricular domain and apply it to study dissipation and pumping efficiency across MV configurations.

4. Quantify apical mixing and evaluate how MV-driven jet strength and direction modulate apical renewal.

5. Measure the energetic cost of MR under prescribed kinematics; evaluate the effect of regurgitant volume and assess mechanism-dependent effects (Type II vs. Type IIIb).

1.4.2 Thesis overview

Chapter 2 introduces the YALES2BIO solver and the numerical ingredients for complex cardiac flows (ALE formulation, discretization, turbulence modeling),

and presents a MV model developed in this thesis.
Chapter 3 describes the image-based left heart geometry, boundary conditions, mesh, and solver settings for the reference left heart used for the simulations. It also describes the reference MV configuration, then reports baseline hemodynamics for this reference case.
Chapter 4 presents two parametric studies. Section 4.1 varies global parameters (heart rate and volume) while keeping mitral valve morphology and kinematics fixed, and quantifies their impact on intraventricular velocities and vortices. Section 4.2 varies mitral valve parameters (effective orifice area and leaflet orientation) under the same time-continuous kinematics and ventricular wall motion, and measures the resulting changes in diastolic jet angle and strength as well as vortical topology.
Chapter 5 introduces two complementary approaches. The first is a detailed ventricular kinetic energy budget, used to quantify viscous dissipation and myocardial power, and to enable comparative KE/TKE assessment across MV configurations. The second is a preliminary apical-mixing metric based on a passive scalar, offering an exploratory perspective on transport phenomena in the apex. **Chapter 6** focuses on MR: it defines MR and reviews prior works, then introduces a methodology to impose regurgitation under prescribed kinematics. The chapter analyzes a reference MR case (Type II), investigates the effect of the variation of the regurgitant volume, and compares mechanisms at matched EROA and RV (Type II vs. Type IIIb).

Chapter 2

Complex hemodynamic simulations: the YALES2BIO solver

Chapter contents

2.1 The YALES2BIO solver 32
2.2 Blood flow modeling 32
2.2.1 Governing equations 32
2.2.2 Initial and boundary conditions 33
2.3 Arbitrary Lagrangian-Eulerian (ALE) formulation 34
2.3.1 Governing equations in ALE form 34
2.3.2 Integral formulation 35
2.3.3 Finite-volume discretization and control volumes 35
2.3.4 Low-storage Runge-Kutta time advancement 36
2.3.5 Pressure projection method 38
2.3.6 Turbulence modeling 38
2.4 Valve modeling 40
2.4.1 Legacy immersed-boundary valve model 40
2.4.2 Limitations and motivation for an updated model 41
2.4.3 Improved mitral valve model (present work) 42
2.4.4 Assessment of the proposed model 45

This chapter describes the numerical methods used to simulate patient-specific intracardiac blood flow with the YALES2BIO solver. The YALES2BIO frame-

work is first introduced as a massively parallel finite-volume code for turbulent flows on unstructured meshes, together with the Arbitrary Lagrangian-Eulerian (ALE) formulation employed to handle large, time-dependent cardiac deformations. Particular attention is given to the treatment of cardiac valves: the legacy immersed-boundary model and its limitations are reviewed, followed by the improved mitral valve model developed in this work. Finally, dedicated test cases are presented to validate the new valve model.

2.1 The YALES2BIO solver

All the simulations in this thesis were performed using the in-house YALES2BIO solver [93] (www.imag.umontpellier.fr/~yales2bio/). YALES2BIO is an extension of the YALES2 solver (Yet Another LES Solver, [94]), originally developed in 2007 by V. Moureau at CORIA. YALES2 was initially designed to solve the low-Mach number Navier-Stokes equations, in both incompressible and variable-density contexts, using Large Eddy Simulation (LES) and Direct Numerical Simulation (DNS) approaches within a finite-volume framework on unstructured meshes.

YALES2BIO was built upon this foundation to extend the capabilities of YALES2 to biomechanical applications. Developed at IMAG, it incorporates specific models for cardiovascular and blood-related flows, ranging from organ-scale hemodynamics to cellular-level dynamics. YALES2BIO has been successfully applied and validated in a variety of configurations, including heart flow geometries [47, 70], an FDA's idealized medical device [95], cerebral aneurysms [96] and biomimetic aortic valves [97], to cite a few. The numerical methods implemented in the solver are detailed in the following sections.

2.2 Blood flow modeling

Blood is a complex suspension composed of red blood cells, white blood cells, platelets, and proteins carried in a plasma medium. Due to its particulate composition and shear-thinning behavior, blood exhibits non-Newtonian rheological properties, especially at low shear rates and in microcirculation. However, in large vessels and cardiac cavities, where shear rates are high and vessel diameters exceed roughly 100 μm, these non-Newtonian effects are often considered negligible [98, 99]. In such conditions, blood can be accurately modeled as an incompressible Newtonian fluid for the cardiac simulations performed in this work.

2.2.1 Governing equations

Under these assumptions, blood motion is governed by the incompressible Navier-Stokes equations:

$$\begin{aligned} \frac{\partial \mathbf{u}}{\partial t} + (\mathbf{u} \cdot \nabla)\mathbf{u} &= -\frac{1}{\rho}\nabla p + \nu \nabla^2 \mathbf{u} + \frac{\mathbf{f}}{\rho}, \\ \nabla \cdot \mathbf{u} &= 0. \end{aligned} \tag{2.1}$$

with:

- $\mathbf{u}$: velocity field ($\mathrm{m.s^{-1}}$),
- p: pressure field (Pa),
- ρ: density ($\mathrm{kg.m^{-3}}$),
- ν: kinematic viscosity ($\mathrm{m^2.s^{-1}}$),
- $\mathbf{f}$: volumetric force ($\mathrm{N.m^{-3}}$).

These equations are solved over a moving fluid domain $\Omega_f(t) \subset \mathbb{R}^3$, bounded by $\partial\Omega_f(t)$. The boundary is decomposed as:

$$\partial\Omega_f(t) = \partial\Omega_f^i(t) \cup \partial\Omega_f^w(t) \cup \partial\Omega_f^o(t),$$

with the three parts defined as:

- $\partial\Omega_f^i(t)$: inlet boundaries (e.g., pulmonary veins), where a Dirichlet condition is imposed on the velocity field,
- $\partial\Omega_f^w(t)$: heart wall and vessel walls, moving boundaries where the wall velocity is prescribed,
- $\partial\Omega_f^o(t)$: outlet boundaries (e.g., aorta), where a convective condition is imposed.

2.2.2 Initial and boundary conditions

To complete the mathematical formulation, initial and boundary conditions must be specified over the domain $\Omega_f(t)$ and its boundary $\partial\Omega_f(t)$, decomposed into inflow, wall, and outflow regions as described above.

- **Initial condition:** The velocity field is initialized at $t = 0$ by:

  $$\mathbf{u}(\mathbf{x}, 0) = \mathbf{u}_0(\mathbf{x}) \quad \text{in } \Omega_f(0),$$

  where $\mathbf{u}_0$ is the initial velocity field, extracted from a previous cycle.

- **Wall boundaries:** A no-slip boundary condition is applied on the moving heart walls and vessels:

  $$\mathbf{u}(\mathbf{x}, t) = \mathbf{u}_s(\mathbf{x}, t) \quad \text{on } \partial\Omega_f^w(t),$$

  where $\mathbf{u}_s$ is the wall velocity, extracted from medical imaging and prescribed as a Dirichlet condition. This condition ensures that blood adheres to the moving cardiac tissue.

- **Inlet boundaries:** A Dirichlet velocity condition is imposed at the pulmonary veins:
$$\mathbf{u}(\mathbf{x}, t) = \mathbf{U}_{\text{in}}(\mathbf{x}, t) \quad \text{on } \partial\Omega_f^i(t),$$
where $\mathbf{U}_{\text{in}}$ is a prescribed inflow profile.

- **Outlet boundaries:** A convective outflow condition is applied at the ascending aorta to ensure mass conservation throughout the cardiac cycle. This boundary condition dynamically adjusts the outflow rate to maintain a consistent mass balance, compensating for any variations in the inflow. The convective outflow condition is expressed as:
$$\frac{\partial u(\mathbf{x}, t)}{\partial t} + U^{conv} \frac{\partial u(\mathbf{x}, t)}{\partial \mathbf{n}} = 0, \tag{2.2}$$
where u is the fluid velocity field, $\mathbf{n}$ is the outward normal at the outlet patch, and U^{conv} is the convective velocity.

This problem formulation enables realistic and physiologically consistent simulations of intracardiac blood flow, with boundary data directly linked to patient-specific anatomical and motion information.

2.3 Arbitrary Lagrangian-Eulerian (ALE) formulation

In cardiac flow simulations, the fluid domain undergoes significant deformation due to the motion of the heart walls and valves. Accurately capturing these geometric changes is essential for a physiologically faithful representation of intracardiac blood flow.

A purely Eulerian framework, in which the computational mesh remains fixed in space, cannot accommodate large deformations without frequent remeshing, which is computationally expensive. Conversely, a Lagrangian approach, where the mesh follows the fluid particles, typically leads to severe mesh distortion in regions of high displacement. To overcome these limitations, the Arbitrary Lagrangian-Eulerian (ALE) formulation is used [100, 101]. ALE combines the advantages of both approaches by allowing the mesh to move with an arbitrary velocity $\mathbf{w}$, independently of the fluid velocity $\mathbf{u}$.

2.3.1 Governing equations in ALE form

In the ALE framework, the material time derivative is reformulated to account for mesh motion. The ALE time derivative of a field ϕ is defined as:
$$\left.\frac{\partial \phi}{\partial t}\right|_{\text{ALE}} = \frac{\partial \phi}{\partial t} + \mathbf{w} \cdot \nabla \phi, \tag{2.3}$$

so that the total rate of change observed along a moving mesh includes both local variation and mesh convection.

Let $\Omega(t) \subset \mathbb{R}^3$ be the time-dependent fluid domain, and let $\mathbf{w}$ be the mesh velocity. In the ALE formulation, the convective term is written relative to the mesh motion. The incompressible Navier-Stokes equations become:

$$\left.\frac{\partial \mathbf{u}}{\partial t}\right|_{\text{ALE}} + ((\mathbf{u}-\mathbf{w})\cdot\nabla)\mathbf{u} = -\frac{1}{\rho}\nabla p + \nu\nabla^2\mathbf{u} + \frac{\mathbf{f}}{\rho}, \tag{2.4}$$

$$\nabla\cdot\mathbf{u} = 0. \tag{2.5}$$

The key feature of this formulation is the presence of the convective term $(\mathbf{u}-\mathbf{w})\cdot\nabla\mathbf{u}$, which reflects the relative motion of the fluid with respect to the moving mesh. When $\mathbf{w}=\mathbf{0}$, the formulation reduces to the classical Eulerian case; when $\mathbf{w}=\mathbf{u}$, it corresponds to the Lagrangian description.

In this work, the mesh motion $\mathbf{w}$ is prescribed on $\partial\Omega_f(t)$ using patient-specific kinematic data extracted from medical imaging.

2.3.2 Integral formulation

The numerical scheme implemented in YALES2BIO is based on a finite-volume formulation: the governing equations are integrated over time-dependent control volumes that deform with the moving mesh (see Section 2.3.3 for the geometric construction). Let $\omega(t) \subset \Omega_f(t)$ be an arbitrary control volume moving at the mesh velocity $\mathbf{w}$. Integrating the ALE momentum equation (2.4) over $\omega(t)$ yields:

$$\int_{\omega(t)} \left.\frac{\partial \mathbf{u}}{\partial t}\right|_{\text{ALE}} dV \;+\; \int_{\omega(t)} \Big[(\mathbf{u}-\mathbf{w})\cdot\nabla\Big]\mathbf{u}\, dV \;=\; \int_{\omega(t)} \left(-\frac{1}{\rho}\nabla p + \nu\nabla^2\mathbf{u} + \frac{\mathbf{f}}{\rho}\right) dV. \tag{2.6}$$

Because the control volume $\omega(t)$ changes with time, the first integral still contains a local time derivative. Applying the Reynolds transport theorem (see Chnafa and Thibaud's PhD thesis [102, 103]), one rewrites (2.6) as:

$$\left.\frac{\partial}{\partial t}\right|_{\text{ALE}} \int_{\omega(t)} \mathbf{u}\, dV \;+\; \int_{\omega(t)} \nabla\cdot\Big[(\mathbf{u}-\mathbf{w})\,\mathbf{u}\Big]\, dV \;=\; \int_{\omega(t)} \text{RHS}\, dV, \tag{2.7}$$

where "RHS" denotes the pressure, viscous, and body-force terms already defined in (2.6). The governing equations are now expressed entirely in integral form over a domain $\omega(t)$ that deforms smoothly with the mesh, making them directly amenable to a finite-volume discretization.

2.3.3 Finite-volume discretization and control volumes

To numerically solve the Navier-Stokes equations, the fluid domain is partitioned into mesh elements. YALES2BIO adopts a finite-volume formulation, in which the spatial discretization results from integrating the governing equations over

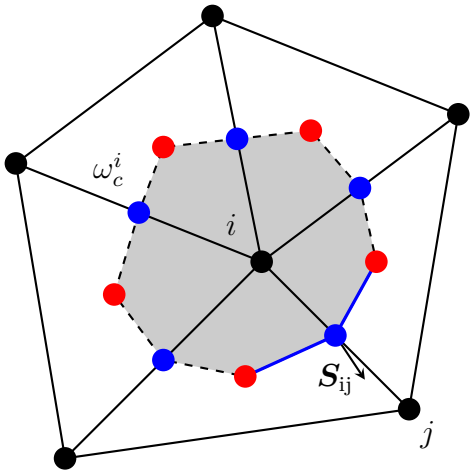


Figure 2.1: Control volume ω_c^i around the node i of an unstructured triangular mesh. The control volume is built by linking the centroids of adjacent mesh elements (red dots) and the midpoints of the edges containing the node i (blue dot). The surface patch S_{ij} to the node pair (i, j) is highlighted in blue, and $\boldsymbol{S}_{\mathrm{ij}} = S_{ij}\boldsymbol{n}_{\mathrm{ij}}$ is its associated non-normalized pair face normal. Figure extracted from the PhD of Garreau [104].

polyhedral control volumes. The control volume ω_c^i associated with a node i is node-centered; its construction in 2D is illustrated in Fig. 2.1.

The dual control volume ω_c^i is a convex polygon (or polyhedron in 3D) that fully partitions the computational domain, *i.e.*, it covers the domain completely without gaps or overlaps. Its volume is defined by:

$$V_i \;=\; \int_{\omega_c^i} \mathrm{d}V. \tag{2.8}$$

The volume average of an arbitrary field ϕ then reads:

$$\overline{\phi}_{\omega_c^i} \;=\; \frac{1}{V_i}\int_{\omega_c^i} \phi\,\mathrm{d}V.$$

Here, $\partial\omega_c^i$ denotes the boundary of ω_c^i, and $S_{ij} \subset \partial\omega_c^i$ the face shared with the neighbouring control volume j (highlighted in blue in Fig. 2.1). The face average of ϕ over S_{ij} is then:

$$\overline{\phi}_{S_{ij}} \;=\; \frac{1}{S_{ij}}\int_{S_{ij}} \phi\,\mathrm{d}S.$$

The practical discretizations of these integrals follow the procedures detailed in the PhD theses of Vantieghem and Garreau [104, 105].

2.3.4 Low-storage Runge-Kutta time advancement

Time integration relies on a four-stage low-storage Runge-Kutta method (LSRK4) [106] recast in the ALE framework and coupled, after the last stage, with Chorin's

projection to enforce incompressibility (see Section 2.3.5). Integrating Eq. (2.7) from $t^n = t^0 + n\Delta t$ to t^{n+1} gives:

$$\int_{t^n}^{t^{n+1}} \frac{\partial}{\partial t}\Big|_{\mathrm{ALE}} \Big[\int_{\omega(t)} \mathbf{u}\, dV\Big]\, dt + \int_{t^n}^{t^{n+1}} \int_{\omega(t)} \nabla\cdot\Big[(\mathbf{u}-\mathbf{w})\mathbf{u}\Big]\, dV\, dt = \int_{t^n}^{t^{n+1}} \int_{\omega(t)} \mathrm{RHS}\, dV\, dt. \tag{2.9}$$

$$V^{n+1}\mathbf{u}^{n+1} - V^n\mathbf{u}^n + \int_{t^n}^{t^{n+1}} \int_{\omega(t)} \nabla\cdot\Big[(\mathbf{u}-\mathbf{w})\mathbf{u}\Big]\, dV\, dt = \int_{t^n}^{t^{n+1}} \int_{\omega(t)} \mathrm{RHS}\, dV\, dt. \tag{2.10}$$

Velocity predictor. The four sub-steps read:

$$\begin{aligned} \mathbf{u}^0 &= \mathbf{u}^n, \\ \mathbf{u}^i &= \mathbf{u}^n \frac{V^n}{V^i} \;+\; \alpha_i \frac{\Delta t}{V^i} \int_{\omega_c(t^i)} \Big[\mathrm{RHS}\big(\mathbf{u}^{i-1}\big) \\ &\qquad - \nabla\cdot\Big(\big(\mathbf{u}^{i-1} - \mathbf{w}^{n+1}\big)\,\mathbf{u}^{i-1}\Big)\Big]\, \mathrm{d}V, \quad i = 1,\dots,4, \\ \mathbf{u}_\star^{n+1} &= \mathbf{u}^4. \end{aligned} \tag{2.11}$$

where $\mathbf{u}_\star^{n+1}$ is the predicted (non-solenoidal) velocity field and $\boldsymbol{\alpha} = \left[\frac{1}{4}, \frac{1}{3}, \frac{1}{2}, 1\right]$. When the mesh is fixed ($\mathbf{w} = 0$) the volumes satisfy $V^i = V^n$ and Eq. (2.11) reduces to the classical LSRK4.

Mesh update. Grid nodes are updated once per Runge-Kutta stage with a second set of low-storage coefficients so that the mesh occupies the correct mid-point configuration required by the discrete geometric conservation law [107, 108]. Assuming the nodal mesh velocity $\mathbf{w}^{n+1}$ remains constant over the whole time step, the node positions are advanced according to:

$$\begin{aligned} \mathbf{x}^0 &= \mathbf{x}^n, \\ \mathbf{x}^i &= \mathbf{x}^{i-1} + \beta_i\, \Delta t\, \mathbf{w}^{n+1}, \quad i = 1,\dots,4, \\ \mathbf{x}^{n+1} &= \mathbf{x}^4 + \beta_f\, \Delta t\, \mathbf{w}^{n+1}, \end{aligned} \tag{2.12}$$

with $\boldsymbol{\beta} = \left[\frac{1}{8}, \frac{1}{24}, \frac{1}{12}, \frac{1}{4}\right]$ and $\beta_f = \frac{1}{2}$. After the four sub-steps the grid lies at the intermediate time $t^{n+\frac{1}{2}}$; the final push β_f transports it to t^{n+1}.

Discrete geometric conservation [107]. At each stage the control-volume V^i must satisfy:

$$V^i - V^n = -\alpha_i\, \Delta t \int_{\omega_c(t^i)} \nabla\cdot\mathbf{w}^{n+1}\, dV, \qquad i = 1,\dots,4, \tag{2.13}$$

so that the mesh nodes are advected in such a way that the volume swept by the mesh nodes equals the volume change between t_n and t_i.

2.3.5 Pressure projection method

To enforce incompressibility in the ALE framework, the velocity field predicted after the Runge-Kutta stages is projected onto a divergence-free space using Chorin's projection method [109].

The predicted velocity $\mathbf{u}_\star^{n+1}$ obtained after the explicit Runge-Kutta update is generally non-solenoidal:

$$\nabla \cdot \mathbf{u}_\star^{n+1} \neq 0.$$

To recover a divergence-free velocity field $\mathbf{u}^{n+1}$ satisfying:

$$\nabla \cdot \mathbf{u}^{n+1} = 0,$$

a pressure field evaluated at the intermediate time $t^{n+\frac{1}{2}}$ is introduced to correct the velocity:

$$\mathbf{u}^{n+1} = \mathbf{u}_\star^{n+1} - \frac{\Delta t}{\rho} \nabla p^{n+\frac{1}{2}}.$$

Enforcing the incompressibility constraint leads to a Poisson equation for the pressure at $t^{n+\frac{1}{2}}$:

$$\nabla^2 p^{n+\frac{1}{2}} = \frac{\rho}{\Delta t} \nabla \cdot \mathbf{u}_\star^{n+1}.$$

A Deflated Preconditioned Conjugate Gradient (DPCG) algorithm developed by Malandain [110] is employed to solve this Poisson equation. Once the pressure field is obtained by solving the Poisson equation, the corrected velocity is updated in the control volume:

$$\mathbf{u}^{n+1} = \mathbf{u}_\star^{n+1} - \frac{\Delta t}{\rho} \nabla p^{n+\frac{1}{2}}.$$

This projection step ensures that the final velocity field at time t^{n+1} is divergence-free and satisfies the incompressible Navier-Stokes equations in their ALE form.

2.3.6 Turbulence modeling

Accurately modeling turbulence is essential in cardiac flow simulations due to the transitional and turbulent regimes that occur during phases such as ventricular filling and ejection. Direct Numerical Simulation (DNS), which resolves all turbulent scales, requires extremely fine meshes and is therefore computationally prohibitive for the type of simulations considered in this work. Conversely, Reynolds-Averaged Navier-Stokes (RANS) approaches rely on time-averaging and empirical closure models that tend to oversimplify the highly unsteady and spatially inhomogeneous nature of intracardiac turbulence, failing to capture key features such as vortex breakdown, jet instability, and transitional shear layers.

For these reasons, Large-Eddy Simulation (LES) is adopted as a compromise between accuracy and computational feasibility. LES explicitly resolves the large turbulent eddies, while the smaller scales are modeled using a subgrid-scale (SGS) model.

In LES, the incompressible Navier-Stokes equations are spatially filtered to separate resolved and unresolved scales. Denoting the filtered (resolved) velocity field by $\overline{u_i}$, the equations become:

$$\begin{aligned} \frac{\partial \overline{u_i}}{\partial t} + \frac{\partial \overline{u_i u_j}}{\partial x_j} &= -\frac{1}{\rho}\frac{\partial \overline{p}}{\partial x_i} + \nu \frac{\partial^2 \overline{u_i}}{\partial x_j \partial x_j} + \frac{f_i}{\rho}, \\ \frac{\partial \overline{u_i}}{\partial x_i} &= 0. \end{aligned} \tag{2.14}$$

The nonlinearity introduces the unclosed term $\overline{u_i u_j}$. To isolate the effect of the unresolved scales, the subgrid-scale (SGS) stress tensor is defined as:

$$\tau_{ij}^{\text{sgs}} = \overline{u_i u_j} - \overline{u_i}\,\overline{u_j}.$$

Using this definition, the momentum equation can be rewritten in closed form for the resolved variables:

$$\begin{aligned} \frac{\partial \overline{u_i}}{\partial t} + \frac{\partial \overline{u_i}\,\overline{u_j}}{\partial x_j} &= -\frac{1}{\rho}\frac{\partial \overline{p}}{\partial x_i} + \nu \frac{\partial^2 \overline{u_i}}{\partial x_j \partial x_j} - \frac{\partial \tau_{ij}^{\text{sgs}}}{\partial x_j} + \frac{f_i}{\rho}, \\ \frac{\partial \overline{u_i}}{\partial x_i} &= 0. \end{aligned} \tag{2.15}$$

In this work, the σ-model [111] is used. The chosen SGS model for the residual-stress tensor τ_{ij}^{sgs} is:

$$\tau_{ij}^{\text{sgs}} = -2\nu^{\text{sgs}}\overline{S}_{ij}, \tag{2.16}$$

where $\overline{S}_{ij} = \frac{1}{2}\left(\frac{\partial \overline{u_i}}{\partial x_j} + \frac{\partial \overline{u_j}}{\partial x_i}\right)$. The turbulent viscosity is defined as:

$$\nu^{\text{sgs}} = (C_\sigma\,\Delta)^2\, D(\mathbf{u}), \tag{2.17}$$

where Δ is the local filter width, C_σ is a model constant, and $D(\mathbf{u})$ is a differential operator specific to the turbulent model.

Substituting this yields the final form of the filtered momentum equation used in the simulations:

$$\begin{aligned} \frac{\partial \overline{u_i}}{\partial t} + \frac{\partial \overline{u_i}\,\overline{u_j}}{\partial x_j} &= -\frac{1}{\rho}\frac{\partial \overline{p}}{\partial x_i} + \frac{\partial}{\partial x_j}(\nu + \nu^{\text{sgs}})\frac{\partial^2 \overline{u_i}}{\partial x_j \partial x_j} + \frac{f_i}{\rho}, \\ \frac{\partial \overline{u_i}}{\partial x_i} &= 0. \end{aligned} \tag{2.18}$$

In the σ-model [111], the differential operator is defined as:

$$D(\mathbf{u}) = \frac{\sigma_3(\sigma_1 - \sigma_2)(\sigma_2 - \sigma_3)}{\sigma_1^2}, \tag{2.19}$$

where $\sigma_1 \geq \sigma_2 \geq \sigma_3 \geq 0$ are the three singular values of the resolved velocity gradient tensor.

2.4 Valve modeling

Accurately representing cardiac valves is essential to simulate realistic intracardiac blood flow, as the valve geometry and motion strongly influences inflow patterns and vortex dynamics [48, 49, 59, 112, 113]. The immersed-boundary method (IBM) employed in this work extends the approach originally developed by Chnafa et al. [47] for YALES2BIO. This section begins by reviewing the existing IBM valve model, detailing its overall strategy as well as its simplified geometric and kinematic assumptions. Its main limitations are then discussed, particularly regarding the representation of mitral inflow dynamics. Finally, the improved mitral valve model developed in this thesis is introduced, featuring an anatomy-informed geometry and a time-dependent kinematic law, together with its numerical implementation.

2.4.1 Legacy immersed-boundary valve model

General strategy. The valves are treated with a direct-forcing immersed-boundary formulation embedded in the node-centered finite-volume solver. At every time level t^n a body-force density $\mathbf{f}^n$ is applied to all Eulerian nodes located inside a prescribed valve volume, forcing the intermediate fluid velocity to zero and thereby reproducing a no-slip solid obstacle:

$$\mathbf{f}^n \;=\; -\frac{\mathbf{u}_f^n}{\Delta t} \;-\; \mathrm{RHS}^n, \tag{2.20}$$

where Δt is the time step, $\mathbf{u}_f^n$ is the provisional fluid velocity, and RHS^n represents the sum of convective, viscous, and pressure contributions evaluated at t^n. To guarantee that at least a few mesh nodes lie inside the impermeable region, the leaflets are assigned a small artificial thickness s.

Geometry. Valve annuli are reconstructed from medical images by visual inspection. The contour is discretized as a cloud of Lagrangian markers $\{\mathbf{p}_i\}$, whose coordinates are injected into the numerical domain to define the aortic and mitral annuli.

Aortic valve. The AV is reduced to the regression plane passing through the annulus markers. During systole this plane is fully permeable $\big(\mathbf{f}^n = \mathbf{0}\big)$; during diastole it is given its finite thickness s and becomes impermeable. Because only the intra-ventricular flow upstream of the leaflets is analysed, this crude representation leaves the LV hemodynamics virtually unchanged while keeping the computational cost minimal.

Mitral valve. A more elaborate, yet still kinematically coarse, model is adopted for the MV. The annulus markers define a base plane P_α with geometric center $\mathbf{C}_\alpha$. When the valve is open, an auxiliary plane P_β is generated at a time-dependent distance $l(t)$ from P_α; an elliptic orifice $\epsilon\big[a(t),\, b(t)\big]$ with axes $a(t)$ and $b(t)$ is

defined on P_β, its center $\mathbf{C}_\epsilon$ being offset from $\mathbf{C}_\alpha$ by the eccentricity vector $\mathbf{e}(t)$. The leaflets are represented by triangulated surfaces between the annulus and the ellipse. The configuration switches instantaneously from open (diastole) to closed (systole); no progressive opening or closure is resolved. Figure 2.2 illustrates this geometry.

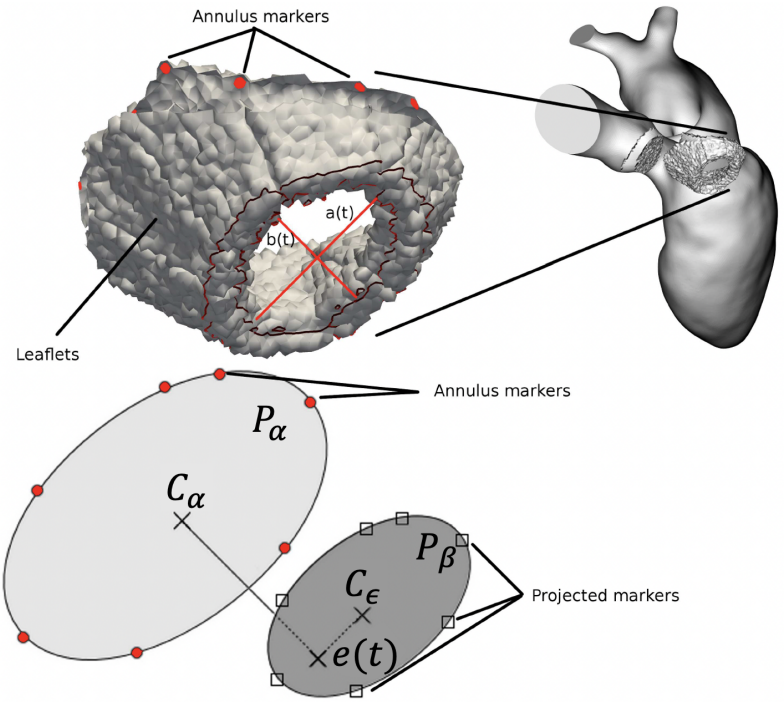


Figure 2.2: **Top left:** annulus markers and reconstructed mitral valve leaflets; the ellipse axes a and b are indicated. **Top right:** complete valve assembly (MV and AV) embedded in the computational domain. **Bottom:** schematic of the MV model. Adapted from Chnafa *et al.* [47].

2.4.2 Limitations and motivation for an updated model

The simplified valve representation described above suffers from several important limitations. Geometrically, the aortic valve is reduced to a flat disc, while the mitral valve leaflets are modeled with excessive and uniform thickness, and it lacks the characteristic anterior-posterior asymmetry. Such simplifications distort the realistic shape and prevent accurate representation of thin-leaflet effects. Kinematically, the instantaneous switching between open and closed states fails to capture the gradual motion and the associated flow features, notably the early-diastolic vortex ring formation and rapid pressure transients observed in experiments. These shortcomings have limited impact from aortic valve flow, since the mitral inflow dominates the left ventricular hemodynamics, justifying the retention of the coarse planar model for the AV. However, for the mitral valve, these approximations strongly affect critical features such as the diastolic

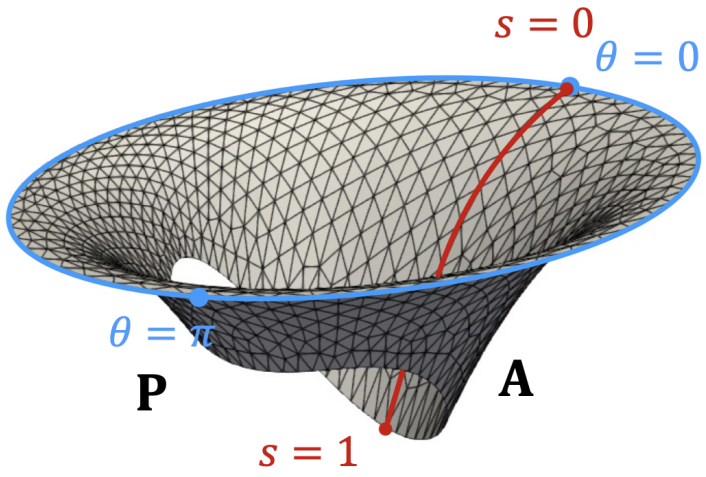


Figure 2.3: Parametric MV geometry for $\varepsilon = 0.35$, $k = 0.6$. Anterior (A) and Posterior (P) leaflets are labeled.

jet angle, vortex-wall interaction, and overall filling efficiency. In addition, the immersed boundary method requires an artificially large leaflet thickness to ensure sufficient numerical resolution inside the immersed region, further compromising the local flow topology. Together, these issues motivated the development of a refined, anatomy-informed mitral valve model with improved geometry, motion description, and numerical implementation, as detailed in Section 2.4.3.

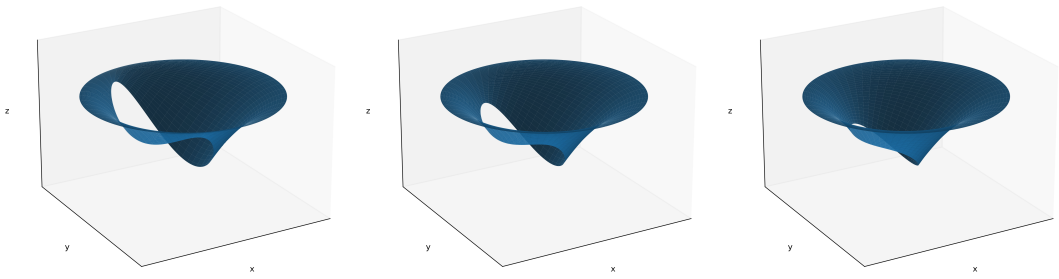
2.4.3 Improved mitral valve model (present work)

2.4.3.1 Geometry

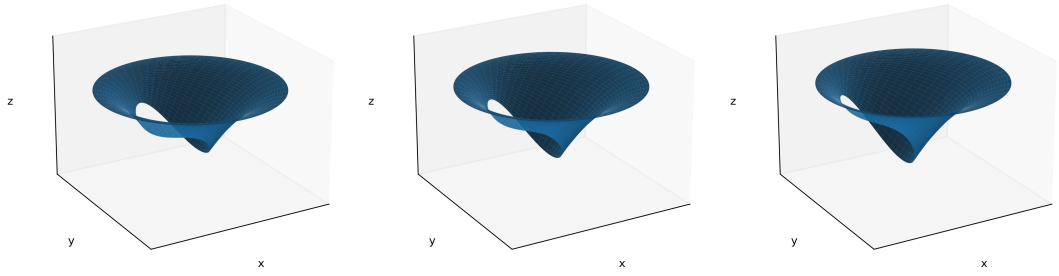
The leaflet surface is generated from the parametric model of Pedrizzetti & Domenichini [54]. The equations describing the position of each Lagrangian nodes at a given time t over the valve read:

$$\begin{aligned} x(\theta, s, t) &= R\cos\theta\Big(1 - s\cos\varphi(\theta, t)\Big) - \varepsilon Rs\cos\varphi(\theta, t), \\ y(\theta, s, t) &= R\sin\theta\Big(1 - sk\cos\varphi(\theta, t)\Big), \\ z(\theta, s, t) &= -s^2\left[\frac{1+k}{2} - \varepsilon\cos\theta + \frac{1-k}{2}\cos 2\theta\right] R\sin\varphi(\theta, t), \end{aligned} \tag{2.21}$$

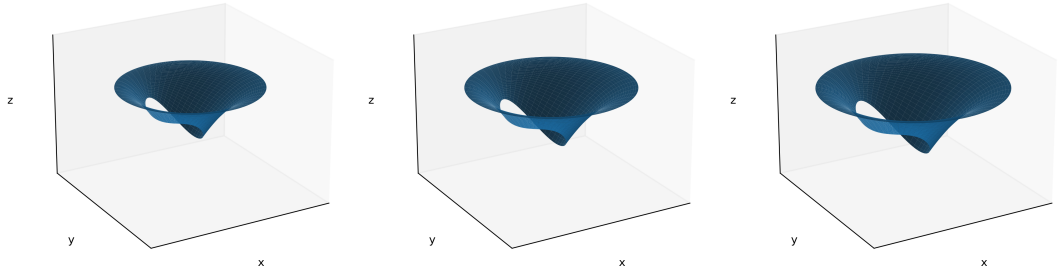
where R is the radius, ε the asymmetry of the valve, and k the leaflet curvature (see Figure 2.4 for an illustration of the effect of these parameters). In these equations, the coordinates θ and s are used to determine the position of each node of the valve and span the ranges $[0, 2\pi]$ and $[0, 1]$, respectively, as shown in Figure 2.3. φ is the opening angle of the valve, and allows a continuous evolution from the closed ($\varphi = 0$) to the open ($\varphi = \varphi_{max}$) position.



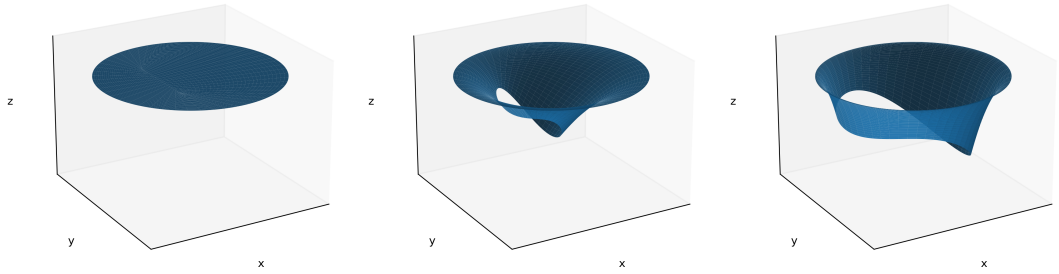
(a) Variation of k ($k = 0.2$, 0.5, 0.8) with $R = 27$mm, $\varepsilon = 0.35$, and $\varphi = 45°$.



(b) Variation of ε ($\varepsilon = 0.30$, 0.45, 0.60) with $R = 27$mm, $k = 0.6$, and $\varphi = 45°$.



(c) Variation of R ($R = 21$, 24, 27 mm) with $k = 0.6$, $\varepsilon = 0.35$, and $\varphi = 45°$.



(d) Variation of φ ($\varphi = 0°$, 40°, 70°) with $R = 27$mm, $k = 0.6$, and $\varepsilon = 0.35$.

Figure 2.4: Effect of the main parameters of the parametric mitral valve model.

2.4.3.2 Kinematics

The leaflet motion is parametrized by the opening angle $\varphi(\theta, t)$, with $\theta = 0$ at the anterior midline and $\theta = \pi$ at the posterior. It is written as:

$$\varphi(\theta, t) \;=\; \varphi_{\max}(\theta)\,\Gamma(t),$$

where $\varphi_{\max}(\theta)$ prescribes the peak opening and $\Gamma : [0, T] \to [0, 1]$ is a smooth function ensuring continuous opening and closure over a cardiac period T.

2.4.3.3 Numerical implementation

The fluid is discretized on an Eulerian grid with nodes $\{\mathbf{x}_j\}_{j=1}^{N_E}$ and velocities $\{\mathbf{u}_j\}$, while the valve is represented on a Lagrangian membrane mesh with M nodes $\{\mathbf{X}_m\}_{m=1}^{M}$. The influence of the deformable valve leaflets on the surrounding fluid is captured with a node-based immersed-boundary formulation that introduces a body-force density $\mathbf{f}$ in the incompressible Navier-Stokes equations. For each Lagrangian (solid) node m, the set of neighboring Eulerian nodes $\mathcal{S}(m)$ is defined for interpolation and spreading; its cardinality is denoted $J(m) = |\mathcal{S}(m)|$ (or simply J when constant).

The local fluid velocity seen by node m is reconstructed by interpolating the $J(m)$ neighboring velocities:

$$\mathbf{U}_{\mathbf{m}}^{\text{fluid}} = \text{Interp}\Big(\{\mathbf{u}_j\}\Big).$$

The interaction force is then evaluated as:

$$\mathbf{F}_{\mathbf{m}} \;=\; -\alpha\,\frac{S_{\text{node}}\,h}{\Delta t}\,\Big(\mathbf{U}_{\mathbf{m}}^{\text{fluid}} - \mathbf{U}_{\mathbf{m}}^{\text{valve}}\Big), \tag{2.22}$$

where S_{node} is the surface area associated with node m, h an effective membrane thickness, Δt the time step, $\mathbf{U}_{\mathbf{m}}^{\text{valve}}$ the nodal velocity of the solid, and α a dimensionless attenuation parameter that regulates the resistance of the membrane.

Because the leaflet is modeled as a zero-thickness membrane, a fixed effective thickness $h = h_0$ is introduced so that $S_{\text{node}}\,h_0$ acts as a reference nodal volume. The value of h_0 is chosen to be of the order of the Eulerian mesh size near the valve and is kept constant in space and time across all simulations. This constant h converts the nodal penalty force $\mathbf{F}_m$ into the volumetric body-force density required by the Navier-Stokes equations. Following Sigüenza *et al.* [114], the nodal force $\mathbf{F}_{\mathbf{m}}$ is spread back onto the Eulerian mesh with a regularized-delta kernel implemented through the Reproducing Kernel Particle Method (RKPM) [115, 116], yielding the body-force density $\mathbf{f}_{\mathbf{j}}$ needed for the Navier-Stokes equations. In all simulations reported in the following chapters, the parameter is set to $\alpha = 1$, which effectively blocks the through-leaflet flux while preserving numerical stability. The pre-factor in Eq. 2.22, which includes the valve node surface area, membrane thickness, and time step, ensure that α yields resolution-robust enforcement across different resolutions of the computational meshes. Figure 2.5 summarizes the successive interpolation and spreading steps.

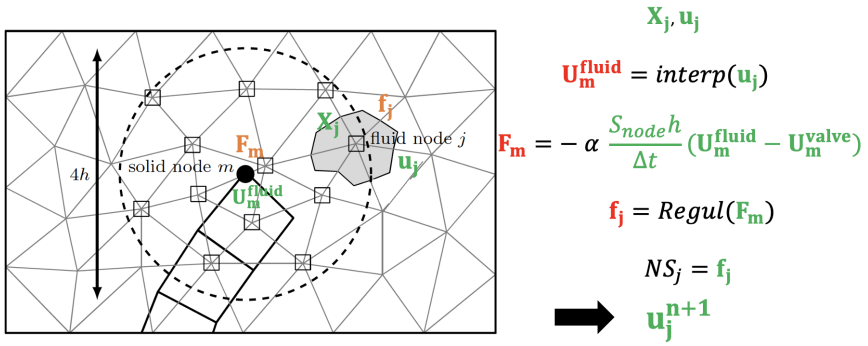


Figure 2.5: Schematic of the RKPM-based immersed-boundary procedure. A solid node m (black circle) interacts with the surrounding Eulerian fluid nodes j (grey squares). **(i)** The fluid velocity is interpolated to the solid node to give $\mathbf{U}_{\text{fluid}}$. **(ii)** The penalty-type force $\mathbf{F}$ is evaluated with Eq. (2.22). **(iii)** $\mathbf{F}$ is regularized and spread back onto the Eulerian grid, yielding the body-force density $\mathbf{f}$ that enters the Navier-Stokes solver. **Right:** flow chart of the same steps; quantities already available at the beginning of each sub-step are shown in green, whereas the unknowns to be computed are shown in red. The left-hand sketch is adapted from Sigüenza *et al.* [114].

2.4.4 Assessment of the proposed model

2.4.4.1 Laminar flow around a circular cylinder

To verify the correct implementation of the updated immersed boundary scheme, a classical benchmark is considered: steady laminar flow around a circular cylinder at low Reynolds number. This test case is widely used in the literature for IB methods [117–123], as it provides well-documented reference data both experimental and numerical. The configuration consists of a cylinder of diameter $D = 0.01$ m positioned at the center of a rectangular domain with dimensions $[-8D,\, 25D] \times [-5D,\, 5D]$. A uniform inlet velocity $U_{\text{inlet}} = 0.03\,\text{m.s}^{-1}$ is prescribed at the left boundary, while free-slip conditions are applied on the top and bottom walls. The Reynolds number based on the cylinder diameter is $Re_D = \frac{U_{\text{inlet}} D}{\nu} = 30$, ensuring a steady, symmetric recirculating wake after transients decay.

Two values of the penalty parameter α in Eq. (2.22) were tested ($\alpha = 1$ and $\alpha = 5$) to assess sensitivity of the method to this parameter. To verify convergence, two probes were placed in the wake region: one near the center of the primary recirculating vortex, and the other near the predicted end of the recirculation bubble. After 6000 iterations, the absolute velocity difference between successive iterations at both probes was below $10^{-9}\,\text{m.s}^{-1}$, indicating that a steady state had been reached. Figure 2.6 shows the computed velocity field for the steady state, with clear formation of two symmetric counter-rotating vortices in the cylinder's wake.

A key quantitative metric for validating IB methods in this flow is the length of the recirculation region l. It is defined along the centerline ($y = 0$) as the

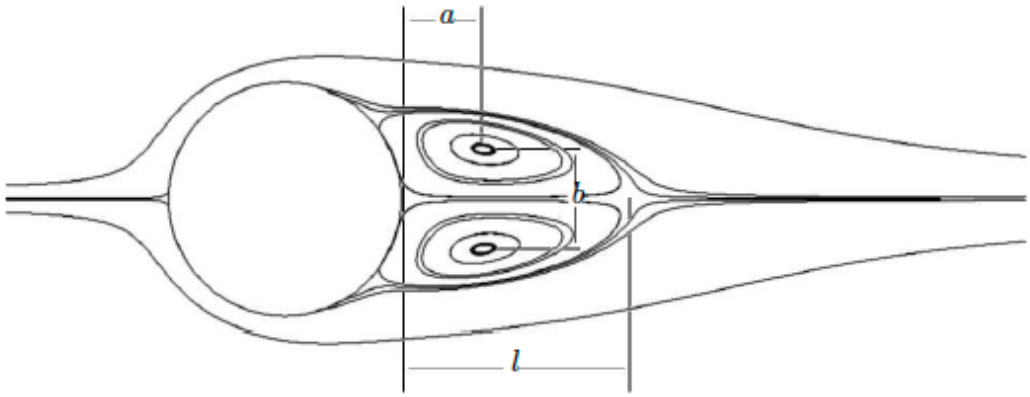


Figure 2.6: Steady-state velocity field around the cylinder at $Re_D = 30$. Two recirculating vortices are visible downstream of the cylinder.

distance from the rear stagnation point on the cylinder to the point where the horizontal velocity component U_x becomes non-negative (i.e. no backflow). The table below compares the present results to previous numerical and experimental studies. The additional quantities a and b denote the semi-major and semi-minor axes of the elliptical approximation of the recirculating vortex.

Table 2.1: Comparison of wake parameters for steady-state flow around a cylinder at $Re_D = 30$ with both experimental and numerical reference data.

Study	$\boldsymbol{l/D}$	$\boldsymbol{a/D}$	$\boldsymbol{b/D}$
Pinelli (numerical) [123]	1.70	0.56	0.52
Coutanceau and Bouard (experiment) [122]	1.55	0.54	0.54
Chnafa (numerical) [102]	1.24	0.47	0.43
Present work ($\alpha = 1$)	1.65	0.68	0.47
Present work ($\alpha = 5$)	1.69	0.68	0.53

The values of l/D obtained with both penalty parameters are close to the reference data, confirming the ability of the RKPM-based immersed-boundary scheme to reproduce the correct recirculation length in steady laminar flow. Slight variations in l/D and b/D reflect the sensitivity of the vortex shape to the IB forcing parameter α, but remain within the range of reported values. Overall, this test case demonstrates that the new implementation yields stable, accurate solutions in a canonical immersed-boundary benchmark problem, supporting its use for the more complex mitral valve simulations presented in later chapters.

2.4.4.2 3D valve in a tube

To further evaluate the behavior of the immersed boundary valve model, a second test case was designed consisting of a three-dimensional tube containing the mitral valve geometry described in Section 2.4.3.1. The computational domain is a

straight cylindrical tube with diameter $D = 0.03$ m and length $L = 0.135$ m, chosen to roughly match characteristic scales of the human heart inflow tract. The valve is positioned at the upper-mid-length, aligned with the tube axis. The simulation setup is illustrated in Figure 2.7, with upstream and lateral views of the geometry.

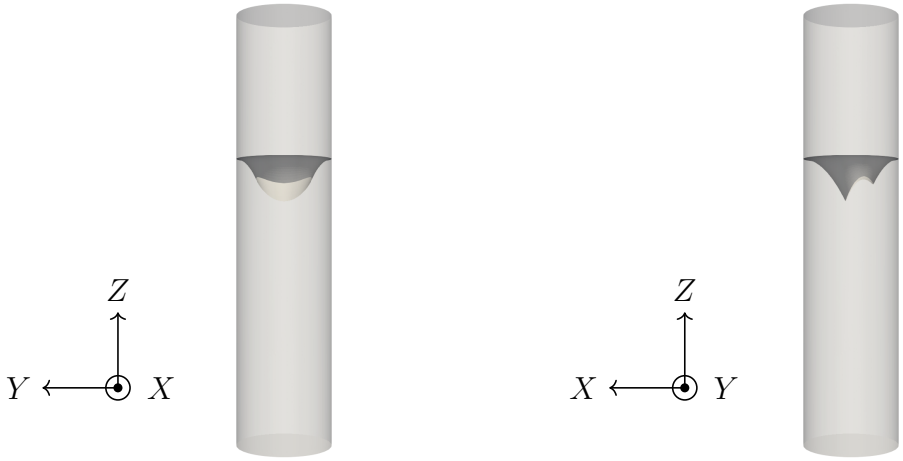


Figure 2.7: Configuration of the 3D test case: mitral valve model placed inside a straight cylindrical tube.

The goal of this test case is to investigate the influence of key numerical and geometric parameters on the valve model's ability to restrict or permit flow, i.e. to quantify its effective blockage or permeability depending on the immersed boundary forcing parameters. The inlet boundary condition was set to $\mathbf{u} = 0.35$ m.s^{-1}. Because the valve reduces the effective flow area, this choice produces a through-valve jet of approximately $1\,\mathrm{m\,s^{-1}}$, representative of the peak diastolic mitral velocity. The mesh resolution for both the Eulerian fluid grid and the Lagrangian valve surface was chosen to be approximately 1 mm, consistent with the resolution used in the full heart simulations.

In this context, "effective blockage/permeability" is quantified by assessing the numerical leakage through the immersed-boundary valve. Ideally, an impermeable interface would yield zero net flux across the valve surface. In practice, exact impermeability is not achieved numerically, and a small through-surface flow remains. This through-flow is quantified as:

$$Q_{\mathrm{leak}} = \int_{S_{\mathrm{valve}}} \mathbf{u}\cdot\mathbf{n}\,\mathrm{d}S,$$

where $\mathbf{u}$ is the local velocity and $\mathbf{n}$ the outward unit normal to the valve surface S_{valve}. Numerically, the integral is computed as a discrete sum over all surface facets.

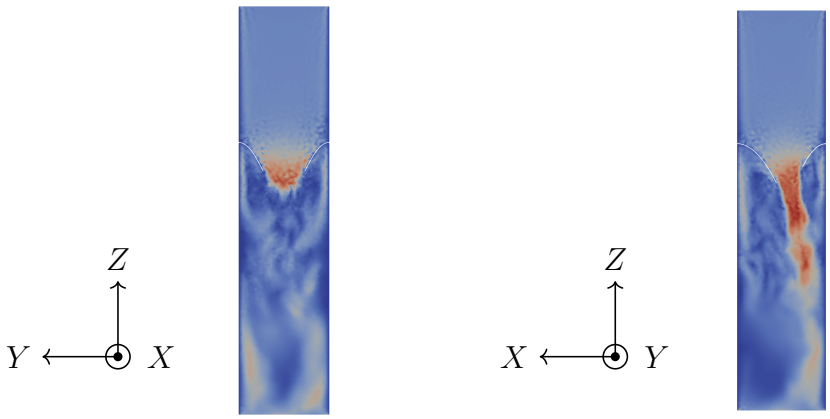
Simulations were performed for varying values of the penalty coefficient α and different time steps Δt, allowing a systematic study of their impact on the valve's hydraulic performance. Table 2.2 summarizes the different combinations

of α and Δt tested in these simulations. The resulting velocity fields are shown in Figure 2.8.

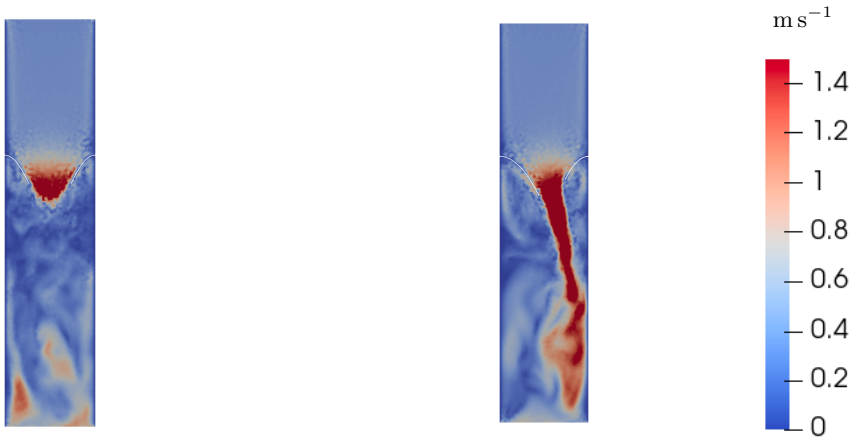
Table 2.2: Summary of the six test configurations. A fixed time step was prescribed in each case, so variations in CFL reflect differences in the velocity field induced by the immersed boundary forcing. Reported CFL values correspond to the maxima measured during the simulations.

$\boldsymbol{\alpha}$	$\boldsymbol{\Delta t}$ (s)	$\mathbf{CFL_{max}}$
1	3×10^{-4}	0.45
1	1×10^{-4}	0.17
1	3×10^{-5}	0.07
2	1×10^{-4}	0.20
2	3×10^{-5}	0.08
3	3×10^{-5}	0.08

This configuration provides a controlled setting to calibrate the IBM, evaluate its sensitivity to numerical parameters, and verify that the resulting flow resistance is consistent with expected valve-like behavior before applying the method to the full ventricular geometry. Figure 2.9 shows the leakage through the valve for all tested configurations. As α increases, the valve blocks the flow more effectively. However, the time step Δt has an even stronger influence on the leakage.



(a) $\alpha = 1$, $\Delta t = 3 \times 10^{-4}\,\mathrm{s}$



(b) $\alpha = 1$, $\Delta t = 3 \times 10^{-5}\,\mathrm{s}$



(c) $\alpha = 3$, $\Delta t = 3 \times 10^{-5}\,\mathrm{s}$

Figure 2.8: Velocity field in the tube at $t = 0.30\,\mathrm{s}$ for three different cases.

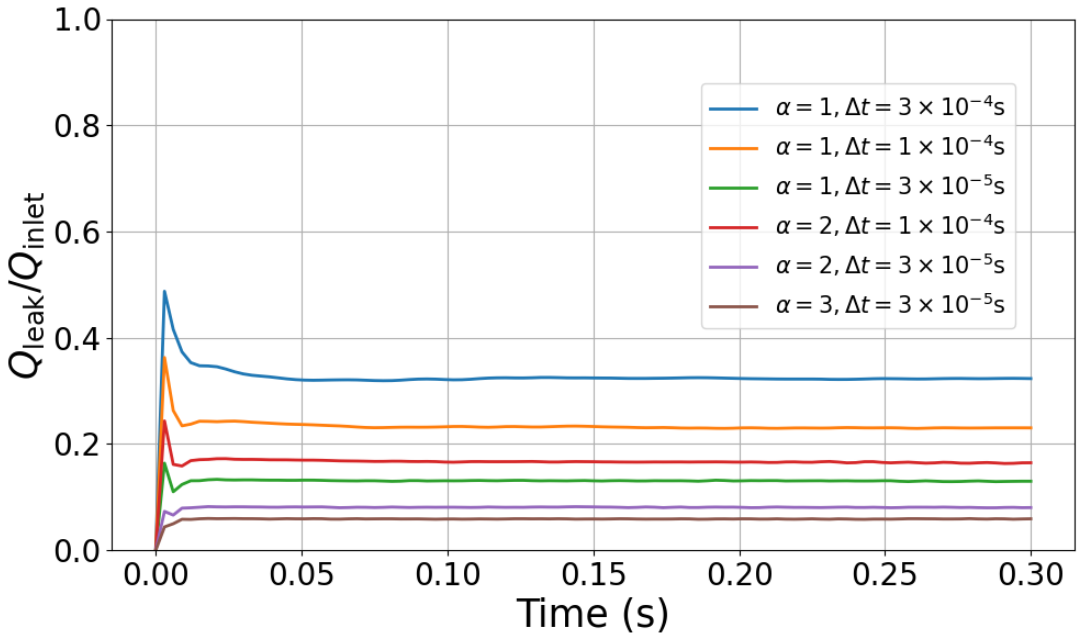


Figure 2.9: Leakage through the valve for the six test configurations.

Chapter 3

Intraventricular hemodynamics

Chapter contents

3.1 Description of the model 52
3.1.1 Image-based left heart geometry 52
3.1.2 Boundary conditions 53
3.1.3 Numerical solver and mesh 55
3.1.4 Valve model 57
3.1.5 Leakage verification and parameter selection 58
3.2 Hemodynamics over one cardiac cycle 59
3.2.1 Qualitative description 60
3.2.2 Atrial inflow and pre-filling vortex seeding 62
3.2.3 Ventricular filling 62
3.2.4 Systolic ejection 65
3.2.5 Conclusion 67

This chapter aims to characterize the blood flow within the left ventricle under normal conditions. The objective is to describe the large-scale flow features that emerge over a cardiac cycle, based on numerical simulations of a healthy heart. The first part of the chapter presents the computational model used in this study, including the anatomical geometry, valve representations, and boundary conditions. The second part is dedicated to the analysis of the intraventricular flow itself, highlighting the temporal evolution of key structures such as jets, vortices, and their interaction with the cardiac motion.

3.1 Description of the model

3.1.1 Image-based left heart geometry

The geometry used in this study was derived from medical images. The heart comes from a cardiac CT examination performed on a patient treated at the University Hospital of Toulouse Rangueil (France), as initially described by Chnafa et al. [47]. The data were fully anonymized and retrospectively analyzed in accordance with the hospital's regulations. The CT exam consists of N = 10 medical images along the cardiac cycle of period $T = 1$ s with a spatial resolution of 2x2x2 mm. The process involved analyzing a set of N images of a patient's heart recorded at different times of the cardiac cycle. Among these images, one was chosen as the template image (at the end of the E-wave), and segmentation was performed using a classical thresholding method [124] to extract the region of interest. In order to perform motion-prescribed flow simulations, not only the computational domain should be known at each instant, but the displacement of the endocardium has to be known to impose the wall boundary conditions. The movement of the endocardium was obtained using image registration [125]. For each non-template image, a transformation was sought based on the voxel gray level to map them on the template image. The outcome of this process was N fields of deformation corresponding to the N instants throughout the cardiac cycle (of course, for the template image, the deformation field is the identity). To obtain the geometry for any instant over the cardiac cycle, a Fourier interpolation was employed, using $m = 5$ Fourier modes to ensure periodicity of the motion. The resulting geometry represents a patient-specific left heart evolving over time in a way which is fully consistent with the geometry changes observed in the medical images. Further details on the methodology can be found in prior studies [47, 70]. The result is a patient-specific left heart geometry, accounting for individualized deformations, and encompassing key anatomical structures such as the aorta, the LV and atrium, and the four pulmonary veins. This computational domain is presented Figure 3.1. The motion of the endocardium is identical to the one published by Chnafa et al. [47], whose flow has been validated by comparison with the literature. The main characteristics of the patient-specific left heart considered are gathered in Table 3.1. The Heart Rate (HR) is 60 bpm. The E/A ratio is the ratio of the flow rate at the MV at the E-wave over the flow rate at the MV at the A-wave. Specifically, at the E-wave ($t/T = 0.51$) the flow rate was $Q = 410$ mL.s^{-1}, and at the A-wave ($t/T = 0.98$) the flow rate was $Q = 75$ mL.s^{-1}, resulting in a ratio of 5.5. In this case this ratio is indicative of a pathological condition. The End Diastolic Volume (EDV) and the End Systolic Volume (ESV) are the volume of the ventricle at the end of diastole and systole, respectively. The Stroke Volume (SV) is the difference between EDV and ESV, that is the volume of blood pumped from the LV per beat. The Cardiac Output (CO) is the volume of blood being pumped by the LV per unit time; it is defined by $CO = SV \times HR$. The Ejection Fraction (EF) is the volumetric fraction of blood ejected from the ventricle with each heartbeat: $EF = SV/EDV \times 100$. All the values reported in Table 3.1

correspond to a normal situation, except the E/A ratio (and, to a lesser extent, the ejection fraction) which is more relevant to a restrictive filling condition. Note however that this condition cannot be confirmed in absence of more clinical data. Figure 3.1 present the computational domain.

Table 3.1: Main characteristics of the geometry of the heart used in this study.

Parameter	**Present simulation**	**Normal range**
Heart rate (bpm)	60	60–100
E/A ratio	5.5	1.0–2.0
End Diastolic Volume (EDV) (mL)	140	65–240
End Systolic Volume (ESV) (mL)	70	16–143
Stroke Volume (SV) (mL)	70	55–100
Cardiac Output (CO) (L.min^{-1})	4.2	4.0–8.0
Ejection Fraction (%)	50	55–70

3.1.2 Boundary conditions

The inflow boundary condition $Q(t)$ imposed at the four pulmonary veins was determined from the mass conservation principle:

$$\begin{aligned} Q(t) &= \frac{dV_{LA}}{dt} \text{ when the MV is closed,} \\ Q(t) &= \frac{dV_{LA}}{dt} + \frac{dV_{LV}}{dt} \text{ when the MV is open.} \end{aligned} \tag{3.1}$$

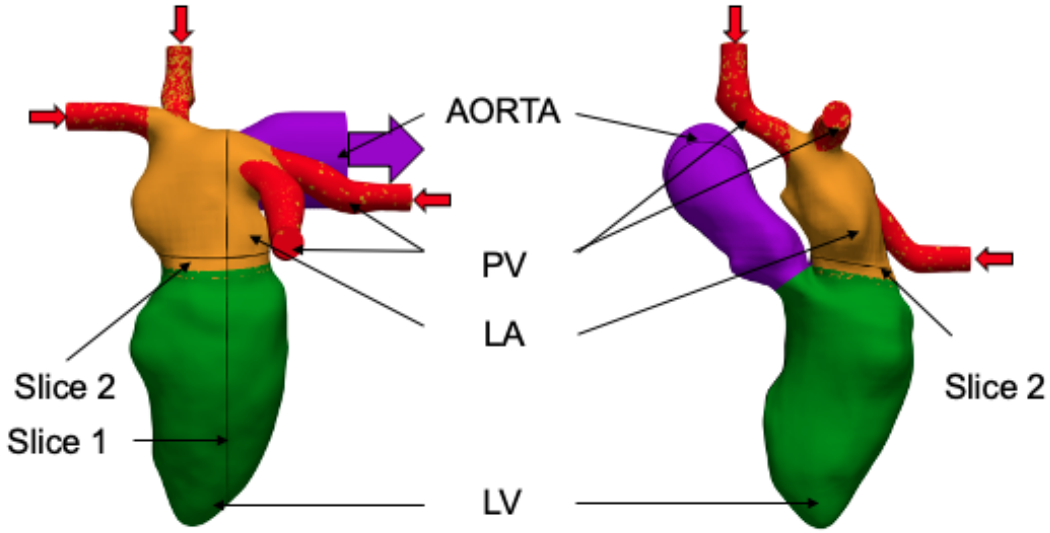
In Eq. (3.1), $Q(t)$ is the inflow, V_{LA} is the volume of the atrium (on Fig 3.1, in orange + red) and V_{LV} is the volume of the ventricle (in green on Fig 3.1). It was chosen to set the flow rate equally distributed at each of the four pulmonary veins. The velocity at the inlet is given by:

$$u_j(t) = -\frac{Q(t)}{A_j(t)}\xi_j n_j(t), \tag{3.2}$$

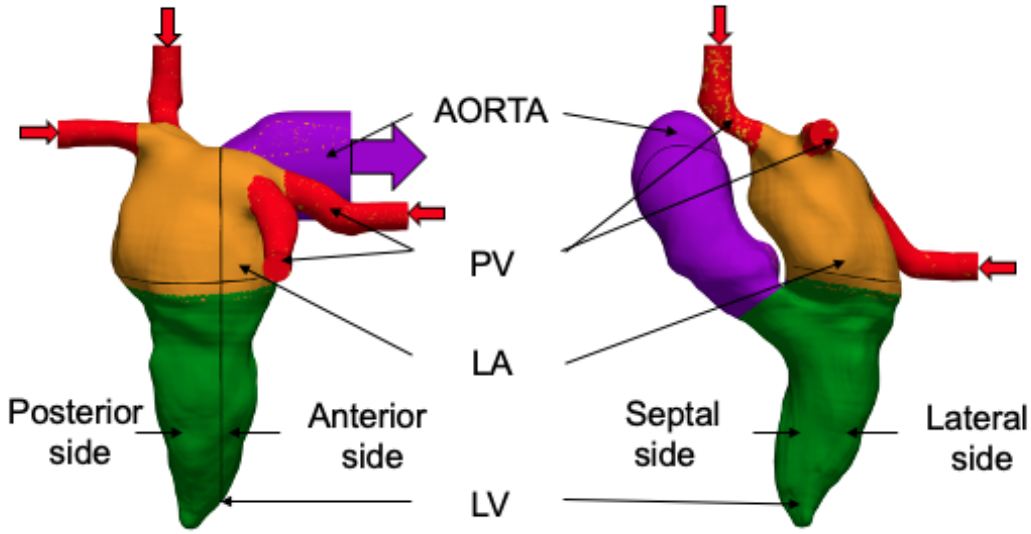
where n_j is the outward normal vector, A_j is the area of inlet condition j ($j = 1, \ldots, 4$), and ξ_j represents the distribution factor. Assuming a uniform distribution, ξ_j was set to 0.25 for all j. Furthermore, a uniform velocity profile was imposed at the inlet of each pulmonary vein. The curve of the inflow is displayed in Figure 3.2a.

The convective outflow boundary condition of Chapter 2, Eq. (2.2), is employed. The convective velocity $U^{conv}$is determined by ensuring that the volumetric flow rate at the outlet equals the sum of the volumetric flow rates at the inlets, thereby satisfying mass conservation. Specifically:

$$U^{conv} = \frac{1}{A_{out}}(\sum_{j=1}^{4} Q_j - \frac{dV}{dt}), \tag{3.3}$$



(a)



(b)

Figure 3.1: Computational domain: The 4 pulmonary veins are highlighted in red, the Left Atrium (LA) in orange, the LV in green, and the Aorta in purple. The black lines indicate the positions of the slices used to display the flow. Specifically, the vertical line represents slice #1, while the nearly horizontal line corresponds to slice #2. (a) Domain at $t/T = 0.01$ (start systole) (b) Domain at $t/T = 0.38$ (end systole).

where A_{out} is the cross-sectional area of the ascending aorta, $\frac{dV}{dt}$ is the variation of the volume and Q_j are the flow rates at the four pulmonary vein inlets. This ensures that the outflow adapts dynamically to match the total inflow, maintaining mass conservation throughout the cycle. The curve of the outflow is displayed in Figure 3.2b.

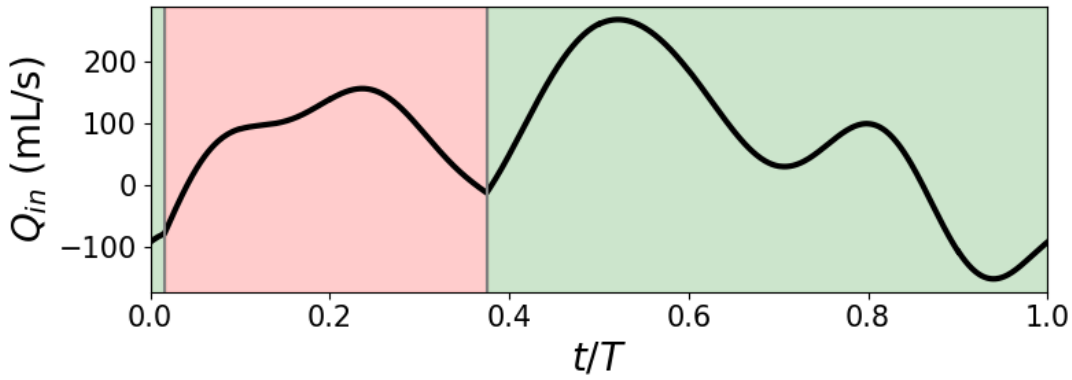
A no-slip condition was applied to the heart walls.

3.1.3 Numerical solver and mesh

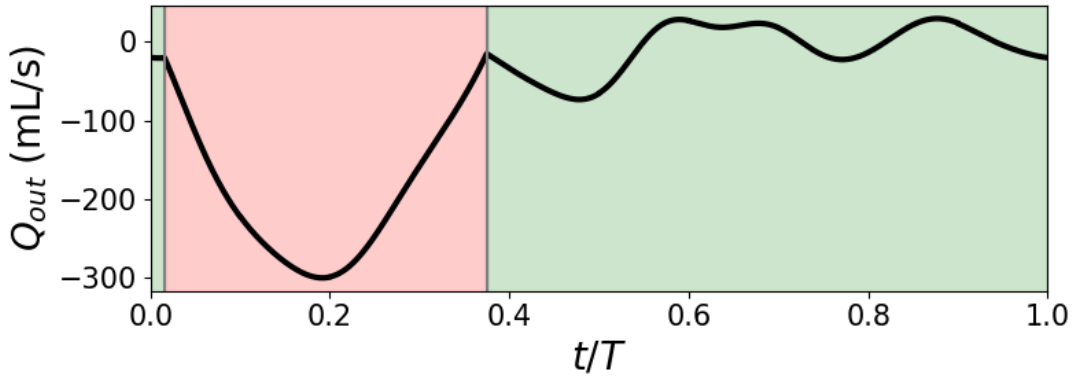
Blood was modeled as an incompressible Newtonian fluid, whose motion is governed by the incompressible Navier-Stokes Equations (NSE). The NSE were solved thanks to a finite-volume formalism, implemented in the in-house YALES2BIO solver [93] (www.imag.umontpellier.fr/~yales2bio/). A centered fourth-order scheme was used to approximate the spatial gradients within the Arbitrary Lagrangian-Eulerian formalism, while an explicit low-storage four-step Runge-Kutta scheme was applied for time-stepping. The pressure term was accounted for thanks to the Chorin's projection-correction method [109]. More details of the numerical method are given Chapter 2.

The left heart geometry was discretized with three million tetrahedral elements of typical size 0.8 mm. This element size was chosen to adequately resolve the characteristic scales of the flow features, such as the jet width and vortex structures. The Kolmogorov length scale η was evaluated to be of the order of $2\text{x}10^{-5}$ m (See [47] for more details), indicating that a Direct Numerical Simulation (DNS) would require more than a billion cells. Consequently, Large Eddy Simulation (LES) was adopted. The quality of the LES was assessed using the Pope criterion [126], which showed that during the phase of highest turbulent activity ($t/T = 0.65$), more than 80% of the turbulent kinetic energy was captured in 85% of the computational domain, confirming the suitability of the mesh for this study. The large scales of the flow were resolved, while the smaller subgrid scales (SGS) were modeled using SGS models. The σ-model [111], which is well suited to represent wall-bounded turbulent/transitional flows, was used to mimic the effect of the SGS on the dynamics of the resolved ones. The time step calculation was based on a CFL (Courant–Friedrichs–Lewy condition) number of 0.1. This value was chosen to ensure numerical stability and to minimize numerical leakage through the valve (see Section 2.4 for the valve modeling), which should ideally remain perfectly impermeable. This choice ensures that the numerical leakage remains below a few percent of the maximum flow rate, maintaining high accuracy in the simulation. Consequently, the temporal resolution of the simulation varied between [0.03 - 0.1] ms.

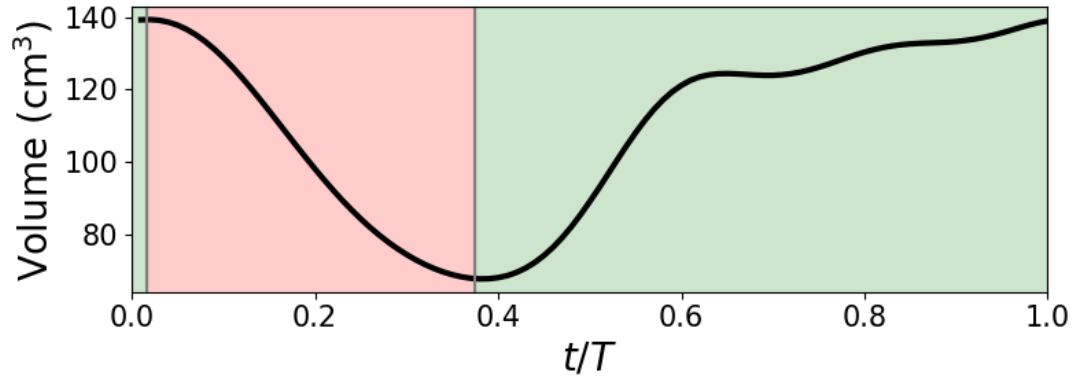
To mitigate the effect of cycle-to-cycle fluctuations, all the analyses were performed after the flow has been phase-averaged. Initially, 5 cycles were run to disregard initial conditions, followed by 15 cycles used to obtain the phase-averaged data. In this thesis, the post-processing of the data was performed using ParaView [127]. More precisely, the phase-averaged fields were computed



(a)



(b)



(c)

Figure 3.2: Top plot: Flow rate at the inlet (total of the 4 pulmonary veins) during the cardiac cycle. Middle plot: Flow rate at the outlet (aorta). Bottom plot: Volume during a cycle. Red and green backgrounds mark systole and diastole, respectively.

by averaging, for each phase index, the corresponding solution snapshots over the retained cycles. Since each simulated cycle was stored using the same temporal sampling (100 instants per cycle), the mean velocity field at a given phase was obtained as the average of the velocity fields at that phase over all cycles, and the associated fluctuating component was defined as the deviation from this mean.

3.1.4 Valve model

The geometry and motion of the cardiac valves are difficult to recover from medical images because of their limited spatio-temporal resolution. For the aortic valve, the annulus position is extracted from the images and the valve is modeled as a planar patch that alternates between permeable and impermeable states depending on the cardiac phase; given its limited impact on LV intraventricular flow, no further geometric detail is included. By contrast, the mitral valve is expected to significantly shape LV hemodynamics [113, 128]. The MV is represented as an infinitely thin surface whose annulus position follows the medical images, while the leaflet shape is prescribed by the three-dimensional parametric model of Pedrizzetti and Domenichini [54] (see also Section 2.4.3.1).

For completeness, the leaflet surface is written in terms of the annular angle $\theta \in [0, 2\pi]$ and the curvilinear coordinate $s \in [0, 1]$:

$$\begin{aligned} x(\theta, s, t) &= R\cos\theta\left(1 - s\cos\varphi(\theta, t)\right) \; - \; \varepsilon R\, s\cos\varphi(\theta, t), \\ y(\theta, s, t) &= R\sin\theta\left(1 - sk\cos\varphi(\theta, t)\right), \\ z(\theta, s, t) &= -\, s^2\left(\frac{1+k}{2} - \varepsilon\cos\theta + \frac{1-k}{2}\cos 2\theta\right) R\sin\varphi(\theta, t), \end{aligned} \tag{3.4}$$

where R is the annular radius, ε the leaflet asymmetry, and k a curvature parameter. The opening angle $\varphi(\theta, t)$ evolves continuously from the closed state ($\varphi = 0$) to the open state ($\varphi = \varphi_{\max}$) according to:

$$\varphi(\theta, t) \;=\; \varphi_{\max}(\theta)\,\Gamma(t),$$

with $\theta = 0$ at the anterior leaflet midline and $\theta = \pi$ at the posterior midline. To control jet orientation and effective area, different peak angles are allowed for the anterior and posterior leaflets, φ_{ant} and φ_{post}. The spatial envelope is:

$$\varphi_{\max}(\theta) = \begin{cases} \varphi_{\text{ant}} + \dfrac{\varphi_{\text{post}} - \varphi_{\text{ant}}}{\pi}\,\theta, & 0 \le \theta < \pi, \\ \varphi_{\text{post}} - \dfrac{\varphi_{\text{post}} - \varphi_{\text{ant}}}{\pi}\,(\theta - \pi), & \pi \le \theta \le 2\pi, \end{cases} \tag{3.5}$$

and the temporal envelope $\Gamma(t) \in [0, 1]$ is chosen as a smooth tanh-based function of the normalized time t/T (with T the cardiac period), with coefficients (a_i, b_i)

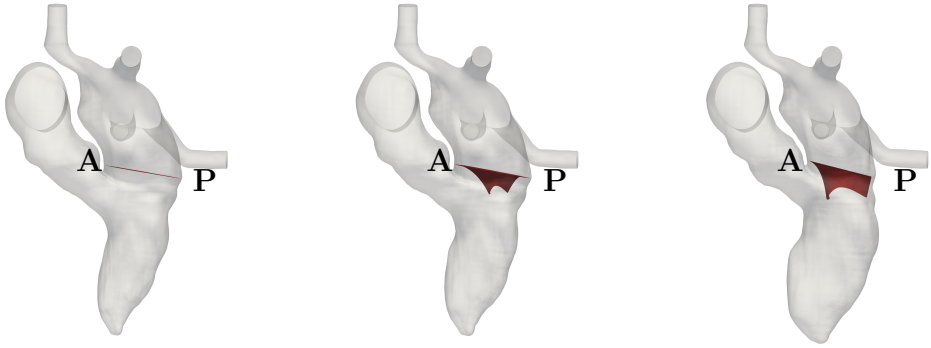


Figure 3.3: MV embedded in the patient-specific LV mesh at opening fractions of 0%, 50%, and 100%. Anterior (A) and posterior (P) leaflets are labeled.

tuned to match the imaged opening/closure timings:

$$\Gamma(t) = \begin{cases} \frac{1+\tanh\left(a_1 - b_1\, t/T\right)}{2}, & t/T < 0.2, \\ \frac{1+\tanh\left(b_2\, t/T - a_2\right)}{2}, & 0.2 \le t/T < 0.7, \\ \frac{1+\tanh\left(a_3 - b_3\, t/T\right)}{2}, & \text{otherwise}, \end{cases}$$

with $(a_1, b_1, a_2, b_2, a_3, b_3) \approx (0.36,\ 33.33,\ 26,\ 62.5,\ 33.69,\ 33.33)$. The opening/closure timings were prescribed to remain within physiological ranges: for a cardiac period $T = 1$ s, the valve opening transition was set to occur over ~ 80 ms ($\Delta t/T \approx 0.08$), and the closure transition over ~ 150 ms ($\Delta t/T \approx 0.15$) around the onset of systole (systolic duration ≈ 0.375 s). For simplicity, the MV is held at its maximum opening during most of diastole. These values provide a simple kinematic law while remaining consistent with reported mitral valve timing estimates [54, 129]. The resulting leaflet placement at three opening fractions is illustrated in Fig. 3.3, and the temporal envelope $\Gamma(t)$ is shown in Fig. 3.4.

Beyond timing, the geometric parameters are adjusted to remain consistent with physiological MV function. The asymmetry is set to $\varepsilon = 0.35$ (anterior leaflet about twice the posterior [88]), and the ellipticity parameter to $k = 0.6$. The annular radius R follows the imaged annulus and varies between 21.6 and 26.1 mm over the cycle. Leaflet peak angles φ_{ant} and φ_{post} are selected to obtain a jet oriented along the septal wall [14] and to keep the effective orifice area within 4–6 cm^2 with a peak transmitral speed between 0.6 and 1.0 m.s^{-1}; a representative choice is $\varphi_{\text{ant}} \approx 45°$, $\varphi_{\text{post}} \approx 90°$.

3.1.5 Leakage verification and parameter selection

Building on the simplified tube test case of Chapter 2 (Section 2.4.4.2), the sealing performance of the immersed-boundary mitral model was verified in the

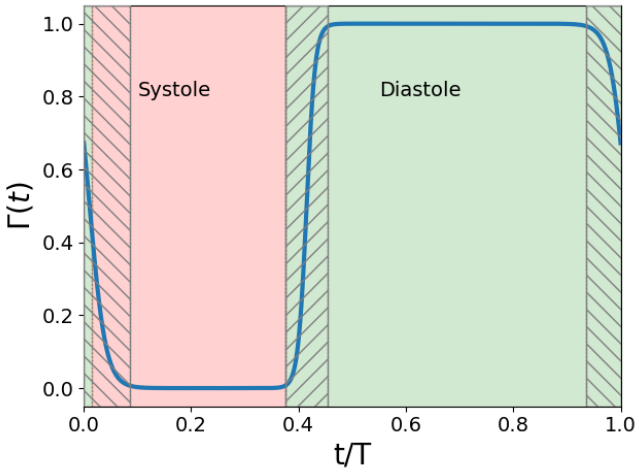


Figure 3.4: Temporal evolution of the opening law $\Gamma(t)$ over one cardiac cycle. Systole (red) corresponds to closure; diastole (green) to the open phase; hatched bands indicate the opening/closure transitions.

patient-specific LV geometry. The objective is to ensure that the no-penetration condition is sufficiently enforced while keeping time stepping accurate and stable.

Because LV velocities vary strongly over the cycle (unlike the test case in Section 2.4.4.2, where a fixed time step was used and no CFL was reported), an adaptive time step capped by CFL ≤ 0.1 is employed. This choice sets the smallest Δt during diastole (when speeds are maximal) and was found to limit immersed-boundary leakage.

Consistent with the sensitivities highlighted by the tube case, the time step Δt primarily controls artificial leakage through the closed leaflets, while the penalty coefficient α has a secondary effect within the range relevant to the present simulations. The parameters are therefore fixed to $\alpha = 1$ with CFL $= 0.1$, yielding time steps between 0.03 and 0.10 ms over the cardiac cycle.

With these parameters, the instantaneous flow rate across the mitral surface (Q_{leak}, see Section 2.4.4.2 for the definition) is computed during the closed phase over one cycle and averaged over five cycles. Figure 3.5 shows the resulting leakage. Integrating the leakage flow over one cycle and normalizing by the mitral inflow volume yields a leakage fraction of about 7%. While not strictly zero, this level is acceptable for the intended simulations and does not alter the global hemodynamic picture discussed in Section 3.2. This verification step supports the choice of numerical parameters adopted in all subsequent LV simulations.

3.2 Hemodynamics over one cardiac cycle

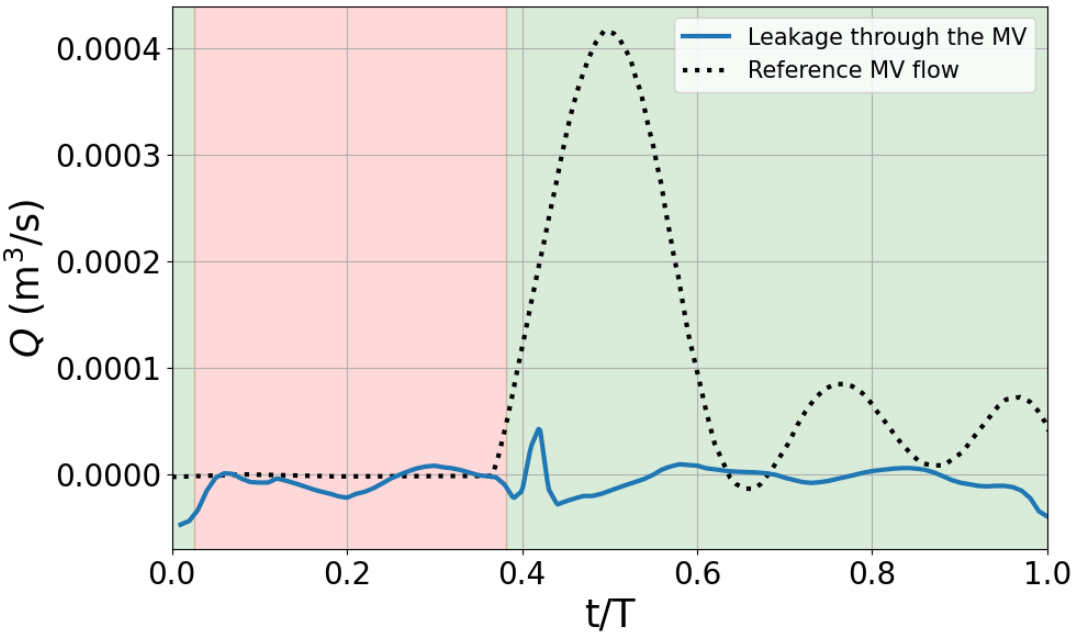


Figure 3.5: Leakage flow rate through the mitral valve over one cardiac cycle in the LV model (average over five cycles; $\alpha = 1$, CFL $= 0.1$). Background colors indicate cardiac phases (red: systole, green: diastole).

3.2.1 Qualitative description

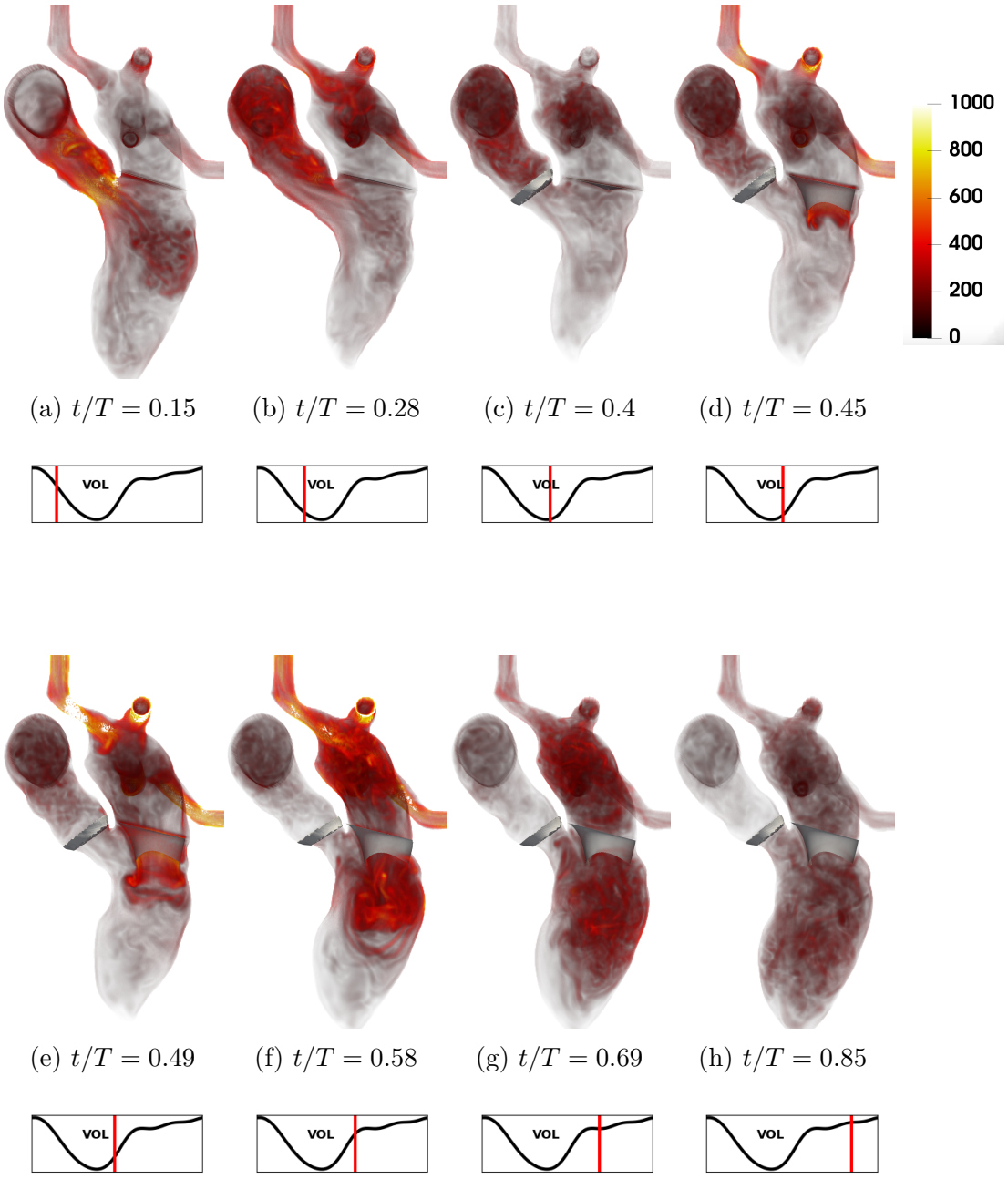
This section provides a qualitative overview of flow dynamics over the cardiac cycle, before examining each phase in detail. To illustrate the global evolution of flow structures, the three-dimensional vorticity magnitude is considered, defined as:

$$\boldsymbol{\omega} = \nabla \times \boldsymbol{u},$$

where $\boldsymbol{u}$ is the velocity field. The vorticity characterizes the local rotation of the fluid and is commonly used to identify coherent structures such as vortices.

Figure 3.6 shows volume renderings of the non-dimensional vorticity magnitude at eight key time points during the cardiac cycle. The lower row in each group of subfigures illustrates the corresponding time position along the ventricular volume curve.

Around the beginning of systole ($t/T = 0.15$, Fig. 3.6a), blood begins to enter the left atrium through the four pulmonary veins. The jets from the different pulmonary veins converge and interact in the atrial cavity ($t/T = 0.28$, Fig. 3.6b), while the mitral valve remains closed. As the mitral valve begins to open and the aortic valve closes ($t/T = 0.40$, Fig. 3.6c), early diastole begins. The MV opening widens and blood begins to flow from the atrium to the ventricle. This initiates the E-wave jet, which grows and progresses along the ventricular wall (see Figs. 3.6d-3.6f). The left ventricle simultaneously expands in response to the incoming flow.



(a) $t/T = 0.15$ (b) $t/T = 0.28$ (c) $t/T = 0.4$ (d) $t/T = 0.45$

(e) $t/T = 0.49$ (f) $t/T = 0.58$ (g) $t/T = 0.69$ (h) $t/T = 0.85$

Figure 3.6: Volume rendering of non-dimensional vorticity magnitude at different times of the simulation. Below each images, the curve represent the ventricular volume over time, with the red line indicating the current time in the cardiac cycle.

As diastole progresses ($t/T = 0.49$ to 0.69, Figs. 3.6e–3.6g), the jet velocity gradually decreases, and the vortex structure expands to fill the entire ventricular volume. By the end of diastole ($t/T = 0.85$, Fig. 3.6h), the vorticity is relatively weak but distributed throughout all the ventricle.

Following this phase, the mitral valve closes and the aortic valve reopens, initiating systole. The ventricle contracts, ejecting blood through the aortic valve and into the systemic circulation (see again $t/T = 0.15$, Fig. 3.6a). From Fig. 3.6a to Fig. 3.6c, the ventricular volume is clearly decreasing, indicating active systolic contraction. During this period, blood is ejected into the aorta while the left atrium is simultaneously filled via the pulmonary veins.

This overview illustrates the succession of phases across the cardiac cycle, from atrial filling to ventricular ejection, and highlights the progressive evolution of flow structures. A phase-by-phase quantitative analysis follows in Secs. 3.2.2–3.2.4.

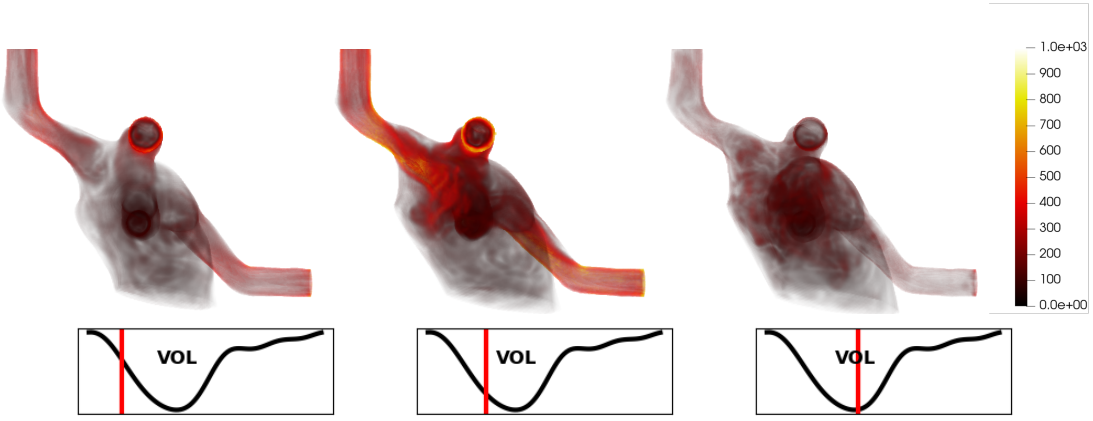
3.2.2 Atrial inflow and pre-filling vortex seeding

Blood enters the left atrium through the four pulmonary veins and rapidly organizes into a coherent swirling motion, as shown in Fig. 3.7a. Panel (a) displays isosurfaces of the non-dimensional vorticity magnitude at three representative instants during systole ($t/T = 0.15$, 0.26, and 0.40). Panel (b) highlights the mutual entrainment of the four venous inflows and the resulting flow complexity. Finally, Panel (c) presents the in-plane velocity field on slice #2 (see Fig. 3.1), just above the mitral valve. The flow exhibits a clear counterclockwise movement before arriving at the MV level, preconditioning the direction of the E-wave jet.

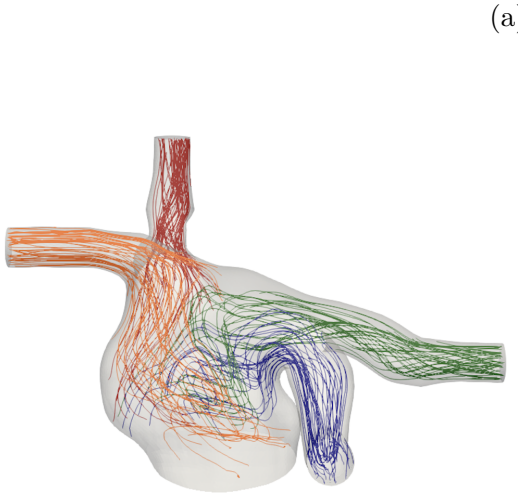
3.2.3 Ventricular filling

When the pressure in the left atrium exceeds that in the left ventricle, the mitral valve opens, in this case at $t/T = 0.375$. Blood then flows from the atrium into the ventricle, forming the E-wave jet. As shown in Fig. 3.8, the jet travels along the ventricular wall and reaches a peak velocity of 0.95 $\mathrm{m.s^{-1}}$ during early diastole. Around mid-diastole, a large vortex begins to develop in the central region of the ventricle (label (a) in Fig. 3.8d), accompanied by a smaller, secondary vortex (label (b)) located between the jet and the ventricular wall, on the side of the posterior mitral leaflet. The primary vortex rotates in a clockwise direction, while the smaller one rotates counter-clockwise. As the inflow decelerates (Fig. 3.8f), the main vortex expands and eventually fills most of the ventricular cavity, organising the flow for the subsequent ejection phase.

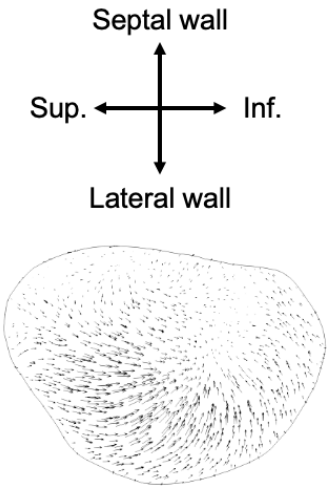
This large vortex is clearly visible in Fig. 3.9, which displays the phase-averaged velocity field at $t/T = 0.7$, corresponding to the mid-to-late diastolic phase of the cardiac cycle. This structure is commonly interpreted as functionally beneficial, as it may contribute to redirecting the flow towards the aortic valve and thus assist systolic ejection [16, 130]. In this visualization, green regions delineate individual



(a)

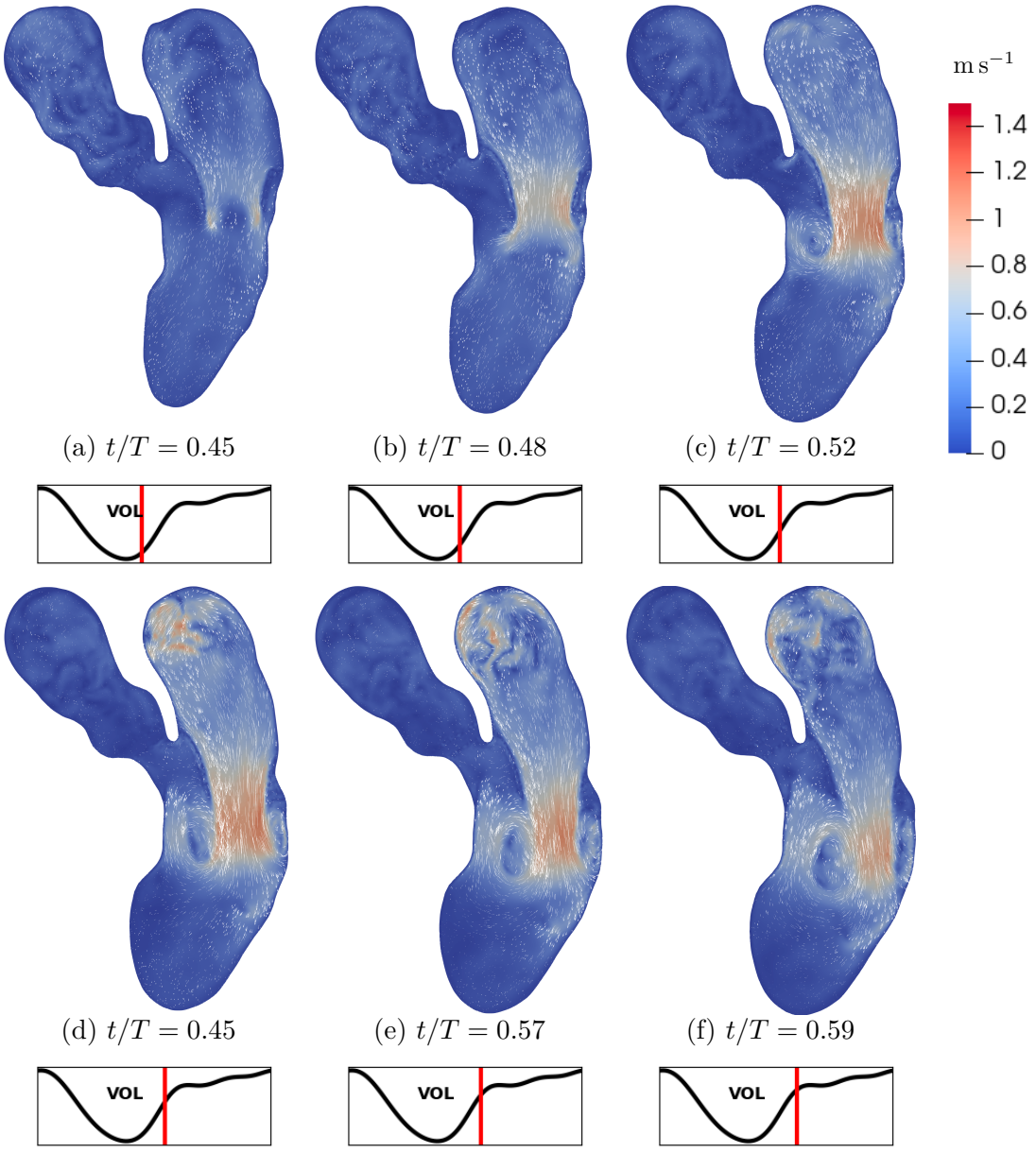


(b)



(c)

Figure 3.7: Flow in the Atrium. (a) Volume rendering of non-dimensional vorticity magnitude. From left to right: $t/T = 0.15$ (first part of systole), $t/T = 0.26$ (second part of systole) and $t/T = 0.4$ (end systole). (b) Visualization of the flow coming from the four pulmonary veins. Each color represents streamlines for a different PV. (c) Velocity field arriving at the MV annulus at $t/T = 0.4$, in the plane slice 2 defined in Fig 3.1.Plane is viewed from the top of the heart in the apex direction. The septal wall represent the aorta side.



(a) $t/T = 0.45$ (b) $t/T = 0.48$ (c) $t/T = 0.52$

(d) $t/T = 0.45$ (e) $t/T = 0.57$ (f) $t/T = 0.59$

Figure 3.8: Phase-averaged velocity field at different times of a cardiac cycle in the plane slice #1 defined in Fig 3.1. Below each images, the curve represent the ventricular volume over time, with the red line indicating the current time in the cardiac cycle.

vortical structures within the ventricle, and red markers indicate the approximate centers of rotation.

Although various quantitative methods have been proposed to identify intraventricular vortices [131], a simplified heuristic approach was adopted here. The center of the main vortex was first identified manually based on regions of locally low velocity magnitude, corresponding to the approximate center of rotation. From this location, eight radial lines were drawn at equal angular intervals of $\pi/4$ radians. Along each line, the in-plane velocity was sampled, and the point of maximum magnitude was recorded. These eight points delineate the outer dynamic boundary of the vortex, corresponding to the zone of strongest recirculation. By connecting these points to form a closed polygon, the approximate area of the vortex was estimated. For this reference case, the resulting main vortex area was 10.6 cm^2.

In addition, a smaller counter-clockwise vortex can be observed just below the aortic valve. Its circulation appears to originate from the main ventricular vortex, suggesting a downstream transfer of angular momentum from the central cavity towards the outflow region.

As the inflow subsides and diastole comes to an end, the large intraventricular vortex remains coherent and gradually migrates apically, pre-aligning the blood volume for the upcoming ejection phase.

This large, clockwise vortex observed around mid-to-late diastole is consistent with chamber-wide patterns reported in 4D Flow MRI and in vitro phantom studies. In vivo, phase-contrast MRI commonly resolves a coherent diastolic vortex ring forming downstream of the mitral orifice and persisting into late filling, redirecting flow toward the LV outflow tract [20]. In vitro measurements likewise document a dominant intraventricular vortex that grows as the E-wave decelerates and organizes the subsequent ejection [27, 132]. The timing (emergence during E-wave deceleration), the orientation (clockwise in the apical long-axis view), and the footprint (a single coherent core occupying a substantial fraction of the cavity) agree with these reports.

3.2.4 Systolic ejection

At $t/T = 0.0158$, systole begins. The mitral valve is closed, and the aortic valve opens (instantaneously in the present simulation). Initially, the velocity field remains low throughout the left heart, as shown in Fig. 3.10a, but the flow rapidly develops as the ventricle contracts.

As the pressure in the ventricle exceeds that in the aorta, ejection starts, and blood is expelled through the aortic valve. The flow accelerates rapidly, forming a high-speed jet oriented toward the aortic outflow tract. At $t/T = 0.18$, shown in Fig. 3.10b, the velocity reaches a peak value of approximately 1 $m.s^{-1}$. The jet is well directed along the septal wall and follows a clear path through the outflow tract.

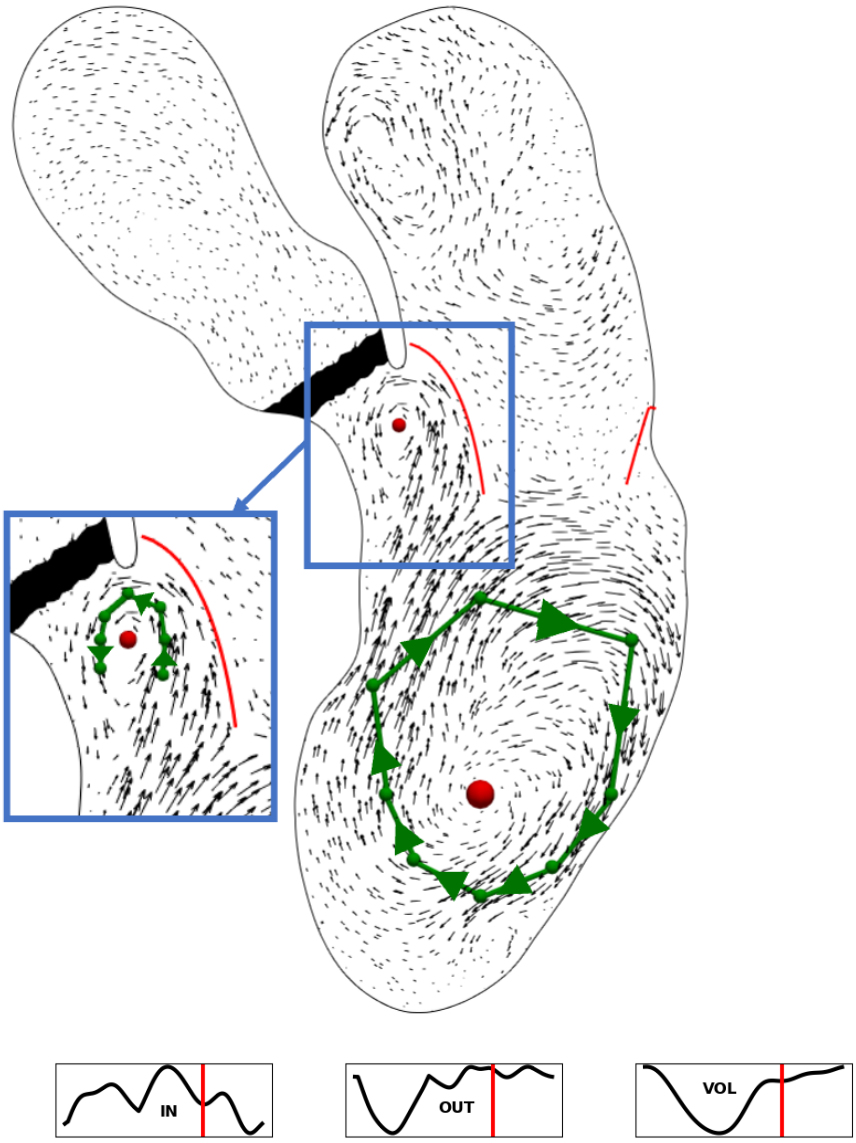
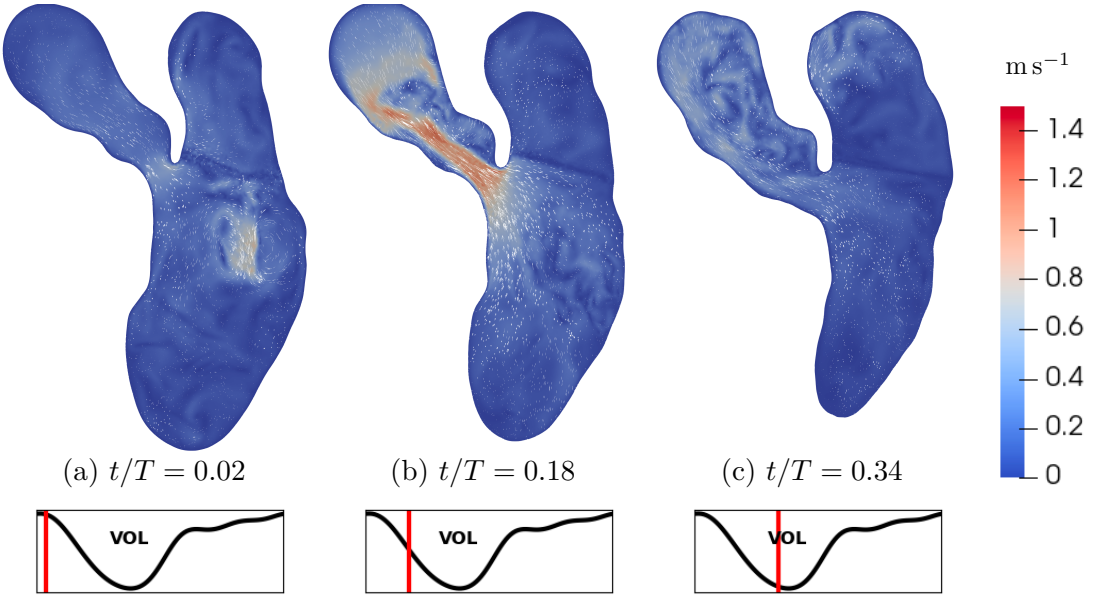


Figure 3.9: Phase-averaged velocity field at $t/T = 0.7$ (mid-diastole) in the plane slice #1 defined in Fig 3.1. Green regions denote the different vortices within the ventricle, while red markers indicate their respective center. Below each images, the curves represent the flow at the entrance (the 4 pulmonary veins), exit (the aorta), and the ventricular volume over time, with the red line indicating the current time in the cardiac cycle.



(a) $t/T = 0.02$ (b) $t/T = 0.18$ (c) $t/T = 0.34$

Figure 3.10: Phase-averaged velocity field at different times of a cardiac cycle in the plane slice #1 defined in Fig. 3.1. See Fig. 3.8 for the curves displayed beneath the top-row panels.

At $t/T = 0.34$ (Fig. 3.10c), the ejection slows as the ventricular volume approaches its minimum.

This phase of ejection occurs simultaneously with the refilling of the left atrium by the pulmonary veins (a process previously described in Section 3.2.2). This temporal overlap between ventricular ejection and atrial filling highlights the coordinated function of the left heart.

3.2.5 Conclusion

This chapter presented a comprehensive description of the left heart flow over a full cardiac cycle. The dynamics of the main flow structures, including the formation of the E-wave jet, the development of intraventricular vortices, and the systolic ejection jet, were analysed in relation to the cardiac geometry and valve behaviour.

In addition to highlighting the synchronisation between atrial and ventricular flow, this global overview provides the foundation for further investigations. In particular, it now enables a detailed analysis of the sensitivity of intraventricular flow to both global physiological variations (such as heart rate and volume) and local anatomical features (notably the geometry and orientation of the mitral valve), as explored in Chapter 4. Furthermore, it opens the door to a quantitative study of energy transport and dissipation mechanisms within the left heart, which will be addressed in Chapter 5.

Chapter 4

Parametric Study

Chapter contents

4.1 Effect of heart rate and volume variations 70
4.1.1 Numerical setup 70
4.1.2 Reference configuration 70
4.1.3 Parametric study 71
4.1.4 Results 71
4.1.5 Conclusion and limitations 75
4.2 Effect of the mitral valve on intraventricular hemodynamics . . . 78
4.2.1 Materials and methods 79
4.2.2 Results 81
4.3 Overall conclusion 85

This chapter is dedicated to assessing the sensitivity of intraventricular flow to different classes of parameters: global physiological variations (such as cardiac frequency and volume), and local geometric characteristics (in particular, the morphology of the mitral valve). While these two aspects are treated separately, this approach provides complementary perspectives on how both general physiological conditions and detailed anatomical features influence the flow. The first part focuses on variations in heart volume and heart rate, while the second part investigates the hemodynamic consequences of mitral valve geometry, based on a model developed specifically for this study.

4.1 Effect of heart rate and volume variations

4.1.1 Numerical setup

In this section, the same computational setup as in Chapter 3 is employed, except that the mitral valve is represented using the legacy model introduced by Chnafa *et al.*: a thick, cone-shaped obstacle that switches instantaneously between fully closed and fully open states (see Section 2.4.1 and [47]). In this configuration, valve closure occurs at $t/T = 0.158$ and opening at $t/T = 0.375$. The choice of this legacy model is motivated by the fact that the primary objective here is not to investigate the influence of the mitral valve itself, but rather to assess the effects of heart rate and volume variations on intraventricular hemodynamics; the detailed impact of valve morphology will be addressed later using the refined model.

4.1.2 Reference configuration

The parametric analysis is based on a reference case, whose anatomical and physiological characteristics are summarized in Table 4.1.

Table 4.1: Parameters of the reference heart model.

Parameter	**Value**
Heart rate (bpm)	60
Apex-to-mitral valve distance (cm)	8.8
Maximum left ventricular diameter (cm)	5.0
Pulmonary root–mitral valve distance (cm)	5.5
Maximum left atrial diameter (cm)	4.0

To characterize the flow regimes, two dimensionless numbers are considered:

- **Reynolds number:**
$$Re \;=\; \frac{U\,(2R)}{\nu},$$
where U is the peak velocity at the MV level, $R = \sqrt{ab}$ is the effective mitral radius, and ν is the kinematic viscosity. This parameter quantifies the ratio of inertial to viscous forces in the flow. Increasing values indicate a growing dominance of inertial effects, with the possibility of transition to turbulence at sufficiently high values.

- **Womersley number:**
$$Wo \;=\; R\sqrt{\frac{\omega}{\nu}},$$
where $\omega = 2\pi/T$ is the cardiac angular frequency (with T the cardiac period). This number characterizes the relative importance of unsteady (pulsatile)

effects in the flow. High values indicate pronounced temporal oscillations and a reduced viscous penetration depth.

For the reference configuration ($a = 15$ mm, $b = 8$ mm, $\nu = 4 \times 10^{-6}$ m^2 s^{-1}, $T = 1$ s and $U_{\max} = 0.9$ m s^{-1}), the maximum Reynolds number near the mitral valve is $Re_{\max} \approx 5000$, suggestinAg a transitional regime with possible turbulence, and the Womersley number is $Wo \approx 14$, confirming the significant influence of unsteadiness.

The objective of this study is to evaluate how variations in heart rate and volume affect the intraventricular flow dynamics, and whether these effects can be predicted based on dimensional analysis relative to the reference case.

4.1.3 Parametric study

Starting from the reference pathological left ventricle model, four additional simulations were defined to probe, separately, the effects of heart rate and ventricular size. Heart rate modulation was imposed by prescribing the cardiac period T to obtain 45 and 80 bpm (Case 1 and Case 2), while keeping the anatomy fixed at the reference effective radius $R_{\text{ref}} = 11.0$ mm. Global changes in chamber volume were modeled by an isotropic geometric scaling of the reference anatomy and are reported via the effective mitral radius $R = \sqrt{ab}$. A mild contraction to $R \simeq 9.3$ mm (approximately -15% relative to R_{ref}, Case 3) and a dilation to $R \simeq 13.1$ mm (approximately $+20\%$, Case 4) were considered. In each case, the inflow waveforms at the pulmonary veins were rescaled consistently with the prescribed cardiac period and ventricular volume, while all other modeling assumptions were kept identical. The time-averaged quantities presented in the following analyses were computed by averaging over these 25 cycles, in order to mitigate the influence of cycle-to-cycle variability and ensure statistical convergence. The parameters for all five cases are summarized in Table 4.2.

These configurations allow for a systematic investigation of how variations in cardiac frequency and anatomical scaling influence intraventricular flow dynamics. The comparison of these cases serves to evaluate whether such variations induce predictable modifications in flow topology and intensity, and whether these changes can be interpreted through the lens of non-dimensional analysis. This approach makes it possible to assess whether the reference case can serve as a predictive baseline for altered cardiac conditions involving changes in heart size and/or rate.

The following section presents a detailed comparison of the flow fields across the five configurations, with particular emphasis on jet characteristics, vortex formation, and flow organization during the diastolic phase.

4.1.4 Results

To investigate the influence of heart rate and volume variations on intraventricular flow, several measurement probes were strategically placed within the heart geometry, as illustrated in Figure 4.1.

Table 4.2: Parametric cases layout.

	Case 2	
	Bpm: 80 T: 1.3s R: 11mm $Re = 6700$ $Wo = 16$	
Case 3	**Reference**	**Case 4**
Bpm: 60 T: 1s R: 9.3mm $Re = 3600$ $Wo = 12$	Bpm: 60 T: 1s R: 11mm $Re = 5000$ $Wo = 14$	Bpm: 60 T: 1s R: 13.1mm $Re = 7200$ $Wo = 17$
	Case 1	
	Bpm: 45 T: 0.75s R: 11mm $Re = 3750$ $Wo = 12$	

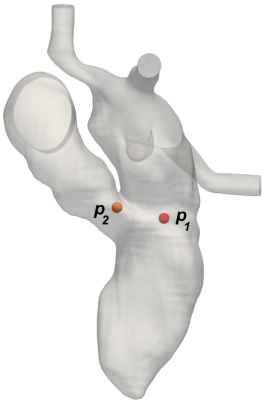


Figure 4.1: Location of velocity probes within the left heart cavity.

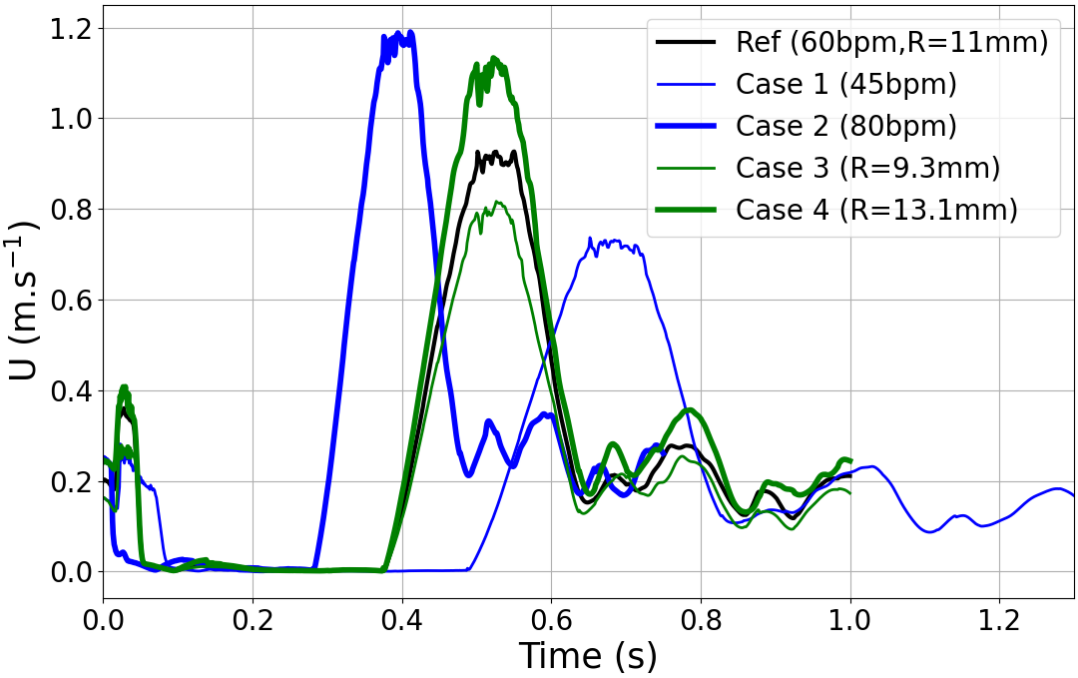


Figure 4.2: Mean velocity near the mitral valve, averaged over 25 cardiac cycles.

The initial analysis focuses on a probe located just downstream of the mitral valve (probe p_1, in red in Figure 4.1). Figure 4.2 presents the time evolution of the mean velocity at this location, averaged over 25 cardiac cycles.

In this figure, the black curve corresponds to the reference configuration, while green and blue curves represent variations in heart volume and heart rate, respectively. As expected, increasing the cardiac volume results in higher velocities, since the fluid must travel a longer distance over the same time interval. Conversely, a reduced cardiac size leads to lower flow velocities. Similarly, an increase in heart rate shortens the duration of the cycle, requiring the blood to be propelled more rapidly, thereby increasing the observed velocity peak. This highlights that significant differences arise in the absolute velocity profiles depending on physiological parameters.

To compare heterogeneous configurations on equal footing, variables are non-dimensionalized using the cardiac period T and the effective mitral radius R.

$$\tilde{t} = \frac{t}{T}, \qquad \tilde{U} = \frac{U}{R/T} = U\,\frac{T}{R}.$$

This choice removes trivial changes associated with period and size, so that remaining differences primarily reflect changes in the underlying dynamics.

When plotted in this non-dimensional form, the velocity traces collapse onto a single curve across all cases (Figure 4.3). This collapse indicates that, to leading order, the near-mitral inflow is governed by similar dynamics once trivial period/size effects are factored out.

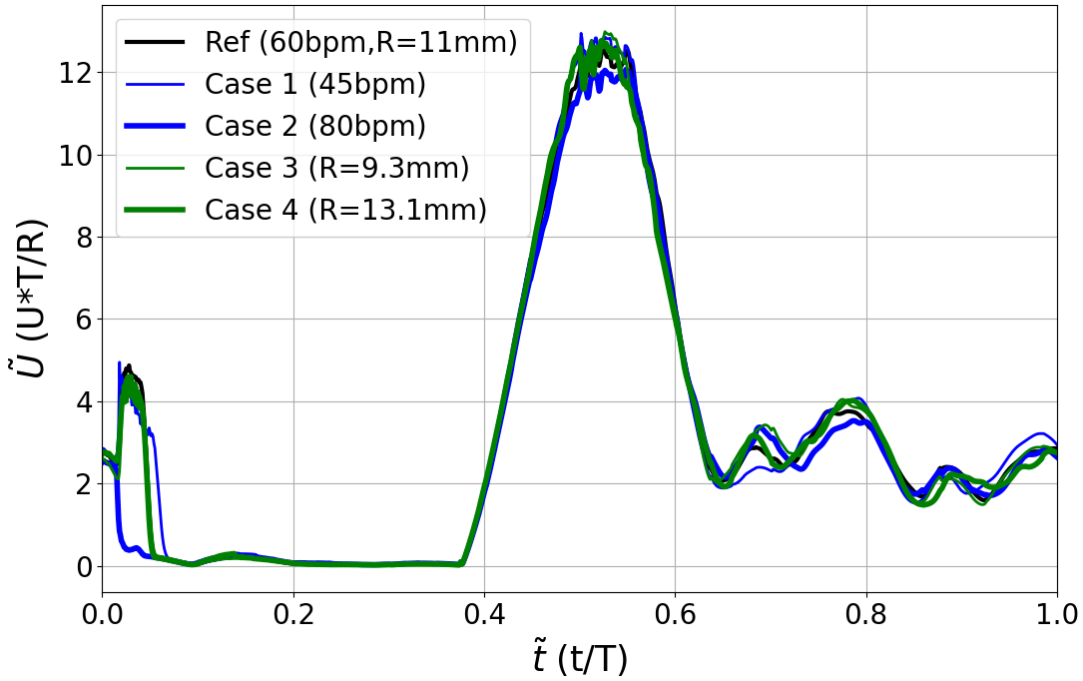


Figure 4.3: Non-dimensionalized mean velocity near the mitral valve.

A similar result is observed at the level of the aortic outflow tract (probe p_2, in orange), where the normalized velocity profiles again exhibit close agreement across all configurations, as shown in Figure 4.4.

To further assess the effect of heart rate and volume on the global flow organization, qualitative comparisons were conducted using instantaneous fields of normalized velocity and vorticity at characteristic phases of the cardiac cycle.

The normalized velocity fields are displayed in Figure 4.5, showing similar jet orientation and penetration characteristics for all cases. The corresponding vorticity fields (Figure 4.6) reveal analogous rotational structures across the parametric space.

In addition, the coherent vortical structures were identified using the Q-criterion, a widely employed diagnostic to extract vortex cores in unsteady flow fields. The criterion is defined as:

$$Q = \frac{1}{2}\left(\|\mathbf{\Omega}\|^2 - \|\mathbf{S}\|^2\right), \tag{4.1}$$

where $\mathbf{\Omega}$ and $\mathbf{S}$ are the antisymmetric and symmetric parts, respectively, of the velocity gradient tensor $\nabla\mathbf{u}$.

Figure 4.7 shows the Q-criterion iso-surfaces at normalized time $t/T = 0.45$, capturing the diastolic vortex ring inside the left ventricle. Despite variations in geometry and driving frequency, the vortical structures exhibit comparable size, position, and symmetry after normalization. To quantitatively assess this observation, the main vortex ring in the ventricle was approximated as an ellipse, and its characteristic dimensions w (width) and l (length) were extracted. These values

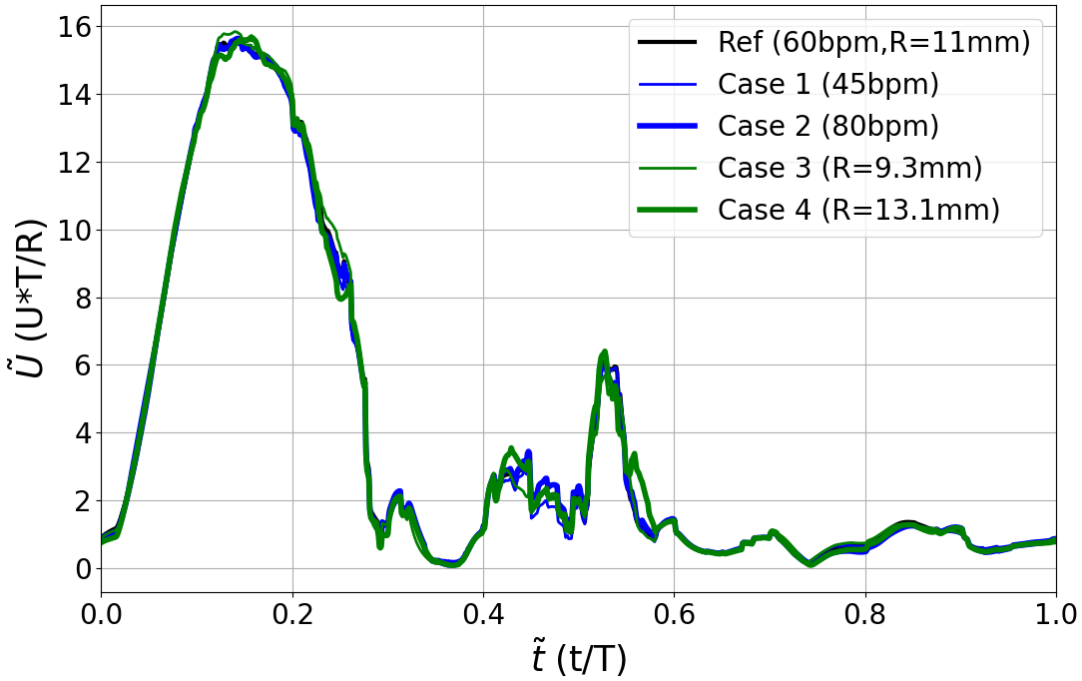


Figure 4.4: Non-dimensionalized mean velocity near the aortic valve.

were normalized by the respective radius R of each case. Table 4.3 summarizes the results, confirming that the vortex dimensions remain nearly invariant in the non-dimensional space.

Table 4.3: Normalized vortex dimensions at $t/T = 0.45$ for each case.

Case	$\boldsymbol{w/R}$	$\boldsymbol{l/R}$
Reference	2.18	2.82
Case 1	2.18	2.82
Case 2	2.18	2.82
Case 3	2.19	2.74
Case 4	2.12	2.77

These results reinforce the hypothesis that moderate variations in heart rate and anatomical scale do not significantly alter the flow topology when expressed in a normalized framework.

4.1.5 Conclusion and limitations

The present analysis demonstrates that intraventricular hemodynamics are robust to moderate changes in heart rate and cardiac volume. Normalized velocity profiles, vortex dynamics, and jet characteristics all exhibit consistent patterns across the different cases studied.

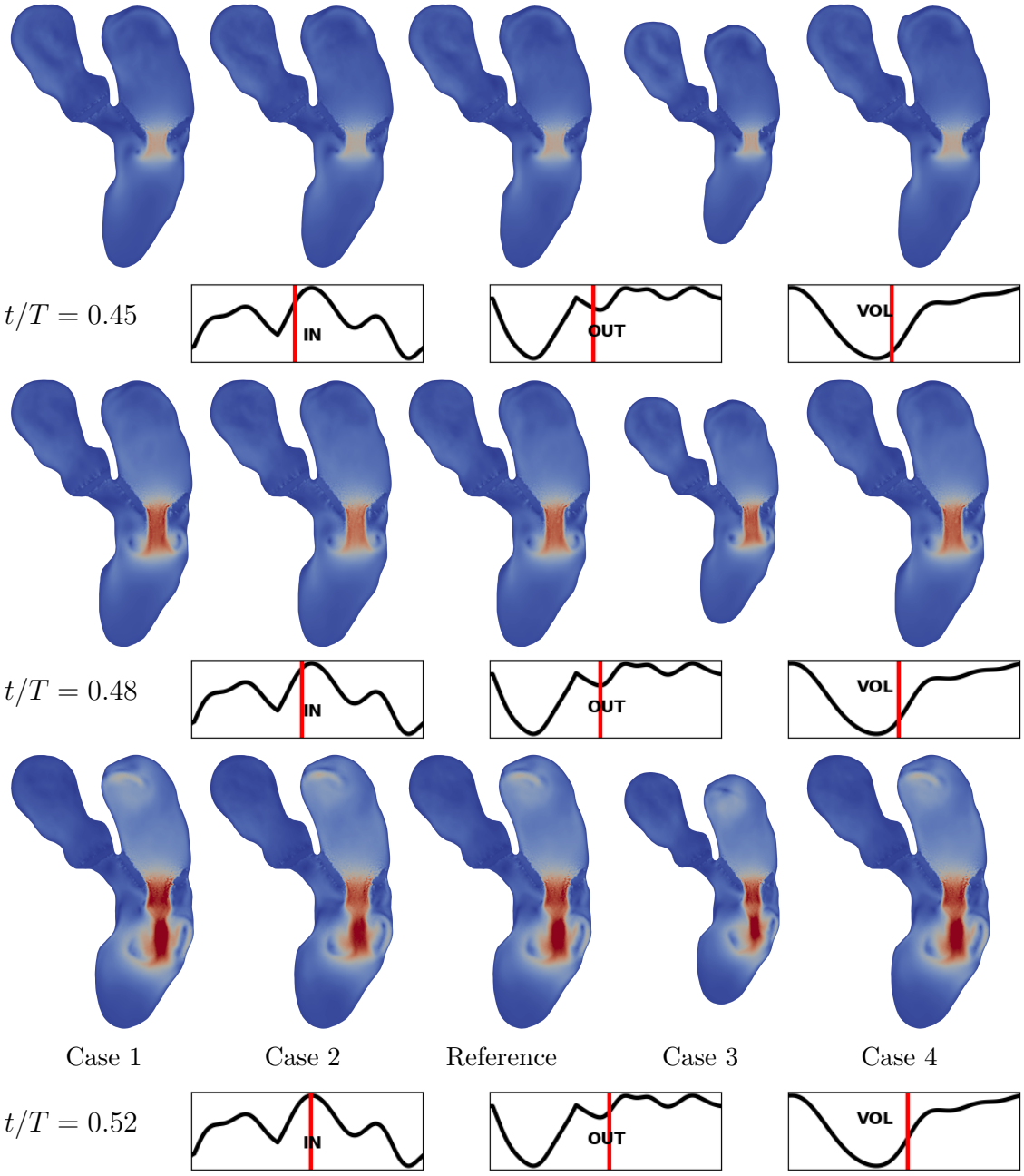


Figure 4.5: Volume rendering of non-dimensional velocity magnitude at different times (t/T) during diastole. Each row corresponds to a specific time instant. Below each set of images, the curves represent the flow at the entrance (the 4 pulmonary veins), exit (the aorta), and the ventricular volume over time, with the red line indicating the current time in the cardiac cycle. Case definitions and parameter values are given in Table 4.2.

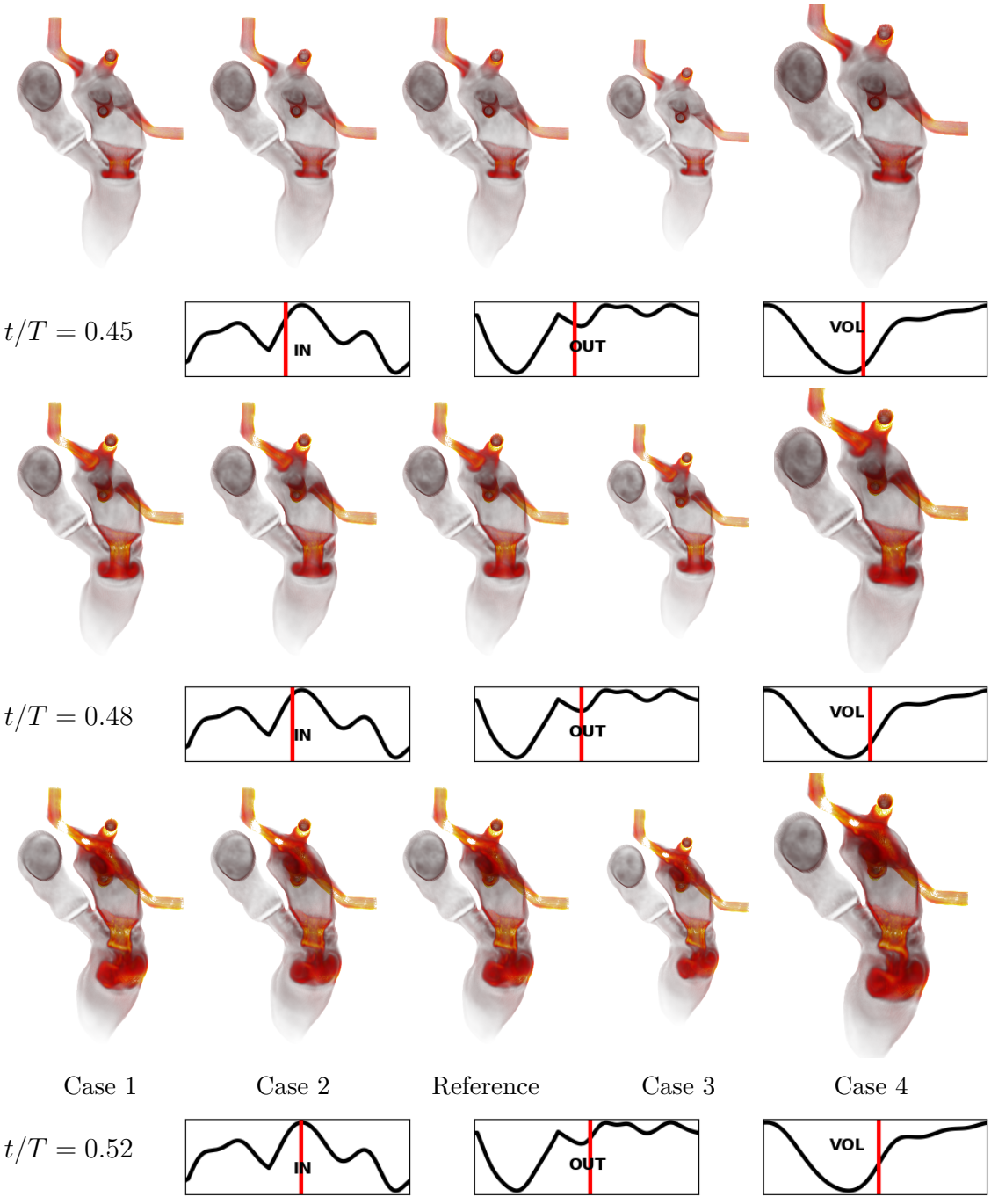
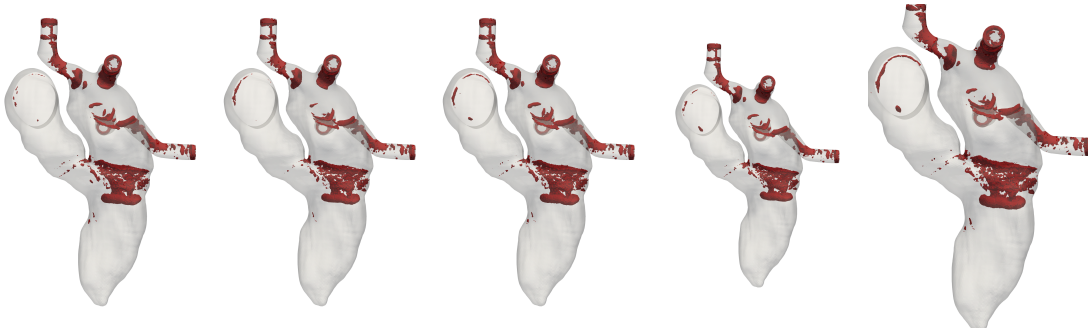


Figure 4.6: Volume rendering of non-dimensional vorticity magnitude (non-dimensionalised by the period T) at different times (t/T) in a cardiac cycle. Case definitions and parameter values are given in Table 4.2.



(a) Case 1 (b) Case 2 (c) Reference (d) Case 3 (e) Case 4

Figure 4.7: Q-criterion iso-surfaces at $t/T = 0.45$ for the five cases.

Nonetheless, some limitations must be acknowledged:

- The duration of systole and diastole was kept constant across all simulations. In physiological conditions, however, heart rate variations are typically associated with changes in the systole-to-diastole ratio, which may affect filling and ejection dynamics. Within the moderate HR range investigated here (45–80 bpm), this ratio varies only mildly, which motivated restricting the exploration to this interval.

- The geometrical scaling applied in this study was isotropic. In real clinical scenarios, cardiac dilatation is often anisotropic, with localized or asymmetrical remodeling of ventricular walls.

These simplifications may limit the generalizability of the results. Future work should incorporate more physiologically realistic modifications to both geometry and timing to further validate the predictive capability of the non-dimensional approach.

While changes in heart rate and volume produce predictable effects that can be largely captured through dimensionless analysis, they fail to capture more localized and potentially critical features of the cardiac flow. The mitral valve, due to its upstream location and direct interaction with the inflow jet, plays a decisive role in shaping the intraventricular dynamics. The following section focuses on evaluating the influence of the MV geometry using a detailed and physiologically inspired model.

4.2 Effect of the mitral valve on intraventricular hemodynamics

Because the MV sits upstream of the ventricle, its geometry can strongly influence intraventricular flow. This section examines the influence of the mitral valve on the hemodynamics within the left ventricle.

4.2.1 Materials and methods

The numerical methods used in this study are the same as those detailed in Chapter 2. In this section, only the parameters related to the mitral valve are modified. For reference, the equations governing the position of the valve nodes are:

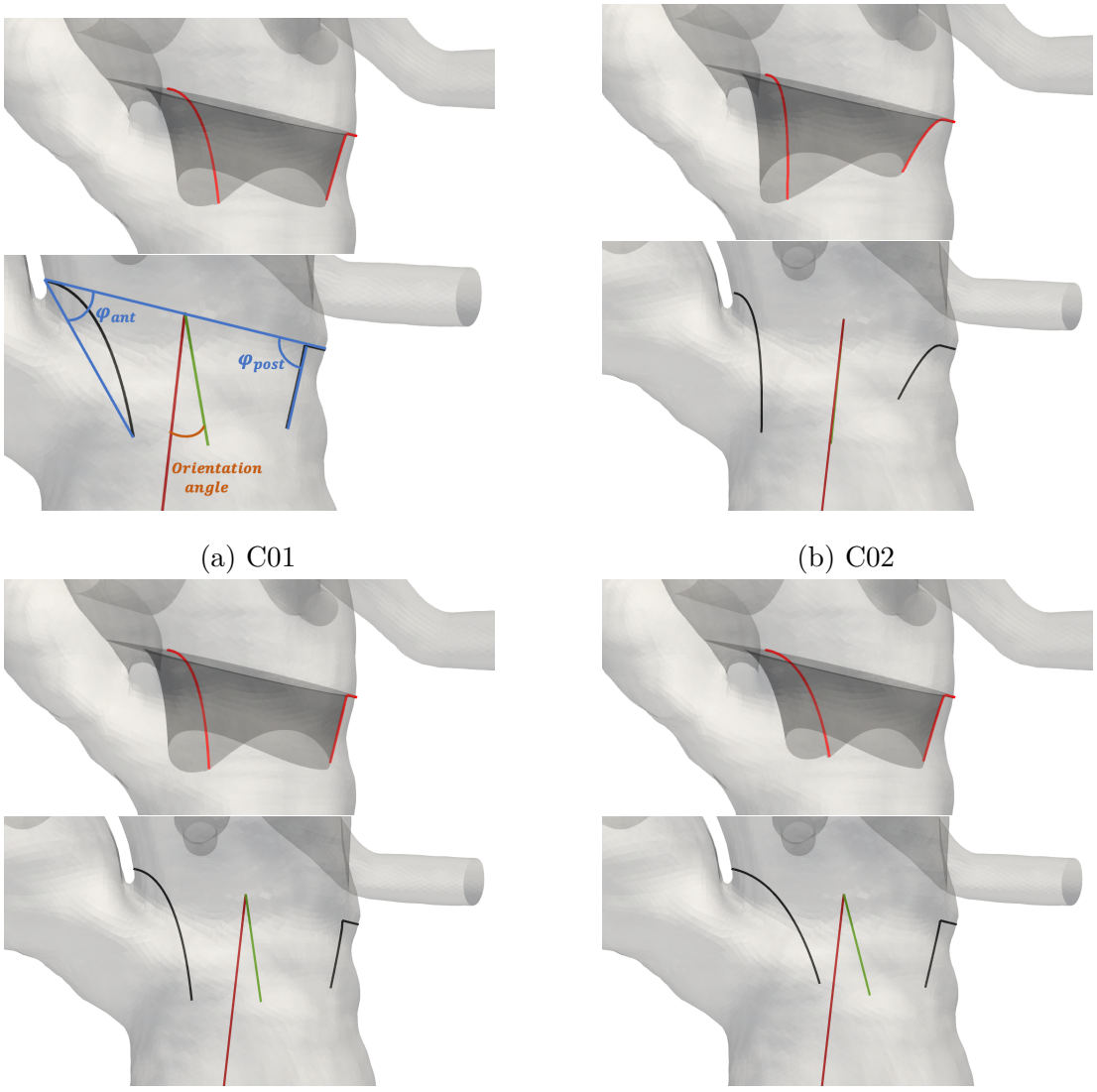
$$\begin{aligned} x(\theta, s, t) &= R\cos\theta\Big(1 - s\cos\varphi(\theta, t)\Big) - \varepsilon R s\cos\varphi(\theta, t), \\ y(\theta, s, t) &= R\sin\theta\Big(1 - sk\cos\varphi(\theta, t)\Big), \\ z(\theta, s, t) &= -s^2\left[\frac{1+k}{2} - \varepsilon\cos\theta + \frac{1-k}{2}\cos 2\theta\right] R\sin\varphi(\theta, t). \end{aligned} \tag{4.2}$$

The valve model introduced in Section 2.4 was combined with the reference configuration defined in Chapter 3, which reproduces physiological intraventricular flow patterns. Briefly, the mitral valve geometry was parameterized by the asymmetry ratio $\varepsilon = 0.35$ (anterior leaflet twice the size of the posterior [88]) and the ellipticity $k = 0.6$. The annular radius R varied dynamically over the cardiac cycle (21.6–26.1 mm), and the opening angles of the leaflets were chosen to achieve a physiologically realistic jet orientation and velocity (0.6–1.0 m . s^{-1}), with an orifice area between 4 and 6 cm^2 [133]. For the reference case (C01), the anterior and posterior leaflet angles were set to $\varphi_{ant} \approx 45°$ and $\varphi_{post} \approx 90°$, ensuring the jet developed along the ventricular wall [14].

Three additional cases were considered relative to the reference: one with modified jet orientation but unchanged orifice area (C02), one with increased opening area and unchanged orientation (C03), and one mimicking a pathological case with anterior leaflet calcification (C04). For these cases, the values of ε, k, and R remained identical to C01 to ensure consistent baseline geometry. The term *calcification* here refers to a simplified pathological scenario in which only the effective opening area and angle are changed, without modeling changes in leaflet stiffness or opening kinetics. The main characteristics of cases C01–C04 are summarized in Table 4.4, with their geometries visualized in Figure 4.8. In Table 4.4, the orientation angle refers to the angle between the MV-apex line (depicted in red in Figure 4.8) and the valve axis (shown in green in Figure 4.8). Figure 4.8 illustrates the different orientation angles (between C01 and C02) and different opening areas (between C01 and C03). The calcification of the anterior leaflet (C04) changes both the opening area and the angle.

Table 4.4: Values of the parameters for the four different cases considered, with $\varepsilon = 0.35$ and $k = 0.6$.

Case	φ_{ant}	φ_{post}	**Open area MV (cm^2)**	**Orientation angle**	**Objective**
C01	45°	90°	4.3	16°	Reference Case
C02	65°	65°	4.3	1°	Different Orientation
C03	50°	95°	4.95	15°	Wider Opening
C04	37°	90°	3.8	21°	Calcification



(a) C01

(b) C02

(c) C03

(d) C04

Figure 4.8: Different cases with the maximum opening. For all cases, $\varepsilon = 0.35$, $k = 0.6$, and $R = 17.5$ mm. For each case, the top image shows the 3D view of the valve within the heart, while the bottom image displays the 2D projection of the valve on slice 1 (visible in Fig. 3.1) and in red in the 3D view of the valve. The red line represents the MV-apex line, while the green line indicates the axis of the valve, which connects the centers of the top and bottom cross section area.

4.2.2 Results

The atrial flow, detailed in Section 3.2.2, remains identical across all four valve configurations.

The significance of MV geometry is mainly pronounced during diastole. At the onset of diastole, the MV opens, allowing the passage of blood from the atrium to the ventricle, leading to the generation of the E-wave jet, as depicted in Figure 4.9. On the top row of Figure 4.9, representing the onset of diastole, differences between the mitral valves can be observed. However, the main disparities become apparent as the cardiac cycle progresses slightly, depicted here in the middle row of Figure 4.9. In the first case of the middle row of Figure 4.9 (case C01), the jet adheres to the ventricular wall with a velocity of 0.95m.s^{-1}. When the orientation of the MV changes (case C02), the maximum velocity remains constant, but the jet no longer follows the wall. Instead, it is directed towards the center of the ventricle. In the case of a larger MV opening (case C03), the jet travels a shorter distance and has a lower intensity, with $U_{\max} = 0.75\text{m.s}^{-1}$. In the last case (case C04), the jet follows the ventricular wall but penetrates further toward the apex than in case C01, with also a higher maximum velocity of $U_{\max} = 1.1\text{m.s}^{-1}$. Table 4.5 gathers the maximum velocities observed at the MV level in all four cases.

These differences in jet behavior lead to distinct flow structures within the left ventricle, as seen in the bottom row of Figure 4.9. In case C04, the jet reaches the apex of the ventricle, whereas in case C03, it remains confined to the upper region. Such differences in the E-wave jet dynamics significantly affect the formation of intraventricular vortices. The vortex ring that forms at the head of the inflow jet is a well-known marker of jet penetration and has been extensively studied [13, 16, 128, 130].

Table 4.5: Peak inflow speed at the mitral valve and area(s) of the dominant vortex structure(s) at $t/T = 0.70$. In case C02, two coherent vortices are present at this phase; the reported values therefore correspond to the areas of the "up" (toward the LV outflow tract) and "down" (toward the apex) structures. In the other cases, a single dominant vortex is present (see Fig. 4.11).

Case	**Max Velocity at MV (m.s^{-1})**	**Area of main vortices at $t/T = 0.7$ (cm^2)**
C01	0.95	10.6
C02	0.95	Up: 4.5, Down: 2.5
C03	0.75	5.2
C04	1.1	5.3

Due to cycle-to-cycle variations [70], visualizing the end-diastole vortex is more challenging; the following analysis is thus performed after the flow has been phase-averaged. Figure 4.10 shows the phase-averaged velocity $t/T = 0.57$ (mid-diastole) in a vertical plane at the center of the heart. This plane allows visualization of the entire ventricle for all four cases, and the vortex at mid-diastole is clearly visible. A large vortex is observed in case C01 in the center of the ventricle during

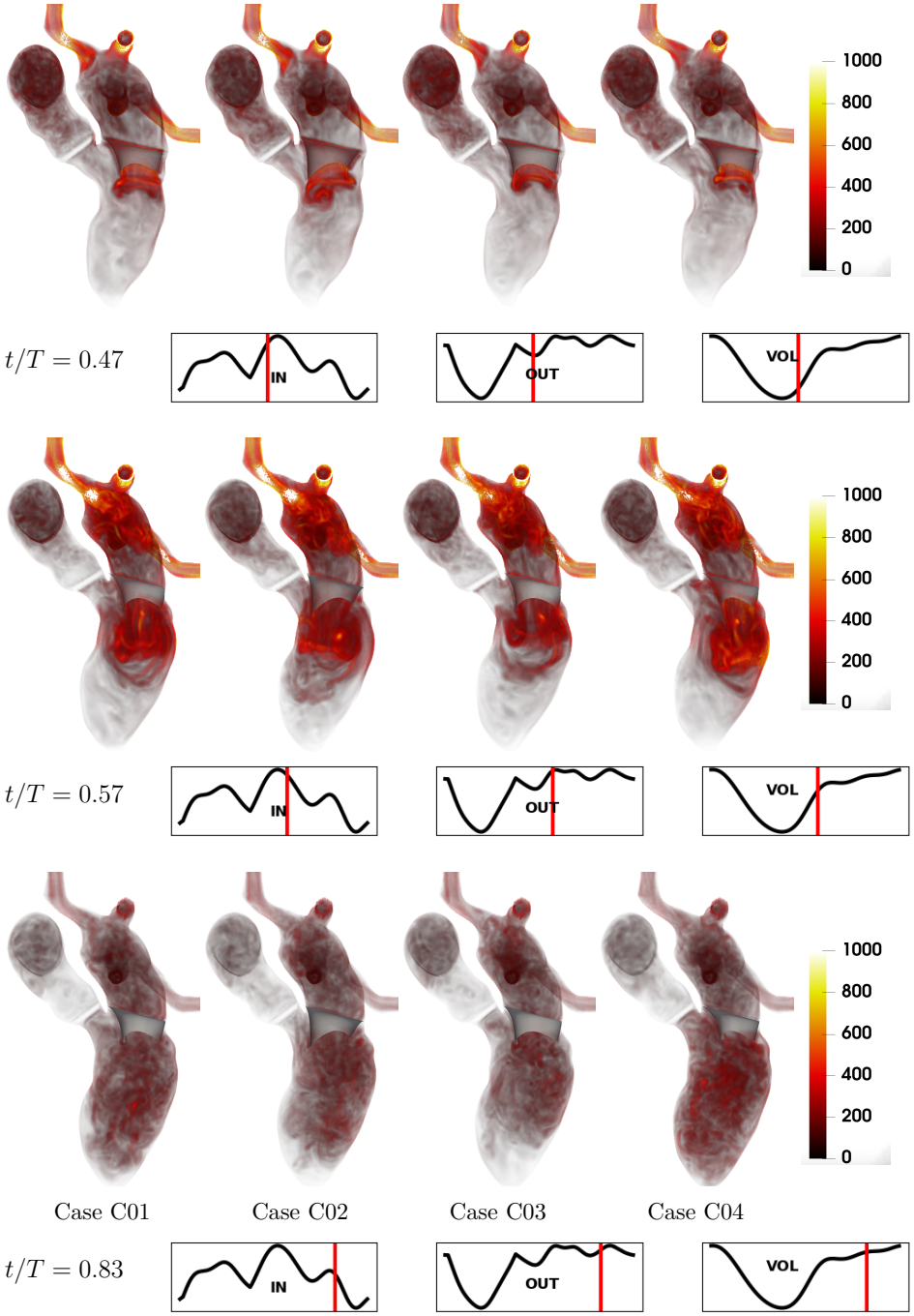


Figure 4.9: Volume rendering of non-dimensional vorticity magnitude (non-dimensionalised by the period T) at different times (t/T) in a cardiac cycle. Each row corresponds to a specific time instant. **Top:** $t/T = 0.47$ (start diastole). **Middle:** $t/T = 0.57$ (beginning–mid diastole). **Bottom:** $t/T = 0.83$ (end diastole). Below each set of images, the curves represent the flow at the entrance (the 4 PV), exit (the aorta), and the ventricular volume over time, with the red line indicating the current time in the cardiac cycle. For the vorticity colour scale, black represents $\omega = 0$, red indicates $\omega = 500$, yellow corresponds to $\omega = 800$, and white to $\omega = 1000$.

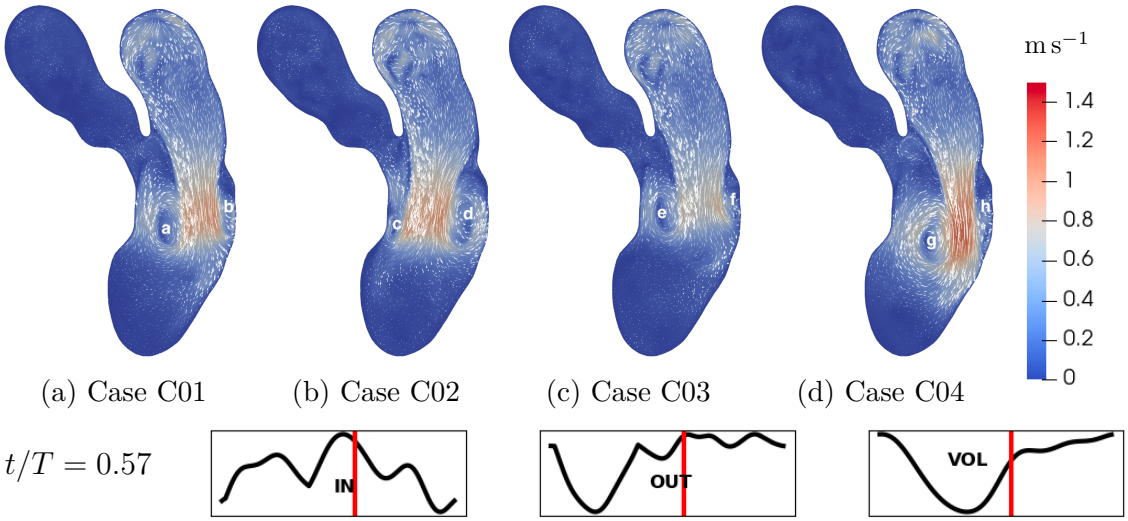
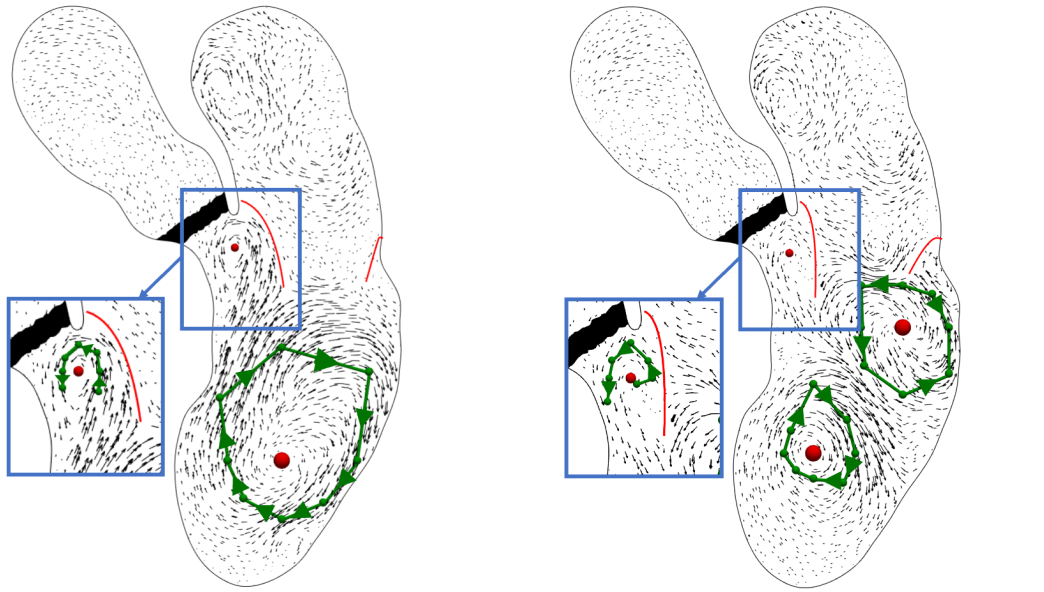


Figure 4.10: Phase-averaged velocity field at $t/T = 0.57$ (beginning-mid diastole) in the plane slice #1 defined in Fig 3.1. The labels represent the vortices mentioned in the main text. See Figure 4.9 for the curves at the bottom of the Figure.

mid-diastole (see label (a) on the Figure), accompanied by a smaller vortex (b) between the jet and the ventricular wall on the side of the posterior mitral leaflet. The large one is oriented in the clockwise direction, while the smaller one is in the counter-clockwise direction. In case C02, with the jet oriented towards the apex, a significant vortex is formed on the posterior side (d), and a smaller one appears on the anterior side of the jet (c). In C03, the distribution of vortices is similar to that in C01, but they are smaller in size. In the last case, a substantial vortex is present in the ventricle (g), and the vortex to the right of the jet (h) is notably weaker.

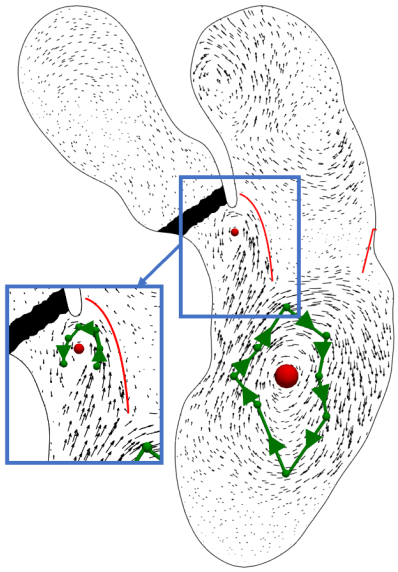
Figure 4.11 depicts the phase-averaged velocity field at $t/T = 0.7$, representing the mid-to-late diastolic phase of the cardiac cycle. Green regions denote vortical structures within the ventricle, and red markers indicate their centers. To characterize the sizes of vortices, the same procedure introduced in Section 4.1.4 is applied. Briefly, vortex centers are identified, and their extent is estimated from surrounding points determined along eight evenly spaced directions, allowing the area of each vortex to be approximated (Table 4.5). This provides a simple yet consistent measure of vortex size to compare across cases.

In case C01 (Fig. 4.11a), a large vortex occupies much of the ventricular space, rotating clockwise. This vortex is often highlighted for its presumed assistance to the heart, helping the ejection of blood in the aorta during systole [16, 130]. When the MV opens wider (case C03, Fig. 4.11c), this vortex shifts upwards in the ventricle, and its formation is not as clear as in case C01. In case C04 (Fig. 4.11d), where the main jet follows the ventricular wall, the vortex is offset towards this wall. Although its height matches the one of case C01, its width is reduced. In case C02, (Fig. 4.11b), a different pattern emerges due to the non-physiological orientation of the MV. This leads to the modification of the

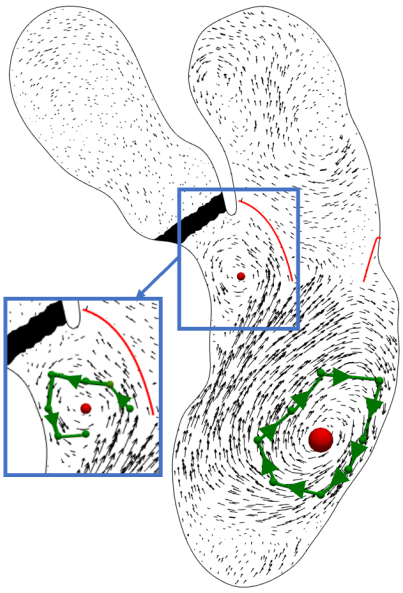


(a) Case C01

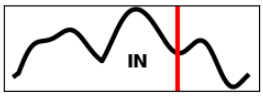
(b) Case C02



(c) Case C03



(d) Case C04





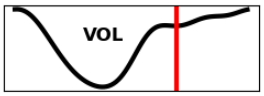


Figure 4.11: Phase-averaged velocity field at $t/T = 0.7$ (mid-diastole) in the plane slice #1 defined in Fig 3.1. Green regions denote the different vortices within the ventricle, while red markers indicate their respective centers. See Figure 4.9 for the curves at the bottom of the Figure.

flow within the ventricle, resulting in the observation of two vortices in the LV: one in the apex, rotating clockwise, and another between this vortex and the MV, rotating counterclockwise.

Additionally, just below the AV, an anti-clockwise vortex is observed in all four cases. This vortex appears smaller in cases C02 and C03, while in the other two cases, its size is nearly identical. In all cases except C02, the blood within this vortex seems to originate from the ventricular vortex, although its formation is less distinct in C02.

Conclusion

Across cases C01–C04, mitral valve geometry exerts a first-order control on diastolic intraventricular flow. Variations in orientation redirect the E-wave jet (wall-adherent versus more axial), which reorganizes the diastolic vortex topology. Variations in effective orifice area modulate the peak velocity and the extent/strength of vortical structures; wider openings yield lower $U_{\max}$ and less penetrative jets. The calcification-like configuration (reduced area with altered angle) combines these effects and produces the strongest, deepest wall-guided jet, and displaced vortices.

4.3 Overall conclusion

This chapter contrasted the effects of global physiological scaling (heart rate and heart size) with those of local mitral valve morphology on intraventricular hemodynamics. Within the explored range (HR = 45–80 bpm; effective radius $R \simeq$ 9.3–13.1 mm, i.e. -15% to $+20\%$ around $R_{\text{ref}} = 11.0$ mm), global variations mainly produce a dimensional rescaling of the flow. Once signals are expressed in non-dimensional form, velocity waveforms and vortex dimensions nearly collapse across cases, indicating that the reference configuration provides a reliable predictive baseline under similarity scaling.

In contrast, MV morphology acts as a first-order organizer of the diastolic flow. Modest changes in leaflet orientation and effective orifice area qualitatively alter jet trajectory and the ensuing vortex topology. A calcification-like configuration, combining reduced area with altered angle, amplifies peak speeds and promotes deeper wall-guided penetration, with implications for near-wall shear and washout patterns. These findings show that while HR/size changes are largely captured by non-dimensional similarity, MV geometry breaks similarity and must be modeled explicitly whenever jet topology and derived hemodynamic metrics are of interest, including vortex metrics, kinetic energy, turbulent kinetic energy, viscous dissipation, and shear-based markers.

Given the significant impact of mitral valve geometry on the flow patterns inside the ventricle and on the vortices, it prompts the question of whether these flow differences lead to substantial variations in the heart's efficiency. To

quantify this effect, the next chapter develops a kinetic energy balance of the intraventricular flow.

Chapter 5

Advanced hemodynamic analysis

Chapter contents

5.1 Introduction 88
5.2 Materials and methods 88
5.3 Kinetic energy budget 89
5.3.1 Methodology 89
5.3.2 Results 93
5.3.3 Discussion 98
5.4 Mixing in the left ventricle 99
5.5 Overall conclusion 102

This chapter develops an advanced analysis of how mitral valve geometry modulates left ventricular hemodynamics. An intraventricular energy balance is first established to assess pumping efficiency, quantifying cycle-averaged kinetic energy, turbulent kinetic energy, viscous dissipation, and pressure work. Intraventricular transport and mixing are then examined, with a focus on residence-time patterns. [1]

[1] The material presented in this chapter forms the core of a manuscript submitted to the *International Journal for Numerical Methods in Biomedical Engineering*: S. Bru, S. Mendez, D. Garcia, and F. Nicoud, *Effect of the mitral valve on the intraventricular hemodynamics*, submitted.

5.1 Introduction

The heart acts as a pump whose performance depends on how effectively myocardial work is transformed into organized intraventricular flow [134, 135]. Beyond morphology and bulk flow patterns (which can be insufficient for diagnosis on their own [6]) a fluid–mechanical, energetics-based perspective is useful: cardiac efficiency can be discussed in terms of how kinetic energy (KE) is produced, transported, and dissipated over the cardiac cycle, and how these processes relate to myocardial effort [70, 136, 137]. This motivates quantitative tools that complement flow visualization for diagnosis and for anticipating dysfunction before structural remodeling occurs. For the broader context (including medical imaging, experimental studies, and numerical modeling) see Chapter 1.3.

Clinical imaging has highlighted prominent diastolic vortical structures, most notably the E-wave vortex ring and a mid-to-late diastolic swirl, often hypothesized to facilitate organized filling and efficient ejection [16, 128, 130, 138, 139]. Their contribution to efficiency remains debated, with studies reporting both favorable and negligible effects [12, 67, 75, 136].

Direct quantification of dissipation and pressure work from imaging alone is challenged by spatial resolution and noise [13, 132, 140]. Computational hemodynamics helps bridge this gap by providing time-resolved pressure and dissipation fields under controlled conditions, and by enabling factor isolation (e.g. modifying mitral valve design at fixed anatomy and motion). In this chapter, a patient-specific, image-driven left-heart model that includes the left atrium is employed to deliver realistic inflow at the MV; the upstream atrium can modulate intraventricular structure and outflow efficiency [46, 71, 86]. To isolate valve-driven effects, the MV opening area and orientation are varied while keeping global geometry and wall motion fixed.

Section 5.3 formulates the kinetic energy balance (to the author's knowledge, the first complete ventricular budget reported for an in vivo left heart geometry). Section 5.3.2 compares energetic terms across MV configurations to quantify how valve design modulates costs. Complementarily, Section 5.4 analyzes apical washout/mixing. The main flow features underlying these results are summarized in Chapter 3 (Section 4.2).

5.2 Materials and methods

The numerical framework introduced in Chapters 2–4 is employed. The solver, spatial and temporal discretization, wall kinematics, and boundary conditions are identical to those used previously; only the mitral valve parameters are varied. Specifically, the four MV configurations defined in Chapter 4, Section 4.2 (C01–C04) are reused, while keeping the left heart geometry and deformations unchanged.

5.3 Kinetic energy budget

5.3.1 Methodology

The objective is to assess the efficiency of the cardiac pump from a fluid mechanics perspective. To achieve this, it is natural to consider the kinetic energy budget within the heart. More specifically, since the MV does not impact the hemodynamics in the atrium, the present analysis focuses on the ventricle only. Figure 5.1 provides details of the flow domain considered. The inlet (mitral plane, MP; red) is a fixed planar section located just above the MV. The heart muscle, representing the wall of the domain, is shown in blue and moves during the cardiac cycle. $D(t)$ is the ventricular domain at time t and Ω_t represents the fixed domain which is such that $\Omega_t = D(t)$ at time t. The outlet (aortic plane, AP; orange) is a fixed planar section just below the aortic valve. The outward normals of each part of the domain are labeled as n_{MP}, n_W and n_{AP}, respectively.

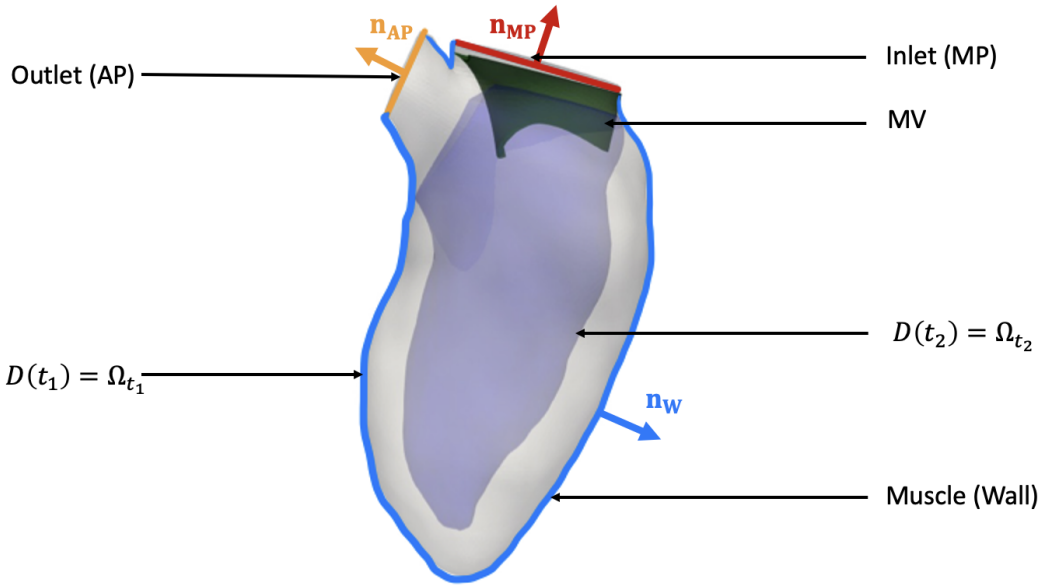


Figure 5.1: Details of the flow domain over which the kinetic energy budget is established. The inlet (Mitral Plane (MP)) is above the MV and the outlet (Aortic Plane (AP)) under the AV. The outward normals are represented as arrows. $D(t)$ is the ventricular domain at time t and Ω_t represents the fixed domain which is such that $\Omega_t = D(t)$ at time t.

The boundary of the Ω_t domain is defined as $\partial\Omega_t = MP \cup AP \cup Wall$.

The intracardiac flow is obtained by solving the filtered Navier-Stokes equations:

$$\frac{\partial \rho u_i}{\partial t} + \frac{\partial \rho u_j u_i}{\partial x_j} = -\frac{\partial p}{\partial x_i} + \frac{\partial \tau_{ij}}{\partial x_j} + \rho F_i, \tag{5.1}$$

where u_i and p are low-pass versions of the exact velocity and pressure. No specific notation is used for denoting the filtered quantities to simplify the writing, and also to reflect that the low-pass filtering is not performed explicitly; rather, one relies on the finite size of the finite-volume mesh to retain the larger scales, as most often done in Large Eddy Simulations. In this view, τ_{ij} has two contributions: the viscous stress associated to the (resolved) filtered velocity field, τ_{ij}^R, and the subgrid scales stress, τ_{ij}^{SGS}. Note that for a Newtonian incompressible fluid, the former simply reads $\tau_{ij}^R = 2\mu S_{ij}$, where S_{ij} is the filtered strain-rate tensor. Making use of the Boussinesq assumption, one may model the small scales contribution as $\tau_{ij}^{SGS} = 2\mu_{SGS} S_{ij}$, where μ_{SGS} is the eddy-viscosity provided by the σ-model [111] as already mentioned in Section 2.3.6.

By multiplying this equation (5.1) by the velocity field, one obtains the transport equation of the kinetic energy (KE) per mass unit, $e_c = \frac{1}{2}u_i u_i$, of the particles of blood. It reads:

$$\frac{\partial \rho e_c}{\partial t} + \frac{\partial \rho u_j e_c}{\partial x_j} = -u_i \frac{\partial p}{\partial x_i} + u_i \frac{\partial \tau_{ij}}{\partial x_j} + \rho u_i F_i. \tag{5.2}$$

Since the flow in the heart is potentially turbulent, the subgrid scale stress tensor is not necessarily negligible compared to τ_{ij}^R. Since $\tau_{ij} = 2(\mu + \mu_{SGS})S_{ij}$ and accounting for the incompressibility constraint $\frac{\partial u_i}{\partial x_i} = 0$:

$$\frac{\partial \rho e_c}{\partial t} + \frac{\partial \rho u_j e_c}{\partial x_j} = -\frac{\partial p u_i}{\partial x_i} + \frac{\partial \tau_{ij} u_i}{\partial x_j} - 2(\mu + \mu_{SGS})S_{ij}S_{ij} + \rho u_i F_i. \tag{5.3}$$

Integrating the left hand side of the equation over Ω_t at time t and making use of the Green-Ostrogradski theorem leads to:

$$\begin{aligned} \underbrace{\iiint_{\Omega_t} \left(\frac{\partial \rho e_c}{\partial t} + \frac{\partial \rho u_j e_c}{\partial x_j} \right) dV}_{\text{I}} &= \iiint_{\Omega_t} \frac{\partial \rho e_c}{\partial t} dV + \iiint_{\Omega_t} \frac{\partial \rho u_j e_c}{\partial x_j} dV \\ &= \iiint_{\Omega_t} \frac{\partial \rho e_c}{\partial t} dV + \oiint_{\partial \Omega_t} \rho e_c u_j n_j dS \\ &= \iiint_{\Omega_t} \frac{\partial \rho e_c}{\partial t} dV + \oiint_{\partial \Omega_t} \rho e_c \mathbf{u} \cdot \mathbf{n} dS. \end{aligned} \tag{5.4}$$

Here, $\mathbf{u}$ denotes the fluid velocity evaluated on $\partial\Omega_t$. With $\mathbf{V_D}$ representing the velocity of the domain boundary $D(t)$ and using the Reynolds transport theorem, one obtains:

$$\begin{aligned} I = \iiint_{\Omega_t} \frac{\partial \rho e_c}{\partial t} dV + \oiint_{\partial \Omega_t} \rho e_c \mathbf{V_D} \cdot \mathbf{n} dS + \oiint_{\partial \Omega_t} \rho e_c (\mathbf{u} - \mathbf{V_D}) \cdot \mathbf{n} dS \\ = \frac{d}{dt} \iiint_{D(t)} \rho e_c dv + \oiint_{\partial \Omega_t} \rho e_c (\mathbf{u} - \mathbf{V_D}) \cdot \mathbf{n} dS. \end{aligned} \tag{5.5}$$

The AP and MP areas of $\partial\Omega_t$ are considered non-moving, so that $\mathbf{V_D} = 0$. On the contrary, the muscle area is considered impermeable ($\mathbf{u} = \mathbf{V_D}$). Under these conditions, it comes:

$$I = \frac{d}{dt}\iiint_{D(t)} \rho e_c dv + \oiint_{AP} \rho e_c \mathbf{u}\cdot\mathbf{n_{AP}} dS + \oiint_{MP} \rho e_c \mathbf{u}\cdot\mathbf{n_{MP}} dS. \tag{5.6}$$

The normal (n_{AP} and n_{MP}) are depicted in Figure 5.1. Integrating the four terms of the right-hand side of Eq. (5.3) leads to:

$$-\iiint_{\Omega_t} \frac{\partial p u_i}{\partial x_i} dV = -\oiint_{\partial\Omega_t} p u_i n_i dS = -\oiint_{\partial\Omega_t} p\mathbf{u}\cdot\mathbf{n} dS, \tag{5.7}$$

$$\iiint_{\Omega_t} \frac{\partial \tau_{ij} u_i}{\partial x_j} dV = \oiint_{\partial\Omega_t} \tau_{ij} u_i n_j dS, \tag{5.8}$$

$$-\iiint_{\Omega_t} 2(\mu + \mu_{SGS}) S_{ij} S_{ij} dV = -\psi, \tag{5.9}$$

$$\iiint_{\Omega_t} \rho u_i F_i dV = \iiint_{\Omega_t} \rho \mathbf{F}\cdot\mathbf{u} dV. \tag{5.10}$$

The term ψ represents the dissipation within the system. Since the Reynolds number is a few hundreds or thousands, it is expected that the viscous contribution at the boundaries, Eq. (5.8), is very small and can be neglected. This is indeed confirmed by the simulations that its magnitude is very small, with a maximum value of 7×10^{-7} W, at least 1 million times smaller than the expected order of magnitude of the heart's mechanical power (1 W). Therefore, it can be considered negligible in the overall energy balance.

Because the fluid is considered incompressible, the computed pressure is defined up to an additive, time-dependent constant. Indeed, the pressure contributes to the flow motion through its gradient only, see Eq. (5.1). For a homogeneous pressure P_{LV}, Eq. (5.7) reads:

$$\oiint_{\partial\Omega_t} P_{\mathrm{LV}} \mathbf{u}\cdot\mathbf{n} dS = P_{\mathrm{LV}} \oiint_{\partial\Omega_t} \mathbf{u}\cdot\mathbf{n} dS = 0. \tag{5.11}$$

To remove this arbitrariness, the computed pressure p is replaced by $p - p_s + P_{\mathrm{LV}}$, where p_s is the spatially averaged pressure over AP (measured in the simulation) and P_{LV} is the reconstructed physiological ventricular pressure. The pressure term then reads:

$$\begin{aligned}\oiint_{\partial\Omega_t} p\,\mathbf{u}\cdot\mathbf{n}\,dS &= \oiint_{\partial\Omega_t} (p - p_s + P_{\mathrm{LV}})\,\mathbf{u}\cdot\mathbf{n}\,dS \\ &= \oiint_{AP} P_{\mathrm{LV}}\,\mathbf{u}\cdot\mathbf{n}_{AP}\,dS + \oiint_{Wall} (p - p_s + P_{\mathrm{LV}})\,\mathbf{u}\cdot\mathbf{n}_W\,dS \\ &\quad + \oiint_{MP} (p - p_s + P_{\mathrm{LV}})\,\mathbf{u}\cdot\mathbf{n}_{MP}\,dS.\end{aligned} \tag{5.12}$$

The second term in the right hand side of Eq. (5.12) is related to the power provided by the heart muscle to the intraventricular fluid:

$$\mathcal{P}_{muscle} = -\oiint_{Wall} (p - p_s + P_{\mathrm{LV}})\mathbf{u} \cdot \mathbf{n_W} dS. \tag{5.13}$$

Gathering Eqs. 5.6,5.9, 5.10 and 5.12 in the integrated version of Eq. 5.3, the final kinetic energy budget reads:

$$\begin{aligned} \mathcal{P}_{muscle} = &\underbrace{\oiint_{AP} P_{\mathrm{LV}}\mathbf{u} \cdot \mathbf{n_{AP}} dS}_{P_{AP}} + \underbrace{\oiint_{AP} \rho e_c \mathbf{u} \cdot \mathbf{n_{AP}} dS}_{E_{AP}} \\ &+ \underbrace{\oiint_{MP} (p - p_s + P_{\mathrm{LV}})\mathbf{u} \cdot \mathbf{n_{MP}} dS}_{P_{MP}} + \underbrace{\oiint_{MP} \rho e_c \mathbf{u} \cdot \mathbf{n_{MP}} dS}_{E_{MP}} \\ &+ \underbrace{\psi}_{\text{Dissipation}} + \underbrace{\frac{d}{dt} \iiint_{D(t)} \rho e_c dV}_{\text{Storage}} - \underbrace{\iiint_{\Omega_t} \rho \mathbf{F} \cdot \mathbf{u} dV}_{\text{MV}}. \end{aligned} \tag{5.14}$$

In Eq. (5.14), ψ is the only term which represents a net energy loss. P_{AP} and P_{MP} are the power of the pressure force exerted on the aorta and received from the atrium, respectively. E_{AP} and E_{MP} represent the energy flux provided and received by the ventricle. *Storage* stands for the energy storage, which necessarily tends to zero after phase averaging due to the periodicity of the cardiac motion. *MV* refers to the MV power, which also corresponds to some energy loss if it is negative. Post-processing of the data, including evaluation of the terms in Eq. (5.14) and visualization of the results, was performed using ParaView [127].

Because $P_{\mathrm{LV}}(t)$ is not directly available from the incompressible CFD formulation, it is reconstructed with a time-varying elastance description of the ventricle: at each instant, the LV pressure is proportional to the volume above a dead volume V_0 and an instantaneous stiffness $E(t)$. Following Reymond *et al.* (their Eq. (17) and Fig. 1B), $E(t)$ is expressed as $E_{\max}E_n(t)$, where $E_n(t) \in [0, 1]$ is a normalized waveform over one cardiac cycle; this normalized elastance has been reported as relatively consistent across subjects. The LV cavity pressure then reads:

$$P_{\mathrm{LV}}(t) \;=\; E_{\max}\, E_n(t) \Big[V_{\mathrm{LV}}(t) - V_0\Big]. \tag{5.15}$$

In the following, $P_{\mathrm{LV}}(t)$ is used consistently as the ventricular pressure reference in the energy budget. Parameter choices are tied to the present heart model and kept within healthy-adult physiology. For this purpose, the normalized elastance waveform of Reymond *et al.* was adopted, with its maximum positioned at $t_{\max} = 350$ ms (Fig. 5.2). This value lies within the adult physiological range of 262–383 ms. $V_0 = 40$ mL is set based on the observed LV-volume range; $E_{\max} = 3$ mmHg mL^{-1} is selected so that the reconstructed pressure attains a physiological systolic level. Both values lie within intervals reported in the literature, namely $V_0 \in [-50, 300]$ mL and $E_{\max} \in [1.0, 6.0]$ mmHg mL^{-1}. The

resulting $P_{\mathrm{LV}}(t)$ and the corresponding PV loop are shown in Fig. 5.3. Note that the conclusions drawn in Section 5.3.2 are robust to the choice made for these parameters.

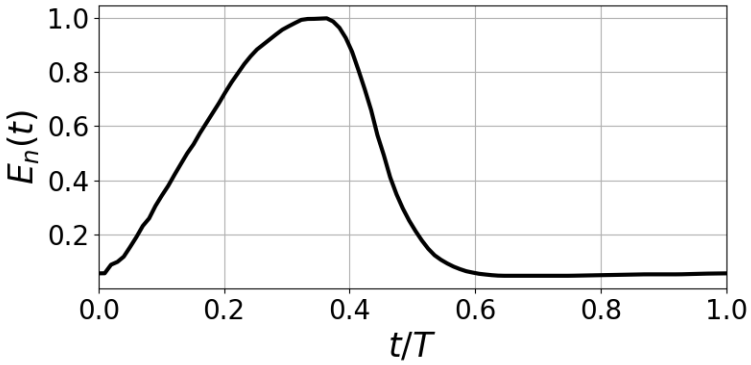


Figure 5.2: Normalized elastance waveform $E_n(t)$ adapted from Reymond *et al.* [141].

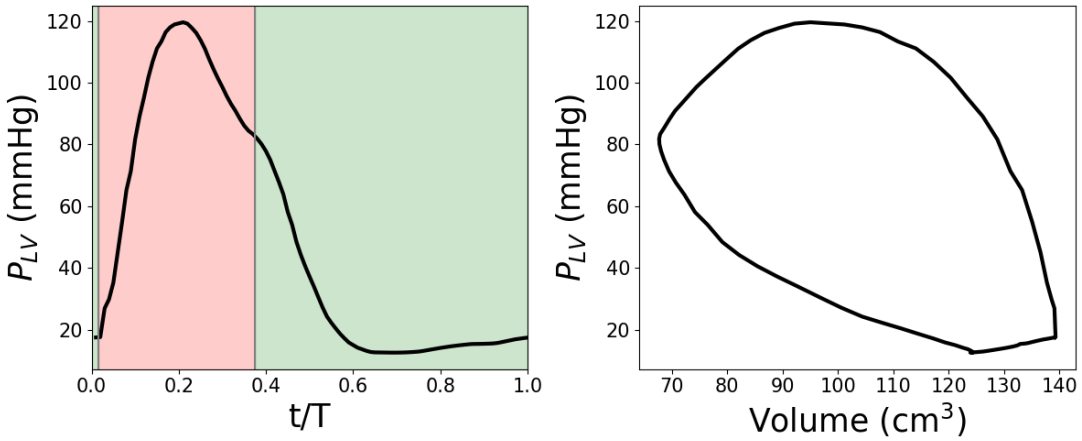


Figure 5.3: Reconstructed ventricular pressure $P_{LV}(t)$ over one cardiac cycle and the corresponding pressure–volume (PV) loop. The pressure is computed from the time-varying elastance relation in Eq. (5.15) using the normalized elastance waveform of Reymond *et al.* [141].

5.3.2 Results

The curves representing the various terms contributing to Eq. (5.14) are shown in Figure 5.4; note that the four cases exhibit nearly identical curves. Figure 5.4 also indicates that the kinetic energy balance is dominated by the three pressure terms $\mathcal{P}_{muscle}$, P_{MP} and P_{AP}. The orange curve represents the error between $\mathcal{P}_{muscle}$ and the sum of all the other terms. It is important to note that the "Error" is plotted on a different scale, using the right axis, compared to the other terms. For all the four

cases it is only a small fraction of the largest contributors to the budget (around 3% error), and it does not depend on the valve design considered. It is most probably due to the fact that KE is usually not conserved at the discrete level even if mass and momentum conservation are well met [142]. It remains that the values obtained closely align with those reported by other research groups, with the peak value of $\mathcal{P}_{muscle}$ around 6 W [67, 112]. The effect of the MV design on the kinetic energy budget is better seen in Figure 5.5 which displays the time evolution of the intraventricular viscous dissipation for the different cases considered. This figure reveals that altering the orientation of the jet (from C01 to C02) has no discernible impact on diastolic dissipation. However, a thicker jet (C03) results in markedly reduced dissipation, while a stronger jet (as in case C04, representing anterior leaflet calcification) leads to increased dissipation. Diastolic dissipation may serve as a complementary metric for characterizing MV pathologies [12, 21, 138–140].

The integration of power dissipation over time allows for assessing the energy lost due to viscous effects. This can be compared to the energy expended to propel blood during the contraction phase by considering the following ratio:

$$R = \frac{\int_0^T \psi \, \mathrm{d}t}{\int_{\text{systole}} \mathcal{P}_{muscle} \, \mathrm{d}t}. \tag{5.16}$$

As shown in Table 5.1, the ratio R remains very small, on the order of a few percent, regardless of the mitral valve geometry. These results suggest that viscous dissipation does not play a significant role in the overall efficiency of the heart. Moreover, the table shows that the total energy delivered by the ventricle does not vary significantly with changes in mitral valve geometry, nor does the maximum power delivered (maximum of $\mathcal{P}_{muscle}$ during systole). These findings are consistent with previous studies [67, 75].

Table 5.1: Quantitative Energy Parameters. Note that the integral of $\mathcal{P}_{muscle}$ is computed only over systole.

Case	$\int \boldsymbol{\psi}\ \mathbf{d}t$ (mJ)	$\int \boldsymbol{\mathcal{P}_{muscle}}\ \mathbf{d}t$ (mJ)	**R** (%)	$\boldsymbol{\mathcal{P}_{muscle}}$ max (W)	$\int \boldsymbol{E_{TKE}}\ \mathbf{d}t$ ($\mathrm{J \cdot s \cdot m^{-3}}$)	$\int \boldsymbol{E_{KE}}\ \mathbf{d}t$ ($\mathrm{J \cdot s \cdot m^{-3}}$)	$\mathbf{R_{KE}}$ (%)
C01	8.4	987	0.9	5.23	0.76	2.57	29
C02	8.6	987	0.9	5.23	0.72	2.57	28
C03	6.4	987	0.7	5.23	0.55	2.09	27
C04	11.7	988	1.2	5.24	1.05	3.35	31

To ensure that the mesh resolution did not significantly affect the results, a finer mesh (23 million tetrahedral cells with average size 0.4 mm) was tested for the reference case (C01). The dissipation-to-power ratio differed by less than 2% between the fine and coarse meshes, indicating minimal sensitivity to spatial resolution. Similarly, the integrated energy budget error showed only a 3% variation between the two configurations. Given these small differences and

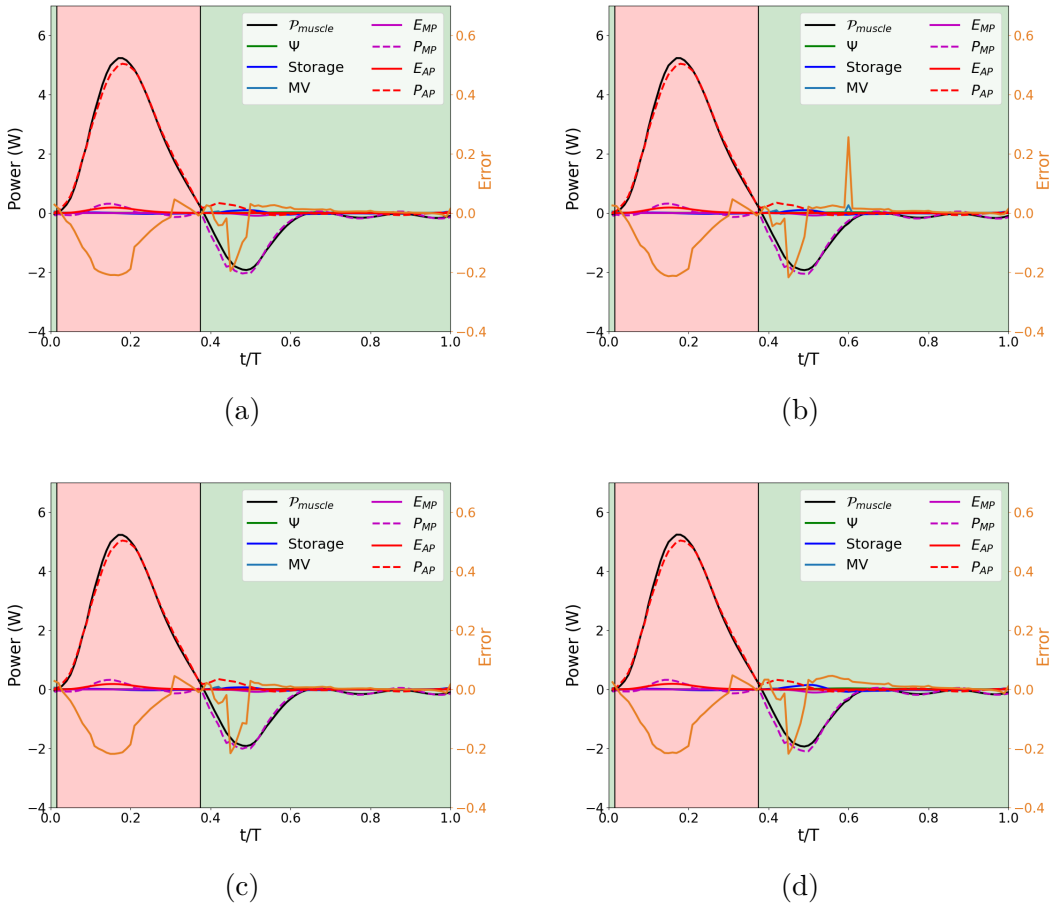
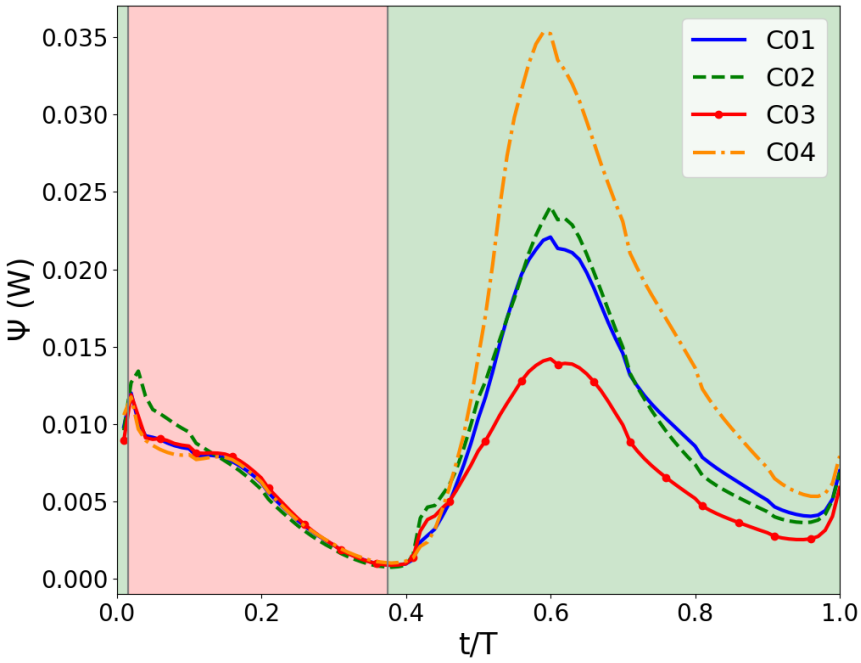


Figure 5.4: Kinetic energy balance for (a) case C01, (b) C02, (c) C03, and (d) C04 (see Table 4.4) during a cycle (averaged over 20 cycles). See Eq. (5.14) for the definition of the different terms. "Error" is the difference between the left-hand and the right-hand sides of Eq. (5.14), which should be zero in the absence of any numerical approximation. Note that the "Error" is plotted on a different scale (right axis) compared to the other terms.

the significantly lower computational cost of the coarser mesh, all subsequent simulations were performed using this more efficient configuration.

Although dissipation can indicate potential issues with the MV, it remains impractical for clinical evaluation due to the need for accurate computation of velocity gradients, which current imaging modalities (such as echocardiography and 4D flow MRI) struggle to provide reliably. The spatial and temporal resolution of these techniques, as well as uncertainties in velocity measurements, limit their ability to capture dissipation accurately. In contrast, quantifying energy fluctuations presents a feasible alternative. Numerous studies have used MRI to assess energy fluctuations [21–24, 136, 140, 143, 144], which is more accessible than dissipation calculation.

To quantify fluctuations within the LV, the fluctuating component of velocity



(a)

Figure 5.5: Intraventricular viscous dissipation (ψ) during a cardiac cycle (averaged over 20 cycles) for the four cases considered.

is examined. The velocity can be decomposed into two parts: the phase-averaged component $\overline{u_i}$ and the fluctuating component u_i':

$$u_i = \overline{u_i} + u_i'. \tag{5.17}$$

Here, $\overline{u}$ denotes a phase average at fixed cardiac phase, and $u_i' = u_i - \overline{u_i}$. On this basis, the kinetic energy densities (per unit volume) in the LV are defined as the turbulent kinetic energy (TKE) density E_{TKE} and the mean-flow kinetic energy density E_{KE}, both expressed in $\mathrm{J \cdot m^{-3}}$.

$$E_{TKE} = \frac{1}{2}\rho\,\overline{u_i' u_i'}, \qquad E_{KE} = \frac{1}{2}\rho\,\overline{u_i}\,\overline{u_i}. \tag{5.18}$$

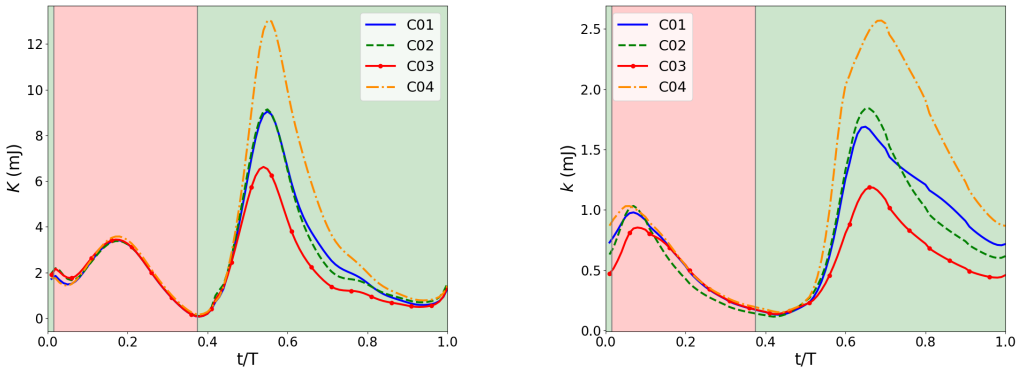
The volume-integrated energies over the LV volume $V(t)$ are:

$$k(t) = \int_{V(t)} E_{TKE}\,\mathrm{d}V, \qquad K(t) = \int_{V(t)} E_{KE}\,\mathrm{d}V, \tag{5.19}$$

which quantify the total mean-flow and turbulent kinetic energies within the LV.

Consistently, R_{KE} (often referred to as turbulence intensity) can be calculated as:

$$R_{KE} = \frac{\int_0^T k(t)\,\mathrm{d}t}{\int_0^T K(t)\,\mathrm{d}t}\,. \tag{5.20}$$



(a) (b)

Figure 5.6: (a) Volume-integrated kinetic energy of the phase-averaged velocity, $K(t) = \int_{V(t)} E_{KE}\,\mathrm{d}V$. (b) Volume-integrated turbulent kinetic energy, $k(t) = \int_{V(t)} E_{TKE}\,\mathrm{d}V$.

Figures 5.6a and 5.6b show the evolution of $K(t)$ and $k(t)$ over a cycle for the four MV configurations. In each case, the volume-integrated mean-flow kinetic energy peaks during systole (around $t/T = 0.2$) and early diastole ($t/T = 0.55$). The former maximum corresponds to the strong flow towards the aorta, while the latter reflects the E-wave filling jet. The fluctuation energy $k(t)$ also exhibits two peaks: a smaller one in early systole (around $t/T \approx 0.1$) and a dominant one during diastole (around $t/T \approx 0.7$). As expected, a higher maximum mitral inflow velocity (Table 4.5) is associated with a higher $K(t)$ peak (Fig. 5.6a). This is clearly observed in case C04, where the anterior leaflet calcification results in a narrower and faster jet, leading to the largest kinetic energy peak during early diastole. Conversely, case C03, which features a wider opening area and thus a slower inflow, exhibits a noticeably lower $K(t)$ and $k(t)$ peak. Regarding leaflet orientation (C01 vs. C02), $K(t)$ shows no discernible change and $k(t)$ varies only modestly (peak $\sim$ 1.7–1.8 mJ, slightly larger for the non-physiological orientation, C02). Given numerical and sampling uncertainties, strong conclusions cannot be drawn based solely on peak values. Consistently, the difference in peak viscous dissipation is also small (Fig. 5.5); thus, neither peak dissipation nor peak $k(t)$ clearly separates these two orientations in the present setup. From a practical standpoint, however, TKE is more readily measurable in vivo since it does not require spatial gradients and can be estimated from intravoxel velocity variance in 4D Flow MRI, whereas dissipation relies on velocity gradients and is markedly sensitive to spatial resolution and noise. For this reason, TKE remains a pragmatic candidate metric even if the effect size is modest. In line with these results, KE/TKE can discriminate valve abnormalities that primarily alter jet strength (e.g., C03 and C04), as reflected by lower and higher peaks, respectively; however, not all alterations are captured. Changes in leaflet orientation, for example, leave $K(t)$ essentially unchanged and modify $k(t)$ only slightly, making differences difficult to detect, especially with cycle-integrated metrics (C01 vs.

C02) or temporally coarse MRI. Notably, despite the variations between cases, R_{KE} remains close across configurations (around 25–30%, see Table 5.1).

5.3.3 Discussion

Despite the presence of turbulent activity during diastole [70], the amount of energy dissipated by the different eddies remains marginal and does not compromise the efficiency of the cardiac pump. The same is true regarding the large vortex displayed in Figure 4.11, C01 and often seen as a major hydrodynamic feature to favor the ejection of blood through the aorta [128, 145]. The characteristics of this vortex (size and position) are strongly modified in C03 and C04, and its existence is even questionable in C02. The kinetic energy peak varies significantly among some of the cases (ranging from 6 to 12 mJ), as well as the peak of turbulent kinetic energy (ranging from 1 to 2.5 mJ). Still, the corresponding amount of energy dissipated remains small compared to the overall energy spent by the muscle during the cardiac cycle (about 1-2%). This finding is consistent with recent studies [12, 50, 67, 75, 136] which are questioning the effective role of the diastolic vortex in the heart functioning. The numerical results also confirm that dissipation and turbulent KE could serve as effective indicators of mitral valve performance, although their reliability may vary.

The role of turbulence dissipation in cardiac function remains debated. Some studies suggest that a swirling flow filling the entire left ventricular cavity during diastole enhances both blood inflow and ejection [16, 128, 130, 138, 139]. However, the findings indicate that disrupting this large recirculation leads to minimal energy loss compared to the total myocardial output. This observation thus casts doubt on the usefulness of measuring turbulent kinetic energy with cardiac magnetic resonance imaging or vector flow mapping by Doppler echocardiography to characterize the pumping efficiency [4, 5, 7, 146, 147]. It also suggests that the orientation of a mitral bioprosthesis may have little impact from an energetic standpoint. Nonetheless, it is important to note that impaired flow patterns can promote blood stasis, increasing the risk of cardiogenic embolic events, an aspect not addressed in the present study [148]. A deeper analysis of how altered intraventricular circulation influences blood residence time and regional stagnation could provide further insights.

This study is subject to several limitations. Firstly, the analysis was based on a single geometric configuration, potentially limiting its ability to fully encompass the diverse anatomical and physiological variations present in real cardiac structures. Pathological as well as healthy geometries could exhibit distinct flow patterns and energy dissipation behaviors, which were not explored in this investigation. The finding of a low level of dissipation in healthy conditions is consistent with previous studies, which have also reported minimal energy loss in the left ventricle under normal physiological conditions [67, 75].

Secondly, the mitral valve model used in the simulations is not directly reconstructed from medical imaging. Instead, it is based on an established model from

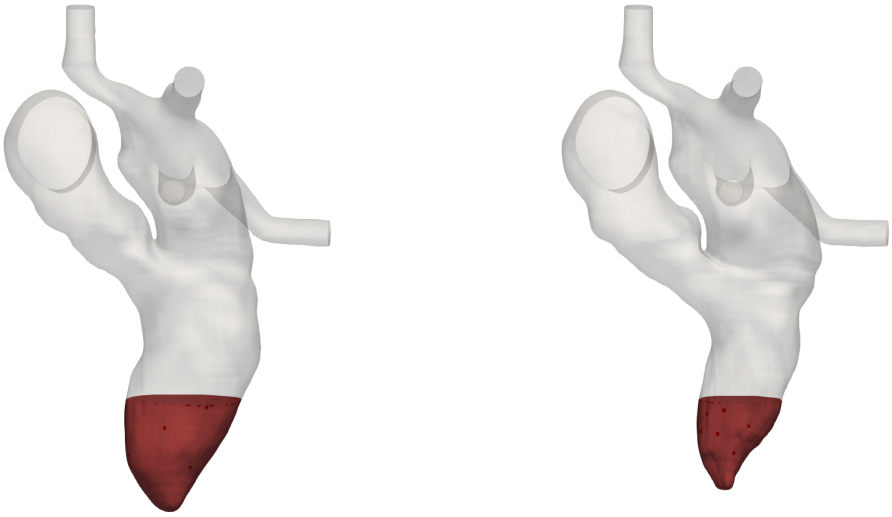
the literature, which effectively captures key features of the valve, but the use of a patient-specific valve geometry could provide more accurate insights. Furthermore, none of the cases of MV considered involved mitral regurgitation (MR), a pathological condition of the utmost medical interest. In particular, exploring different types and severities of MR could provide a more comprehensive understanding of its influence on cardiac efficiency. Another limitation lies in the inability of the image registration process to fully capture trabeculations and their contribution to volume changes. Furthermore, the model assumes that the mitral valve remains fully open throughout diastole, including during diastasis, whereas in reality, a partial closure occurs due to pressure equilibration between the left atrium and the left ventricle. While diastasis plays an important role in hemodynamics [59, 74, 149, 150] and this constitutes a simplification, the model still captures the characteristic mitral inflow pattern, including its reduction during diastasis, as observed in [59]. Another approach, such as fluid-structure interaction (FSI), could improve the accuracy of mitral valve modeling and its interaction with different flow structures, but it would significantly increase computational costs. Moreover, while FSI would allow for a more detailed assessment of myocardial stresses, it also introduces challenges such as the estimation of material properties and boundary conditions. Given that the primary focus here is on ventricular fluid dynamics, a prescribed wall motion approach derived from medical imaging was adopted, as it is more relevant to the objectives of this study.

5.4 Mixing in the left ventricle

Effective blood mixing in the left ventricle plays a crucial role in preventing thrombus formation. In particular, the apical region is prone to flow stagnation: low local velocities can lead to prolonged blood residence times, creating favorable conditions for clot initiation and growth. Such phenomena are clinically relevant in various pathologies, including dilated cardiomyopathy, left ventricular aneurysms, and cases of severe mitral regurgitation, where apex washout is often impaired. Understanding how LV flow dynamics promote or hinder blood renewal in the apex is therefore essential for assessing thromboembolic risk and evaluating the hemodynamic performance of different mitral valve configurations.

To assess mixing in the LV, a control volume was defined at the apex, as illustrated in Fig. 5.7, shown at both mid-systole and end-systole. The temporal evolution of this apical volume, $V_{\text{Apex}}(t)$, normalized by the cardiac cycle duration T, is reported in Fig. 5.8.

To quantify apical renewal, a passive scalar field ϕ was introduced, governed by a constant source term s and evolving in time as $\phi = st$. This scalar acts as a surrogate for blood elements entering the LV, enabling us to measure washout efficiency and identify stagnation zones. Low values of ϕ correspond to recently arrived blood, whereas high values indicate fluid that has remained in the LV for longer periods.



(a) (b)

Figure 5.7: Studied apical volume at (a) mid-systole and (b) end-systole.

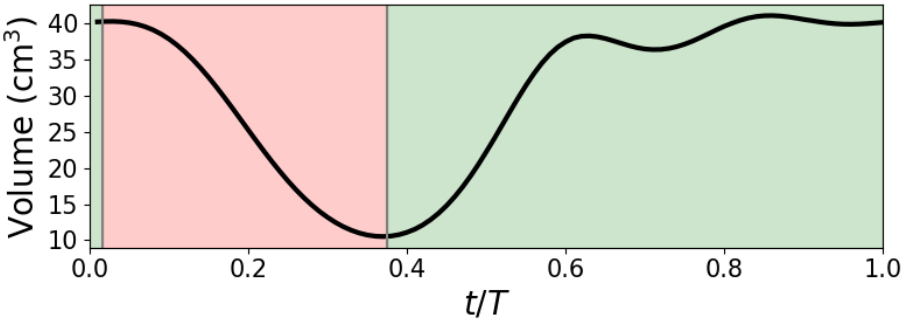
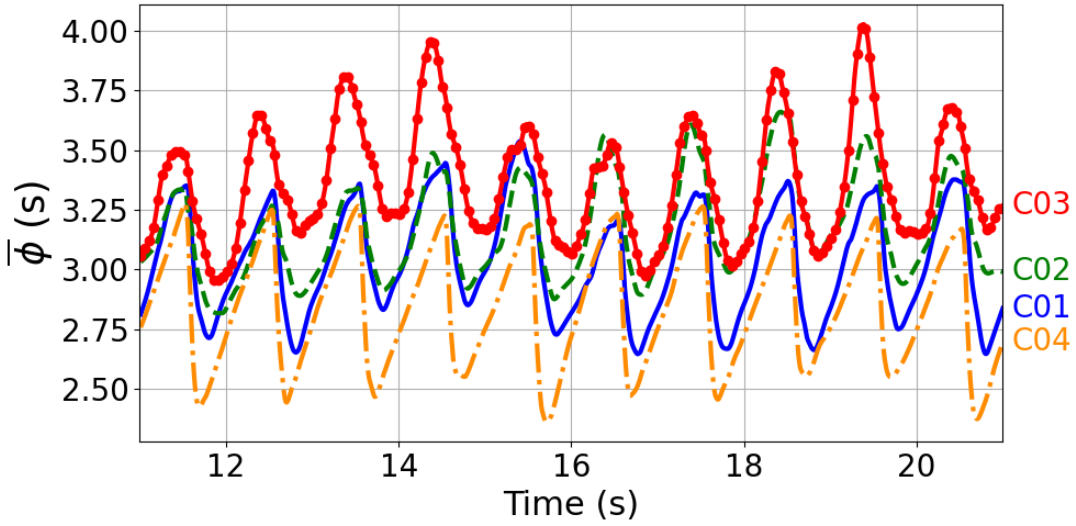


Figure 5.8: Instantaneous LV volume $V_{\mathrm{LV}}(t)$ over time.

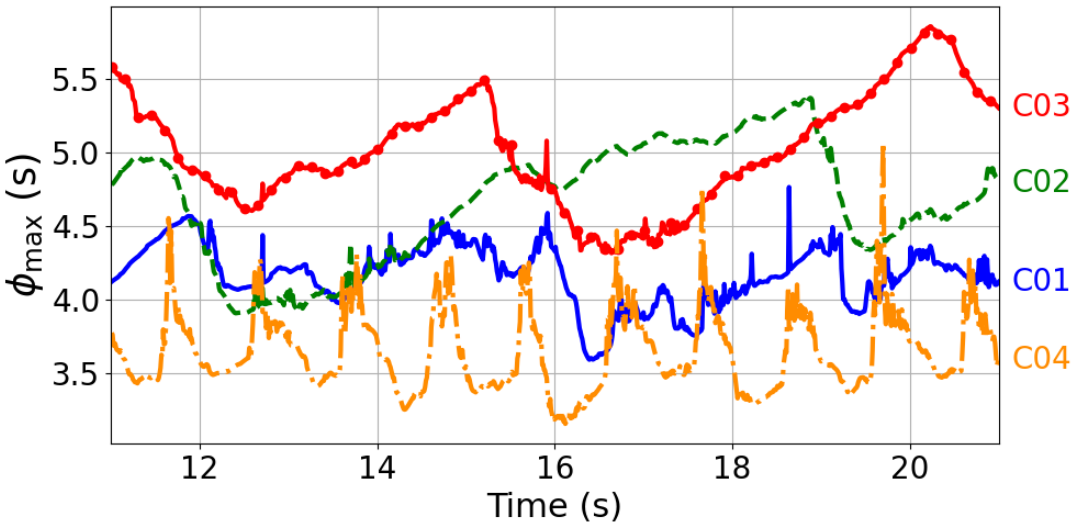
Two quantities are extracted from the scalar field within the apical control volume: the spatial average $\overline{\phi}(t)$ and the maximum value $\phi_{\max}(t)$. The former provides a global metric of blood age in the apex, while the latter indicates the longest residence time of any blood element within the region.

$$\overline{\phi}(t) = \frac{1}{V_{\mathrm{Apex}}(t)} \int_{V_{\mathrm{Apex}}(t)} \phi(\mathbf{x}, t)\, \mathrm{d}V, \qquad \phi_{\max}(t) = \max_{\mathbf{x} \in V_{\mathrm{Apex}}(t)} \phi(\mathbf{x}, t) \tag{5.21}$$

The temporal evolution of these quantities over ten cardiac cycles is shown in Fig. 5.9. Note that the scalar field ϕ was initialized well before the beginning of the plotted window. The simulation was run for 11 cardiac cycles prior to the displayed time range, allowing the scalar to reach a statistically steady distribution that no longer depends on its initialization. As a result, the values of ϕ at the start of the plotted interval ($t = 11$ s) already reflect the cumulative residence time of blood elements, and should not be interpreted as freshly introduced fluid.



(a) Temporal evolution of $\overline{\phi}(t)$ (volume-averaged scalar in the apex) for all MV configurations.



(b) Temporal evolution of $\phi_{\max}(t)$ (maximum scalar in the apex) for all MV configurations.

Figure 5.9: Passive scalar evolution in the apex over a 10-cycle window. High values of ϕ indicate poor washout and potential blood stagnation. The scalar was initialized 11 cycles earlier, so values at $t = 11$ s already reflect prior residence times.

For all configurations, $\overline{\phi}(t)$ exhibits a clear cyclic pattern, peaking near end-systole when the apical volume contains the oldest blood, and decreasing during early diastole as the mitral jet reaches the apex. Modifying MV parameters changes both the peak amplitude and the rate of decay of $\overline{\phi}(t)$. Among the configurations, C03 shows the highest peak values (up to 4 s), indicating the

least efficient renewal. The jet-reoriented case (C02) also leads to consistently higher mean scalar levels compared to the reference case C01, suggesting that the new jet trajectory may be less effective at penetrating the apex. Conversely, C04 consistently reaches the lowest minima (around 2.4 s), reflecting more complete and regular apical flushing. Importantly, in all configurations, scalar values above 2 s persist over multiple cycles, which is comparable to two full cardiac cycles (with $T = 1$ s), confirming that portions of blood can remain trapped in the apex for extended periods.

The maximum scalar $\phi_{\max}(t)$ provides complementary insights into stagnation. Configuration C03 again stands out, with sustained high values exceeding 5.5 s, revealing that some blood elements remain in the apex for more than five cardiac cycles. C02 shows intermittent stagnation events, with occasional peaks above 5 s, while C01 stays below 4.5 s with relatively regular oscillations. Configuration C04 displays the most favorable behavior: $\phi_{\max}(t)$ exhibits a highly cyclic pattern, with clear and sharp drops during each early diastole. Although the maximum scalar does not return to zero, it remains consistently lower than in other configurations, indicating more regular and effective (though not complete) flushing of the apex.

These results highlight the importance of both early-diastolic jet strength and orientation in ensuring proper apical washout.

5.5 Overall conclusion

This chapter quantified the intraventricular energy budget and apical mixing for four mitral valve configurations differing in leaflet orientation and effective orifice area, under identical wall kinematics and boundary conditions.

Across C01–C04, clear differences were observed in flow organization, including changes in jet strength/orientation, vortex patterns, and the magnitude and timing of both mean-flow kinetic energy and fluctuation energy. These differences are also reflected in viscous dissipation: a wider opening lowers diastolic dissipation, whereas the calcification-like setting increases it, with the reoriented jet close to the reference case. Nevertheless, at the cycle level the kinetic energy budget is dominated by pressure terms, and the fraction of myocardial work lost to viscous effects remains small (dissipation ratio $R \approx 0.7$–1.2%). Total systolic work and peak myocardial power vary only marginally between cases. In short, MV-induced topology changes noticeably affect KE/TKE and dissipation, but they translate into only limited changes in pumping efficiency under the present conditions.

The apical-mixing analysis leads to the same message. Early-diastolic jet strength and direction chiefly govern apical renewal: the wider-opening case shows the least efficient washout, the calcification-like case the most efficient, and this time the orientation-change case is visibly less efficient than the reference. These differences are moderate yet consistent, and they matter for stasis-related risk.

These findings motivate the next step: the study of mitral regurgitation. Unlike the configurations considered here, MR introduces a systolic backflow across the MV that coexists with forward aortic ejection. Part of the myocardial

work then drives a regurgitant volume that does not contribute to forward stroke, which should therefore markedly increase dissipation. One should therefore expect a larger efficiency penalty, and poorer washout due to the recirculation. The next chapter investigates these MR specific effects on the intraventricular energy balance and transport metrics.

Chapter 6

Study of mitral regurgitation

Chapter contents

6.1 Mitral regurgitation: definition 106
6.1.1 Clinical presentation and classification 106
6.1.2 State of the art: approaches for studying mitral regurgitation 108
6.2 Methodology 109
6.3 Reference case for regurgitation: analysis 112
6.4 Analysis of the effect of regurgitant volume on energy loss 115
6.5 Analysis of the MR mechanism on energy loss 119
6.6 Overall conclusion 121

This chapter quantifies the hemodynamic cost of mitral regurgitation in the left heart under prescribed kinematics and a controlled mitral geometry. After defining MR (its clinical presentation and classification) and reviewing current medical imaging and computational approaches, the numerical methodology is detailed. A reference primary MR (Type II) case is established and its flow energetics analyzed. The influence of the regurgitant volume on viscous dissipation and energy loss is assessed at fixed systolic opening and effective regurgitant orifice area, and mechanism-dependent effects are isolated by comparing Type II and Type IIIb MR at matched EROA and RV.

6.1 Mitral regurgitation: definition

6.1.1 Clinical presentation and classification

Mitral regurgitation is a valvular heart disorder characterized by retrograde blood flow from the left ventricle to the left atrium during systole due to incomplete closure of the mitral valve. This backward flow raises left atrial and ventricular volumes and pressures, which can lead to left atrial dilation, pulmonary hypertension, ventricular remodeling, and ultimately heart failure if untreated. It is the second most frequent valvular heart disease in Europe [151, 152].

MR can be classified into two main types depending on the origin of the dysfunction: primary (organic) and secondary (functional) MR [153]. Primary MR results from structural abnormalities of the mitral valve apparatus, such as leaflets, chordae tendineae, or papillary muscles. Common causes include mitral valve prolapse, rheumatic disease, infective endocarditis, and connective tissue disorders. Treatment is often surgical, via valve repair or replacement. Secondary MR, by contrast, occurs despite anatomically normal valve structures and is caused by geometric and functional changes in the LV or LA, most often in the setting of ischemic or dilated cardiomyopathy, or chronic atrial fibrillation. These alterations lead to annular dilation, leaflet tethering, and impaired coaptation. Initial treatment is usually medical, targeting the underlying heart failure, with interventional options such as mitral clipping or annuloplasty considered if symptoms persist.

MR occurs during the systolic phase of the cardiac cycle, specifically beginning at the onset of isovolumetric contraction. In a healthy heart, this phase features a rapid rise in LV pressure while both the mitral and aortic valves remain closed. In MR, incomplete closure of the mitral valve allows blood to regurgitate into the LA as soon as LV pressure exceeds LA pressure. This regurgitant flow persists throughout systole, encompassing both isovolumetric contraction and ejection. The regurgitant volume during systole leads to a significant increase in LA volume and pressure.

In acute MR, the sudden onset of regurgitation does not allow time for compensatory adaptations. Consequently, there is an abrupt increase in LA pressure, leading to pulmonary edema and reduced forward cardiac output, which can be rapidly life-threatening. In contrast, chronic MR develops gradually, allowing the heart to implement compensatory mechanisms. Initially, the LV dilates to accommodate the increased volume, maintaining stroke volume and cardiac output (a phase known as compensated MR). Over time, however, these mechanisms may fail, leading to LV dysfunction and the onset of symptoms such as dyspnea and fatigue, marking the transition to decompensated MR.

Clinically, MR is classified according to its underlying mechanism and its severity. These classifications guide diagnosis, therapeutic decision-making, and prognosis. One widely adopted system is Carpentier's functional classification, which categorizes MR based on mitral leaflet motion:

- **Type I:** Normal leaflet motion. Regurgitation results from annular dilation

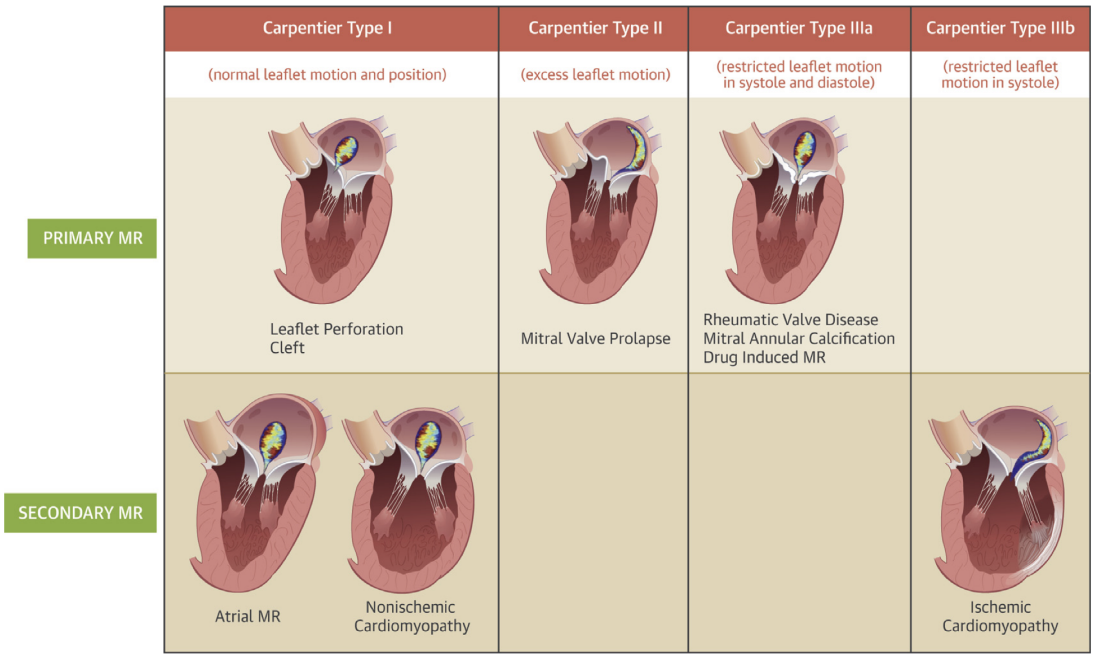


Figure 6.1: Carpentier classification of mitral regurgitation mechanisms (Extracted from El Sabbagh et al. [154]).

or leaflet perforation. The regurgitant jet is typically central.

- **Type II:** Excessive leaflet motion due to prolapse or flail, often caused by chordal rupture or elongation. The jet is usually eccentric, directed away from the affected leaflet.
- **Type III:** Restricted leaflet motion.
  - **Type IIIa:** Restriction during both systole and diastole, commonly associated with rheumatic disease.
  - **Type IIIb:** Restriction predominantly during systole, often due to LV remodeling in ischemic cardiomyopathy.

This classification provides essential insight into the underlying mechanism of MR and is particularly useful for guiding surgical repair strategies. Figure 6.1 illustrates the different Carpentier types and highlights their relationship with primary and secondary MR.

To quantify MR severity, several Doppler-based echocardiographic parameters are commonly used, each reflecting a different aspect of the regurgitant flow:

- **Effective regurgitant orifice area (EROA)** represents the functional orifice through which blood flows back from the LV to the LA during systole. It serves as an anatomical indicator of the size of the leak. A larger EROA generally implies more severe MR. An EROA of $\geq 0.4\,\mathrm{cm}^2$ is typically considered the threshold for severe MR.

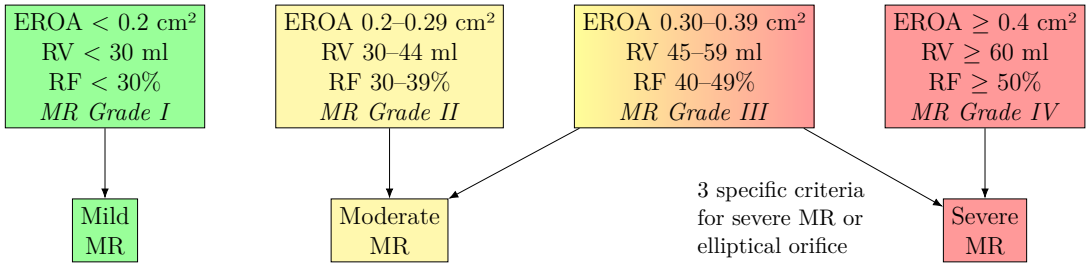


Figure 6.2: Classification of mitral regurgitation severity, based on Doppler echocardiographic criteria (adapted from Zoghbi et al. [155]).

- **Regurgitant volume (RV)** corresponds to the actual volume of blood that regurgitates into the LA with each heartbeat. It is calculated as the difference between total LV stroke volume and the forward stroke volume delivered to the aorta. A regurgitant volume of ≥ 60 mL is a strong indicator of severe MR.
- **Regurgitant fraction (RF)** expresses the proportion of total LV stroke volume that is regurgitated back into the LA. It is calculated as the ratio of regurgitant volume to total stroke volume and is usually expressed as a percentage. A regurgitant fraction of $\geq 50\%$ is associated with severe MR.

Together, these metrics offer a comprehensive view of MR severity: EROA reflects anatomical lesion severity, RV quantifies the absolute volume overload, and RF assesses the relative impact of regurgitation on global ventricular function. Figure 6.2 presents a schematic overview of MR severity levels based on these criteria.

6.1.2 State of the art: approaches for studying mitral regurgitation

6.1.2.1 Medical imaging

The accurate assessment of MR relies on advanced cardiac imaging, which provides key insights into etiology, mechanism, severity, and hemodynamic consequences. Among these, echocardiography and CMR are paramount.

Transthoracic echocardiography (TTE) is the first-line modality for MR. It offers a comprehensive evaluation of mitral morphology, leaflet motion, and regurgitant jets. Color Doppler enables visualization of the jet, and spectral Doppler supports flow and gradient quantification. A multiparametric approach is recommended to grade severity, combining EROA, regurgitant volume (RV), vena contracta width, and jet characteristics [155], as shown in Figure 6.2.

When image quality is limited or anatomy is complex, transesophageal echocardiography (TEE) provides higher spatial resolution and detailed views of the mitral apparatus. TEE is particularly valuable for preoperative planning, intraoperative monitoring, and for the evaluation of prosthetic valves or endocarditis.

Three-dimensional TEE further improves lesion localization and guides surgical or transcatheter interventions [153, 156–158].

Cardiac Magnetic Resonance (CMR) complements TTE/TEE when images are limited or measurements disagree. Using volumetric methods, CMR provides reproducible RV/RF and reference-standard LV/LA volumes and function [159]. It is therefore very useful with multiple or eccentric jets and whenever precise quantification is needed for decision-making [160–163].

6.1.2.2 Numerical simulations of mitral regurgitation

Over the past decade, image-based CFD has emerged as a powerful framework to investigate MR across the left heart, combining prescribed cardiac motion with either explicit leaflet kinematics or immersed representations of the mitral valve. These studies typically reconstruct the LA and LV anatomy and flow fields from cardiac CT or cine-MRI, impose chamber and valvular kinematics, and solve the Navier–Stokes equations to quantitatively analyze regurgitant jets, wall shear stress, residence times, and energy-related metrics [48, 59, 72, 83].

FSI studies provide mechanistic insight by coupling leaflet/chordal mechanics with intracardiac flow, clarifying how specific etiologies affect coaptation and jet formation. FSI also enables the quantification of tissue stresses relevant to repair durability [74, 164]. While such simulations are essential for understanding etiology and guiding intervention, this chapter focuses on flow energetics under prescribed kinematics, where image-based CFD affords direct, cycle-resolved estimates of viscous energy dissipation within the LA and LV.

In this chapter, the objective is to isolate, in Type II MR (posterior leaflet prolapse into the LA), the effect of regurgitant volume on viscous dissipation for a fixed regurgitant-orifice geometry and EROA (three RV levels) (Section 6.4). To investigate the impact of MR type, a Type IIIb configuration (posterior leaflet with a persistent intraventricular opening) is also included, with identical EROA and regurgitant volume to one of the Type II cases to isolate mechanism-dependent differences (Section 6.5). The methodology is presented in Section 6.2.

6.2 Methodology

The numerical framework is identical to that introduced in Chapter 2. The computational domain and cardiac anatomy follow Chapter 3, Section 3.1. Relative to the healthy baseline, mitral regurgitation is introduced through two targeted modifications: a prescribed systolic opening angle of the posterior leaflet, denoted $\varphi_{\text{post}}^{\text{sys}}$, which specifies its configuration during systole, and an adjustment of the inlet boundary condition to impose a regurgitant flow. The specification and implementation of the latter modification are detailed below.

To simulate mitral regurgitation, the inlet boundary condition (corresponding to pulmonary venous inflow) was modified to account for a prescribed retrograde

flow from the LV into the LA during systole. In the healthy configuration, the inlet flow rate is defined as:

$$Q(t) = \begin{cases} \frac{dV_{\mathrm{LA}}}{dt} & \text{when the mitral valve is closed,} \\ \frac{dV_{\mathrm{LA}}}{dt} + \frac{dV_{\mathrm{LV}}}{dt} & \text{when the mitral valve is open.} \end{cases} \tag{6.1}$$

To induce regurgitation, a target regurgitant volume (RV) was prescribed over the systolic interval $[t_{\mathrm{start}}, t_{\mathrm{end}}]$, and the inlet flow rate was adjusted accordingly. A smooth temporal profile $f(t)$ was defined over systole:

$$f(t) = \frac{1}{2}\left(1 - \cos\left(2\pi \cdot \frac{t - t_{\mathrm{start}}}{t_{\mathrm{end}} - t_{\mathrm{start}}}\right)\right) \tag{6.2}$$

The corresponding regurgitant flow rate $Q_{\mathrm{MR}}(t)$ was then defined as:

$$Q_{\mathrm{MR}}(t) = Q_{\max} \cdot f(t). \tag{6.3}$$

where $Q_{\max}$ is chosen such that the total regurgitant volume matches the prescribed RV:

$$\int_{t_{\mathrm{start}}}^{t_{\mathrm{end}}} Q_{\mathrm{MR}}(t)\, dt = \mathrm{RV}. \tag{6.4}$$

The modified inlet flow rate is finally obtained by subtracting this regurgitant component during systole:

$$Q_{\mathrm{inlet_{MR}}}(t) = Q_{\mathrm{inlet}}(t) - Q_{\mathrm{MR}}(t), \quad t \in [t_{\mathrm{start}}, t_{\mathrm{end}}] \tag{6.5}$$

Outside the systolic interval, the inlet condition remains unchanged.

As an example, Figure 6.3 shows the modified inlet profile for a prescribed RV of 25 mL. In this case, the regurgitant component $Q_{\mathrm{MR}}(t)$ (green) is superimposed on the healthy inlet signal (blue), resulting in the final modified inlet profile $Q_{\mathrm{inlet_{MR}}}$ (orange).

Given the ventricular volume in this model (EDV=140 mL, ESV=70 mL), the chosen RV corresponds to a regurgitant fraction (RF) of approximately 35%, which is consistent with moderate mitral regurgitation severity (see Figure 6.2). The corresponding outlet flow rate is shown in Figure 6.4, where the reduction in aortic forward flow due to regurgitation is clearly visible.

The framework described in Section 5.3 is adopted for the energetic analysis, consistent with Chapter 5. The muscle power balance is thus written as:

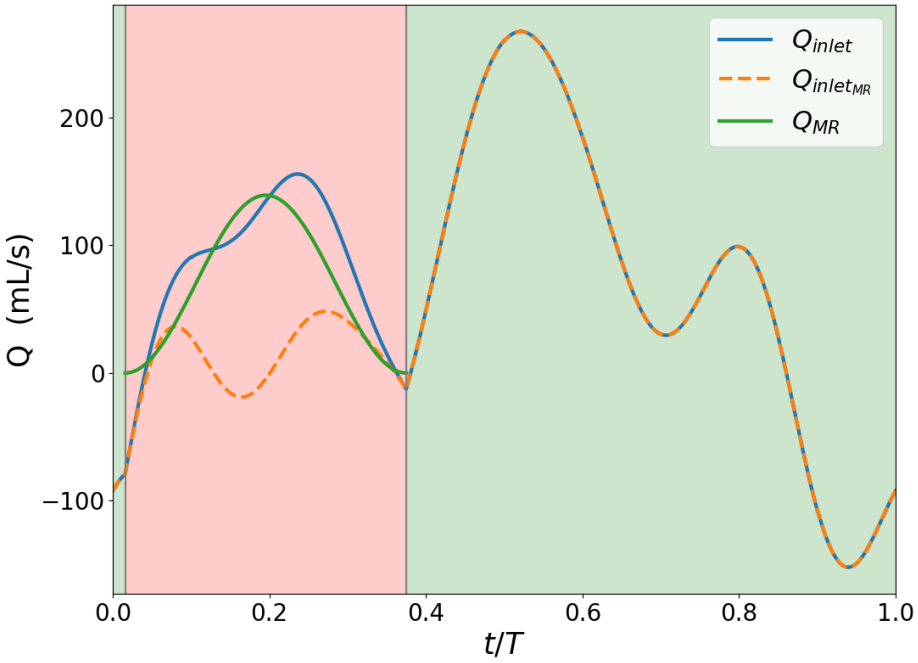


Figure 6.3: Modified inlet flow rate for a regurgitant volume of 25 mL. The original inlet signal is shown in blue, the prescribed regurgitant flow Q_{MR} in green, and the resulting modified inlet profile $Q_{\mathrm{inlet_{MR}}}$ in orange.

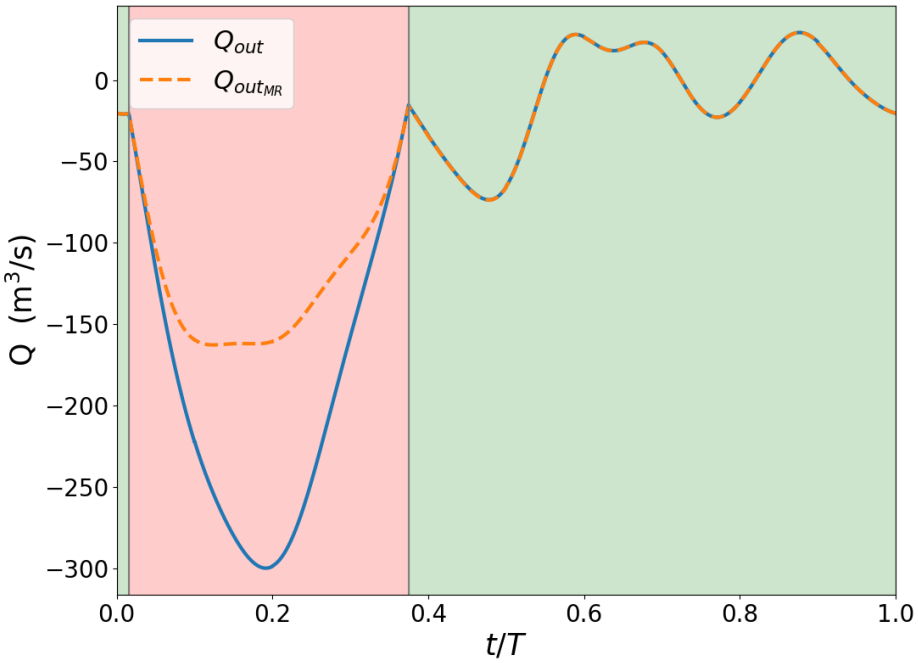


Figure 6.4: Modified outlet flow rate for a regurgitant volume of 25 mL. The original (healthy) outlet flow is shown in blue, and the regurgitant case in orange.

$$\begin{aligned}\mathcal{P}_{muscle} = &\underbrace{\oiint_{AP} P_{LV}\mathbf{u}\cdot\mathbf{n_{AP}}dS}_{P_{AP}} + \underbrace{\oiint_{AP}\rho e_c\mathbf{u}\cdot\mathbf{n_{AP}}dS}_{E_{AP}}\\ &+\underbrace{\oiint_{MP}(p-p_s+P_{LV})\mathbf{u}\cdot\mathbf{n_{MP}}dS}_{P_{MP}} + \underbrace{\oiint_{MP}\rho e_c\mathbf{u}\cdot\mathbf{n_{MP}}dS}_{E_{MP}}\\ &+\underbrace{\psi}_{\text{Dissipation}} + \underbrace{\frac{d}{dt}\iiint_{D(t)}\rho e_c dV}_{\text{Storage}} - \underbrace{\iiint_{\Omega_t}\rho\mathbf{F}\cdot\mathbf{u}dV}_{\text{MV}}.\end{aligned} \tag{6.6}$$

Under these conditions, the terms P_{MP} and E_{MP} may be positive during systole, and then correspond to an energy loss. When these terms are negative, they reflect normal heart function (specifically, blood flowing from the atrium to the ventricle during diastole) without additional dissipation due to mitral regurgitation. The additional energy loss is then defined from $\mathcal{L}_{MR} = P_{MP} + E_{MP}$. The ratio of the loss will then be:

$$R_{MR} = \frac{\int_{\text{systole}} \mathcal{L}_{MR}\ \mathrm{d}t + \int \psi\ \mathrm{d}t}{\int_{\text{systole}} \mathcal{P}_{muscle}\ \mathrm{d}t} \tag{6.7}$$

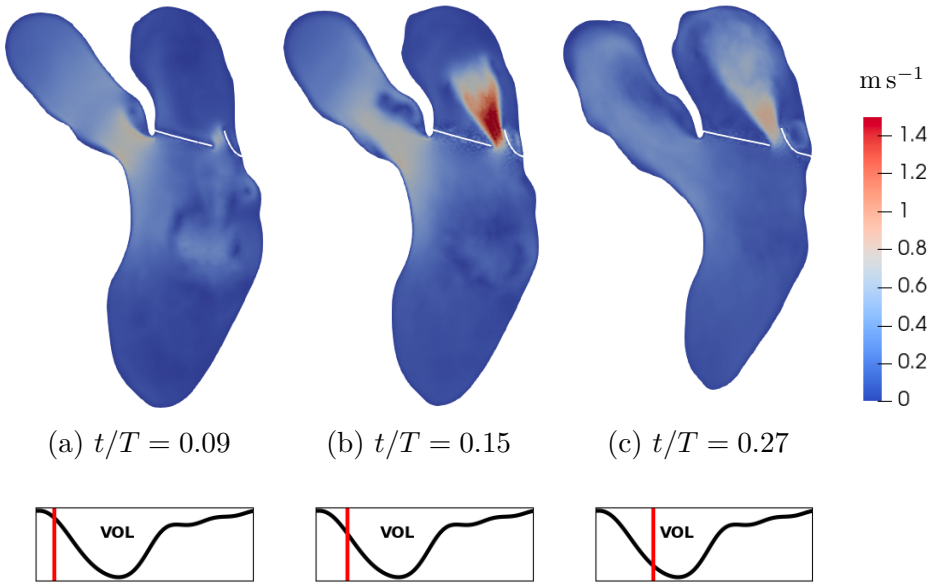
6.3 Reference case for regurgitation: analysis

To establish a baseline for the analysis of mitral regurgitation, a Type II case was simulated, characterized by prolapse of the posterior leaflet into the left atrium. The posterior leaflet opening angle was fixed at $\varphi_{\text{post}}^{\text{sys}} \approx -40°$, resulting in an effective regurgitant orifice area (EROA) of approximately 0.25 cm^2. The regurgitant volume was set to 25 mL, so that part of the LV outflow returns to the LA.

From theoretical considerations, such a geometry is expected to generate regurgitant jet velocities in the range of 4–5 m.s^{-1}. In practice, accurately modeling regurgitant flow is more challenging than simulating healthy valve function, and in the present numerical representation the mitral valve remains slightly permeable at closure. This numerical leakage reduces the peak jet velocity. As a result, the maximum regurgitant jet speed here is about 2 m.s^{-1}. Despite this lower peak, the jet is clearly identifiable and suitable for detailed analysis.

The jet enters the LA at $t/T = 0.09$ (Fig. 6.5a), its velocity increases through systole, and reaches a maximum of 2 m.s^{-1} at $t/T = 0.15$ (Fig. 6.5b). After this peak, the jet weakens, and the remainder of the cardiac cycle proceeds similarly to the reference case C01 during diastole (see Chapter 3, Section 3.2.3).

Since the parameter selection in this initial case was exploratory, an additional simulation was carried out with a smaller posterior leaflet opening angle ($\varphi_{\text{post}}^{\text{sys}} \approx -35°$, see Table 6.1). As shown in Fig. 6.6, the smaller opening produces a slightly



(a) $t/T = 0.09$ (b) $t/T = 0.15$ (c) $t/T = 0.27$

Figure 6.5: Phase-averaged velocity field (averaged over 20 cycles) at different times of systole.

stronger regurgitant jet at mid-systole ($t/T = 0.20$), leading to a modest change in the flow field (consistent with a smaller orifice for a similar imposed RV).

Table 6.1: Parameter values defining the two regurgitant configurations (C05 and C05_{bis}). The posterior leaflet angle $\varphi^{\text{sys}}_{\text{post}}$ corresponds to the opening angle during systole.

Case	**RV (mL)**	$\boldsymbol{\varphi}^{\text{sys}}_{\text{post}}$	**EROA (cm^2)**
C05	25	$-40°$	0.25
C05_{bis}	25	$-35°$	0.23

To assess whether the observed differences in jet strength significantly affect viscous energy losses, the intraventricular dissipation ψ was computed, as well as the total dissipation within the atrium and ventricle ($\psi_{\text{Atrium+Ventr}}$) for both configurations. As shown in Fig. 6.7, dissipation levels remain of the same order of magnitude between the two regurgitant cases (C05 and C05_{bis}). However, when compared to the healthy reference (C01), a slight increase in dissipation is observed during systole, consistent with the additional viscous losses induced by the regurgitant jet. It should be noted that the vertical axes differ between panels (a) and (b), as dissipation in the atrium is not negligible compared to that in the ventricle. Based on the similarity of the two pathological configurations, the first case ($\varphi^{\text{sys}}_{\text{post}} \approx -40°$, RV = 25 mL) is retained as the reference for subsequent analyses, denoted C05_{25mL} from now on.

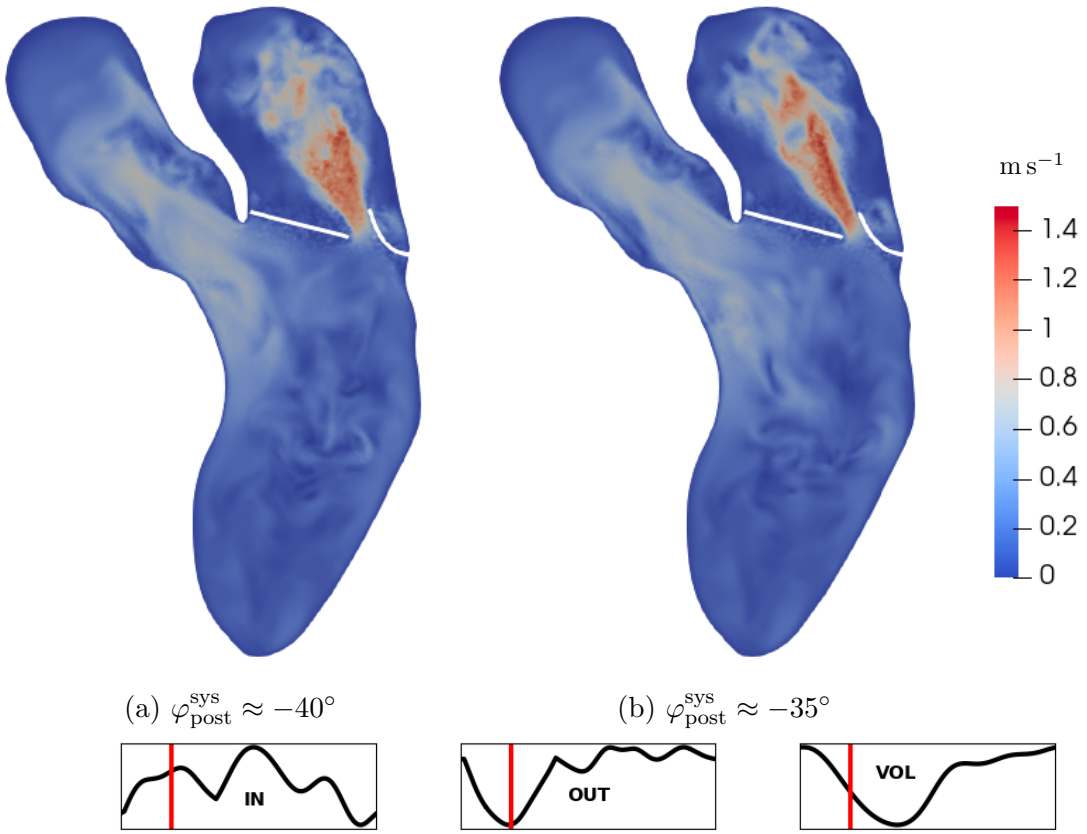
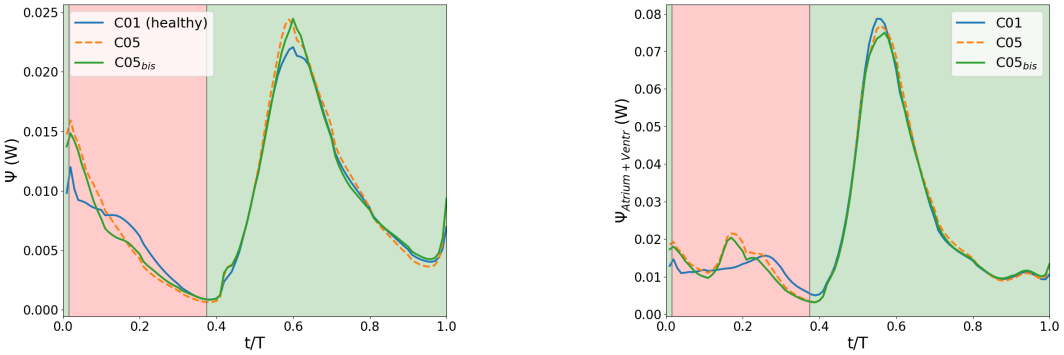
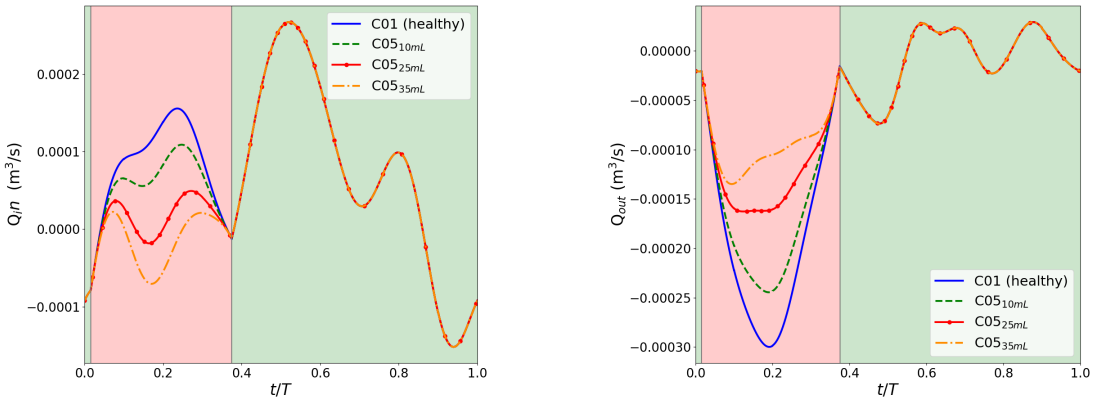


Figure 6.6: Instantaneous velocity field at $t/T = 0.2$ (mid-systole) for two different posterior leaflet opening angles. Parameter values are summarized in Table 6.1.



(a) (b)

Figure 6.7: (a) Instantaneous intraventricular viscous dissipation (ψ) during a cardiac cycle. (b) Total viscous dissipation within the atrium and ventricle ($\psi_{\text{Atrium+Ventr}}$). Parameter values are summarized in Table 6.1. In both panels, the healthy reference case (C01) is added for comparison. Note that the vertical axes differ between (a) and (b).



(a) (b)

Figure 6.8: (a) Inlet flow rate for the healthy case (C01) and the three regurgitation cases. (b) Outlet flow rate.

6.4 Analysis of the effect of regurgitant volume on energy loss

Starting from the type II regurgitation configuration described earlier (posterior leaflet prolapse towards the atrium), three target regurgitant volumes were considered: 10, 25, and 35 mL. The case RV = 25 mL serves as the baseline; two additional cases at 10 and 35 mL explore lower and higher severity of regurgitation, yielding regurgitant fractions of 15%, 36%, and 50%, respectively. Table 6.2 summarizes all MR cases studied here, including the type IIIb configuration introduced in Section 6.5.. The inlet and outlet flow rates for these cases, together with the healthy reference C01, are shown in Fig. 6.8. Outside systole, the curves overlap, as expected (MV fully open).

Table 6.2: Simulated mitral regurgitation cases. Case $C05_{25mL}$ corresponds to the reference configuration introduced in Table 6.1.

Case	**RV (mL)**	**RF (%)**	**Carpentier type**	**Mechanism**
$C05_{10mL}$	10	15	II	Posterior leaflet prolapse
$C05_{25mL}$	25	36	II	Posterior leaflet prolapse
$C05_{35mL}$	35	50	II	Posterior leaflet prolapse
$C06_{25mL}$	25	36	IIIb	Restricted systolic closure

As illustrated in Figure 6.9, for the same systolic valve opening the regurgitant jets are similarly oriented (toward the atrial center), but their magnitude scales with RV. The peak systolic regurgitant velocity is approximately 1.1 m.s^{-1} for $C05_{10mL}$, 2.0 m.s^{-1} for $C05_{25mL}$, and 2.9 m.s^{-1} for $C05_{35mL}$. The forward velocity at the aortic valve varies inversely with RV, decreasing from about 1.1 m.s^{-1}

(10 mL) to 0.8 m.s^{-1} (25 mL) and 0.6 m.s^{-1} (35 mL), consistent with the trends reported by Bennati et al. [72].

As shown in Figure 6.10, which shows the global power balance for all cases, the most pronounced variations across configurations occur in the aortic and mitral power terms, P_{AP} and P_{MP} (with AP/MP denoting the aortic/mitral planes). In the healthy case, P_{AP} is nearly equal to the muscle power $\mathcal{P}_{\text{muscle}}$ during systole, indicating that the mechanical power generated by the ventricle is mainly used to drive aortic ejection. In the presence of regurgitation, a fraction of this power is redirected through the mitral valve, so that P_{AP} progressively decreases with increasing RV, whereas P_{MP} increases with RV, approaching the magnitude of P_{AP} for the 50% regurgitant fraction. Outside systole, these values revert to those of the healthy case, and the remaining terms are essentially unchanged (apart from a slight decrease in $\mathcal{P}_{\text{muscle}}$; see Table 6.3).

The next step is to examine how these differences translate into energy loss. As explained in Section 6.2, in the presence of MR the loss term $\mathcal{L}_{MR} = P_{MP} + E_{MP}$ adds to the viscous dissipation ψ during systole. The ventricular dissipation ψ is first plotted to assess differences with the healthy case (Figure 6.8a); the magnitude is similar for all cases, regardless of RV. In contrast, when plotting $\mathcal{L}_{MR} + \psi$ (Figure 6.11b), there is a marked rise in dissipation during systole with clear differences between RV levels. As expected, larger RV produces larger losses, with instantaneous values reaching up to ≈3 W for the 35 mL case.

In MR, the loss rate is evaluated as:

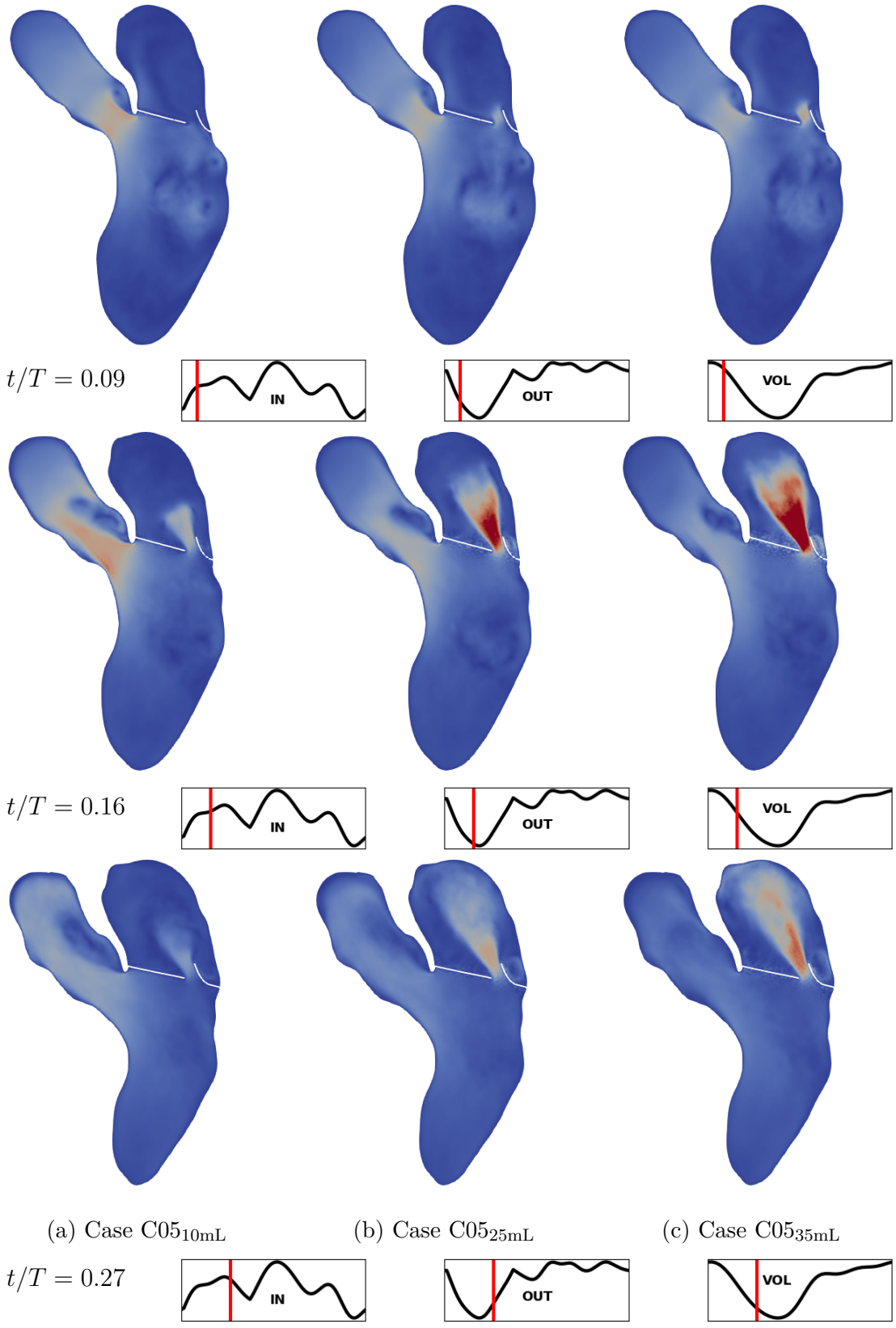
$$R_{MR} = \frac{\int_{\text{systole}} \mathcal{L}_{MR}\ \mathrm{d}t + \int \psi\ \mathrm{d}t}{\int_{\text{systole}} \mathcal{P}_{muscle}\ \mathrm{d}t} \tag{6.8}$$

Table 6.3 reports, for each RV, the regurgitant fraction, the total loss work $\int_{\text{systole}} \mathcal{L}_{MR}\, dt + \int \psi\, dt$, the muscle power $\int_{\text{systole}} \mathcal{P}_{muscle}\, dt$, their ratio R_{MR}, and the peak $\mathcal{P}_{muscle}$.

Table 6.3: Quantitative Energy Parameters for the three MR cases. RF denotes the regurgitant fraction, and R is the ratio of dissipated energy to muscle work defined in Eq. 5.16. Note that the integrals of $\mathcal{P}_{muscle}$ and $\mathcal{L}_{MR}$ are computed only over systole.

Case	**RF (%)**	$\int \boldsymbol{\mathcal{L}_{MR}}\ \mathbf{dt}+$ $\int \boldsymbol{\psi}\ \mathbf{dt}$ (mJ)	$\int \boldsymbol{\mathcal{P}_{muscle}}\ \mathbf{dt}$ (mJ)	**R (%)**	$\boldsymbol{\mathcal{P}_{muscle}}$ max (W)
$C05_{10mL}$	15	120	980	12	5.17
$C05_{25mL}$	36	357	971	37	5.11
$C05_{35mL}$	50	490	967	50	5.08

Even for the case with only 15% RF, the value $R_{MR} \approx 12\%$ is obtained, indicating a substantial efficiency penalty in the presence of MR (to be compared with ≈ 0.9% without regurgitation; see Table 5.1). Note that, for all cases, this



(a) Case $C05_{10mL}$ (b) Case $C05_{25mL}$ (c) Case $C05_{35mL}$

Figure 6.9: Phase-averaged velocity field at different times of systole for the 3 different cases. See Fig. 6.6 for the velocity scale.

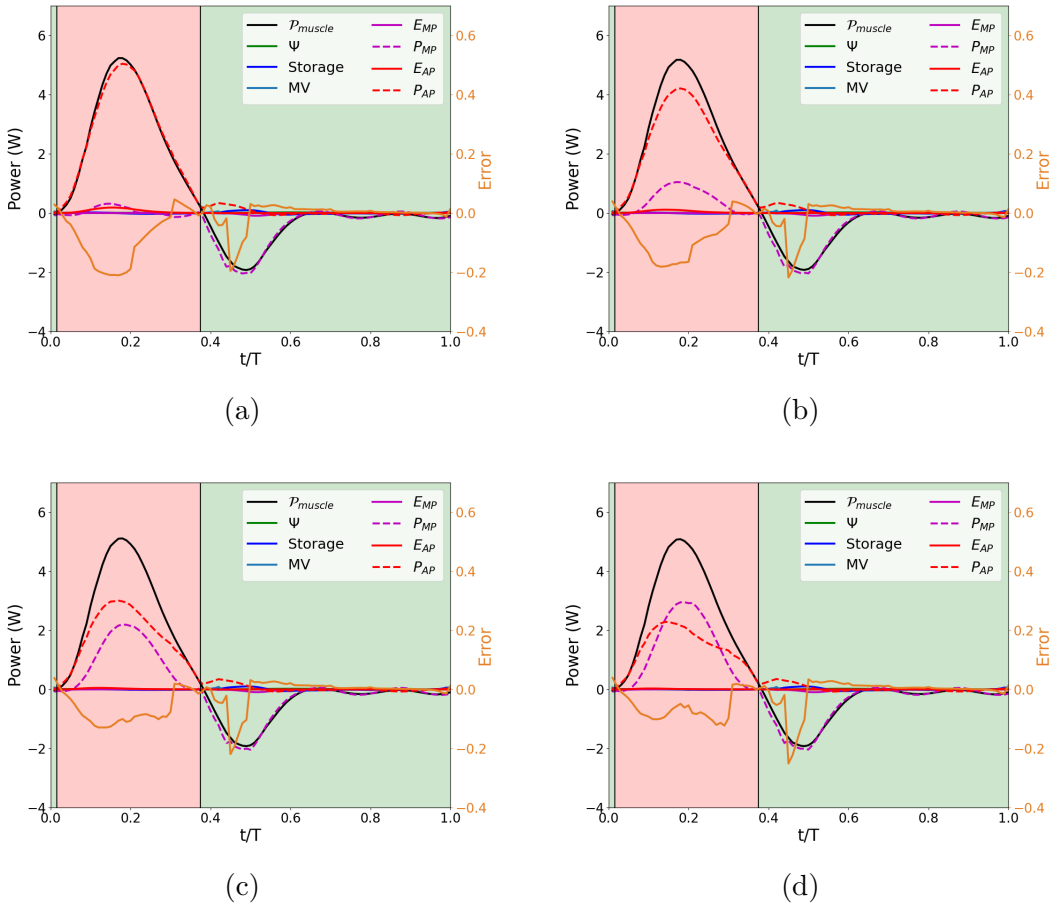


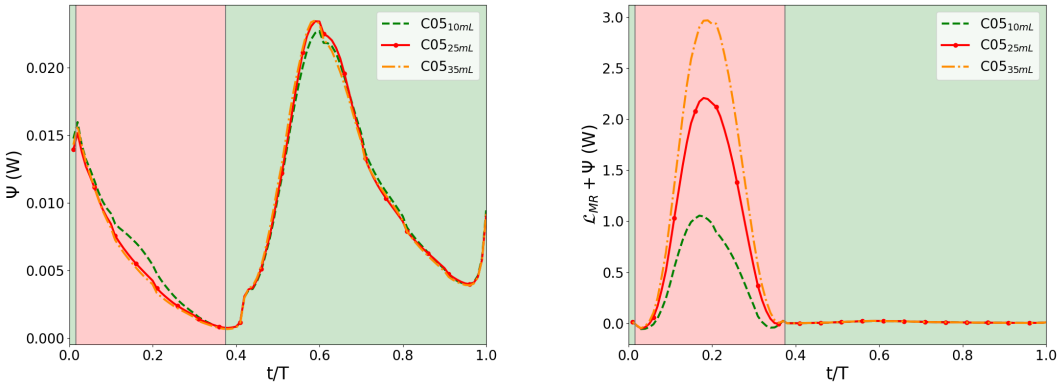
Figure 6.10: Kinetic energy balance for (a) case C01 (healthy case), (b) $C05_{10mL}$, (c) $C05_{25mL}$, and (d) $C05_{35mL}$ during a cycle (averaged over 20 cycles).

loss is almost exclusively related to the $\mathcal{L}_{MR}$ term since the regurgitation flow does not induce significant viscous dissipation in the ventricle (see Figure 6.11a).

At fixed systolic valve opening and EROA, increasing RV strengthens the regurgitant jet and markedly raises the systolic loss term $\mathcal{L}_{\mathrm{MR}}$, whereas ψ remains comparable to the healthy case. Consequently, the loss ratio R_{MR} rises from $\approx 12\%$ (RV $= 10\,\mathrm{mL}$, RF 15%) to $\approx 50\%$ (RV $= 35\,\mathrm{mL}$, RF 50%) despite nearly unchanged peak muscular power (~ 5 W). Thus, the efficiency loss comes almost entirely from retrograde flow into the atrium rather than from enhanced viscous dissipation.

As in Section 5.4, ventricular mixing is assessed by tracking the evolution of a passive scalar ϕ in an apical control volume. Figure 6.12 shows the temporal evolution of both the volume-averaged scalar $\overline{\phi}(t)$ and the local maximum $\phi_{\max}(t)$ over a 10-cycle window, for the healthy MV configuration (C01) and the three regurgitant cases.

The results reveal a clear hierarchy in apical washout efficiency: $\overline{\phi}(t)$ increases with regurgitant volume. In the healthy case (C01), the scalar fluctuates between



(a) (b)

Figure 6.11: (a) Intraventricular viscous dissipation (ψ) during a cardiac cycle (averaged over 20 cycles) for the three cases considered. (b) Total Energy loss ($\mathcal{L}_{MR} + \psi$) during a cardiac cycle (averaged over 20 cycles) for the three cases considered.

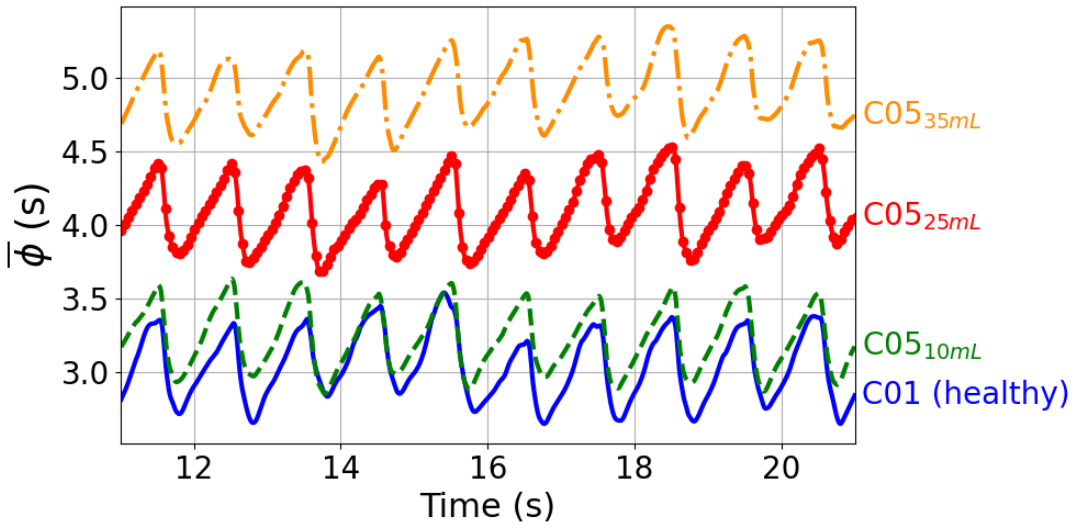
2.8 and 3.5 s, with a strong periodic signature. The mild regurgitant case ($C05_{10mL}$) closely follows this behavior, indicating that low regurgitant volumes have limited impact on apical renewal. In contrast, configurations with larger regurgitant volumes show progressively worse washout: in $C05_{25mL}$, $\overline{\phi}(t)$ remains elevated throughout the cycle, while in $C05_{35mL}$ it reaches peak values near 5.2 s and fails to return to a low baseline, suggesting sustained blood entrapment.

The evolution of $\phi_{\max}(t)$ reinforces these observations. Both C01 and $C05_{10mL}$ remain below 4.5 s, with little temporal variation, while the more severe cases show larger peaks. In $C05_{25mL}$, $\phi_{\max}$ often exceeds 5 s, and in $C05_{35mL}$ it reaches up to 7 s, confirming that some blood elements persist in the apex for multiple cycles.

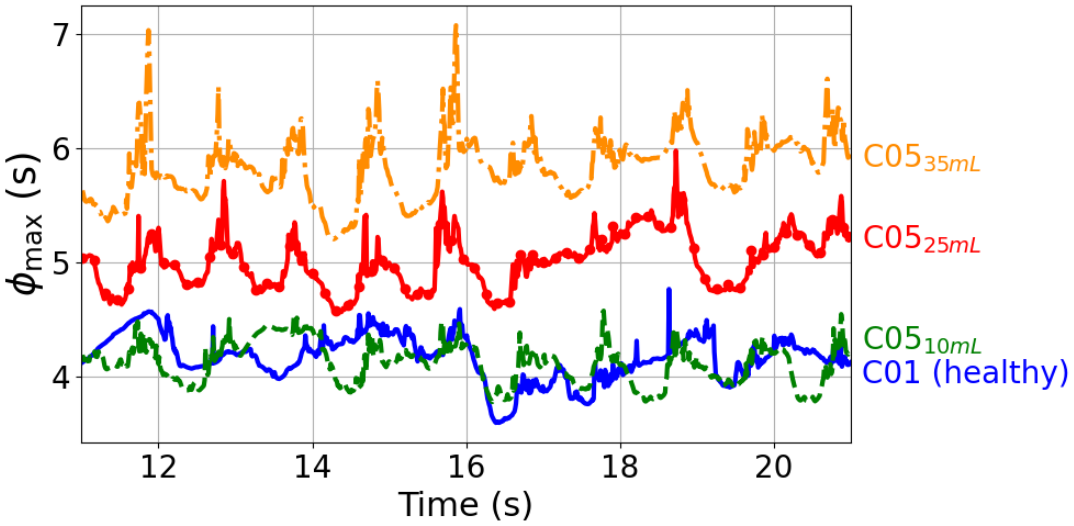
These findings highlight the impact of mitral regurgitation on intraventricular mixing: while mild regurgitation has limited effect, larger regurgitant volumes substantially hinder apical washout. This leads to local scalar accumulation and longer blood residence times, which may contribute to increased thromboembolic risk.

6.5 Analysis of the MR mechanism on energy loss

In addition to $C05_{25mL}$ (Type II, RV = 25 mL), a Type IIIb configuration was simulated, characterized by systolic tethering of the posterior leaflet that leaves an intraventricular regurgitant gap. To isolate mechanistic effects, the EROA and RV were matched to $C05_{25mL}$. As shown in Figure 6.13, the Type IIIb jet is



(a) Temporal evolution of $\overline{\phi}(t)$ (volume-averaged scalar in the apex) for all MV configurations.



(b) Temporal evolution of $\phi_{\max}(t)$ (maximum scalar in the apex) for all MV configurations.

Figure 6.12: Passive scalar evolution in the apex over a 10-cycle window. High values of ϕ indicate poor washout and potential blood stagnation. The scalar was initialized 11 cycles earlier, so values at $t = 11$ s already reflect prior residence times.

redirected toward the lateral atrial wall, appears slimmer, and exhibits a slightly lower peak speed of about 1.8–1.9 $\mathrm{m.s^{-1}}$ (vs. 2.0 m . $\mathrm{s^{-1}}$ for C05).

Despite these differences in jet orientation and local velocity, the energy loss traces are essentially the same for the two cases (Figure 6.14). For the same EROA and RV, changing the MR mechanism from Type II (prolapse) to Type IIIb (tethering) alters jet direction and peak speed but does not meaningfully change the energy loss. In this setting, the efficiency penalty of MR is largely determined by regurgitant volume, not by the specific jet morphology.

6.6 Overall conclusion

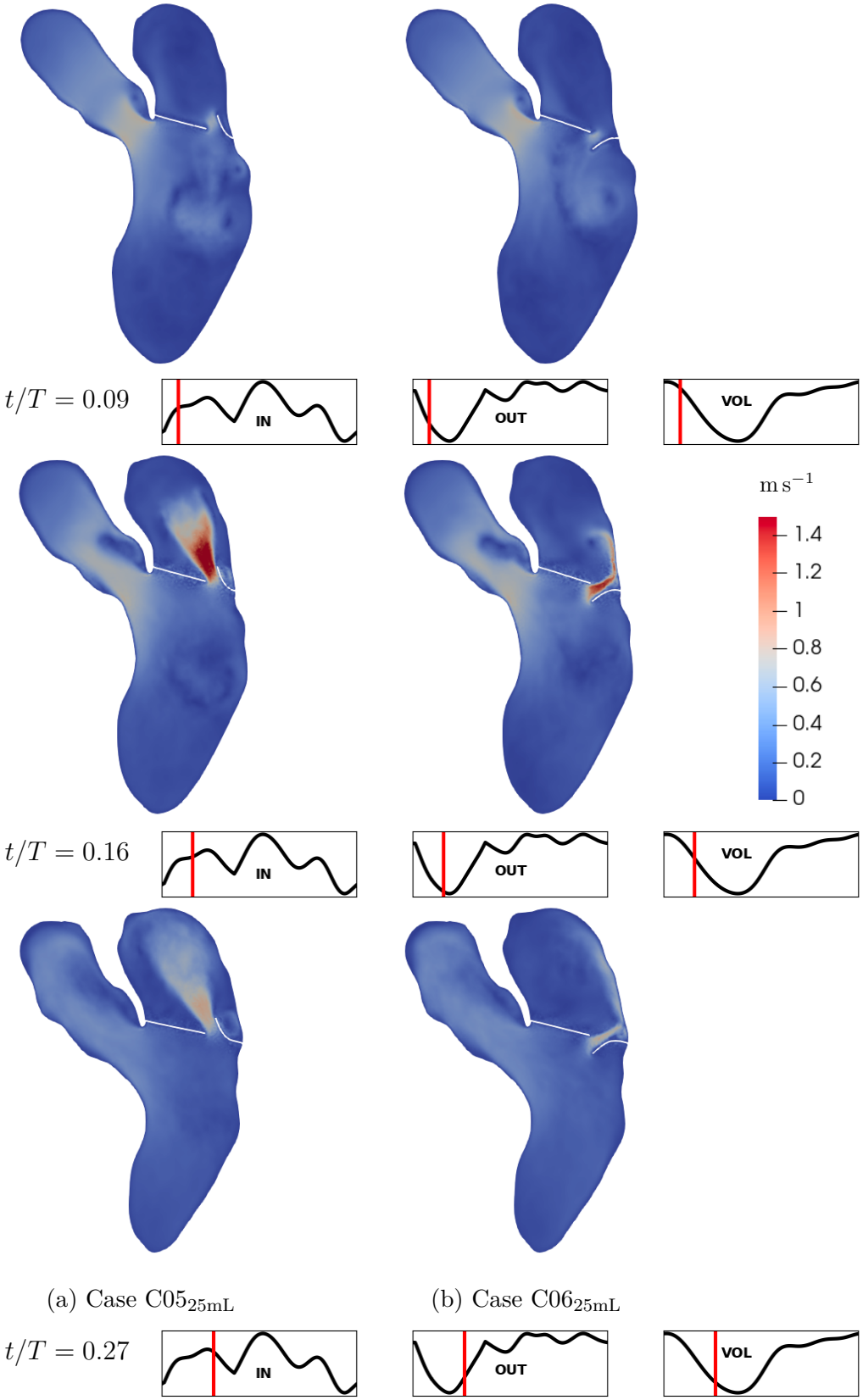
This chapter examines how MR alters intracardiac energetics. Under prescribed kinematics and a controlled mitral geometry (fixed systolic opening and EROA), the distribution between viscous dissipation in the chambers (ψ) and losses due to blood reflux through the mitral valve during systole ($\mathcal{L}_{MR} = P_{MP} + E_{MP}$) was quantified and related to the muscle power supplied.

Two main findings emerged. First, for a Type II configuration, increasing RV from 10 mL to 35 mL (RF from 15% to 50%) strengthens the regurgitant jet but leaves ψ in the LV of similar magnitude to the healthy case. The efficiency penalty is instead dominated by $\mathcal{L}_{MR}$ during systole, such that the loss ratio R_{MR} increases markedly (from about 12% to about 50%), despite a peak $\mathcal{P}_{\text{muscle}}$ that remains approximately 5 W. Second, when comparing mechanisms at matched EROA and RV (Type II prolapse versus Type IIIb tethering), the jet orientation differs markedly (with only modest changes in peak speed), yet the energy loss $\int(\mathcal{L}_{MR} + \psi)\, dt$ remains essentially unchanged. In this setting, regurgitant volume, rather than detailed jet morphology, emerges as the primary driver of the energetic loss.

This study is subject to several limitations. First, the study was designed to isolate first-order effects under controlled conditions, and several limitations follow from these choices. Some modeling parameters (for example, setting the posterior-leaflet opening within $\varphi^{\text{sys}}_{\text{post}} \approx 35°$–$40°$) were selected as representative rather than patient-specific; they were not tuned to individual imaging data, and no exhaustive sensitivity analysis to opening angle or to the temporal profile of regurgitation was performed. Consequently, numerical values should be interpreted as trends under prescribed kinematics rather than as patient-level predictions.

In addition, the closure geometry of the MV is idealized. In the present model, full closure is represented by a nearly planar disk, whereas in vivo MV closure follows a saddle-shaped annulus. This simplification is inconsequential in the healthy case (no systolic jet), but in MR it can bias the initial jet orientation. A more realistic closure geometry is expected to better capture the direction of the jet toward the atrial roof or lateral wall and to refine local dissipation estimates.

Finally, numerical aspects of the closure representation must be acknowledged. With the current approach, the leaflet occludes approximately one grid cell around its surface. To maintain physiological forward flow, a slightly larger opening is



(a) Case $\mathrm{C05}_{25\mathrm{mL}}$ (b) Case $\mathrm{C06}_{25\mathrm{mL}}$

Figure 6.13: Phase-averaged velocity field at different times of systole for the 2 different cases.

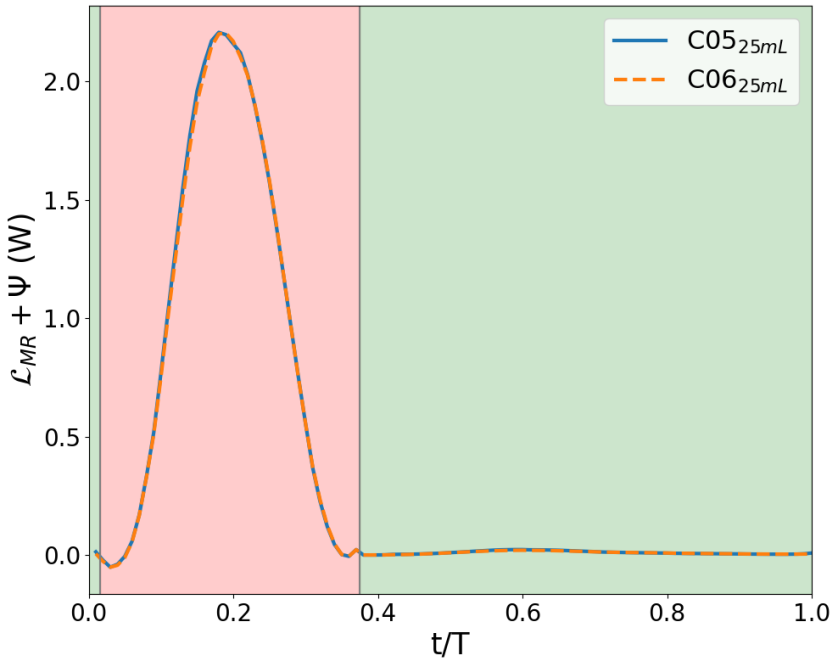


Figure 6.14: Total Energy loss ($\mathcal{L}_{MR} + \psi$) during a cardiac cycle (averaged over 20 cycles) for the two cases considered.

required, and the MV does not seal perfectly. This residual numerical permeability acts as a small parallel leakage, which likely reduces the pressure drop and, in turn, leads to an underestimation of energy loss. While these effects do not affect the qualitative conclusions, they may bias absolute values.

Despite these limitations, the framework captures a robust message: under fixed kinematics, most of the efficiency penalty of MR is expended on retrograde flow across the mitral plane, whereas additional viscous dissipation contributes comparatively little.

Chapter 7

Main results, discussion & perspectives

Chapter contents

7.1 Main results . . . 126
7.1.1 Image-based framework and valve modeling . . . 126
7.1.2 Global scaling vs. local valvular effects . . . 126
7.1.3 Energetic analysis and mixing without regurgitation . . . 126
7.1.4 Energetic cost of mitral regurgitation . . . 126
7.2 Discussion of modeling choices and consequences . . . 127
7.2.1 Prescribed kinematics on an image-based domain . . . 127
7.2.2 Mitral valve representation . . . 127
7.2.3 Geometric precision . . . 127
7.2.4 Turbulence modeling and resolution . . . 128
7.2.5 Mixing metric . . . 128
7.3 Perspectives: from washout to thrombosis risk in the apex . . . 128

In this last chapter, the main findings and conclusions drawn from this thesis are recalled. The physical and numerical modeling choices and their consequences are then discussed. Finally, the feasibility of investigating blood coagulation in the left-ventricular apex is assessed, with a brief rationale and a possible methodological pathway outlined.

7.1 Main results

7.1.1 Image-based framework and valve modeling

A high-fidelity, image-based computational framework for the left heart was used, based on the YALES2BIO solver (moving-domain finite volumes with pressure projection and turbulence modeling). Building on this framework, the present work introduces an improved parametric mitral valve model that controls leaflet asymmetry and prescribes smooth, time-continuous opening/closure angles on a dynamically deforming annulus. A kinetic-energy budget tailored to the moving ventricular domain was derived, separating muscle power, pressure work across the aortic and mitral planes, storage, and viscous dissipation. In addition, a passive-scalar metric for apical mixing was proposed.

7.1.2 Global scaling vs. local valvular effects

Within the explored range (heart rate 45–80 bpm; geometric scale 0.85–1.20), global variations in rate/size primarily induce a dimensional rescaling: once signals are expressed in non-dimensional form, probe velocities and normalized vortex dimensions nearly collapse. By contrast, mitral valve morphology (orientation and opening area) acts as a first-order organizer of the diastolic jet and the vortical topology, with clear consequences for intraventricular transport.

7.1.3 Energetic analysis and mixing without regurgitation

The energy budget in the ventricle is dominated by pressure terms; viscous dissipation integrated over one cycle remains a small fraction of the myocardial work (dissipation ratio typically ~ 0.7–1.2%). Differences in mitral valve geometry produce noticeable changes in kinetic energy, fluctuation energy, and jet-driven structures, but these translate into limited variations in pumping efficiency under the present assumptions. Apical mixing is chiefly controlled by early-diastolic jet strength and direction: wider openings (weaker jets) yield poorer apical renewal, whereas stronger, wall-guided jets improve washout; the orientation effect is present but more moderate.

7.1.4 Energetic cost of mitral regurgitation

A controlled methodology was introduced to impose mitral regurgitation under prescribed kinematics. For fixed orifice and kinematics, increasing regurgitant volume strengthens the regurgitant jet, yet intraventricular viscous dissipation remains close to healthy levels. The efficiency penalty is dominated by the retrograde loss at the mitral plane during systole; the corresponding loss ratio increases markedly with regurgitant volume, while peak muscle power remains nearly unchanged. At matched orifice area and regurgitant volume, changing the lesion mechanism (prolapse versus systolic tethering) redirects the jet but does

not materially change the cycle-integrated loss, identifying the regurgitant volume as the primary driver of the energetic cost in this controlled setting.

7.2 Discussion of modeling choices and consequences

7.2.1 Prescribed kinematics on an image-based domain

Using prescribed wall and annular motion enables controlled studies and a direct linkage to imaging, while avoiding the complexity and extensive parameterization required by fully coupled electromechanics and fluid–structure interaction. The trade-off is that feedback from hemodynamics to myocardial deformation is not captured, and afterload/preload are not solved in a closed loop. Consequently, conclusions should be interpreted as trends under the imposed kinematics. In the specific case of mitral regurgitation, the left atrium does not dilate in response to systolic backflow because atrial motion is prescribed; as a result, the pressure/volume response of the atrium to the regurgitant inflow is not represented, only the intrachamber flow is altered.

7.2.2 Mitral valve representation

The parametric valve provides continuous opening/closure and control over leaflet asymmetry and orientation, but closure is idealized (nearly planar) rather than saddle-shaped. In regurgitation, this can bias initial jet orientation. In addition, the leaflet motion is prescribed (no FSI) and the mitral valve is not patient-specific: despite being anatomically inspired, it remains an idealized geometry, which may affect absolute values (while preserving qualitative trends).

Nevertheless, the simulations conducted in this work indicate that these geometric and kinematic idealizations exert only a limited influence on the macroscopic, cycle-integrated metrics used to assess efficiency (such as ventricular pressure work, dissipation, and loss fraction). Within the investigated parameter ranges, the sensitivity of these metrics to leaflet details is weak, and the modeling simplifications above are therefore unlikely to alter the central conclusions regarding global pumping efficiency and the relative impact of mitral valve parameters.

7.2.3 Geometric precision

From a fluid-mechanics standpoint, explicitly representing the chordae tendineae is expected to increase dissipation by generating additional shear layers and small-scale vortical activity within the inflow jet. However, their extreme slenderness and branching render explicit geometric discretization challenging on patient-scale meshes. A practical alternative (not pursued in the present work for reasons of time) is to adopt a reduced-order representation of the chordae. As a pragmatic first step, each chord could be idealized as a one-dimensional fiber exerting a

linear drag on the fluid; its action can be mapped onto the Eulerian grid using, for example, the heterogeneous, edge-based immersed-boundary formulation of Béród *et al.*, available in YALES2BIO [96]. This approach dispenses with explicit meshing of slender strands by imposing localized force densities along polyline supports, thereby retaining near-fiber wakes and jetting at modest computational cost.

7.2.4 Turbulence modeling and resolution

Large-eddy modeling with an explicit subgrid closure captures dominant unsteady structures but may smooth small-scale fluctuations. A mesh-sensitivity check on the reference case showed a negligible change in the dissipation-to-power ratio; nonetheless, absolute TKE levels and near-wall shear depend on resolution and modeling, calling for cautious interpretation when comparing to modalities with limited spatial resolution.

7.2.5 Mixing metric

The passive-scalar ϕ offers a practical surrogate for washout and residence. It isolates jet-driven renewal but does not encode biochemical pathways or cellular-scale aggregation; it should therefore be viewed as a hydrodynamic indicator rather than a direct thrombosis predictor.

7.3 Perspectives: from washout to thrombosis risk in the apex

The analyses presented throughout this work have primarily focused on how mitral valve morphology influences the efficiency of intraventricular flow, notably through kinetic energy metrics and flow structure characterization. However, these mechanical modifications may also have important implications from a pathophysiological perspective. In particular, altered flow patterns can affect the local stasis of blood, potentially increasing the risk of thrombus formation, especially in low-shear regions such as the ventricular apex.

From a physiological standpoint, the development and propagation of thrombi are closely tied to local flow conditions. In particular, altered shear rates and turbulent structures have been shown to promote platelet activation and coagulation initiation [165]. In the context of intraventricular flows, regions of low shear and high stasis, such as the apex, may thus act as nucleation sites for thrombus formation, especially under pathological conditions like mitral regurgitation or abnormal vortex dynamics.

Most existing computational studies addressing thrombosis have focused on device-related flows, particularly in the context of LVADs. These configurations have provided a rich framework for developing multi-constituent models that

account for shear exposure, blood stasis, and surface interactions. Several recent works have used such models to predict thrombin generation and platelet deposition near inflow cannulae, and to construct thrombotic risk maps informed by local flow features [166, 167]. Although these approaches are not directly translatable to native hearts, they offer valuable methodological insights into the coupling of transport and coagulation mechanisms in intraventricular environments.

By contrast, the native left ventricle has received far less attention in this regard. A notable exception is the study by Seo *et al.* [77], who proposed a coupled chemo–fluidic framework to investigate thrombus formation in infarcted ventricles with apical aneurysms. Their simulations combined Navier–Stokes equations with a biochemical model including thrombin generation, platelet activation, and fibrin polymerization. A key conclusion from their work is that global pump function metrics (ejection fraction, stroke volume) do not reliably predict local coagulation potential. Instead, spatially resolved flow-derived metrics, such as near-wall residence time and local shear rate, were found to be better predictors of thrombus-prone regions.

Two main strategies have emerged for explicitly assessing thrombotic risk using computational models. The first relies on fully coupled chemo–fluidic frameworks, which simulate the transport and reaction of key biochemical species involved in coagulation (e.g. thrombin, fibrin, activated platelets) alongside the resolved flow field. The second, less expensive approach uses hemodynamic surrogates (such as residence time, wall shear stress, or scalar transport), possibly augmented by simplified kinetic models. These complementary methodologies have been reviewed in [168, 169], which highlight the main trade-offs between accuracy, complexity, and computational cost.

Within this thesis, it has been shown that intraventricular washout is sensitive to jet orientation and vortex dynamics (Section 5.4), and that mitral regurgitation further amplifies apical stasis (Section 6.4). In the most severe case, blood elements could remain trapped in the ventricle for up to seven cardiac cycles, suggesting markedly impaired clearance. These findings provide a strong motivation to investigate whether such prolonged residence times can indeed translate into higher coagulation potential.

A possible extension of this work would therefore be to complement the washout analysis with a simplified biochemical model of thrombin generation. This approach is inspired by the work of Chen [170], who developed a reduced-order (0D) framework to simulate coagulation dynamics in venous valve sinuses. The core idea is to represent the region of interest as a well-mixed control volume where species concentrations evolve under the combined effects of biochemical reactions and exchange with the surrounding flow.

The evolution of the concentration $\bar{C}_i$ of a given species within this zone is described by the transport-reaction equation:

$$\frac{d\bar{C}_i}{dt} = R_i + k_{\text{flow}}(C_i^{\text{up}} - \bar{C}_i),$$

where C_i^{up} denotes the upstream concentration, R_i is the biochemical reaction rate, and the exchange rate $k_{\text{flow}} = Q^+/V$ depends on the inflow Q^+ and the control volume V. These parameters can be extracted from CFD results using a post-processing workflow in Paraview [127] (see Figure 7.1).

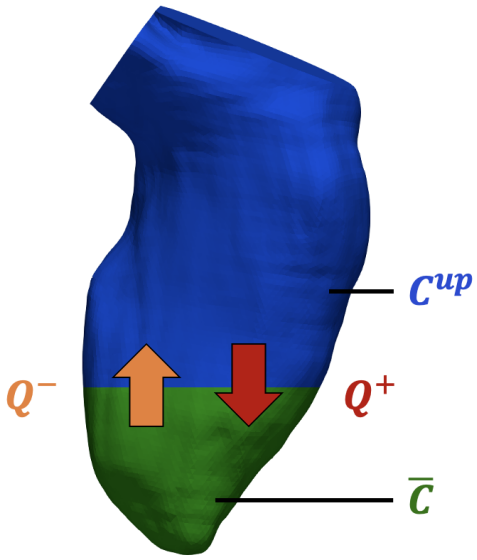


Figure 7.1: Illustration of the simplified apical transport-reaction model. The apex is modeled as a control volume (green) with average species concentration $\bar{C}$, receiving inflow Q^+ from the upstream region (blue, with concentration C^{up}) and releasing outflow Q^-. The exchange rate $k_{\text{flow}} = Q^+/V$ governs the coupling between transport and local biochemical reactions.

Applying this methodology to the left ventricular apex appears consistent with the observations made in this thesis. In several configurations, this region exhibited prolonged residence times and limited exchange, making it a plausible candidate for localized thrombin generation. Its geometry and flow dynamics bear some resemblance to venous valve pockets, where similar modeling strategies have proven effective.

Within this framework, several coagulation scenarios (such as varying tissue factor expression, thrombin inhibition, or flow conditions) could be explored to estimate relative thrombotic risk under controlled transport dynamics. Although simplified, this approach would offer a computationally accessible means of introducing biochemical components into cardiac flow simulations, complementing existing mechanical indicators (e.g. residence time or vortex persistence) with estimations of local activation potential.

A key consideration in this type of modeling is the selection of an appropriate coagulation scheme. As discussed in our recent evaluation work [171] (included in Appendix 8.2), standard kinetic models often require substantial adaptation to capture thrombin generation under non-standard or pathological conditions.

Because these models both require adaptation and provide the definition of the reaction term R_i, it is particularly important to select and tailor the coagulation scheme to the specific flow environment of the ventricular apex.

While not directly implemented in this work, such an approach could represent a promising extension of CFD-based cardiac modeling. More broadly, it illustrates how simulation frameworks developed here may serve as a foundation for future investigations into cardiac pathophysiology.

Chapter 8

Appendix

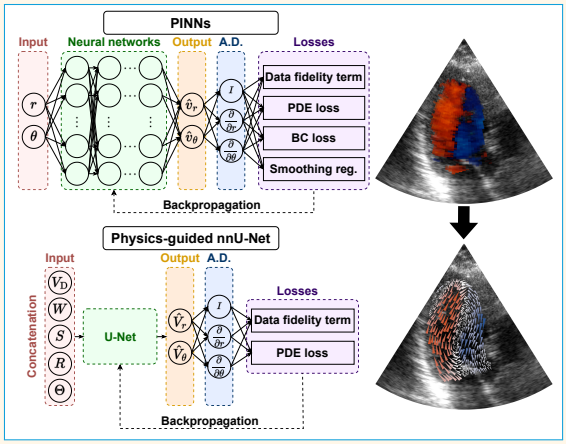
8.1 Physics-Guided Neural Networks for Intraventricular Vector Flow Mapping

This appendix includes the article *Physics-Guided Neural Networks for Intraventricular Vector Flow Mapping* by Ling *et al.* (IEEE T-UFFC, 2024), to which I contributed by providing numerical simulations of left-heart hemodynamics. Specifically, I generated patient-specific CFD datasets with several mitral valve configurations (opening angles and orientations, see Section 4.2), thereby creating diverse intraventricular flow patterns. These data served as ground truth for synthesizing Doppler sequences and were used to validate the machine-learning approaches developed in the study. The paper proposes two alternatives to classical iVFM: physics-informed neural networks (PINNs) and a physics-guided nnU-Net; both embed physical constraints and are benchmarked against CFD-derived references and in vivo color Doppler. Results show performance comparable to iVFM, with the nnU-Net offering quasi–real-time inference and improved robustness to sparse or truncated scanlines. This collaboration with medical imaging experts from the CREATIS laboratory in Lyon illustrates how advanced simulations can support physics-guided learning and its translation to clinical ultrasound imaging.

Physics-Guided Neural Networks for Intraventricular Vector Flow Mapping

Hang Jung Ling, Salomé Bru, Julia Puig, Florian Vixège, Simon Mendez, Franck Nicoud, Pierre-Yves Courand, Olivier Bernard*, and Damien Garcia*

***Abstract*— Intraventricular vector flow mapping (*i*VFM) seeks to enhance and quantify color Doppler in cardiac imaging. In this study, we propose novel alternatives to the traditional *i*VFM optimization scheme by utilizing physics-informed neural networks (PINNs) and a physics-guided nnU-Net-based supervised approach. When evaluated on simulated color Doppler images derived from a patient-specific computational fluid dynamics model and *in vivo* Doppler acquisitions, both approaches demonstrate comparable reconstruction performance to the original *i*VFM algorithm. The efficiency of PINNs is boosted through dual-stage optimization and pre-optimized weights. On the other hand, the nnU-Net method excels in generalizability and real-time capabilities. Notably, nnU-Net shows superior robustness on sparse and truncated Doppler data while maintaining independence from explicit boundary conditions. Overall, our results highlight the effectiveness of these methods in reconstructing intraventricular vector blood flow. The study also suggests potential applications of PINNs in ultrafast color Doppler imaging and the incorporation of fluid dynamics equations to derive biomarkers for cardiovascular diseases based on blood flow.**



***Index Terms*— Cardiac flow, color Doppler, deep learning (DL), echocardiography, physics-guided neural networks (PGNNs), physics-informed neural networks (PINNs), ultrasound, vector flow imaging**

I. Introduction

AMONG the methods aiming to perform intracardiac flow imaging by color Doppler, intraventricular vector flow mapping (*i*VFM) [1]–[5] stands out as a post-processing approach applicable to clinical color Doppler acquisitions. The *i*VFM algorithm relies on a constrained least squares optimization scheme (see Section II-A for more details).

Recently, physics-informed neural networks (PINNs) [6] have emerged as a novel approach for data-driven optimization by integrating neural networks (NNs) and the laws of physics during the optimization process. The physical laws, often described by partial differential equations (PDEs), are incorporated into the loss function to enforce the correctness of the solutions. Automatic differentiation [7] has proven to be efficient in computing partial derivatives in PINNs. In cases involving strong non-linear PDEs in the spatiotemporal domain, extensions to PINNs, such as conservative PINNs (cPINNs) and extended PINNs (XPINNs), have been proposed [8].

PINNs have found applications predominantly in fluid mechanics [8]. In the medical field, Arzani et al. [9] utilized PINNs to recover blood flow from sparse data in 2D stenosis and aneurysm models. Kissas et al. [10] applied PINNs to predict arterial blood pressure from 4D flow MRI data. In the ultrasound domain, PINNs have been primarily used for modeling wave propagation [11], shear wave elastography

Manuscript received 19 March 2024; accepted 5 June 2024. This work was supported by: MEGA Doctoral School (ED 162); French National Research Agency (ANR) through the “4D-iVFM” [ANR-21-CE19-0034-01] and “ORCHID” [ANR-22-CE45-0029-01] projects; LABEX PRIMES [ANR-11-LABX-0063] and LABEX CELYA [ANR-10-LABX-0060] of Université de Lyon within the program “Investissements d’Avenir” [ANR-11-IDEX-0007]; GENCI-IDRIS (HPC resources) [2023-AD010313603R1].

This work involved human subjects or animals in its research. Approval of all ethical and experimental procedures and protocols was granted by the Human Ethical Review Committee of the University of Montreal Hospital Research Center (CRCHUM).

H. J. Ling, J. Puig, P.-Y. Courand, O. Bernard, and D. Garcia are with INSA-Lyon, Universite Claude Bernard Lyon 1, CNRS, Inserm, CREATIS UMR 5220, U1294, F-69621, Lyon, France (e-mail: hangjung.ling@gmail.com, hang-jung.ling@insa-lyon.fr; damien.garcia@creatis.insa-lyon.fr).

S. Bru, S. Mendez, and F. Nicoud are with IMAG UMR 5149, University of Montpellier, Montpellier, France.

F. Vixège is with Univ. Grenoble Alpes, CNRS, Grenoble INP, LEGI, Grenoble, France.

P.-Y. Courand is also with the Cardiology Dept., Hôpital Croix-Rousse, Hospices Civils de Lyon, Lyon, France, and the Cardiology Dept., Hôpital Lyon Sud, Hospices Civils de Lyon, Lyon, France.

F. Nicoud is also with the Institut Universitaire de France (IUF), France.

Highlights

- **Our PINNs, with dual-stage optimization and pre-optimized weights, demonstrated flexibility and performance comparable to the original *i*VFM approach for vector flow mapping using color Doppler.**
- **Our physics-guided nnU-Net-based supervised approach achieved robust intraventricular blood flow reconstruction with quasi-real-time inference, even on sparse and truncated Doppler data.**
- **Our study introduced innovative AI-driven and physics-guided approaches for clinical vector flow mapping, paving the way for enhanced diagnostic accuracy of cardiovascular diseases.**

[12], and regularizing velocity field given by ultrafast vector flow imaging [13].

While PINNs have demonstrated effectiveness on sparse and incomplete data, their application remains unexplored in scenarios where one or more velocity components are missing, as is the case in *i*VFM. Color Doppler imaging provides only scalar information—the Doppler velocity, representing the noisy radial velocity—from which we aim to derive both the radial and angular velocity components of intraventricular blood flow.

PINNs often require re-optimization for new cases with different initial or boundary conditions, which can be time-consuming. A potential solution is physics-guided supervised learning [14], which produces output that adheres to the laws of physics by using a physics-constrained training dataset, with optional physical regularization terms. Once trained, inference can be performed seamlessly on unseen data, provided their distribution closely resembles that of the training dataset.

In this paper, we investigated the feasibility of using physics-based NNs for vector flow mapping, exploring both a physics-guided supervised approach implemented through the nnU-Net framework [15] and two variants of PINNs. Our contributions included:

1) Training a physics-guided supervised approach based on nnU-Net, which showed high robustness on sparse and truncated data with nearly real-time inference speed;
2) Implementing two PINNs variants based on the penalty method to perform vector flow mapping, achieving performance comparable to the original *i*VFM algorithm;
3) Utilizing dual-stage optimization and pre-optimized weights from a selected Doppler frame, which enhanced PINNs' performance and reduced the optimization time of PINNs by up to 3.5 times.

II. Related Work

A. Intraventricular Vector Flow Mapping

As introduced in [1], a vector blood flow map within the left ventricle can be obtained from clinical color Doppler echocardiography by solving a minimization problem. This optimization task is governed by two equality constraints: C_1, representing the mass conservation equation, and C_2, representing the free-slip boundary conditions. The first constraint ensures the 2D free-divergence of the optimized velocity field, while the second constraint enforces that the normal component of the blood velocity is zero relative to the endocardial surface. Additionally, a smoothing regularization, further detailed in Section III-A, is incorporated to impose spatial smoothness of the velocity field. Equation (1) expresses the mathematical formulation of this problem.

In (1), $(\hat{v}_r, \hat{v}_\theta)$ denote the estimated radial and angular blood velocity components. Here, Ω stands for the domain of interest, i.e., the left ventricle cavity, with its endocardial boundary denoted by $\partial\Omega$. The term ω indicates the weights of the data fidelity term. Weights equal to normalized Doppler power values in the range of $[0, 1]$ were used with *in vivo* Doppler data, as they reflect the reliability of the Doppler velocity. For simulated data, we used ω equal to one. v_D refers to the sign-inverted Doppler velocity (positive velocities for movement away from the probe) to ensure the sign compatibility between v_D and the v_r. The vectors $\boldsymbol{n}_\mathrm{W} = (n_{\mathrm{W}_r}, n_{\mathrm{W}_\theta})$ and $\boldsymbol{v}_\mathrm{W} = (v_{\mathrm{W}_r}, v_{\mathrm{W}_\theta})$ represent a unit vector perpendicular to the endocardial wall and a velocity vector of the endocardial wall, respectively.

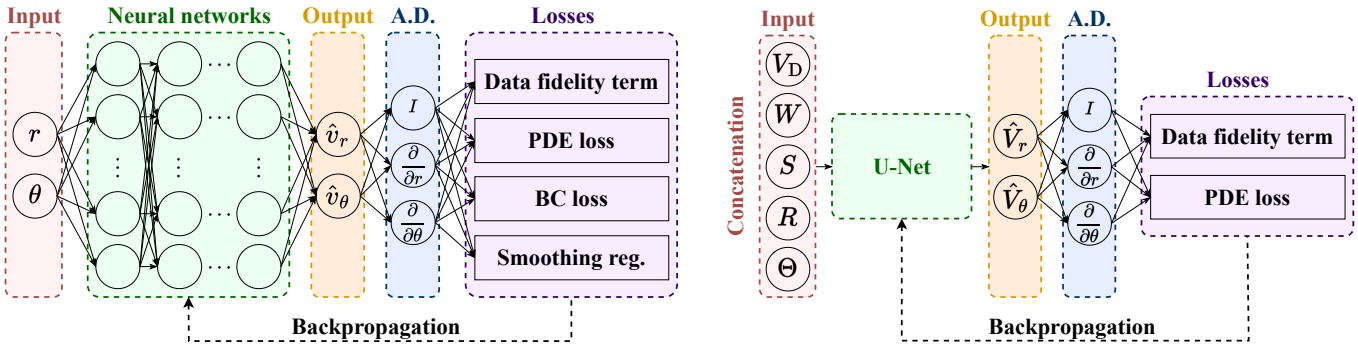
The *i*VFM method [1] linearizes the constrained problem (1) and solves it using Lagrange multipliers and a least squares optimization scheme, which reduces the number of supervisedly determined parameters to just one, namely, the smoothing regularization weight.

$$\hat{\boldsymbol{v}} = (\hat{v}_r, \hat{v}_\theta) = \arg\min_{(v_r, v_\theta)} \underbrace{\int_\Omega \omega \, \|v_r - v_\mathrm{D}\| \, d\Omega}_{\text{closely match the Doppler data}}$$
subject to:
$$\begin{cases} C_1 = r\mathrm{div}(\hat{\boldsymbol{v}}) = r\dfrac{\partial \hat{v}_r}{\partial r} + \hat{v}_r + \dfrac{\partial \hat{v}_\theta}{\partial \theta} = 0 & \text{on } \Omega \\ C_2 = (\hat{\boldsymbol{v}} - \boldsymbol{v}_\mathrm{W}) \cdot \boldsymbol{n}_\mathrm{W} = (\hat{v}_r - v_{\mathrm{W}_r}) n_{\mathrm{W}_r} \\ \qquad + (\hat{v}_\theta - v_{\mathrm{W}_\theta}) n_{\mathrm{W}_\theta} = 0 & \text{on } \partial\Omega \end{cases} \tag{1}$$

B. Physics-Informed Neural Networks

Unlike the conventional least squares Lagrangian optimization, such as in *i*VFM, PINNs use an iterative scheme with multi-layer perceptrons (MLPs) to iteratively refine and reach the optimal solution. PINNs offer the advantage of being flexible, especially in the optimization scheme, regardless of the linearity of the problem [6]. When additional complex physical constraints need to be incorporated, PINNs require minimal architectural modifications, typically requiring only the adaptation of the loss function. However, this process can be challenging when applied to standard approaches involving non-linear constraints.

When addressing a constrained optimization problem using PINNs, the problem is reformulated into a series of loss functions, which often involve conflicting objectives. To manage



(a) PINNs (b) Physics-guided nnU-Net

Fig. 1. Architectures of PINNs and physics-guided nnU-Net. A.D. refers to automatic differentiation. In (a), the 2D input of PINNs has a shape of $(\boldsymbol{B} \times \mathbf{2})$, where $\boldsymbol{B}$ is the batch size. $\boldsymbol{r}$ and $\boldsymbol{\theta}$ denote radial and angular coordinates. In (b), nnU-Net takes a 4D input of shape $(\boldsymbol{B} \times \mathbf{5} \times \mathbf{192} \times \mathbf{40})$, which is the concatenation of sign-inverted dealiased Doppler velocity $\boldsymbol{V}_{\mathrm{D}}$, weight matrix $\boldsymbol{W}$, left ventricular segmentation $\boldsymbol{S}$, radial coordinate array $\boldsymbol{R}$, and angular coordinate array $\boldsymbol{\Theta}$.

multi-objective optimization in PINNs, a linear scalarization of the losses is commonly used:

$$\mathcal{L}_{\mu}(\theta_{\mathrm{NN}}) = \sum_{j=1}^{N} \mu_j \mathcal{L}_j(\theta_{\mathrm{NN}}), \quad \mu_j \in \mathbb{R}_{>0}, \tag{2}$$

with μ_j representing the penalty coefficients or the loss weights, $\mathcal{L}_{1,\cdots,N}$ being the multiple losses derived from the original constrained optimization problem, and θ_{NN} representing the network parameters. All the losses involved in PINNs' optimization are functions of θ_{NN}. However, for better readability of the equations, θ_{NN} is omitted in the subsequent loss expressions.

Among the methods with linear scalarization, two notable approaches are the soft constraints and penalty methods. The soft constraints approach uses fixed penalty coefficients throughout the optimization. However, determining optimal coefficients can be challenging, especially as the number of objectives (N) increases, making this approach generally less favored in PINNs optimization.

In contrast to the soft constraints approach, the penalty method involves varying coefficients. Various techniques have been proposed to adapt these coefficients during optimization. Examples include GradNorm [16], SoftAdapt [17] or ReLoBRaLo [18]. GradNorm and SoftAdapt dynamically adjust the loss weights based on the relative training rates of different losses. ReLoBRaLo can be seen as a combination of the former two techniques, which incorporates a moving average for loss weights and a random look-back mechanism. The random look-back mechanism is controlled by a variable that determines whether the loss statistics of the previous steps or those of the first step are used to compute the coefficients.

Recently, an alternative method called Augmented Lagrangian (AL) has been proposed for solving constrained optimization problems using PINNs [19], [20]. Similar to the penalty method, the AL approach involves penalty terms, but it also introduces a term designed to mimic a Lagrange multiplier.

In situations where optimizing initial or boundary conditions is difficult, some studies have proposed imposing those conditions as hard constraints by utilizing a distance function and an analytical approximation of the conditions [21], [22]. Although it is feasible to impose hard constraints on the output of NNs, it is often challenging and more appropriate for problems with several initial or boundary conditions.

III. Methods

In this study, we addressed the constrained optimization problem of *i*VFM (1) through NNs aided by physics: a physics-guided supervised approach based on nnU-Net and PINNs using the penalty method. Specifically, we studied two variants of PINNs: 1) PINNs with the ReLoBRaLo weight-adapting strategy (RB-PINNs); 2) Augmented Lagrangian PINNs (AL-PINNs). Schematic representations of the general architectures of PINNs and nnU-Net for intraventricular vector flow reconstruction are shown in Fig. 1a and Fig. 1b, respectively.

The following subsections introduce the loss functions to be optimized in PINNs (Section III-A), provide implementation details for PINNs (Section III-B to III-E), discuss the physics-guided nnU-Net approach (Section III-F), and present the evaluation metrics (Section III-G).

A. PINNs' Loss Functions

In line with the previous *i*VFM method, we decomposed the mathematical formulation in (1) into several objectives to be optimized [see (3)–(6)]: 1) $\mathcal{L}_1$: data fidelity term; 2) $\mathcal{L}_2$: mass conservation residual loss (PDE loss); 3) $\mathcal{L}_3$: boundary condition residual loss (BC loss); 4) $\mathcal{L}_4$: smoothing regularization.

For the PDE loss, namely $\mathcal{L}_2$, the partial derivatives were computed using automatic differentiation . On the contrary, for $\mathcal{L}_4$, the partial derivatives were obtained using finite difference methods with 2D convolution kernels, as spatial smoothness could not be computed with automatic differentiation. This was done by setting the weights of the 3×3 convolution kernels to the central finite difference coefficients with second-order accuracy.

The norm $\|\cdot\|$ used for computing the $\mathcal{L}_1$, $\mathcal{L}_2$, and $\mathcal{L}_3$ was the Smooth L1 loss or Huber loss with $\beta = 1.0$ and *sum* reduction over all the samples unless otherwise stated. The Smooth L1 loss uses a squared term if the absolute error falls below β and an absolute term otherwise, making it less sensitive to outliers than the mean squared error.

$$\begin{cases} \mathcal{L}_1 = \omega \left\| \hat{v}_r - v_{\mathrm{D}} \right\| & \text{on } \Omega \quad (3) \\ \mathcal{L}_2 = \left\| r\dfrac{\partial \hat{v}_r}{\partial r} + \hat{v}_r + \dfrac{\partial \hat{v}_\theta}{\partial \theta} \right\| & \text{on } \Omega \quad (4) \\ \mathcal{L}_3 = \left\| (\hat{v}_r - v_{\mathrm{W}_r}) n_{\mathrm{W}_r} + (\hat{v}_\theta - v_{\mathrm{W}_\theta}) n_{\mathrm{W}_\theta} \right\| & \text{on } \partial\Omega \quad (5) \\ \mathcal{L}_4 = \displaystyle\sum_{k \in \{r,\theta\}} \left\{ \left(r^2 \frac{\partial^2 v_k}{\partial r^2} \right)^2 + 2 \left(r \frac{\partial^2 v_k}{\partial r \partial \theta} \right)^2 + \left(\frac{\partial^2 v_k}{\partial \theta^2} \right)^2 \right\} & \text{on } \Omega \quad (6) \end{cases}$$

B. RB-PINNs

1) Global Loss: The global loss function to be optimized in RB-PINNs was defined as:

$$\mathcal{L}_{\mu,\theta_{\mathrm{NN}}} = \underbrace{\mu_1 \mathcal{L}_1}_{\substack{\text{data fidelity} \\ \text{term}}} + \underbrace{\mu_2 \mathcal{L}_2 + \mu_3 \mathcal{L}_3}_{\text{PDE \& BC losses}} + \underbrace{\mu_4 \mathcal{L}_4}_{\substack{\text{smoothing} \\ \text{reg.}}}, \quad (7)$$

where $\mu_1, \mu_2, \mu_3 \in \mathbb{R}_{>0}$ are adaptive penalty coefficients, and μ_4 is the smoothing regularization weight. We heuristically set μ_4 to $10^{-7.5}$.

Algorithm 1: ReLoBRaLo update strategy

Initialize $\mu_j(1) = 1, j \in \{1, 2, 3\}$.
for $i = 1, \ldots, I$ **do**
  Forward pass and compute losses
  $\mathcal{L}_j(i) \leftarrow \mathcal{L}_j$
  if $i >= 2$ **then**
    $\hat{\mu}_j^{(i,i-1)} \leftarrow n_{\text{loss}} \times \text{Softmax}\left(\frac{\mathcal{L}_j(i)}{\mathcal{T}\mathcal{L}_j(i-1)+\epsilon} \right)$
    $\hat{\mu}_j^{(i,1)} \leftarrow n_{\text{loss}} \times \text{Softmax}\left(\frac{\mathcal{L}_j(i)}{\mathcal{T}\mathcal{L}_j(1)+\epsilon} \right)$
    $\mu_j(i) \leftarrow \alpha\left(\rho\mu_j(i-1) + (1-\rho)\hat{\mu}_j^{(i,1)} \right) + (1-\alpha)\hat{\mu}_j^{(i,i-1)}$
  end
  Compute final loss using (7) and do backpropagation to update network parameters:
  $\boldsymbol{\theta}_{\mathrm{NN}} \leftarrow \boldsymbol{\theta}_{\mathrm{NN}} - \eta_{\theta_{\mathrm{NN}}} \nabla_{\theta_{\mathrm{NN}}} \mathcal{L}_{\mu,\theta_{\mathrm{NN}}}(i)$
end

2) Update Strategy for Loss Weights: Algorithm 1 details the ReLoBRaLo update strategy introduced in [18] for determining the loss weights, i.e., μ_1, μ_2, and μ_3. In this algorithm, n_{loss} represents the total number of losses for which the loss weights are updated; in our case, $n_{\text{loss}} = 3$. $\hat{\mu}_j^{(i,i')}$ computes the scaling based on the relative improvement of $\mathcal{L}_j$ between the iterations i' and i. $\mu_j(i)$ is defined as the weight for $\mathcal{L}_j$ at the i^{th} iteration, obtained through an exponential decay. The algorithm's hyperparameters consist of α for the exponential decay rate, ρ for a Bernoulli random variable with an expected value close to 1, $\mathcal{T}$ for temperature, and I for the total number of iterations. We heuristically set $\alpha = 0.999$, $\mathbb{E}(\rho) = 0.999$, and $\mathcal{T} = 1.0$, as this combination yielded the best results for our problem. θ_{NN} denotes the learnable network parameters, $\eta_{\theta_{\mathrm{NN}}}$ is the learning rate used for updating network parameters, and $\nabla_{\theta_{\mathrm{NN}}}$ is the gradient of the final loss with respect to θ_{NN}.

C. AL-PINNs

1) Global Loss: For AL-PINNs, we defined its global loss as:

$$\mathcal{L}_{\lambda,\mu,\theta_{\mathrm{NN}}} = \underbrace{\mathcal{L}_1}_{\substack{\text{data fidelity} \\ \text{term}}} + \underbrace{\langle \boldsymbol{\lambda_1}, \boldsymbol{C_1} \rangle + \langle \boldsymbol{\lambda_2}, \boldsymbol{C_2} \rangle}_{\substack{\text{PDE \& BC losses} \\ \text{(Lagrange multipliers)}}} + \underbrace{0.5 \times \mu \times (\mathcal{L}_2 + \mathcal{L}_3)}_{\text{PDE \& BC losses (penalty)}} + \underbrace{\mu_4 \mathcal{L}_4}_{\substack{\text{smoothing} \\ \text{reg.}}}. \quad (8)$$

In this equation, λ_1 and λ_2 are learnable real Lagrange multipliers related to the two constraints: the mass conservation, C_1, and the free-slip boundary condition, C_2. The notation $\langle \cdot, \cdot \rangle$ refers to the inner product of two vectors. The learnable penalty coefficient for the two physical constraints is denoted by $\mu \in \mathbb{R}_{>0}$. Similar to RB-PINNs, μ_4 was set heuristically to $10^{-7.5}$.

Algorithm 2: Augmented Lagrangian update strategy

Initialize $\boldsymbol{\lambda_j} = \vec{0}, \mu = 2, j \in \{1, 2\}$.
for $i = 1, \ldots, I$ **do**
  Forward pass and compute losses
  $\mathcal{L}_{\lambda,\mu,\theta_{\mathrm{NN}}}(i) \leftarrow \mathcal{L}_{\lambda,\mu,\theta_{\mathrm{NN}}}$
  Compute final loss using (8) and do backpropagation to simultaneously update network parameters, learnable $\boldsymbol{\lambda_j}$ as well as μ:
  $\boldsymbol{\theta}_{\mathrm{NN}} \leftarrow \boldsymbol{\theta}_{\mathrm{NN}} - \eta_{\theta_{\mathrm{NN}}} \nabla_{\theta_{\mathrm{NN}}} \mathcal{L}_{\lambda,\mu,\theta_{\mathrm{NN}}}(i)$
  $\boldsymbol{\lambda_j} \leftarrow \boldsymbol{\lambda_j} + \eta_\lambda \nabla_{\lambda_j} \mathcal{L}_{\lambda,\mu,\theta_{\mathrm{NN}}}(i)$
  $\mu \leftarrow \mu + \eta_\mu \nabla_\mu \mathcal{L}_{\lambda,\mu,\theta_{\mathrm{NN}}}(i)$
end

2) Update Strategy for Loss Weights: We applied the gradient ascent method [20] to update λ_1, λ_2, and μ, as decribed in Algorithm 2. In the original approach [20], μ remains constant throughout the optimization process, but we proposed to update this penalty coefficient to better adhere to the original AL method [23]. In our experiments, the gradient ascent method showed higher optimization stability and was less prone to gradient explosion compared to the original AL update rule proposed in [23]. In Algorithm 2, θ_{NN}, $\eta_{\theta_{\mathrm{NN}}}$, and $\nabla_{\theta_{\mathrm{NN}}}$ represents the learnable network parameters, the learning rate for updating network parameters, and the gradient of the final loss with respect to θ_{NN}, respectively. $\nabla_{\lambda_j} \cdot$ and $\nabla_\mu \cdot$ denote the gradient of the final loss with respect to λ_j and μ; I indicates the total number of iterations; η_λ and η_μ are the learning rates for the learnable Lagrange multipliers λ_j and μ. The selection of appropriate learning rates is critical in preventing gradient overflow when dealing with physical losses that involve unbounded Lagrange multipliers. Their values are discussed in Section IV-B.1.

D. Dual-Stage Optimization

To improve the convergence of our PINNs, we introduced a dual-stage optimization strategy: 1) an optimization stage using the AdamW [24] optimizer for the first 90% of the iterations to converge to a rough solution; 2) a fine-tuning stage using the L-BFGS [25] optimizer, which is not sensitive to learning rates, for the remaining iterations to obtain an optimal final solution. This approach aimed to reduce the optimization time of PINNs. An ablation study was performed using RB-PINNs to assess the potential improvement of this strategy.

E. PINNs' Architecture, Weight Initialization, and Sampling Strategy

1) Network Architecture: For both PINNs implemented in this paper, we utilized an MLP with six hidden layers, each containing 60 neurons, with the *tanh* activation function. This architecture resulted in approximately 18.6k trainable parameters.

2) Weight Initialization: We first applied the dual-stage optimization to a Doppler frame selected at the end of the early filling phase using RB-PINNs. The resulting weights were then saved as pre-optimized weights and used as initialization for all subsequent PINNs models before optimization on new Doppler data. This initialization technique aimed to accelerate the optimization process of our PINNs and enhance their performance. A second ablation study was carried out to justify this choice.

3) Sampling Strategy: Leveraging the regularly spaced polar grid of color Doppler imaging and its relatively small size, we utilized all sample points within the left ventricle on the grid for both data and collocation points. These data points were used to compute the data fidelity term, while the PDE loss and smoothness term were evaluated from the collocation points. For the boundary condition residual loss, all extracted points on the boundary were considered.

F. Physics-Guided nnU-Net

We trained a physics-guided nnU-Net (refer to Fig. 1b for its architecture) with configurations similar to those described in [26, Table I] on both simulations and *in vivo* data. We adapted the loss function to L1 loss for supervised regression. Additionally, to enforce mass conservation in the predicted velocity field, we incorporated $\mathcal{L}_2$ in the loss function as a physical regularization term with a weight of $\gamma = 10^{-3}$. Both supervised and regularization terms were masked with the left ventricular binary segmentation, restricting loss computation to the region of interest. The final loss was expressed as:

$$\mathcal{L}_{\gamma,\theta_{\text{NN}}} = \underbrace{\left\|\hat{V}_r - V_{r_{\text{ref}}}\right\|_1 + \left\|\hat{V}_\theta - V_{\theta_{\text{ref}}}\right\|_1}_{\text{data fidelity term}} + \gamma \underbrace{\left\| r\frac{\partial \hat{V}_r}{\partial r} + \hat{V}_r + \frac{\partial \hat{V}_\theta}{\partial \theta}\right\|_1}_{\text{PDE loss}}, \tag{9}$$

where $(V_{r_{\text{ref}}}, V_{\theta_{\text{ref}}})$ represent the reference velocity field given by simulations or predicted velocity field by *i*VFM [1], considered as the gold standard for *in vivo* data.

Unlike PINNs that directly take coordinates (r, θ) as input, nnU-Net requires image data. Our nnU-Net's input was a concatenation of: 1) dealiased color Doppler image before scan-conversion for *in vivo* data or alias-free image for simulated data; 2) a weight matrix with normalized Doppler powers in the range of $[0, 1]$ for *in vivo* data or containing ones for simulated data; 3) binary segmentation of the left ventricle cavity; 4) radial coordinate array; 5) angular coordinate array. More details about the training dataset are given in Section IV-A.2.

During training, we applied data augmentations, including random rotation ($[-15, 15]°$), random zoom ($[0.7, 1.4]$), and random scanline masking. With the latter, a block of n consecutive scanlines was randomly masked out with a step size of m. In our experiments, $m = 10$ and n was a random integer between 0 and 9. This strategy simulated sparse Doppler data, enhancing the model's robustness and generalizability.

G. Evaluation Metrics

We assessed the performance of RB-PINNs, AL-PINNs, and nnU-Net using simulated Doppler images from a patient-specific computational fluid dynamics (CFD) model (see Section IV-A.1). Evaluation metrics, including squared correlation (r^2) and normalized root-mean-square error (nRMSE), were computed by comparing predicted and ground truth velocity fields within the left ventricle.

1) Squared Correlation: We defined the squared correlation as follows:

$$r^2_{v_k} = \text{Corr}(\hat{v}_k, v_{k_{\text{CFD}}})^2, \quad k \in \{r, \theta\}, \tag{10}$$

where Corr is the Pearson correlation coefficient.

2) nRMSE: For both the radial and angular components, we computed the root-mean-square errors normalized by the maximum velocity defined by:

$$\text{nRMSE} = \frac{1}{\max \|v_{\text{CFD}}\|_2} \sqrt{\frac{1}{n}\sum_{k=1}^{n} \|\hat{v}_k - v_{\text{CFD}_k}\|_2^2}, \tag{11}$$

where n stands for the number of velocity samples in the left ventricular cavity. For the nRMSE metrics shown in Tables I, II, and IV, we considered both velocity components and reported them as $(\tilde{x} \pm \sigma_{\text{rob}})$. Here, $\tilde{x}$ signifies the median, while $\sigma_{\text{rob}} = 1.4826 \times \text{MAD}$ represents the robust standard deviation (std.), with MAD denoting the mean absolute deviation.

IV. Experimental Setup and Results

A. Dataset

1) Patient-specific Computational Fluid Dynamics (CFD) Heart Model: To validate our approaches, we utilized a new patient-specific physiological CFD model of cardiac flow developed by the IMAG laboratory. This model features a more realistic mitral valve compared to the previous version [27], [28]. We followed the same method described in [1, Sec. 2.3] to generate 100 simulated Doppler images evenly

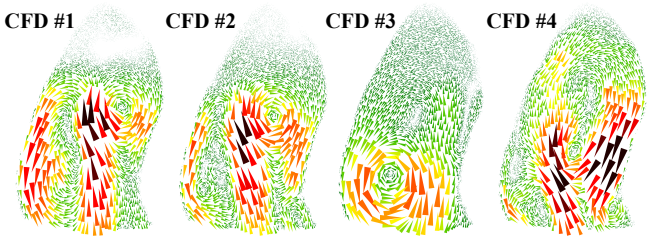


Fig. 2. Simulated color Doppler image during early filling derived from patient-specific CFD heart models with four variants of mitral valves. CFD #1-3 represent cases following mitral valve replacement with a bioprosthetic valve, while CFD #4 is a normal case.

TABLE I
ABLATION STUDY ON 100 SIMULATED DOPPLER IMAGES USING RB-PINNS. OPTIMIZATION TIME IS CONSISTENT (100 SECONDS PER FRAME) ACROSS ALL CONFIGURATION COMBINATIONS. DEFAULT SETTINGS ARE HIGHLIGHTED IN PURPLE.

Pre-optimized weights	Dual-stage optimization	$r^2(\uparrow)$ v_r	$r^2(\uparrow)$ v_θ	nRMSE [%]($\downarrow$) ($\tilde{x} \pm \sigma_{\text{rob}}$)
✘	✘	0.88	0.23	4.3 ± 2.2
✘	✔	0.97	0.57	2.8 ± 1.2
✔	✘	0.96	0.58	2.4 ± 1.0
✔	✔	**0.99**	**0.66**	$\mathbf{2.2} \pm 1.0$

distributed over a cardiac cycle, with a signal-to-noise ratio (SNR) equal to 50 dB. Each image comprised 80 scanlines with 200 samples per scanline. As Doppler power information was not available, we set the weight for the data fidelity term in both PINNs and *i*VFM to one, i.e., $\omega = W = 1$.

2) CFD and In Vivo Apical Three-Chamber (A3C) Training Dataset for nnU-Net : Based on the CFD model described in Section IV-A.1, we introduced variations to the mitral valve geometry, by modifying opening angle and orientation, to simulate three distinct cases following mitral valve replacement with a bioprosthetic valve (CFD #1-3) [29]. CFD #1 and #2 corresponded to two different inflow jet orientations, with a slight increase in mitral valve cross-sectional area in CFD #2. CFD #3 mimicked blood flow with a wide-opened mitral valve, resulting in a weak jet with limited penetration. CFD #1-3 were included as training/validation data for the nnU-Net, while the unaltered model representing a normal case (CFD #4) was used for testing. Fig. 2 provides an example of a simulated color Doppler image during early filling for each CFD model. Although these four models shared the underlying cardiac geometry, modifications to the mitral valve resulted in sufficiently diverse intraventricular flows to reduce the training bias.

Due to the limited availability of simulated Doppler data for training a supervised model, we chose to include *in vivo* A3C duplex (B-mode + color Doppler) data in our training dataset. This decision was further elaborated in Section V-A. These data aligned with the dataset of prior studies [26], [30], acquired using a Vivid 7 ultrasound system (GE Healthcare, USA) with a GE 5S cardiac sector probe (bandwidth = 2–5 MHz). Further details about this dataset can be found in [26, Sec. III-A.1].

We processed the *in vivo* A3C data to ensure high-quality training data. We initially filtered out low-quality data, resulting in a compilation of 92 Doppler echocardiographic cineloops from 37 patients, totaling 2668 frames. Subsequently, we performed preprocessing using ASCENT [26], [31]. This process involved segmenting the left ventricle cavity on B-mode images to define the region of interest and boundary conditions, which varied across frames, and correcting aliased pixels on the corresponding color Doppler images. Finally, we applied the *i*VFM method to reconstruct the 2D vector field in the left ventricle, serving as the gold standard for training the nnU-Net. For training purposes, the physics-constrained dataset was split subject-wise into 74/10/8 clinical cineloops plus 2/1/1 CFD simulations, resulting in 2037/434/197 *in vivo* and 200/100/100 simulated images for training/validation/testing.

B. Training Strategies

All methods were implemented in the same PyTorch-based framework to ensure consistent training and optimization. The training configurations for each approach were as follows:

1) RB-PINNs and AL-PINNs : For both RB-PINNs and AL-PINNs, we used a dual-stage optimization strategy, involving two stages with a total of $I = 2500$ iterations. In the first stage, we applied AdamW optimization for $0.9 \times I$ iterations, updating all learnable parameters with a learning rate of $\eta_{\theta_{\text{NN}}} = \eta_\lambda = \eta_\mu = 10^{-5}$. Then, in the fine-tuning stage, which comprised the remaining 10% of the iterations, we utilized L-BFGS optimization. In this stage, only the network parameters were updated, while the learnable loss weights from the first stage were retained. The L-BFGS optimizer was configured with a maximum of ten iterations per optimization step, and the strong Wolfe line search conditions.

This strategy ensured a balance between accuracy and optimization duration, enhancing the stability and efficiency of PINNs' optimization process. The advantage of this strategy was further demonstrated in Section IV-C.1.

2) Physics-Guided nnU-Net : Our physics-guided nnU-Net underwent 1000 epochs of training with the following configurations: a patch size of (192×40) pixels, a batch size of 4, and SGD optimizer with an initial learning rate of 0.01, paired with a linear decay scheduler.

C. Experimental Results

1) Pre-Optimized Weights and Dual-Stage Optimization Enhanced PINNs' Performance: The ablation study presented in Table I highlights that the combination of pre-optimized weights and dual-stage optimization in RB-PINNs yielded the best performance within a fixed optimization time. The dual-stage optimization strategy significantly reduced the optimization time of PINNs methods. Figure 3 provides a visual representation of a case where optimization was conducted using pre-optimized weights with and without dual-stage optimization. In this example, single-stage optimization with AdamW required $3.5\times$ more optimization time to achieve a visually similar solution compared to dual-stage optimization. Subsequent experiments with PINNs followed this optimization

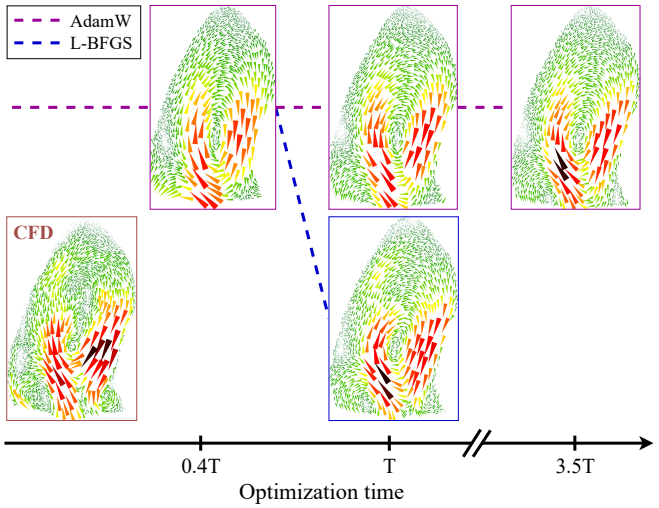


Fig. 3. Dual-stage (AdamW + L-BFGS) versus single-stage (AdamW only) optimization using RB-PINNs initialized with pre-optimized weights. T refers to the total amount of time required for dual-stage optimization. In this example, 3.5 × more time is needed for single-stage optimization (top right) to converge to a similar solution given by dual-stage optimization (bottom right).

strategy—dual-stage optimization with pre-optimized weight initialization.

2) NN-based Approaches Aligned with the Original iVFM : All methods achieved high correlation in the radial velocity estimation on the 100 simulated color Doppler images derived from CFD #4, with $r^2_{v_r} > 0.98$ (see Fig. 4). For angular velocity correlation, both PINNs, RB-PINNs and AL-PINNs performed similarly to *i*VFM, $r^2_{v_\theta} = 0.659$ and 0.669 versus 0.694, while nnU-Net surpassed *i*VFM ($r^2_{v_\theta} = 0.744$). This suggests the effectiveness of a supervised approach in learning intraventricular blood flow patterns. However, nnU-Net tended to be less precise when estimating highly negative radial velocities on simulated Doppler data, potentially due to the limited CFD training samples. Interestingly, all NN methods exhibited more errors for the radial component than *i*VFM, highlighting the high robustness and precision of the physics-constrained *i*VFM approach (see Fig. 5). The nRMSE of *i*VFM ranged between 0.2%-1.6% and 1.4%-21.3% for the radial and angular velocities, respectively. Among all methods, AL-PINNs had the highest nRMSE for angular velocities (2.2% to 23.3%). Despite having the highest nRMSE for radial velocities (3.8% to 6.7%), nnU-Net produced the least errors in angular velocity estimation (2.3% to 13.3%). A cineloop showing the reconstructed field by PINNs and nnU-Net versus CFD can be found in the Supplementary Material ▶.

The final optimized values of the penalty coefficients were (median ± robust std. [min, max]): $\mu_1 = 0.90 \pm 0.11\ [0.32, 1.00]$, $\mu_2 = 0.90 \pm 0.12\ [0.32, 1.02]$, $\mu_3 = 1.19 \pm 0.22\ [0.99, 2.36]$ for RB-PINNs, and $\mu = 2.02 \pm 0.01\ [2.01, 2.07]$ for AL-PINNs.

3) nnU-Net Demonstrated Better Generalizability and Robustness on Sparse Doppler Data: Table II presents metrics for each method on both full and sparse simulated Doppler images. In the evaluation on full data, *i*VFM achieved the highest correlation for radial velocities and the lowest nRMSE, while nnU-Net, trained with the physical regularization term (PDE loss), excelled in the correlation of angular velocities. This implies that incorporating physical regularization helps constrain the nnU-Net's output to better adhere to the laws of physics.

As expected, the performance of all methods was significantly impacted when evaluated on sparse data, where nine out of ten scanlines were masked. Remarkably, nnU-Net, which was trained with both the physical regularization term and the random scanline masking augmentation, demonstrated the least decline in performance. It maintained a high correlation for both radial and angular velocities while achieving the least nRMSE. This finding underscores the benefit of this augmentation in supervised learning for enhanced generalization. Despite having lower correlations than nnU-Net, *i*VFM remained robust, producing a lower nRMSE than RB-PINNs and AL-PINNs.

4) nnU-Net Exhibited Superior Reconstruction Speed: Table III provides a comparison of the training, optimization, and inference times for NN-based approaches against *i*VFM. These metrics were computed using a 16 GB V100 GPU for NN methods and an Intel i5-11500H CPU for *i*VFM. As the only supervised approach in the comparison, nnU-Net required 12 hours of training but achieved the fastest per-frame inference time, taking only 0.05 second. *i*VFM ranked second, with a reconstruction time of 0.2 second per frame. Notably, both PINNs necessitated longer optimization times, around 100 seconds, which is a recognized drawback of this approach.

5) Clinical Application of Vector Blood Flow Mapping: Fig. 6 showcases the intraventricular vector blood flow mapping by various methods on an *in vivo* case at different cardiac phases, including ejection, early filling, diastasis, and late filling. The reconstructed flow patterns by all methods appear relatively similar, with *i*VFM generating the smoothest flow patterns. Although the prominent vortex was less visible during early filling, it became more pronounced at the center of the left ventricle cavity during diastasis. Another example of vector blood flow reconstruction by all four methods on *in vivo* data is given in the Supplementary Material ▶.

6) Robustness of nnU-Net on Truncated Clinical Doppler Data: Unlike other methods that required explicit boundary conditions, nnU-Net learned these conditions implicitly during training. This offered an advantage as it reduced the need for specific knowledge about the flow at the endocardium. Table IV illustrates nnU-Net's behavior under Doppler scanline truncation, achieved by progressively cutting scanlines from both sides towards the center. The metrics were computed within the common region remaining after truncation. The results show stable performance up to a 50% reduction. However, beyond this threshold, a more pronounced decrease in performance was observed. Fig. 7 visually demonstrates nnU-Net's ability to consistently produce accurate intraventricular vector blood flow reconstructions, even with a significant 70% truncation.

V. Discussions

Our study introduces alternative approaches to the physics-constrained *i*VFM algorithm [1], leveraging the power of NNs:

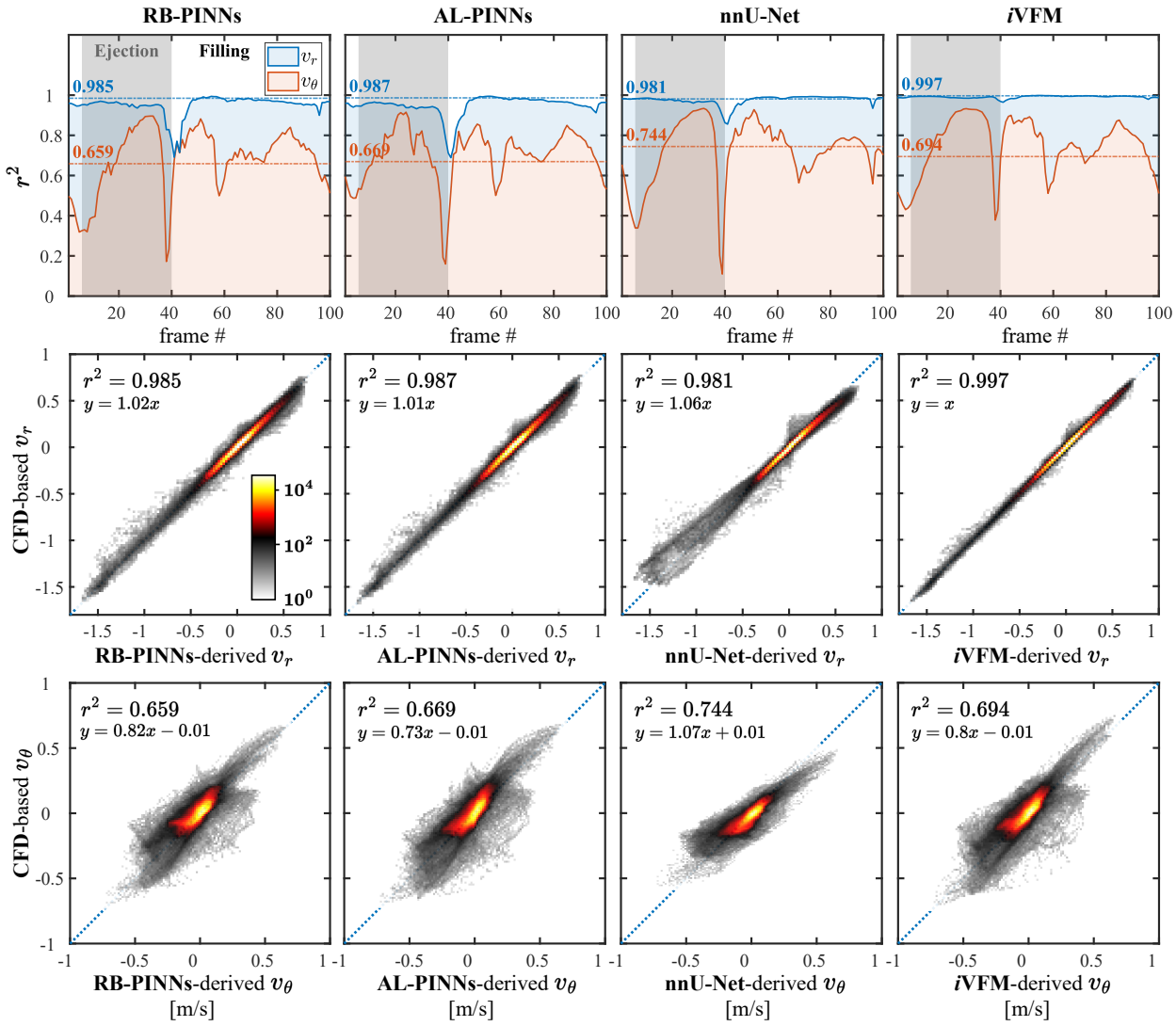


Fig. 4. Top row: time-varying squared correlation between CFD-based velocities and reconstructed velocities by each method; mid and bottom rows: CFD-based velocities versus estimated velocities derived from various methods. For mid and bottom rows, velocity data from 100 simulated color Doppler images were pooled. The binned scatter plots show the number of velocity occurrences.

TABLE II
METRICS COMPUTED ON 100 FULL AND SPARSE SIMULATED DOPPLER IMAGES

Methods	Full data			Sparse data*		
	$r^2(\uparrow)$		nRMSE [%]($\downarrow$) ($\tilde{x} \pm \sigma_{\text{rob}}$)	$r^2(\uparrow)$		nRMSE [%]($\downarrow$) ($\tilde{x} \pm \sigma_{\text{rob}}$)
	v_r	v_θ		v_r	v_θ	
*i*VFM	**1.00**	0.69	**1.7** $\pm$ 1.0	0.85	0.58	3.2 $\pm$ 2.3
RB-PINNs	0.99	0.66	2.2 $\pm$ 1.0	0.86	0.56	3.4 $\pm$ 1.6
AL-PINNs	0.99	0.67	2.5 $\pm$ 1.0	0.80	0.58	3.5 $\pm$ 1.4
nnU-Net‡	0.99	0.60	2.3 $\pm$ 0.9	0.67	0.12	6.0 $\pm$ 3.0
nnU-Net†	0.99	**0.74**	2.1 $\pm$ 0.9	0.64	0.49	6.0 $\pm$ 3.3
nnU-Net	0.98	**0.74**	2.1 $\pm$ 0.9	**0.88**	**0.71**	**2.4** $\pm$ 1.0

* indicates data masked every 9 out of 10 scanlines from the center to the borders.
‡ means training without both physical regularization term (PDE loss) and random scanline masking augmentation.
† signifies training with physical regularization term (PDE loss), but without random scanline masking augmentation.

TABLE III
COMPARISON OF TRAINING, OPTIMIZATION, AND INFERENCE TIMES FOR NN-BASED METHODS AND *i*VFM

Methods	Device	No. trainable parameters	Training time	Optimization/ inference time per frame
*i*VFM	CPU	-	-	0.2 s
RB-PINNs	GPU	18.6 k	-	100 s
AL-PINNs	GPU	18.6 k	-	100 s
nnU-Net	GPU	7 M	12 h	**0.05 s**

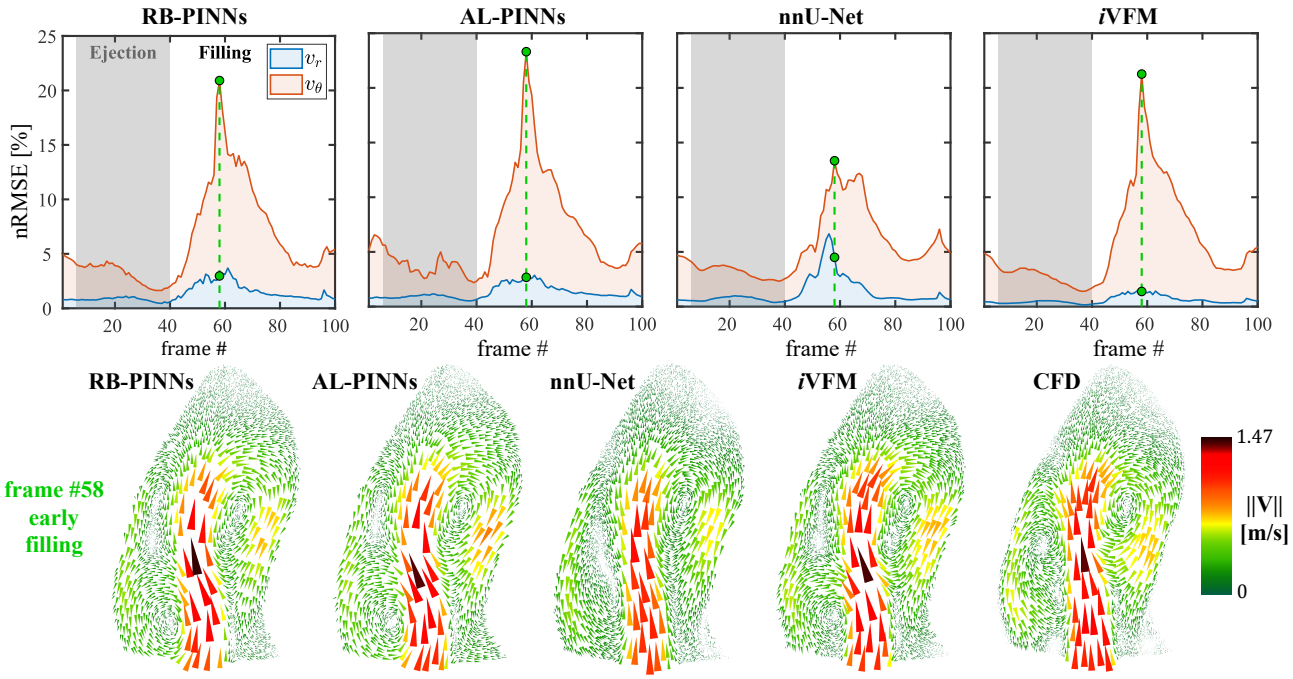


Fig. 5. Normalized root-mean-square errors (nRMSE) between CFD-based and estimated velocity vectors by different techniques.

TABLE IV
NNU-NET'S METRICS COMPUTED ON 8 *in vivo* TEST CINELOOPS OF 197 FRAMES WITH DIFFERENT PERCENTAGES OF SCANLINE TRUNCATION

Percentage of truncation [%]	$r^2(\uparrow)$		nRMSE [%]($\downarrow$) ($\tilde{x} \pm \sigma_{\text{rob}}$)
	v_r	v_θ	
20	0.97	0.96	2.4 ± 1.2
40	0.99	0.92	3.7 ± 1.5
50	0.99	0.87	4.3 ± 1.6
60	0.97	0.75	6.5 ± 2.7
70	0.94	0.59	8.4 ± 2.9

Note: Comparison made with nnU-Net's estimated velocity fields on full scanline data.

PINNs (RB-PINNs and AL-PINNs) and a physics-guided supervised technique (nnU-Net). These methods offer distinct strategies for the inherent constrained optimization problem in *i*VFM.

In the PINNs framework, we addressed the same optimization problem as in *i*VFM, but solved it differently using gradient descent and NNs. By incorporating governing equations, such as mass conservation and boundary conditions, PINNs inherently enforce physical laws during optimization, potentially leading to optimized intraventricular vector velocity fields.

On the other hand, the supervised approach (nnU-Net) was trained on patient-specific CFD-derived simulations and *i*VFM-estimated velocity field on *in vivo* Doppler data. The network learned the underlying flow patterns while adhering to physical principles through the use of physics-constrained labels and the physical regularization term in the loss function. This approach demonstrated robustness to data limitations, such as missing scanlines.

A. PINNs versus Physics-Guided nnU-Net

The application of PINNs deviates from the conventional optimization methods by leveraging NNs to find the optimal solution, which can be advantageous in complex physical problems. Although PINNs may not necessarily outperform analytical or numerical methods in computational efficiency, approximation accuracy, or convergence guarantees [32], they offer a unique advantage in terms of flexibility. This flexibility allows their architecture to remain relatively consistent across various physical optimization problems by adapting the loss functions to be optimized.

In our case of intraventricular blood flow reconstruction, we successfully improved the computational efficiency of PINNs while maintaining accuracy comparable to *i*VFM. This was achieved by implementing a dual-stage optimization with the use of pre-optimized weights. For future exploration, both PINNs architectures could benefit from imposing hard boundary conditions rather than optimizing them in the form of soft constraints. Additionally, better strategies for automatically determining or learning the optimal smoothing regularization weight, rather than relying on heuristic search methods, will be investigated to further improve the robustness of PINNs.

Unlike PINNs, nnU-Net operates within a supervised learning framework, heavily relying on labeled training data. In this study, CFD-derived simulations played a crucial role in providing ground truth velocity fields for training. This explains the high squared correlation achieved by nnU-Net, as the simulated training samples shared the exact heart geometry despite variations in flow patterns due to different mitral valve conditions.

However, when trained exclusively on simulated data, nnU-Net struggled to correctly estimate vector blood flow in *in vivo* color Doppler data due to a distribution shift between the

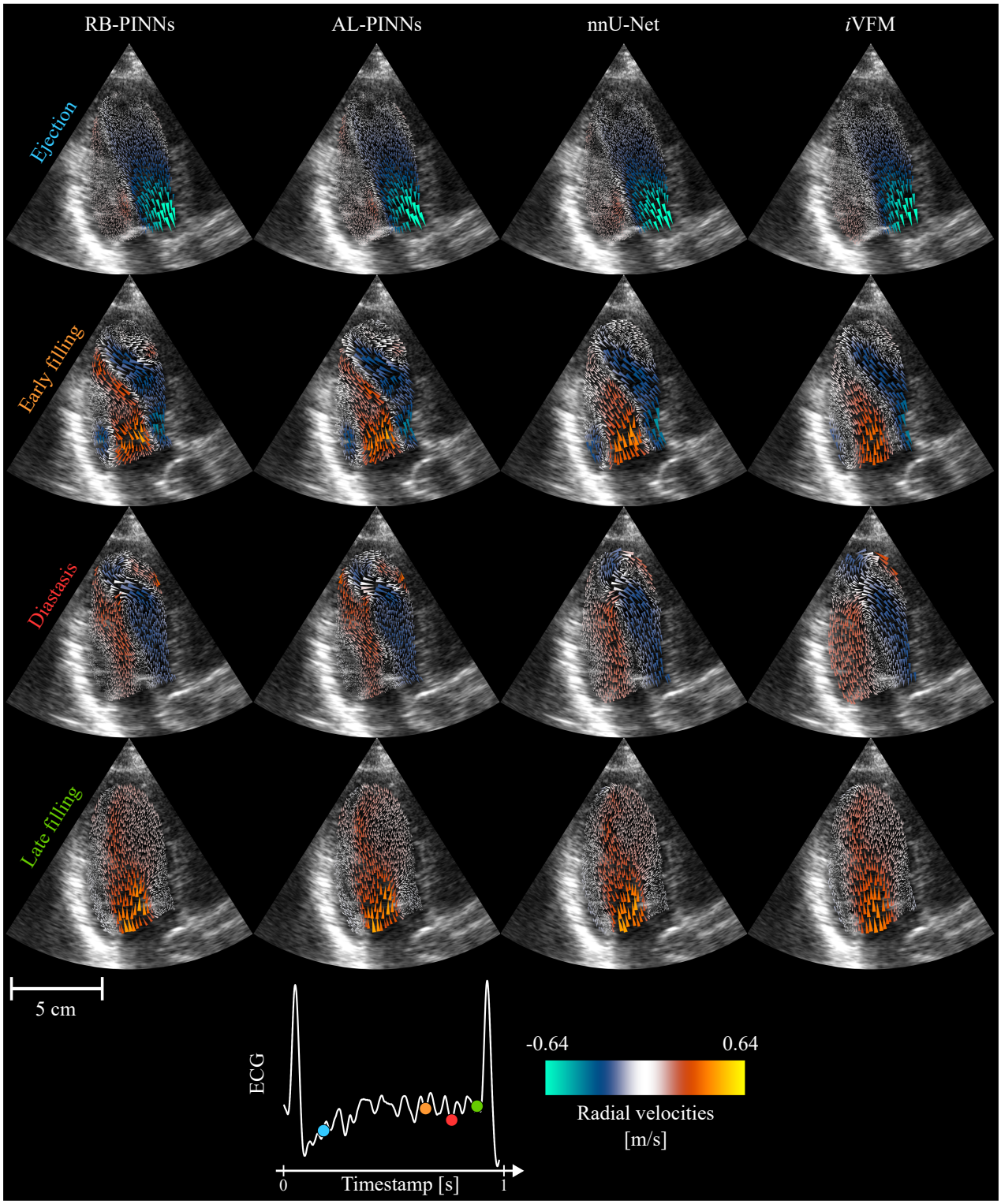


Fig. 6. Reconstruction of intraventricular vector blood flow in a patient using NN-based approaches and *i*VFM. The color of the arrows represents the estimated radial velocity fields.

simulated and real data. This arose from limitations in the current physiological spectrum of the simulations. To bridge this gap, we included *i*VFM-estimated velocities in our training data, allowing nnU-Net to learn from solutions representative of clinical Doppler data generated by the established *i*VFM method. As shown in Fig. 6, nnU-Net effectively learned the underlying flow pattern and physical properties, i.e., the free-divergence and boundary conditions, from the training samples generated by *i*VFM.

Moreover, as illustrated in Fig. 7, nnU-Net can precisely

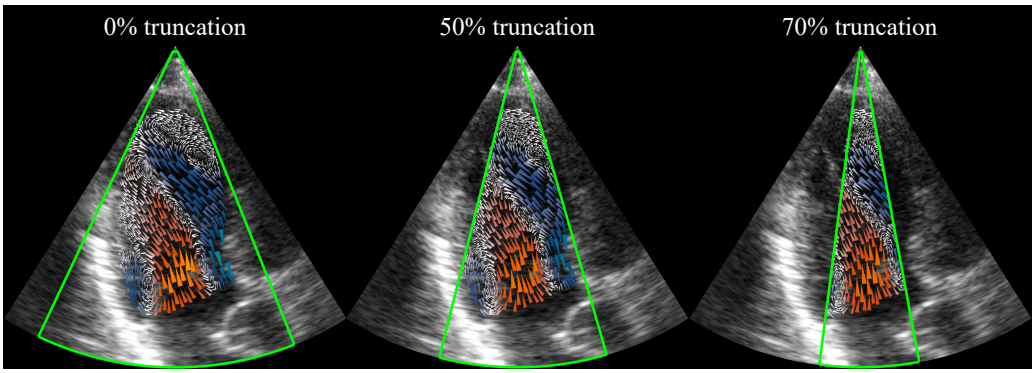


Fig. 7. Intraventricular vector blood flow reconstruction from Doppler data with varying percentages of scanline truncation using physics-guided nnU-Net. The color of the arrows represents the estimated radial velocity fields.

reconstruct intraventricular flow on truncated Doppler data, where PINNs and *i*VFM cannot be directly applied as such due to incomplete and unknown boundary conditions. This potentially makes nnU-Net the preferred candidate for clinical applications, especially considering that most clinical Doppler acquisitions do not capture the entire left ventricular cavity due to limitations in probe placement or patient anatomy. With the added advantage of the shortest inference time, nnU-Net has real-time capabilities suitable for clinical settings. Future work will focus on generating more patient-specific CFD models and creating more realistic simulated Doppler data [33] to avoid the bias associated with using *i*VFM estimates as a reference to train our model.

B. Limitations of Color Doppler and Vector Flow Mapping

Conventional color Doppler echocardiography is subject to various limitations, posing challenges for accurate vector flow mapping. These limitations include clutter signals arising from myocardial tissue and valve leaflets, aliasing artifacts caused by Doppler velocity overshooting beyond Nyquist velocity, and low spatial and temporal resolutions. While the impact of clutter signal filtering on flow reconstruction is acknowledged, its specific effects were not investigated in this study. Our input data were already clutter-filtered (*in vivo* non scan-converted data from a GE scanner) or clutter-free (simulated data). Some researchers address clutter filtering in color flow imaging using deep learning (DL) techniques [34].

The clinical color Doppler data used for training and testing in this study contained only single aliasing, corrected by a DL-based unwrapping algorithm from our previous work [26]. It is important to note that this algorithm may face limitations in scenarios involving multiple aliasing, particularly in valvular disease. A potential solution could involve training a supervised DL model with multi-aliased data and their alias-free labels, such as in interferometric imaging [35] or color Doppler imaging of the femoral bifurcation [36].

The temporal resolution of clinical color Doppler, typically ranging from 10 to 15 frames per second, significantly restricts the use of temporal information. Consequently, the application of physical constraints is limited to those that are not time-dependent, such as mass conservation for an incompressible fluid. Around 25 harmonics are necessary to accurately record pressure time derivatives within the left ventricle with a 5% margin of error [37]. Hence, a color Doppler frame rate of 25 should be ideally sought to characterize intracardiac blood flow. Although we did not address such a strategy in this study, one approach would be to use Doppler information from two or three successive cardiac cycles. To overcome these limitations, advances in increasing the frame rate of color Doppler imaging, such as diverging scan sequences [38], [39], have been explored. Another promising avenue involves utilizing multi-line transmission [40], especially given the robust performance of our models on sparse Doppler data, notably nnU-Net. Higher frame rates offer the possibility of incorporating more complex physical constraints, including vorticity, Euler, or Navier-Stokes equations, potentially enhancing flow reconstruction accuracy. While this might pose challenges for the original *i*VFM due to the non-linear terms in the equations, it aligns seamlessly with PINNs, requiring minimal changes to the loss function.

C. Future Directions

The successful application of PINNs in mapping intraventricular vector flow from color Doppler paves the way for future investigations. Upcoming research will prioritize the integration of high-frame-rate color Doppler with PINNs while incorporating the governing Navier-Stokes equations. This combination aims to leverage the temporal information to obtain a more accurate velocity field and the pressure gradient within the left ventricle.

Furthermore, with the development of our fully automated and robust tools, including left ventricular segmentation, dealiasing, and velocity field reconstruction using NNs, we anticipate extracting potential biomarkers from intracardiac vector blood flow for enhanced clinical insights and diagnostic capabilities.

VI. Conclusion

Our study presents novel approaches based on NNs for intraventricular vector flow mapping, utilizing gradient-based optimization through PINNs (RB-PINNs and AL-PINNs) or physics-guided supervised learning (nnU-Net). These methods offer contrasting strategies to tackle the ill-posed inverse problem for vector flow reconstruction. Our results demonstrate

the remarkable capabilities of both PINNs and nnU-Net in reconstructing intraventricular vector blood flow fields. Particularly noteworthy is nnU-Net's performance, demonstrating quasi-real-time capability, robustness on sparse Doppler data, and independence from explicit boundary conditions. These characteristics position nnU-Net as a promising solution for real-time clinical applications.

Acknowledgment

Olivier Bernard and Damien Garcia share the last authorship for this work. The authors thank François Tournoux (Montreal University—CHUM—CRCHUM) for providing access to the *in vivo* data used in this study.

References

[1] F. Vixège *et al.*, "Physics-constrained intraventricular vector flow mapping by color Doppler," *Phys. Med. Biol.*, vol. 66, no. 24, p. 245019, Dec. 2021.

[2] K. C. Assi *et al.*, "Intraventricular vector flow mapping-a Doppler-based regularized problem with automatic model selection," *Phys. Med. Biol.*, vol. 62, no. 17, pp. 7131–7147, Aug. 2017.

[3] R. Asami, T. Tanaka, K.-i. Kawabata, K. Hashiba, T. Okada, and T. Nishiyama, "Accuracy and limitations of vector flow mapping: left ventricular phantom validation using stereo particle image velocimetory," *J. Echocardiogr.*, vol. 15, no. 2, pp. 57–66, Jun. 2017.

[4] B. A. Meyers, C. J. Goergen, P. Segers, and P. P. Vlachos, "Colour-Doppler echocardiography flow field velocity reconstruction using a streamfunction–vorticity formulation," *J. R. Soc. Interface*, vol. 17, no. 173, p. 20200741, Dec. 2020.

[5] A. S. Daae, M. S. Wigen, S. Fadnes, L. Løvstakken, and A. Støylen, "Intraventricular Vector Flow Imaging with Blood Speckle Tracking in Adults: Feasibility, Normal Physiology and Mechanisms in Healthy Volunteers," *Ultrasound Med. Biol.*, vol. 47, no. 12, pp. 3501–3513, Dec. 2021.

[6] M. Raissi, P. Perdikaris, and G. E. Karniadakis, "Physics-informed neural networks: A deep learning framework for solving forward and inverse problems involving nonlinear partial differential equations," *J. Comput. Phys.*, vol. 378, pp. 686–707, Feb. 2019.

[7] A. Baydin, B. Pearlmutter, A. Radul, and J. Siskind, "Automatic differentiation in machine learning: A survey," *J. Mach. Learn. Res.*, vol. 18, pp. 1–43, Apr. 2018.

[8] S. Cai, Z. Mao, Z. Wang, M. Yin, and G. E. Karniadakis, "Physics-informed neural networks (PINNs) for fluid mechanics: a review," *Acta Mech. Sin.*, vol. 37, no. 12, pp. 1727–1738, Dec. 2021.

[9] A. Arzani, J.-X. Wang, and R. M. D'Souza, "Uncovering near-wall blood flow from sparse data with physics-informed neural networks," *Phys. Fluids*, vol. 33, no. 7, p. 071905, Jul. 2021.

[10] G. Kissas, Y. Yang, E. Hwuang, W. R. Witschey, J. A. Detre, and P. Perdikaris, "Machine learning in cardiovascular flows modeling: Predicting arterial blood pressure from non-invasive 4D flow MRI data using physics-informed neural networks," *Comput. Methods Appl. Mech. Eng.*, vol. 358, p. 112623, Jan. 2020.

[11] L. Wang, H. Wang, L. Liang, J. Li, Z. Zeng, and Y. Liu, "Physics-informed neural networks for transcranial ultrasound wave propagation," *Ultrasonics*, vol. 132, p. 107026, Jul. 2023.

[12] Z. Yin, G.-Y. Li, Z. Zhang, Y. Zheng, and Y. Cao, "SWENet: a physics-informed deep neural network (PINN) for shear wave elastography," *IEEE Trans. Med. Imaging*, pp. 1–1, 2023.

[13] H. Guan, J. Dong, and W.-N. Lee, "Towards Real-time Training of Physics-informed Neural Networks: Applications in Ultrafast Ultrasound Blood Flow Imaging," Sep. 2023, arXiv:2309.04755 [cs.CE].

[14] S. A. Faroughi *et al.*, "Physics-Guided, Physics-Informed, and Physics-Encoded Neural Networks and Operators in Scientific Computing: Fluid and Solid Mechanics," *J. Comput. Inf. Sci. Eng.*, vol. 24, no. 040802, Jan. 2024.

[15] F. Isensee, P. F. Jaeger, S. A. A. Kohl, J. Petersen, and K. H. Maier-Hein, "nnU-Net: a self-configuring method for deep learning-based biomedical image segmentation," *Nat. Methods*, vol. 18, no. 2, pp. 203–211, 2021.

[16] Z. Chen, V. Badrinarayanan, C.-Y. Lee, and A. Rabinovich, "GradNorm: Gradient Normalization for Adaptive Loss Balancing in Deep Multitask Networks," in *Proc. ICML*, Jul. 2018, pp. 794–803.

[17] A. A. Heydari, C. A. Thompson, and A. Mehmood, "SoftAdapt: Techniques for Adaptive Loss Weighting of Neural Networks with Multi-Part Loss Functions," Dec. 2019, arXiv:1912.12355 [cs.LG].

[18] R. Bischof and M. Kraus, "Multi-Objective Loss Balancing for Physics-Informed Deep Learning," Nov. 2021, arXiv:2110.09813 [cs.LG].

[19] L. Lu, R. Pestourie, W. Yao, Z. Wang, F. Verdugo, and S. G. Johnson, "Physics-Informed Neural Networks with Hard Constraints for Inverse Design," *SIAM J. Sci. Comput.*, vol. 43, no. 6, pp. B1105–B1132, Jan. 2021.

[20] H. Son, S. W. Cho, and H. J. Hwang, "Enhanced physics-informed neural networks with Augmented Lagrangian relaxation method (AL-PINNs)," *Neurocomputing*, vol. 548, p. 126424, Sep. 2023.

[21] J. Berg and K. Nyström, "A unified deep artificial neural network approach to partial differential equations in complex geometries," *Neurocomputing*, vol. 317, pp. 28–41, Nov. 2018.

[22] N. Sukumar and A. Srivastava, "Exact imposition of boundary conditions with distance functions in physics-informed deep neural networks," *Comput. Methods Appl. Mech. Eng.*, vol. 389, p. 114333, Feb. 2022.

[23] M. R. Hestenes, "Multiplier and gradient methods," *J. Optim. Theory Appl.*, vol. 4, no. 5, pp. 303–320, Nov. 1969.

[24] I. Loshchilov and F. Hutter, "Decoupled weight decay regularization," in *Proc. ICLR*, 2019.

[25] D. C. Liu and J. Nocedal, "On the limited memory BFGS method for large scale optimization," *Math. Program.*, vol. 45, no. 1, pp. 503–528, Aug. 1989.

[26] H. J. Ling, O. Bernard, N. Ducros, and D. Garcia, "Phase Unwrapping of Color Doppler Echocardiography using Deep Learning," *IEEE Trans. Ultrason. Ferroelectr. Freq. Control*, vol. 70, no. 8, pp. 810–820, Aug. 2023.

[27] C. Chnafa, S. Mendez, and F. Nicoud, "Image-based large-eddy simulation in a realistic left heart," *Comput. Fluids*, vol. 94, pp. 173–187, May 2014.

[28] C. Chnafa, S. Mendez, and F. Nicoud, "Image-Based Simulations Show Important Flow Fluctuations in a Normal Left Ventricle: What Could be the Implications?" *Ann. Biomed. Eng.*, vol. 44, no. 11, pp. 3346–3358, Nov. 2016.

[29] R. Faludi *et al.*, "Left ventricular flow patterns in healthy subjects and patients with prosthetic mitral valves: An in vivo study using echocardiographic particle image velocimetry," *J. Thorac. Cardiovasc. Surg.*, vol. 139, no. 6, pp. 1501–1510, Jun. 2010.

[30] F. Mehregan *et al.*, "Doppler vortography: a color Doppler approach for quantification of the intraventricular blood flow vortices," *Ultrasound Med. Biol.*, vol. 40, no. 1, pp. 210–221, 2014.

[31] H. J. Ling, N. Painchaud, P.-Y. Courand, P.-M. Jodoin, D. Garcia, and O. Bernard, "Extraction of Volumetric Indices from Echocardiography: Which Deep Learning Solution for Clinical Use?" in *Proc. FIMH*, 2023, pp. 245–254.

[32] T. G. Grossmann, U. J. Komorowska, J. Latz, and C.-B. Schönlieb, "Can Physics-Informed Neural Networks beat the Finite Element Method?" Feb. 2023, arXiv:2302.04107 [math.NA].

[33] Y. Sun *et al.*, "A Pipeline for the Generation of Synthetic Cardiac Color Doppler," *IEEE Trans. Ultrason. Ferroelectr. Freq. Control*, vol. 69, no. 3, pp. 932–941, Mar. 2022.

[34] H. Wang, S. Gao, M. Mozumi, M. Omura, R. Nagaoka, and H. Hasegawa, "Preliminary investigation on clutter filtering based on deep learning," *Jpn. J. Appl. Phys.*, vol. 60, p. SDDE21, May 2021.

[35] G. E. Spoorthi, R. K. Sai Subrahmanyam Gorthi, and S. Gorthi, "Phasenet 2.0: Phase unwrapping of noisy data based on deep learning approach," *IEEE Trans. Image Process.*, vol. 29, pp. 4862–4872, 2020.

[36] H. Nahas, J. S. Au, T. Ishii, B. Y. S. Yiu, A. J. Y. Chee, and A. C. H. Yu, "A Deep Learning Approach to Resolve Aliasing Artifacts in Ultrasound Color Flow Imaging," *IEEE Trans. Ultrason. Ferroelectr. Freq. Control*, vol. 67, no. 12, pp. 2615–2628, Dec. 2020.

[37] L. J. Krovetz and S. D. Goldbloom, "Frequency Content of Intravascular and Intracardiac Pressures and Their Time Derivatives," *IEEE Trans. Biomed. Eng.*, vol. BME-21, no. 6, pp. 498–501, Nov. 1974.

[38] D. Posada *et al.*, "Staggered Multiple-PRF Ultrafast Color Doppler," *IEEE Trans. Med. Imaging*, vol. 35, no. 6, pp. 1510–1521, Jun. 2016.

[39] A. Ramalli, A. Rodriguez-Molares, J. Avdal, J. D'hooge, and L. Løvstakken, "High-Frame-Rate Color Doppler Echocardiography: A Quantitative Comparison of Different Approaches," *IEEE Trans. Ultrason. Ferroelectr. Freq. Control*, vol. 67, no. 5, pp. 923–933, May 2020.

[40] A. Ramalli *et al.*, "Real-Time High-Frame-Rate Cardiac B-Mode and Tissue Doppler Imaging Based on Multiline Transmission and Multiline Acquisition," *IEEE Trans. Ultrason. Ferroelectr. Freq. Control*, vol. 65, no. 11, pp. 2030–2041, Nov. 2018.

8.2 Critical evaluation of kinetic schemes for coagulation

This appendix includes the article *Critical Evaluation of Kinetic Schemes for Coagulation* by Ranc *et al.* (PLOS ONE, 2023), to which I contributed as co-author. The study, mostly performed during my internship as a 5th year student, compares two widely used kinetic models of thrombin generation, via the intrinsic and extrinsic pathways, against experimental data obtained from thrombin generation assays, including conditions mimicking coagulation factor deficiencies. The study shows that, while standard models can reproduce physiological thrombin formation, modifications are required to extend their validity under pathological conditions. These findings highlight the importance of tailoring coagulation models to the intended application.

PLOS ONE

RESEARCH ARTICLE

Critical evaluation of kinetic schemes for coagulation

Alexandre Ranc[1], Salome Bru[2], Simon Mendez[3], Muriel Giansily-Blaizot[1], Franck Nicoud[3], Rodrigo Méndez Rojano[3]*

1 Department of Haematology Biology, CHU, Univ Montpellier, Montpellier, France, **2** Polytech, Univ Montpellier, Montpellier, France, **3** IMAG, Univ Montpellier, CNRS, Montpellier, France

* fsae.unam.rodrigo@gmail.com

Check for updates

OPEN ACCESS

Citation: Ranc A, Bru S, Mendez S, Giansily-Blaizot M, Nicoud F, Méndez Rojano R (2023) Critical evaluation of kinetic schemes for coagulation. PLoS ONE 18(8): e0290531. https://doi.org/10.1371/journal.pone.0290531

Editor: Gausal Azam Khan, King Faisal University, SAUDI ARABIA

Received: February 14, 2023

Accepted: August 10, 2023

Published: August 28, 2023

Peer Review History: PLOS recognizes the benefits of transparency in the peer review process; therefore, we enable the publication of all of the content of peer review and author responses alongside final, published articles. The editorial history of this article is available here: https://doi.org/10.1371/journal.pone.0290531

Copyright: © 2023 Ranc et al. This is an open access article distributed under the terms of the Creative Commons Attribution License, which permits unrestricted use, distribution, and reproduction in any medium, provided the original author and source are credited.

Data Availability Statement: All experimental and simulation data are available at Github Repository at https://github.com/rodrigomrxvi/CriticalEvaluationCoagulation.

Abstract

Two well-established numerical representations of the coagulation cascade either initiated by the intrinsic system (Chatterjee et al., PLOS Computational Biology 2010) or the extrinsic system (Butenas et al., Journal of Biological Chemistry, 2004) were compared with thrombin generation assays under realistic pathological conditions. Biochemical modifications such as the omission of reactions not relevant to the case studied, the modification of reactions related to factor XI activation and auto-activation, the adaptation of initial conditions to the thrombin assay system, and the adjustment of some of the model parameters were necessary to align in vitro and in silico data. The modified models are able to reproduce thrombin generation for a range of factor XII, XI, and VIII deficiencies, with the coagulation cascade initiated either extrinsically or intrinsically. The results emphasize that when existing models are extrapolated to experimental parameters for which they have not been calibrated, careful adjustments are required.

1 Introduction

In recent decades, numerical modeling of the coagulation cascade has been used to understand the complex dynamics of thrombin formation [1–3], to identify coagulation factor interactions [4], and to investigate the dynamics of thrombus formation in pathological conditions [5, 6].

Such numerical models of the coagulation cascade are usually used to shed light on the mechanisms leading to clotting disorders. Most of these models aim to reproduce the thrombin generation process, which results from the balance between prothrombin conversion and thrombin inactivation [7]. Thrombin generation can be summarized *in vivo* with the following enzymatic steps based on [8]. Tissue factor (TF) is released by damaged vessels or prothrombotic cells including tumor cells, activated mono-nuclear cells, or micro-vesicles. TF forms a complex with activated factor (F) VII (FVIIa) and activates FX either directly or indirectly through FIX. Then, FXa activates the prothrombin into the key thrombin factor. Prothrombin conversion is self-regulated. Thrombin activates FXI and both the co-factors VIII and V of factors IX and X, respectively, creating feedback loops that increase its generation leading to a thrombin burst. In parallel, thrombin cleaves the fibrinogen into fibrin monomers forming an unstable network which is subsequently stabilized by activated FXIII. On the other hand, the

Funding: RMR was supported by Consejo Nacional de Ciencia y Tecnología (CONACyT) (https://conacyt.mx/), Mexico scholarship and the LabEx Numev (convention ANR-10-LABX-20). FN was awarded by the Agence Nationale de la Recherche (ANR) (the French National Research Agency) under the "Investissements d'avenir" programme with the reference ANR-16- IDEX-0006 (https://anr.fr/). The funders had no role in study design, data collection and analysis, decision to publish, or preparation of the manuscript.

Competing interests: The authors have declared that no competing interests exist.

coagulation cascade can also be triggered by the contact activation system as a result of the interactions of FXII, kininogen, and prekallikrein with negatively charged surfaces. This coagulation route, also known as the intrinsic pathway, was historically neglected due to the absence of clinical phenotype in cases of FXII deficiency but has now a renewed interest due to promising anti-FXI and anti-FXII drugs to limit thrombosis in situations where blood meets artificial surfaces of medical devices [9].

Recently, numerical models of the coagulation cascade have been used to shed light on mechanisms leading to clotting disorders. For example, Link *et al.* [10, 11] performed a global sensitivity analysis using the coagulation model of Kuharsky and Fogelson [12] that led to the identification of FV as a key modifier of thrombin generation among patients with hemophilia A. Their results were confirmed later with additional experimental assays highlighting the value of using the numerical model to build a synthetic data set in order to test specific hypotheses. Another examples of modeling coagulation disorders are the studies by Brummel-Ziedins *et al.* [13] who developed a model for FVII deficiency, and that of Anand *et al.* [14], in which the authors examined protein C and antithrombin deficiencies by comparing their results to thrombin generation experiments initiated by the TF-VIIa complex [15]. Models have also been used to study new treatment strategies that would be further assessed *in vitro*. For instance, Burghaus *et al.* [16] and Brummel-Ziedins *et al.* [17] investigated the rivaroxaban effects. Adams *et al.* [18] and recently Zavyalova *et al.* [19] worked on the possible outcomes of direct thrombin inhibitors.

Despite great progress in thrombin formation simulations, a direct comparison between numerical models and *in vitro* experiments is frequently inappropriate since the models are constructed for specific and ideal conditions, as pointed out by Link *et al.* [11, 20]. A great example of this issue is the study by Chelle *et al.* [21] in which five coagulation models are used to predict thrombin formation under relevant clinical scenarios. They found that the predictive capabilities of the models were far from acceptable and needed an additional optimization step using genetic algorithms to adapt kinetic parameters and reproduce *in vitro* data. In particular, they suggested that performing patient-specific optimization is needed to obtain accurate model predictions. However, if each new application requires patient-specific calibration, the global functionality of the model is reduced.

A further challenge of numerical models is related to the uncertainty of input parameters (such as reaction rates and initial concentrations). This uncertainty is linked to lack of experimental standardization when characterizing reaction rate values [20]. Therefore, it is not surprising to find reaction rate values spanning several orders of magnitude for the same coagulation reaction [22]. To avoid this issue, some authors have suggested that instead of trying to find a universal set of reactions, reduced coagulation models are enough to reproduce the coagulation dynamics [7, 23, 24]. Nevertheless, a prior calibration step is still needed.

A strategy to increase the robustness of coagulation models can be to assess the sensitivity of thrombin formation to coagulation factor deficiencies [2, 3, 25–27]. By doing such sensitivity studies, the robustness of the reaction scheme can be tested more deeply, and the reaction rate values can be tuned in a more relevant way, making sure that the final model is not only able to represent one regime, but rather a whole variety of situations. In addition, predicting thrombin kinetics under pathological conditions (like factor deficiencies) is the ultimate goal of most mathematical models.

In the present work, we evaluated two well-established mathematical models of the coagulation cascade from Chatterjee *et al.* [2] for the contact pathway and from Hockin *et al.* [1] and Butenas *et al.* [3] for the TF pathway. Three clotting factor deficiencies were studied to investigate if the models could reproduce the dynamics of thrombin generation. For each model, the results were compared with experimental data using calibrated automated thrombography

(CAT) [28]. A range of decreasing concentrations of the coagulation factor FVIII was considered in order to represent the hemophilia A condition. In addition, deficient FXII and FXI plasmas were used to probe the initiation of the coagulation cascade with the intrinsic pathway, which is of special interest to medical devices. To the best of our knowledge, this is the first time that these models are tested for a range of deficient FXII, FXI and FVIII plasmas. The comparison of numerical and experimental data allowed us to quantify the accuracy of the models, identify limitations, and suggest adjustments that improved the predictive capabilities of the kinetic schemes.

Section 2 describes the thrombography assay and computational simulations. Experimental and simulation results are presented in Section 3.1 for a range of concentrations of FXII, FXI, and FVIII triggered through the intrinsic pathway. Section 3.2 shows the results for the range of FVIII concentrations triggered with TF pathway. Finally, the results and the limitations of our work are commented in Section 4.

2 Materials and methods

2.1 Ethics statement

We obtained approval from the Montpellier University Hospital ethics committee (Comité Local d'Ethique Recherche, agreement number: IRB-MTP_2023_02_202301342). The need for informed consent was waived on the basis that analyses are done on care sample.

2.2 Plasma samples

Samples used to characterize the contact pathway were derived from lyophilized plasmas. To avoid inter-individual physiological variations of clotting factor levels, lyophilized Standard Human Plasma (SHP®) [Siemens Healthcare, Erlangen, France] constituted of industrial pooled citrated platelet poor plasmas (PPP) and obtained from at least one hundred healthy donors was used. Lyophilized factor immunodepleted plasmas were industrial pooled citrated PPP with a qualified specific factor activity lower than 1% [Siemens Healthcare, Erlangen, Germany]. According to manufacturer specifications, donors were pretested for PT, APTT, factor II, V, VII, VIII, IX, X, XI, XII levels, which were all within the normal range. SHP was diluted with lyophilized factor immunodepleted plasmas (FXII, FXI, and FVIII), in order to obtain a range of final concentrations from less than 1% to 100% (100%, 50%, 15%, 5%, 1% and $< 1\%$ treated as 0% from here on). Silica, mixed with rabbit cephalin in STA®-PTT-A®(Stago, Asnières-sur-Seine, France), was used to initiate the intrinsic pathway.

Inherited deficient frozen plasmas were preferred to lyophilized plasmas to assess the TF coagulation pathway because of higher values for the thrombin generation assay (TGA) parameters. Duchemin *et al.* [29] highlighted the same difference between the lyophilized and immunodepleted haemophiliac plasmas. Frozen plasmas used to assess the TF coagulation pathway were derived from a single patient with hemophilia A (Cryopep, Montpellier, France). To obtain a range of FVIII concentrations from less than 1% to 100% (100%, 50%, 15%, 5%, 1% and $< 1\%$), the hemophilia A plasma was picked with increased amounts of "in-house" fresh frozen PPP plasmas from seven anonymous residual plasmas tested for normal PT, APTT and fibrinogen levels. To avoid any residual platelets, two sequential centrifugations were performed at 2250 g at 20 ˚C for 10 minutes. The "in-house" PPP aliquots were stored at -80 ˚C. The TF coagulation pathway was triggered using the PPP-Reagent LOW (Thrombinoscope®BV, Maastricht, The Netherlands) containing a final TF concentration of 1pM. Low concentrations of TF were chosen to obtain a thrombin generation mainly dependent upon feedback activation loops and FVIII and FIX clotting factors [30].

2.3 Calibrated automated measurement of thrombin generation

Thrombin generation was performed in PPP using Fluoroscan Ascent®(FluCa kit, Thrombinoscope®, Synapse BV, Maastrich, The Netherlands), according to the method described by Hemker *et al.* [28] that measures the thrombin generated thanks to a fluorochrome. 80 μL of plasma were mixed with 20 μL of STA®-PTT-A®or PPP reagent LOW, according to the coagulation pathway tested, and 20 μL of fluorescent reagent FluCa kit. The latter contains the calcium chloride which is mandatory to activate the coagulation cascade and the Fluo-Substrate which is a fluorogenic substrate mixed with the FluoBuffer. Fluorescence intensity was detected at wavelengths of 390 nm (excitation filter) and 460 nm (emission filter), every 20 seconds. Each individual sample was analyzed in triplicate simultaneously with a thrombin calibrator as reference for a stable thrombin activity of approximately 600 nM. The calibrator enables the conversion of the fluorescence signal into thrombin concentration. The signal was treated to correct inner filtering effects, such as substrate consumption and abnormal plasma color. Analyses were conducted on Immulon 2HB round-bottom 96-well plates (Stago—Asnières-sur-Seine, France).

The parameters calculated by Thrombinoscope®software included: (i) endogenous thrombin potential (ETP) to evaluate the overall effect on thrombin generation, (ii) the IIa_{max} which corresponds to the largest value of thrombin, (iii) the time to peak (τ_{max}) which is the time required to reach IIa_{max}, and (iv) the lag time (τ_{lag}) required for the generation of 10 nM of thrombin [28]. The physical interpretation of these quantities is provided in Fig 1.

2.4 Kinetic schemes and mathematical modeling

Two coagulation kinetic models were used in the current study. For the sake of simplicity, the models of Chatterjee *et al.* [2] and Butenas *et al.* [3] are named Int and Ext, respectively, making reference to the intrinsic and extrinsic pathways.

The models were implemented in python, to solve each biochemical scheme, a set of differential equations was obtained by applying the law of mass action to the biochemical reactions belonging to each kinetic model. This representation mimics a closed homogeneous reactor in which the only mechanisms that influence the dynamics of coagulation factors are production and consumption (without diffusive or convective transport of species [31]). The system of equations was then computationally solved to obtain the evolution of coagulation factors in time using the initial conditions displayed in Table 1. Initial conditions were computed from the dilutions used in TGA assays. The nominal initial conditions used in the study were derived accounting for the dilution steps of the calibrated automated thrombinography.

The Int model was published in 2010 and describes the coagulation triggered by the contact pathway [2]. It was built upon the existing model of Hockin *et al.* [1] with additions concerning the contact pathway reactions. The model is triggered by contact activation of factor XII. Since factor immunodepleted plasmas were collected without corn trypsin inhibitor (CTI), the reaction 35 that describes the inhibition of factor XIIa by CTI in Chatterjee *et al.* [2] was suppressed. Moreover, since the thrombin generation is the basis of the analysis performed in the present study, fibrin-related reactions (# 50 to 57 from [2]) were deleted to save computing time without interfering with the thrombin generation. The Ext model was described in the literature by Hockin *et al.* [1] and upgraded in 2004 by Butenas *et al.* [3] with a supplementary reaction that describes the activation of factor X by the activated factor IX (IXa).

The Int and Ext models were modified to align some reactions and kinetic schemes to the studied physiological conditions. The modified formulations were compared with the original numerical models and experimental data from TGA. The rationale for each specific

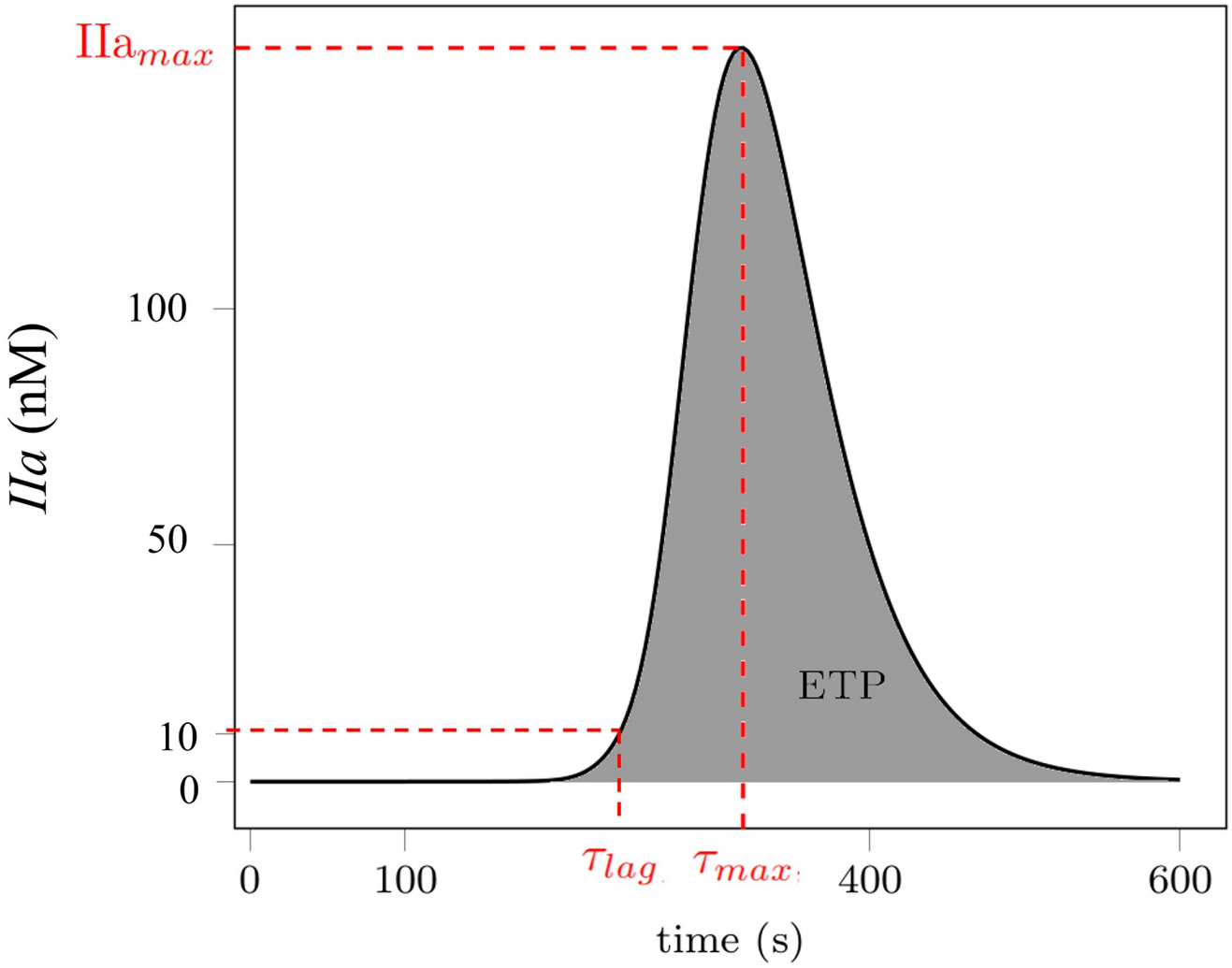


Fig 1. Variables used for *in vitro* and *in silico* comparison: IIa_{max} (peak thrombin concentration), τ_{max} (time to peak), τ_{lag} (time to reach 10 nM of thrombin) and ETP (endogenous thrombin potential) for a thrombin formation curve in time.

https://doi.org/10.1371/journal.pone.0290531.g001

modification is discussed in Section 3. Both the original and modified kinetic schemes used are listed in the S1 Text.

2.5 *In vitro* vs *in silico* comparison

To establish a comprehensive comparison between the *in silico* and *in vitro* results, the ETP, IIa_{max} and τ_{max} variables were considered (see Fig 1). Relative values were computed considering the physiological production of thrombin in PPP as a reference. In the case of Figs 3 and 7, these values are used in order to evaluate the general trend for the different concentrations rather than comparisons using the absolute values.

3 Results

3.1 Int model for the contact pathway

TGA experiments and simulations using the original Int model were conducted over a range of decreasing concentrations of FXII, FXI, and FVIII. Fig 2 shows the simulation results and

Table 1. Initial conditions of Int and Ext models, derived from thrombin generation assay dilution. * TF nominal value, see Section 3.2.

Factor	Int Model Initial Concentrations [nM]	Ext Model Initial Concentration [nM]
VII	6.67	6.67
VII_a	0.0667	0.0667
X	106.67	106.67
IX	60.0	60.0
II	933.0	933.0
VIII	0.4667	0.4667
V	13.33	13.33
TFPI	1.667	1.667
AT	2267.0	2267.0
XII	226.7	NA
PK	300.0	NA
$C1_{INH}$	1667.0	NA
α_1AT	30000.0	NA
α_2AP	667.0	NA
XI	20.67	NA
TF*	NA	0.001

https://doi.org/10.1371/journal.pone.0290531.t001

experimental TGA data for plasma with 100%, 15%, and 0% for FXII, FXI and FVIII. Four main discrepancies are observed:

- Numerical data at a concentration of 100% show a delay and steeper rise in thrombin formation compared to experimental data.
- When the concentration is less than 100%, the original model cannot capture the trend observed experimentally.

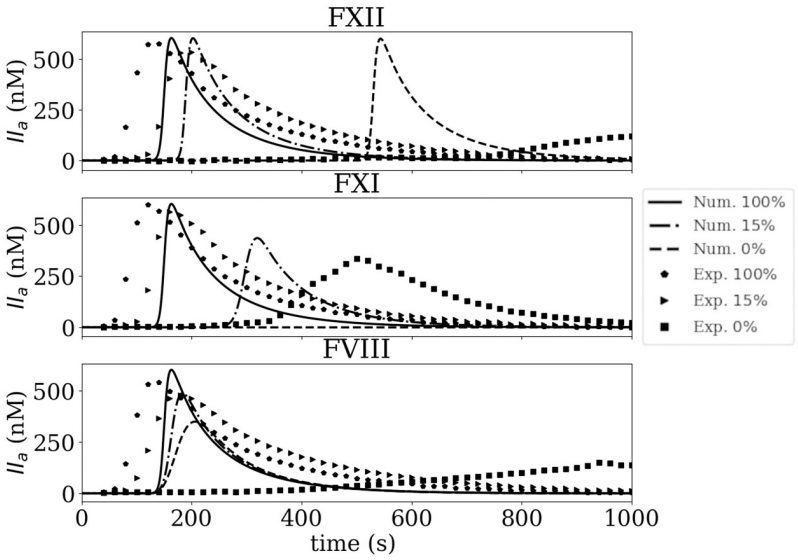


Fig 2. Experimental thrombin formation (from thrombin generation assay) and simulated thrombin formation using the original Int model for FXII, FXI and FVIII at 100%, 15%, and 0%.

https://doi.org/10.1371/journal.pone.0290531.g002

- In the simulations with 0% of FXII the coagulation cascade should not start at all, but the model predicts thrombin generation.
- For the low concentration of FVIII (0%) simulated thrombin production is significantly larger than experimental data.

Fig 3 shows the evolution of relative ETP, IIa_{max} and τ_{max} values for all the FXI, FXII, and FVIII concentrations: 0, 1, 5, 15, 50, and 100%. The original and modified numerical model results are shown along with the experimental data. It can be observed that for the FXI case both ETP and IIa_{max} values predicted by the original model show a descending trend steeper than the experimental data. In terms of τ_{max}, the values computed by the original model are significantly larger than the experimental data. Looking at FXII, the τ_{max} trend is better captured by the original model, however, ETP and IIa_{max} values do not follow the same trend observed experimentally for low concentrations of FXII. In addition, undesired thrombin production is observed for FXII 0% concentration. It is worth saying that *in vitro* thrombin formation for FXII and FXI at 0% cases can be explained by the presence of residual amounts of coagulation factors in the respective immunodepleted plasmas, however, this should not happen numerically. The ETP and IIa_{max} values computed by the original model for FVIII concentrations follow a similar trend as the experimental data, nonetheless, the increased τ_{max} values observed experimentally for decreasing concentrations of factor VIII are not observed at the same level in the simulation using the original model. The modifications made to improve the model are discussed below.

First, *in silico* thrombin formation for FXII the 0% concentration should not take place since factor FXII activation is the starting point of the coagulation case. The reason for normal, yet delayed, thrombin production at 0% concentration relies on the activation of FX and FIX by activated FVII (FVIIa), independently of TF, by reactions:

$$VIIa + IX \leftrightarrow VIIa = IX \rightarrow VIIa + IXa \tag{1}$$

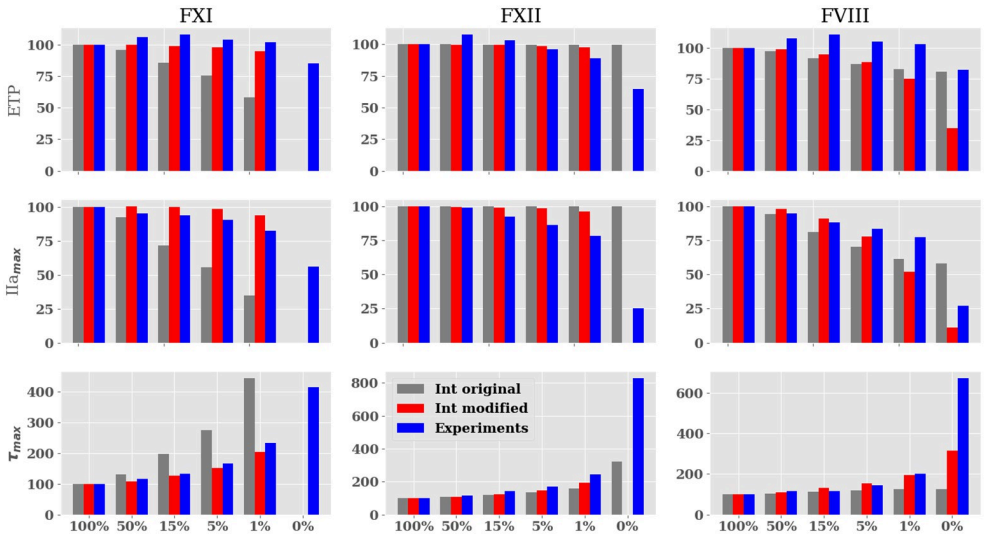


Fig 3. Evolution of the different parameters (%) for each factor concentration range (%) after contact activation. GRAY BAR *In silico* Thrombin Generation obtained by Int original; RED BAR obtained by Int modified; BLUE BAR experimental results. In the 0% experimental case for FXII and FXI thrombin is produced since residual amounts of coagulation factors are still present in plasma.

https://doi.org/10.1371/journal.pone.0290531.g003

$$VIIa + X \leftrightarrow VIIa = X \rightarrow VIIa + Xa \quad (2)$$

This mechanism was originally proposed by Komiyama *et al.* [32] and incorporated in the Int model. Komiyama *et al.* used 1% of the total FVII concentration in its activated state in order to trigger the reactions and characterize the kinetic rates. The trouble with this rationale is that there are at least three forms of FVII: (i) FVII zymogen, (ii) zymogen-like FVII which corresponds to the 1% circulating activated free form of FVII and (iii) activated FVII which is either bound to TF under physiological conditions or unbound in therapeutic contexts corresponding to the recombinant FVIIa (Novoseven®, Novo Nordisk A/S, Danemark). Reactions (1) and (2) do not reflect physiological mechanisms in the absence of circulating TF, but describe the non-physiological recombinant FVIIa (Novoseven®) interactions [32]. Therefore, both reactions (1) and (2) were deleted in the original and modified Int models. Fig 3 shows that by omitting these reactions, simulated thrombin formation at the 0% FXII case is suppressed.

The activation of FXII due to STA®-PTT-A®reagent was set to $k_1 = 5 \times 10^3$. Since the original value of Chatterjee *et al.* [2] was fitted to their experimental data, therefore, it is not universal for FXII contact activation. This arbitrary increase of the kinetic rate was motivated to reduce the τ_{max} value which as shown in Fig 2 lags the experimental data.

$$XII \longrightarrow XIIa \quad (3)$$

The third major modification to the Int model is related to FXI activation mechanisms. In the original model, FXI is activated by FXIIa, thrombin and an auto-activation process, respectively:

$$XIIa + XI \leftrightarrow XIIa = XI \rightarrow XIIa + XIa \quad (4)$$

$$XI + IIa \leftrightarrow XI = IIa \rightarrow XIa + IIa \quad (5)$$

$$XIa + XI \leftrightarrow XIa = XI \rightarrow XIa + XIa \quad (6)$$

In vitro FXI activation by thrombin is mainly reported with circulated platelets [33] and inhibited by fibrinogen [34]. As TGA experiments were performed on platelet poor plasma (PPP), reaction (5) was deleted from the model. The work of Gailani and Bronze [34] is referenced in the original Int model for reaction (4). Gailani and Bronze [34] stated that the kinetic constants were not determined with precision because it exceeded the achievable factor concentration. Thus, the kinetic constants involved in FXI activation by FXIIa were modified to improve the fit with experimental data ($K_1 = 7 \times 10^8$ M^{-1} s^{-1}, $K_{-1} = 200$ s^{-1} $k_{cat} = 0.002$ s^{-1}). With the same rationale, the kinetic constant of reaction (6) describing the FXI auto-activation was reduced to an optimal value of $K_1 = 0.7975 \times 10^6$ M^{-1} s^{-1} 4-fold lower than the value reported by Kramoroff *et al.* [33].

Additional modifications were done regarding the cofactor function of FVIIIa. *In silico* thrombin generation parameters showed a larger pro-coagulant profile compared to *in vitro* data, especially for concentrations of FVIII under 1% (see Figs 2 and 4), suggesting that the numerical model overestimated the enzymatic activity of FIXa controlled by reactions (7) and

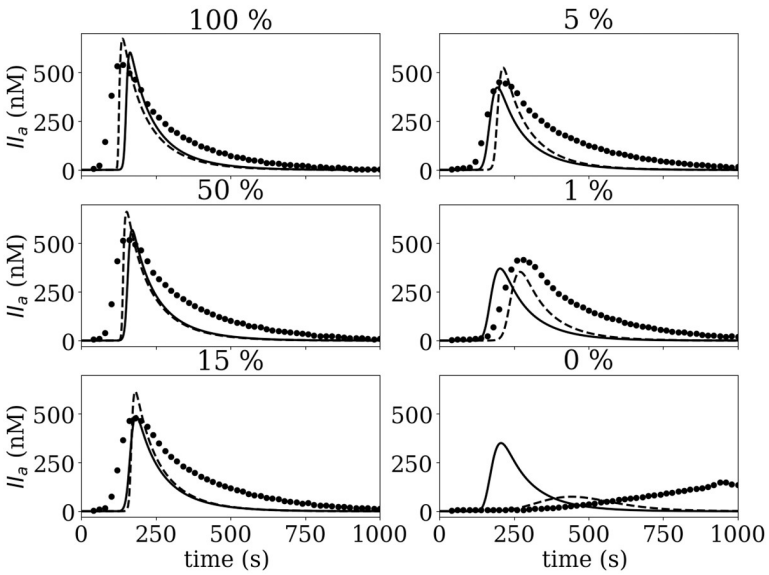


Fig 4. Thrombin generation (TG) for FVIII concentration range after contact activation the solid line - is the *in silico* data obtained by Int original; the dashed line - - is obtained by Int modified, and • is the experimental data.

https://doi.org/10.1371/journal.pone.0290531.g004

(8).

$$IXa = VIIIa + X \leftrightarrow IXa = VIIIa = X \rightarrow IXa = VIIIa + Xa \tag{7}$$

$$IXa + X \leftrightarrow IXa = X \rightarrow IXa + Xa \tag{8}$$

The kinetic constants of reaction (7) and (8) were modified to decrease the activation of the FX by the unbound FIXa and the intrinsic tenase complex FIXa-FVIIIa. The kinetic constants were obtained from Kogan *et al.* [35] who characterized this reaction focusing on the contact system. The aforementioned modifications improved the numerical model predictions of ETP, IIa_{max}, and τ_{max} for the three ranges of coagulation factors concentrations as observed in Fig 3. The only cases in which modifications reduced the accuracy of the numerical model were the ETP and IIa_{max} values for FVIII. To understand better the underlying behavior in the FVIII case, thrombin production is presented in Fig 4. Fig 4 shows the thrombin production curves for the TGA experiment, Int original, and Int modified simulations. A reduction of the pro-coagulant profile can be observed in the modified data, especially for the 1 and 0% cases. In addition, τ_{max} has been increased following the trend observed experimentally. The thrombin formation trend for the modified model appears to have a better agreement with experimental data suggesting that the discrepancy observed in ETP and IIa_{max} values of Fig 3 are not indicative of the actual thrombin formation dynamics at low concentrations.

3.2 Ext model for the TF pathway

Fig 5 compares the original Ext model thrombin formation to experimental TGA considering physiological plasma. The simulation results show a delayed and reduced thrombin formation compared to the experimental data. This is in line with other numerical studies [21] which reported a thrombin peak formation after 1600 seconds for a physiological plasma sample. In contrast, our experimental TGA thrombin formation peaks around 550 seconds.

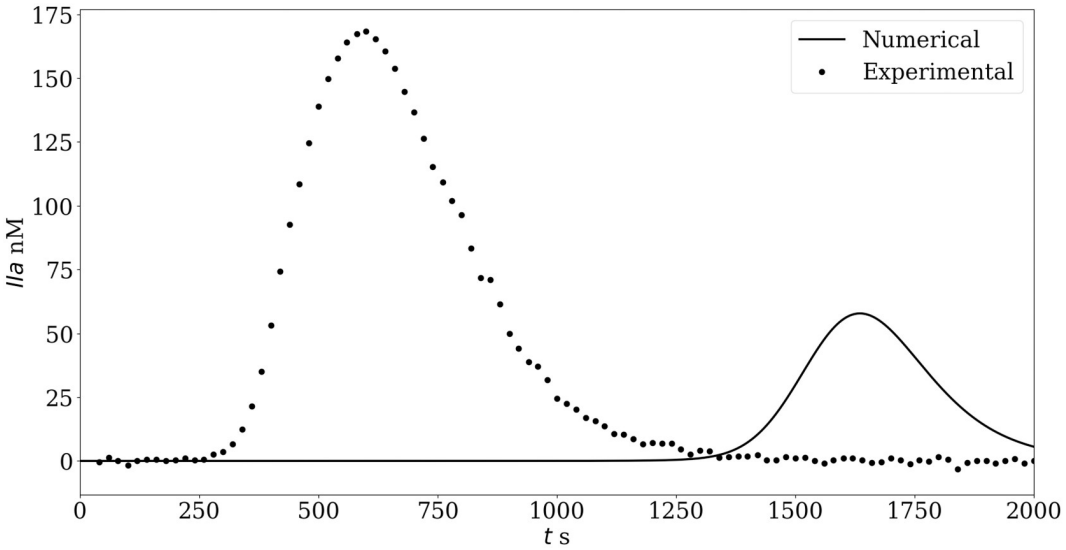


Fig 5. Thrombin formation in a physiological plasma sample. The original Ext model shows a low and delayed thrombin generation.

https://doi.org/10.1371/journal.pone.0290531.g005

A possible explanation for this observation is that the FVIIa-TF complex formation is independent of calcium concentration and may occur *in vitro* during the TGA pre-incubation phase [36]. In that case, at the beginning of the experimental TGA, the calcium can immediately lead to the activation of FX through the FVIIa-TF complex. To verify this hypothesis, the FVIIa-TF complex concentration was changed *in silico*, modifying the initial concentrations of FVIIa-TF and TF from 0 pM/1 pM to 1 pM/0 pM in both in-silico models. The former values correspond to the nominal value (see Table 1) while the latter correspond to the case where all the TF available has been consumed to form the FVIIa-TF complex before the injection of Calcium at the start of the experiment.

Thrombin formation curves for the original and modified Ext models, as well as experimental TGA data, are displayed in Fig 6 for a range of FVIII concentrations. Remarkable agreement between the numerical and experimental data is observed when the initial value of the FVIIa-TF complex was set to 1 pM.

Fig 7 shows the relative values of ETP, IIa_{max}, and τ_{max} for the original model setting the concentration of FVIIa-TF complex to 1pM, the modified Ext model and experimental data. Note that the agreement between the original model with FVIIa-TF = 1 pM and the experimental values is not good for very small FVIII concentrations ($\leq$ 1%). This observation could be explained by an overestimation of FVIII activity in the Ext model. To explore this hypothesis and improve the activity of the uncomplexed FIXa, the kinetic constants of Eq (8) were modified. An arbitrarily 60 fold increase of the catalytic constant (Kcat = 4.8×10^{-2} s^{-1} instead of Kcat = 8.0×10^{-4} s^{-1} from [3]). The modified Ext model improved the results remarkably for ETP, IIa_{max} and τ_{max} variables for the 5, 1, and 0% concentrations. Table 2 summarizes the problems identified to the Int and Ext models and the changes that were introduced.

4 Discussion

Numerical models of the coagulation cascade are capable of capturing complex thrombin formation dynamics under physiological conditions. However, more work is needed to improve

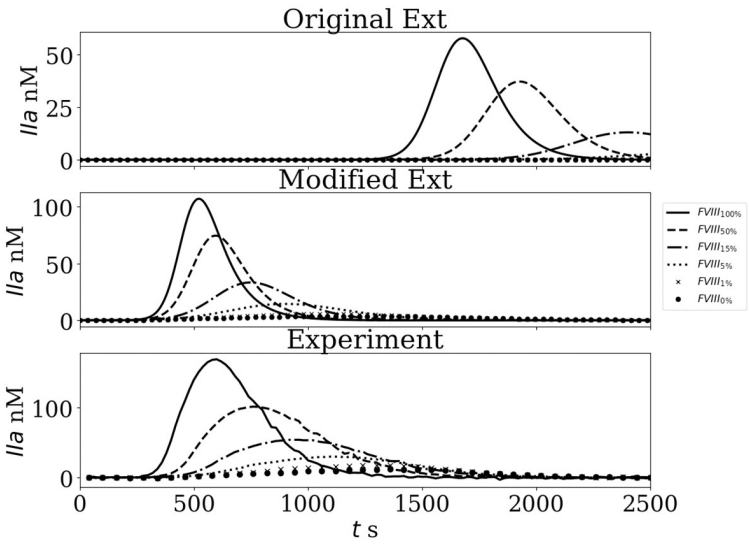


Fig 6. Thrombin generation (TG) for FVIII concentration range after TF activation A: *In silico* TG obtained by the original Ext; B: Obtained by modified Ext; C: Experimental curves.

https://doi.org/10.1371/journal.pone.0290531.g006

their reproducibility and their applicability in different clinical scenarios, as highlighted in the recent review by Chung et al. [38]. In the current work, two well known models of the coagulation cascade were compared with TGA experimental results and proper modifications are suggested to improve their accuracy. The modifications of the Int model for the contact phase are related to excluding reactions that produce spurious delayed thrombin formation due to FVIIa

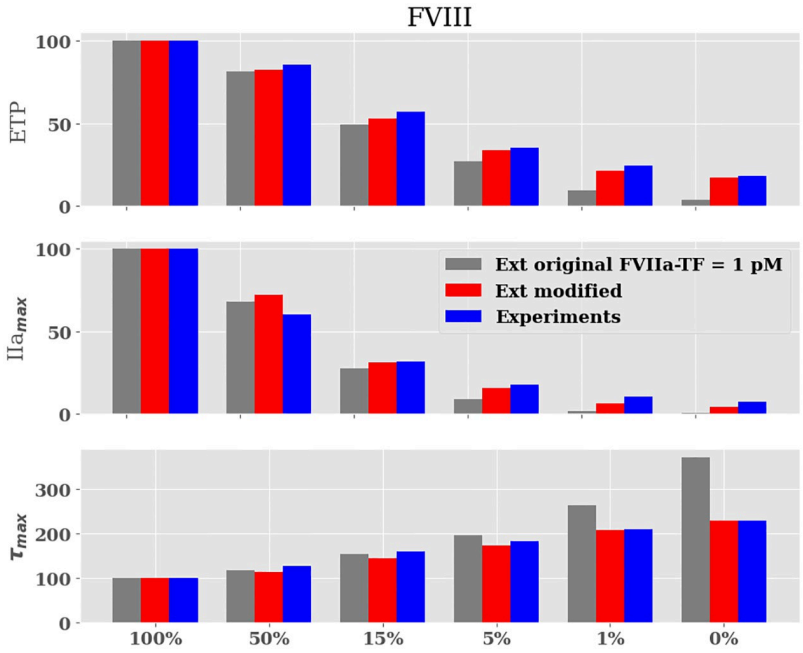


Fig 7. Evolution of the endogenous thrombin potential (ETP). GRAY BAR *In silico* ETP obtained by the original Ext model with the initial concentration FVIIa-TF complex = 1pM; RED BAR obtained by modified Ext model; BLUE BAR experimental results.

https://doi.org/10.1371/journal.pone.0290531.g007

Table 2. Modifications performed for Int and Ext models.

Model	Problems	Changes made
Chatterjee *et al.* [2]	• Thrombin generation despite the absence of FXII and FXI • *In-silico* τ_{max} longer than experimental data • Important thrombin generation decrease when the different FXI rates studied • Excessive thrombin generation for low FVIII concentrations	• reactions (2) and (1) were deleted: VIIa+IX↔VIIa = IX→VIIa+IXa VIIa+X↔VIIa = X→VIIa+Xa • Activation of FXII by reagent *XII* → *XIIa* ($k_1 = 5 \times 10^{-4}$ to $k_1 = 5 \times 10^{-3}$) • reaction (5) was deleted and kinetic constants of reactions (4) and (6) were modified XI+IIa↔XI = IIa→XIa+IIa (deleted) XIIa+XI↔XIIa = XI→XIIa+XIa; ($K_1 = 7 \times 10^8 M^{-1}s^{-1}$, $K_{-1} = 200s^{-1}k_{cat} = 0.002\ s^{-1}$) XIa+XI↔XIa = XI→XIa+XIa; ($K_1 = 0.7975 \times 10^6\ M^{-1}\ s^{-1}$) • kinetic constants for reactions (7) and (8) reactions were modified following [35, 37] IXa = VIIIa + X→IXa = VIIIa+Xa; ($K_M = 0.19 \times 10^{-6}$ M, $k_{cat} = 29\ s^{-1}$) IXa+X→IXa+Xa; ($K_M = 2 \times 10^{-6}$ M, $k_{cat} = 0.000667\ s^{-1}$)
Butenas *et al.* [3]	• Deficient thrombin generation for low FVIII rate (< 5%) • Delayed thrombin formation due to preincubation of TF-FVIIa	• Kcat = 4,8 × 10^{-2} s^{-1} for reaction: IXa + X → Xa + IXa • Initial value of the FVIIa-TF complex was set to 1 pM

https://doi.org/10.1371/journal.pone.0290531.t002

activation in the absence of TF. In addition, FXI activation by thrombin was not considered since platelet poor plasma was used in our study. Then, kinetic constants involved in FXI auto-activation and activation by XIIa were fitted to improve the comparison with TGA results. Another modification regarding excessive procoagulant activity by FVIIIa is proposed to reduce the activation of FX by unbounded FIXa and IXa = VIIIa. As pointed outby Kramoroff et al. [33] and Gailani & Broze [34] the values of the kinetic rates are not precise and thus are susceptible to change. COmpared to the existing Ext model, the main modification consisted in introducing 1 pM initial concentration of FVIIa-TF, which is motivated by the formation of complex FVIIa-TF during the incubation phase of the TGA experiment. This adjustment allowed to shorten the delay of thrombin formation. Lakshmanan *et al.* [39] recently described the same problem of delayed thrombin formation in simulations when compared to experimental data. In their study, the issue was overcome by proposing a feedback activation of FXI and a calibration step of kinetic constants. The delayed thrombin formation was also observed in the study of Pisaryuk et al. [40] in which the original Hockin's model is used to develop a numerical tool to assess individual pharmacokinetic profiles of anticoagulant therapy. Their work showed that simulations differ from the experimental data in terms of lag time and amplitude of the thrombin peak. The authors assumed that these discrepancies were minimal, as the differences were smaller than 15%.

In the current work, the modification on the Int and Ext models improved the comparison for ETP, IIa_{max} and τ_{max} overall. In the 100% 'nominal' case, the predictions of the original model are fairly good. However, under pathological conditions of FXII, FXI and FVIII deficiencies, the modifications proposed substantially improved the comparison with the experiments and prevented artificial thrombin formation for the 0% concentration cases. Nevertheless, in the case of FVIII (< 1%) triggered via the Intrinsic pathway, both the original and modified Int models fail to reproduce the ETP, IIa_{max} and τ_{max}. Therefore, improvements to the model should be further considered when looking at patients with severe hemophilia conditions.

The role of factor XI in the coagulation cascade is not yet fully understood. Initially set aside in favor of FVIII and FIX, FXI and the contact phase are increasingly taken into consideration following the work of Renné *et al.* in FXII-deficient mice [41] and the search for anti-

XI and anti-XII anticoagulants [42–44], which would be less hemorrhagic than those currently available. In the coagulation models, FXI is not present in the model of Hockin *et al.* The addition of factor XI, and associated reactions as done by Chatterjee *et al.* [2] induces excessive thrombin generation. Lakshmanan *et al.* [39] made the same observation and presented results closer to the assays for low concentrations of tissue factor (0.125 μM and 0.25 μM) by including a feedback activation mechanism of FXI. Nevertheless, the role of FXII is not included in their model, and thus cannot be used in bio-material applications. Chen and Diamond [45] developed a reduced order model to evaluate the role of FXIa and fibrinogen in thrombin and fibrin formation in an open system considering flow transport (both diffusion and convection). They highlighted the thrombin-feedback activation of FXIa in thrombin formation pointing out again an important role of FXI in the coagulation cascade. As shown in the current work, the model of Hockin *et al.* responds well to FVIII deficiency. However, due to the lack of modeling regarding FXI activity, the results can be misleading, as pointed out by previous studies and the current results.

The proposed modifications to the Int and Ext models are not universal (as shown in reaction 8 with different values for Int and Ext models) but are well suited for the TGA experimental conditions studied. Thus, they can be used as a valuable tool to explore any scenario that might be costly experimentally. Since the coagulation model still has limitations linked to modeling assumptions, one should be careful when extrapolating the models to open system applications such as thrombosis simulations of medical devices or organ scale studies. Considering the complexity of kinetic schemes of the coagulation cascade, the authors recommend close collaboration between hematologists and modelers when applying coagulation models. Continuous validation of coagulation models in complex situations such as pathological cases is needed in order to broaden their application scope. This remains a necessary effort towards robust and reliable coagulation models that could be used to study coagulation disorders and in drug or bio-medical devices development.

Supporting information

S1 Text. Coagulation reaction schemes used in the original and modified models.
(PDF)

Acknowledgments

The authors would like to thank Prof. Jean-François Schved for his insightful comments.

Author Contributions

Conceptualization: Alexandre Ranc, Muriel Giansily-Blaizot, Franck Nicoud, Rodrigo Méndez Rojano.

Data curation: Alexandre Ranc, Salome Bru, Rodrigo Méndez Rojano.

Formal analysis: Alexandre Ranc, Simon Mendez, Muriel Giansily-Blaizot, Rodrigo Méndez Rojano.

Funding acquisition: Franck Nicoud, Rodrigo Méndez Rojano.

Investigation: Alexandre Ranc, Franck Nicoud.

Methodology: Alexandre Ranc, Franck Nicoud.

Project administration: Simon Mendez.

Resources: Simon Mendez, Muriel Giansily-Blaizot, Franck Nicoud.

Software: Alexandre Ranc, Simon Mendez, Franck Nicoud, Rodrigo Méndez Rojano.

Supervision: Simon Mendez, Muriel Giansily-Blaizot, Franck Nicoud, Rodrigo Méndez Rojano.

Validation: Alexandre Ranc, Salome Bru, Rodrigo Méndez Rojano.

Visualization: Salome Bru, Rodrigo Méndez Rojano.

Writing – original draft: Alexandre Ranc, Rodrigo Méndez Rojano.

Writing – review & editing: Simon Mendez, Muriel Giansily-Blaizot, Franck Nicoud, Rodrigo Méndez Rojano.

References

1. Hockin MF, Jones KC, Everse SJ, Mann KG. model for the stoichiometric regulation of blood coagulation. Journal of Biological Chemistry. 2002; 277(21):18322–18333. https://doi.org/10.1074/jbc.M201173200 PMID: 11893748
2. Chatterjee MS, Denney WS, Jing H, Diamond SL. Systems biology of coagulation initiation: Kinetics of thrombin generation in resting and activated human blood. PLoS Computational Biology. 2010; 6(9): e1000950. https://doi.org/10.1371/journal.pcbi.1000950 PMID: 20941387
3. Butenas S, Orfeo T, Gissel MT, Brummel KE, Mann KG. The significance of circulating factor IXa in blood. Journal of Biological Chemistry. 2004; 279(22):22875–22882. https://doi.org/10.1074/jbc.M400531200 PMID: 15039440
4. Mann KG. Is there value in kinetic modeling of thrombin generation? Yes. Journal of Thrombosis and Haemostasis. 2012; 10(8):1463–1469. https://doi.org/10.1111/j.1538-7836.2012.04799.x PMID: 22642417
5. Biasetti J, Spazzini PG, Swedenborg J, Gasser C. An integrated fluid-chemical model toward modeling the formation of intra-luminal thrombus in abdominal aortic aneurysms. Frontiers in Physiology. 2012; 3 (266):1–16. https://doi.org/10.3389/fphys.2012.00266 PMID: 22934022
6. Seo JH, Abd T, George RT, Mittal R. coupled chemo-fluidic computational model for thrombogenesis in infarcted left ventricles. American Journal of Physiology—Heart and Circulatory Physiology. 2016; 310 (11):H1567–H1582. https://doi.org/10.1152/ajpheart.00855.2015 PMID: 27016582
7. Hemker HC, Kerdelo S, K RMW. Is there value in kinetic modeling of thrombin generation? No (unless. . .). Journal of Thrombosis and Haemostasis. 2012; 10(8):1470–1477. https://doi.org/10.1111/j.1538-7836.2012.04802.x PMID: 22650179
8. Hoffbrand AV, DP S. Essential Haematology. vol. 1. 6th ed. Wiley-Blackwell; 2011.
9. Srivastava P, Gailani D. The rebirth of the contact pathway: a new therapeutic target. Current opinion in hematology. 2020; 27(5):311–319. https://doi.org/10.1097/MOH.0000000000000603 PMID: 32740037
10. Link KG, Stobb MT, Sorrells MG, Bortot M, Ruegg K, Manco-Johnson MJ, et al. A mathematical model of coagulation under flow identifies factor V as a modifier of thrombin generation in hemophilia A. Journal of Thrombosis and Haemostasis. 2020; 18(2):306–317. https://doi.org/10.1111/jth.14653 PMID: 31562694
11. Link KG, Stobb MT, Monroe DM, Fogelson AL, Neeves KB, Sindi SSea. Computationally Driven Discovery in Coagulation. Arteriosclerosis, Thrombosis, and Vascular Biology. 2021; 41(1):79–86. https://doi.org/10.1161/ATVBAHA.120.314648 PMID: 33115272
12. Kuharsky AL, F AL. Surface-mediated control of blood coagulation: the role of binding site densities and platelet deposition. Biophysical Journal. 2001; 80(3):1050–1074. https://doi.org/10.1016/S0006-3495(01)76085-7 PMID: 11222273
13. Brummel Ziedins K, Rivard GE, Pouliot RL, Butenas S, Gissel M, Parhami-Seren B, et al. Factor VIIa replacement therapy in factor VII deficiency. Journal of Thrombosis and Haemostasis. 2004; 2 (10):1735–1744. https://doi.org/10.1111/j.1538-7836.2004.00922.x PMID: 15456484
14. Anand M, Rajagopal K, Rajagopal KR. A model for the formation, growth, and lysis of clots in quiescent plasma. A comparison between the effects of antithrombin III deficiency and protein C deficiency. Journal of Theoretical Biology. 2008; 253(4):725–738. https://doi.org/10.1016/j.jtbi.2008.04.015 PMID: 18539301

15. Butenas S, van't Veer C, KG M. 'Normal' thrombin generation. Blood. 1999; 94(7):2169–2178. https://doi.org/10.1182/blood.V94.7.2169.419k22_2169_2178 PMID: 10498586

16. Burghaus R, Coboeken K, Gaub T, Kuepfer L, Sensse A, Siegmund HUea. Evaluation of the efficacy and safety of rivaroxaban using a computer model for blood coagulation. PLoS ONE. 2011; 4(8):e6669. https://doi.org/10.1371/journal.pone.0017626 PMID: 21526168

17. Brummel-Ziedins K. Models for thrombin generation and risk of disease. Journal of Thrombosis and Haemostasis. 2013; 11(s1):212–223. https://doi.org/10.1111/jth.12256 PMID: 23809125

18. Adams TE, Everse SJ, M KG. Predicting the pharmacology of thrombin inhibitors. Journal of Thrombosis and Haemostasis. 2003; 1(5):1024–1027. https://doi.org/10.1046/j.1538-7836.2003.00127.x PMID: 12871372

19. Zavyalova EG, Ustinov NB, K AM. Exploring the efficiency of thrombin inhibitors with a quantitative model of the coagulation cascade. FEBS Letters. 2020; 594(6):995–1004. https://doi.org/10.1002/1873-3468.13684 PMID: 31736051

20. Link KG, Stobb MT, Di Paola J, Neeves KB, Fogelson AL, Sindi SSea. A local and global sensitivity analysis of a mathematical model of coagulation and platelet deposition under flow. PLoS One. 2018; 13(7):1–38. https://doi.org/10.1371/journal.pone.0200917 PMID: 30048479

21. Chelle P, Morin C, Montmartin A, Piot M, Cournil M, TP B. Evaluation and Calibration of In Silico Models of Thrombin Generation Using Experimental Data from Healthy and Haemophilic Subjects. Bulletin of Mathematical Biology. 2018; 80(8):1989–2025. https://doi.org/10.1007/s11538-018-0440-4 PMID: 29948884

22. Belyaev AV, Dunster JL, Gibbins JM, Panteleev MA, V V. Modeling thrombosis in silico: Frontiers, challenges, unresolved problems and milestones. Physics of Life Reviews. 2018; 26-27:57–95. https://doi.org/10.1016/j.plrev.2018.02.005 PMID: 29550179

23. Ratto N, Tokarev A, Chelle P, Tardy-Poncet B, Volpert V. Clustering of Thrombin Generation Test Data Using a Reduced Mathematical Model of Blood Coagulation. Acta Biotheoretica. 2020; 68(1):21–43. https://doi.org/10.1007/s10441-019-09372-w PMID: 31853681

24. Ratto N, Bouchnita A, Chelle P, Marion M, Panteleev M, Nechipurenko D, et al. Patient-Specific Modelling of Blood Coagulation. Bulletin of Mathematical Biology. 2021; 83(50):1–31. https://doi.org/10.1007/s11538-021-00890-8 PMID: 33772645

25. Danforth CM, Orfeo T, Everse SJ, Mann KG, BZ KE. Defining the Boundaries of Normal Thrombin Generation: Investigations into Hemostasis. PLoS One. 2012; 7(2):e30385. https://doi.org/10.1371/journal.pone.0030385 PMID: 22319567

26. Susree M, Anand M. Importance of Initial Concentration of Factor VIII in a Mechanistic Model of In Vitro Coagulation. Acta Biotheoretica. 2018; 66(3):201–212. https://doi.org/10.1007/s10441-018-9329-8 PMID: 29761301

27. Luan D, Zai M, V JD. Computationally Derived Points of Fragility of a Human Cascade Are Consistent with Current Therapeutic Strategies. PLoS Computational Biology. 2007; 3(7):1347–1359. https://doi.org/10.1371/journal.pcbi.0030142 PMID: 17658944

28. Hemker HC, Giesen P, Al Dieri R, Regnault V, De Smedt E, Wagenvoord Rea. Calibrated automated thrombin generation measurement in clotting plasma. Pathophysiology of Haemostasis and Thrombosis. 2003; 33(1):4–15. https://doi.org/10.1159/000071636 PMID: 12853707

29. Duchemin J, Pan-Petesch B, Arnaud B, Blouch MT, A JF. Influence of coagulation factors and tissue factor concentration on the thrombin generation test in plasma. Thrombosis and Haemostasis. 2008; 99(4):767–773. https://doi.org/10.1160/TH07-09-0581 PMID: 18392335

30. Dargaud Y, Béguin S, Lienhart A. Al Dieri R, Trzeciak C, Bordet JC, et al. Evaluation of thrombin generating capacity in plasma from patients with haemophilia A and B. Thrombosis and Haemostasis. 2005; 93(3):475–480. https://doi.org/10.1160/TH04-10-0706 PMID: 15735797

31. Fogelson AL, N KB. Fluid Mechanics of Blood Clot Formation. Annual Review of Fluid Mechanics. 2015; 47(1):377–403. https://doi.org/10.1146/annurev-fluid-010814-014513 PMID: 26236058

32. Komiyama Y, Pedersen AH, Kisiel W. Proteolytic Activation of Human Factors IX and X by Recombinant Human Factor VIIa: Effects of Calcium, Phospholipids, and Tissue Factor. Biochemistry. 1990; 29(40):9418–9425. https://doi.org/10.1021/bi00492a016 PMID: 2248955

33. Kramoroff A, N JM. In vitro factor XI activation mechanism according to an optimized model of activated partial thromboplastin time test. Blood Coagulation and Fibrinolysis. 2001; 12(4):289–299. https://doi.org/10.1097/00001721-200106000-00010 PMID: 11460013

34. Gailani D, B GJ. Factor XI activation in a revised model of blood coagulation. Science. 1991; 253(5022):909–912. https://doi.org/10.1126/science.1652157 PMID: 1652157

35. Kogan AE, Kardakov DV, K MA. Analysis of the activated partial thromboplastin time test using mathematical modeling. Thrombosis Research. 2001; 101(4):299–310. https://doi.org/10.1016/S0049-3848(00)00405-9 PMID: 11248291

36. Ruf W, Kalnik MW, Lund-Hansen T, TS E. Characterization of factor VIII association with tissue factor in solution: High and low affinity calcium binding sites in factor VII contribute to functionally distinct interactions. Journal of Biological Chemistry. 1991; 266(24):15719–15725. https://doi.org/10.1016/S0021-9258(18)98469-3 PMID: 1874730

37. Rawala-Sheikh R, Ahmad SS, Ashby B, W PN. Kinetics of Coagulation Factor X Activation by Platelet-Bound Factor IXa. Biochemistry. 1990; 29(10):2606–2611. https://doi.org/10.1021/bi00462a025 PMID: 2110473

38. Chung D, Bakshi S, van der Graaf PH. A Review of Quantitative Systems Pharmacology Models of the Coagulation Cascade: Opportunities for Improved Usability. Pharmaceutics. 2023; 15(3):918. https://doi.org/10.3390/pharmaceutics15030918

39. Lakshmanan HHS, Estonilo A, Reitsma SE, Melrose AR, Subramanian J, Zheng TJ, et al. Revised model of the tissue factor pathway of thrombin generation: Role of the feedback activation of FXI. Journal of Thrombosis and Haemostasis. 2022; 20(6):1350–1363. https://doi.org/10.1111/jth.15716 PMID: 35352494

40. Pisaryuk AS, Povalyaev NM, Poletaev AV, Shibeko AM. Systems Biology Approach for Personalized Hemostasis Correction. Journal of Personalized Medicine. 2022; 12(11). https://doi.org/10.3390/jpm12111903 PMID: 36422079

41. Renné T, Pozgajová M, Grüner S, Schuh K, Hu P, Burfeind Pea. Defective thrombus formation in mice lacking coagulation factor XII. The Journal of experimental medicine. 2005; 202(2):271–81. https://doi.org/10.1084/jem.20050664 PMID: 16009717

42. Gailani D, Gruber A. Factor XI as a Therapeutic Target. Arteriosclerosis, Thrombosis, and Vascular Biology. 2016; 36(7):1316–1322. https://doi.org/10.1161/ATVBAHA.116.306925 PMID: 27174099

43. Worm M, Köhler EC, Panda R, Long A, Butler LM, Stavrou EXea. The factor XIIa blocking antibody 3F7: A safe anticoagulant with anti-inflammatory activities. Annals of Translational Medicine. 2015; 3(17):5–9. https://doi.org/10.3978/j.issn.2305-5839.2015.09.07 PMID: 26605293

44. Weitz JI, F JC. Factors XI and XII as targets for new anticoagulants. Frontiers in Medicine. 2017; 4(19):1–6. https://doi.org/10.3389/fmed.2017.00019 PMID: 28286749

45. Chen J, Diamond SL. Reduced model to predict thrombin and fibrin during thrombosis on collagen/tissue factor under venous flow: Roles of γ'-fibrin and factor XIa. PLoS Computational Biology. 2019; 15(8):1–16. https://doi.org/10.1371/journal.pcbi.1007266 PMID: 31381558

List of Figures

1.1 Circulatory loop diagram. Extracted from [2]. 5
1.2 Heart layers. 6
1.3 (a) The four valves of the heart, with the atria and great vessels removed. All valves are shown in the closed position. Extracted from [2]. (b) Left atrium and left ventricle with the papillary muscles and the chordae tendineae. Top: diastole, bottom: systole. 8
1.4 Diagram depicting the various phases of the cardiac cycle. Extracted from [2]. 9

2.1 Control volume ω_c^i around the node i of an unstructured triangular mesh. The control volume is built by linking the centroids of adjacent mesh elements (red dots) and the midpoints of the edges containing the node i (blue dot). The surface patch S_{ij} to the node pair (i, j) is highlighted in blue, and $\boldsymbol{S}_{\text{ij}} = S_{ij}\boldsymbol{n}_{\text{ij}}$ is its associated non-normalized pair face normal. Figure extracted from the PhD of Garreau [104]. . . 36
2.2 **Top left:** annulus markers and reconstructed mitral valve leaflets; the ellipse axes a and b are indicated. **Top right:** complete valve assembly (MV and AV) embedded in the computational domain. **Bottom:** schematic of the MV model. Adapted from Chnafa *et al.* [47]. 41
2.3 Parametric MV geometry for $\varepsilon = 0.35$, $k = 0.6$. Anterior (A) and Posterior (P) leaflets are labeled. 42
2.4 Effect of the main parameters of the parametric mitral valve model. . 43
2.5 Schematic of the RKPM-based immersed-boundary procedure. A solid node m (black circle) interacts with the surrounding Eulerian fluid nodes j (grey squares). **(i)** The fluid velocity is interpolated to the solid node to give $\mathbf{U}_{\text{fluid}}$. **(ii)** The penalty-type force $\mathbf{F}$ is evaluated with Eq. (2.22). **(iii)** $\mathbf{F}$ is regularized and spread back onto the Eulerian grid, yielding the body-force density $\mathbf{f}$ that enters the Navier-Stokes solver. **Right:** flow chart of the same steps; quantities already available at the beginning of each sub-step are shown in green, whereas the unknowns to be computed are shown in red. The left-hand sketch is adapted from Sigüenza *et al.* [114]. 45
2.6 Steady-state velocity field around the cylinder at $Re_D = 30$. Two recirculating vortices are visible downstream of the cylinder. 46

2.7 Configuration of the 3D test case: mitral valve model placed inside a straight cylindrical tube. 47
2.8 Velocity field in the tube at $t = 0.30\,\mathrm{s}$ for three different cases. 49
2.9 Leakage through the valve for the six test configurations. 50

3.1 Computational domain: The 4 pulmonary veins are highlighted in red, the Left Atrium (LA) in orange, the LV in green, and the Aorta in purple. The black lines indicate the positions of the slices used to display the flow. Specifically, the vertical line represents slice #1, while the nearly horizontal line corresponds to slice #2. (a) Domain at $t/T = 0.01$ (start systole) (b) Domain at $t/T = 0.38$ (end systole). 54
3.2 Top plot: Flow rate at the inlet (total of the 4 pulmonary veins) during the cardiac cycle. Middle plot: Flow rate at the outlet (aorta). Bottom plot: Volume during a cycle. Red and green backgrounds mark systole and diastole, respectively. 56
3.3 MV embedded in the patient-specific LV mesh at opening fractions of 0%, 50%, and 100%. Anterior (A) and posterior (P) leaflets are labeled. 58
3.4 Temporal evolution of the opening law $\Gamma(t)$ over one cardiac cycle. Systole (red) corresponds to closure; diastole (green) to the open phase; hatched bands indicate the opening/closure transitions. 59
3.5 Leakage flow rate through the mitral valve over one cardiac cycle in the LV model (average over five cycles; $\alpha = 1$, CFL $= 0.1$). Background colors indicate cardiac phases (red: systole, green: diastole). 60
3.6 Volume rendering of non-dimensional vorticity magnitude at different times of the simulation. Below each images, the curve represent the ventricular volume over time, with the red line indicating the current time in the cardiac cycle. 61
3.7 Flow in the Atrium. (a) Volume rendering of non-dimensional vorticity magnitude. From left to right: $t/T = 0.15$ (first part of systole), $t/T = 0.26$ (second part of systole) and $t/T = 0.4$ (end systole). (b) Visualization of the flow coming from the four pulmonary veins. Each color represents streamlines for a different PV. (c) Velocity field arriving at the MV annulus at $t/T = 0.4$, in the plane slice 2 defined in Fig 3.1.Plane is viewed from the top of the heart in the apex direction. The septal wall represent the aorta side. 63
3.8 Phase-averaged velocity field at different times of a cardiac cycle in the plane slice #1 defined in Fig 3.1. Below each images, the curve represent the ventricular volume over time, with the red line indicating the current time in the cardiac cycle. 64
3.9 Phase-averaged velocity field at $t/T = 0.7$ (mid-diastole) in the plane slice #1 defined in Fig 3.1. Green regions denote the different vortices within the ventricle, while red markers indicate their respective center. Below each images, the curves represent the flow at the entrance (the 4 pulmonary veins), exit (the aorta), and the ventricular volume over time, with the red line indicating the current time in the cardiac cycle. 66

3.10 Phase-averaged velocity field at different times of a cardiac cycle in the plane slice #1 defined in Fig. 3.1. See Fig. 3.8 for the curves displayed beneath the top-row panels. 67

4.1 Location of velocity probes within the left heart cavity. 72
4.2 Mean velocity near the mitral valve, averaged over 25 cardiac cycles. 73
4.3 Non-dimensionalized mean velocity near the mitral valve. 74
4.4 Non-dimensionalized mean velocity near the aortic valve. 75
4.5 Volume rendering of non-dimensional velocity magnitude at different times (t/T) during diastole. Each row corresponds to a specific time instant. Below each set of images, the curves represent the flow at the entrance (the 4 pulmonary veins), exit (the aorta), and the ventricular volume over time, with the red line indicating the current time in the cardiac cycle. Case definitions and parameter values are given in Table 4.2. 76
4.6 Volume rendering of non-dimensional vorticity magnitude (non-dimensionalised by the period T) at different times (t/T) in a cardiac cycle. Case definitions and parameter values are given in Table 4.2. 77
4.7 Q-criterion iso-surfaces at $t/T = 0.45$ for the five cases. 78
4.8 Different cases with the maximum opening. For all cases, $\varepsilon = 0.35$, $k = 0.6$, and $R = 17.5$ mm. For each case, the top image shows the 3D view of the valve within the heart, while the bottom image displays the 2D projection of the valve on slice 1 (visible in Fig. 3.1) and in red in the 3D view of the valve. The red line represents the MV-apex line, while the green line indicates the axis of the valve, which connects the centers of the top and bottom cross section area. 80
4.9 Volume rendering of non-dimensional vorticity magnitude (non-dimensionalised by the period T) at different times (t/T) in a cardiac cycle. Each row corresponds to a specific time instant. **Top:** $t/T = 0.47$ (start diastole). **Middle:** $t/T = 0.57$ (beginning–mid diastole). **Bottom:** $t/T = 0.83$ (end diastole). Below each set of images, the curves represent the flow at the entrance (the 4 PV), exit (the aorta), and the ventricular volume over time, with the red line indicating the current time in the cardiac cycle. For the vorticity colour scale, black represents $\omega = 0$, red indicates $\omega = 500$, yellow corresponds to $\omega = 800$, and white to $\omega = 1000$. 82
4.10 Phase-averaged velocity field at $t/T = 0.57$ (beginning-mid diastole) in the plane slice #1 defined in Fig 3.1. The labels represent the vortices mentioned in the main text. See Figure 4.9 for the curves at the bottom of the Figure. 83
4.11 Phase-averaged velocity field at $t/T = 0.7$ (mid-diastole) in the plane slice #1 defined in Fig 3.1. Green regions denote the different vortices within the ventricle, while red markers indicate their respective centers. See Figure 4.9 for the curves at the bottom of the Figure. 84

5.1 Details of the flow domain over which the kinetic energy budget is established. The inlet (Mitral Plane (MP)) is above the MV and the outlet (Aortic Plane (AP)) under the AV. The outward normals are represented as arrows. $D(t)$ is the ventricular domain at time t and Ω_t represents the fixed domain which is such that $\Omega_t = D(t)$ at time t. . 89
5.2 Normalized elastance waveform $E_n(t)$ adapted from Reymond *et al.* [141]. 93
5.3 Reconstructed ventricular pressure $P_{LV}(t)$ over one cardiac cycle and the corresponding pressure–volume (PV) loop. The pressure is computed from the time-varying elastance relation in Eq. (5.15) using the normalized elastance waveform of Reymond *et al.* [141]. 93
5.4 Kinetic energy balance for (a) case C01, (b) C02, (c) C03, and (d) C04 (see Table 4.4) during a cycle (averaged over 20 cycles). See Eq. (5.14) for the definition of the different terms. "Error" is the difference between the left-hand and the right-hand sides of Eq. (5.14), which should be zero in the absence of any numerical approximation. Note that the "Error" is plotted on a different scale (right axis) compared to the other terms. 95
5.5 Intraventricular viscous dissipation (ψ) during a cardiac cycle (averaged over 20 cycles) for the four cases considered. 96
5.6 (a) Volume-integrated kinetic energy of the phase-averaged velocity, $K(t) = \int_{V(t)} E_{KE}\,\mathrm{d}V$. (b) Volume-integrated turbulent kinetic energy, $k(t) = \int_{V(t)} E_{TKE}\,\mathrm{d}V$. 97
5.7 Studied apical volume at (a) mid-systole and (b) end-systole. 100
5.8 Instantaneous LV volume $V_{\mathrm{LV}}(t)$ over time. 100
5.9 Passive scalar evolution in the apex over a 10-cycle window. High values of ϕ indicate poor washout and potential blood stagnation. The scalar was initialized 11 cycles earlier, so values at $t = 11$ s already reflect prior residence times. 101

6.1 Carpentier classification of mitral regurgitation mechanisms (Extracted from El Sabbagh et al. [154]). 107
6.2 Classification of mitral regurgitation severity, based on Doppler echocardiographic criteria (adapted from Zoghbi et al. [155]). 108
6.3 Modified inlet flow rate for a regurgitant volume of 25 mL. The original inlet signal is shown in blue, the prescribed regurgitant flow Q_{MR} in green, and the resulting modified inlet profile $Q_{\mathrm{inlet_{MR}}}$ in orange. . . . 111
6.4 Modified outlet flow rate for a regurgitant volume of 25 mL. The original (healthy) outlet flow is shown in blue, and the regurgitant case in orange. 111
6.5 Phase-averaged velocity field (averaged over 20 cycles) at different times of systole. 113
6.6 Instantaneous velocity field at $t/T = 0.2$ (mid-systole) for two different posterior leaflet opening angles. Parameter values are summarized in Table 6.1. 114

6.7 (a) Instantaneous intraventricular viscous dissipation (ψ) during a cardiac cycle. (b) Total viscous dissipation within the atrium and ventricle ($\psi_{\text{Atrium+Ventr}}$). Parameter values are summarized in Table 6.1. In both panels, the healthy reference case (C01) is added for comparison. Note that the vertical axes differ between (a) and (b). 114
6.8 (a) Inlet flow rate for the healthy case (C01) and the three regurgitation cases. (b) Outlet flow rate. 115
6.9 Phase-averaged velocity field at different times of systole for the 3 different cases. See Fig. 6.6 for the velocity scale. 117
6.10 Kinetic energy balance for (a) case C01 (healthy case), (b) C05_{10mL}, (c) C05_{25mL}, and (d) C05_{35mL} during a cycle (averaged over 20 cycles). 118
6.11 (a) Intraventricular viscous dissipation (ψ) during a cardiac cycle (averaged over 20 cycles) for the three cases considered. (b) Total Energy loss ($\mathcal{L}_{MR} + \psi$) during a cardiac cycle (averaged over 20 cycles) for the three cases considered. 119
6.12 Passive scalar evolution in the apex over a 10-cycle window. High values of ϕ indicate poor washout and potential blood stagnation. The scalar was initialized 11 cycles earlier, so values at $t = 11$ s already reflect prior residence times. 120
6.13 Phase-averaged velocity field at different times of systole for the 2 different cases. 122
6.14 Total Energy loss ($\mathcal{L}_{MR} + \psi$) during a cardiac cycle (averaged over 20 cycles) for the two cases considered. 123

7.1 Illustration of the simplified apical transport-reaction model. The apex is modeled as a control volume (green) with average species concentration $\bar{C}$, receiving inflow Q^+ from the upstream region (blue, with concentration C^{up}) and releasing outflow Q^-. The exchange rate $k_{\text{flow}} = Q^+/V$ governs the coupling between transport and local biochemical reactions. 130

List of Tables

1.1 Overview of numerical simulations and their levels of modeling. . . . 20
1.2 Overview of numerical simulations and their investigated quantities. . 28

2.1 Comparison of wake parameters for steady-state flow around a cylinder at $Re_D = 30$ with both experimental and numerical reference data. . 46

2.2 Summary of the six test configurations. A fixed time step was prescribed in each case, so variations in CFL reflect differences in the velocity field induced by the immersed boundary forcing. Reported CFL values correspond to the maxima measured during the simulations. 48

3.1 Main characteristics of the geometry of the heart used in this study. . 53

4.1 Parameters of the reference heart model. 70
4.2 Parametric cases layout. 72
4.3 Normalized vortex dimensions at $t/T = 0.45$ for each case. 75
4.4 Values of the parameters for the four different cases considered, with $\varepsilon = 0.35$ and $k = 0.6$. 79
4.5 Peak inflow speed at the mitral valve and area(s) of the dominant vortex structure(s) at $t/T = 0.70$. In case C02, two coherent vortices are present at this phase; the reported values therefore correspond to the areas of the "up" (toward the LV outflow tract) and "down" (toward the apex) structures. In the other cases, a single dominant vortex is present (see Fig. 4.11). 81

5.1 Quantitative Energy Parameters. Note that the integral of $\mathcal{P}_{muscle}$ is computed only over systole. 94

6.1 Parameter values defining the two regurgitant configurations (C05 and $\mathrm{C05_{bis}}$). The posterior leaflet angle $\varphi^{\mathrm{sys}}_{\mathrm{post}}$ corresponds to the opening angle during systole. 113
6.2 Simulated mitral regurgitation cases. Case $\mathrm{C05_{25mL}}$ corresponds to the reference configuration introduced in Table 6.1. 115
6.3 Quantitative Energy Parameters for the three MR cases. RF denotes the regurgitant fraction, and R is the ratio of dissipated energy to muscle work defined in Eq. 5.16. Note that the integrals of $\mathcal{P}_{muscle}$ and $\mathcal{L}_{MR}$ are computed only over systole. 116

Bibliography

[1] World Health Organization. Cardiovascular diseases (cvds). https://www.who.int/news-room/fact-sheets/detail/cardiovascular-diseases-(cvds), 2019. (*p.* 4)

[2] J.G. Betts. *Anatomy and Physiology*. Open Textbook Library. OpenStax College, Rice University, 2013. ISBN 978-1-938168-13-0. (*pp.* 5, 8, 9, and 163)

[3] Shinelle Whiteman, Yusuf Alimi, Mark Carrasco, Jerzy Gielecki, Anna Zurada, and Marios Loukas. Anatomy of the cardiac chambers: A review of the left ventricle. *Translational Research in Anatomy*, 23:100095, 2021. ISSN 2214-854X. doi: https://doi.org/10.1016/j.tria.2020.100095. (*p.* 6)

[4] Partho P. Sengupta, Gianni Pedrizzetti, Philip J. Kilner, Arash Kheradvar, Tino Ebbers, Giovanni Tonti, Alan G. Fraser, and Jagat Narula. Emerging trends in CV flow visualization. *JACC: Cardiovascular Imaging*, 5(3):305–316, 2012. ISSN 1936878X. doi: 10.1016/j.jcmg.2012.01.003. (*pp.* 10 and 98)

[5] D. Rodriguez Munoz, M. Markl, J. L. Moya Mur, A. Barker, C. Fernandez-Golfin, P. Lancellotti, and J. L. Zamorano Gomez. Intracardiac flow visualization: current status and future directions. *European Heart Journal - Cardiovascular Imaging*, 14(11):1029–1038, 2013. ISSN 2047-2404, 2047-2412. doi: 10.1093/ehjci/jet086. (*p.* 98)

[6] Daniel X. Augustine and Liz Howard. Left ventricular hypertrophy in athletes: Differentiating physiology from pathology. *Current Treatment Options in Cardiovascular Medicine*, 20(12):96, 2018. ISSN 1092-8464, 1534-3189. doi: 10.1007/s11936-018-0691-2. (*p.* 88)

[7] Ferit Onur Mutluer, Nikki Van Der Velde, Jason Voorneveld, Johan G. Bosch, Jolien W. Roos-Hesselink, Rob J. Van Der Geest, Alexander Hirsch, and Annemien Van Den Bosch. Evaluation of intraventricular flow by multimodality imaging: a review and meta-analysis. *Cardiovascular Ultrasound*, 19(1):38, 2021. ISSN 1476-7120. doi: 10.1186/s12947-021-00269-8. (*p.* 98)

[8] Brett A. Meyers and Pavlos P. Vlachos. Flow measurements in clinical cardiac imaging. *Physical Review Fluids*, 10(2):020501, 2025. ISSN 2469-990X. doi: 10.1103/PhysRevFluids.10.020501.

[9] Isabella Leo, Angelica Cersosimo, Jessica Ielapi, Jolanda Sabatino, Federico Sicilia, Antonio Strangio, Stefano Figliozzi, Daniele Torella, and Salvatore De Rosa. Intracardiac fluid dynamic analysis: available techniques and novel clinical applications. *BMC Cardiovascular Disorders*, 24(1):716, 2024. ISSN 1471-2261. doi: 10.1186/s12872-024-04371-3. (*p.* 10)

[10] Julia Faurie, Mathilde Baudet, Kondo Claude Assi, Dominique Auger, Guillaume Gilbert, Francois Tournoux, and Damien Garcia. Intracardiac vortex dynamics by high-frame-rate doppler vortography— *In Vivo* comparison with vector flow mapping and 4-d flow MRI. *IEEE Transactions on Ultrasonics, Ferroelectrics, and Frequency Control*, 64(2):424–432, 2017. ISSN 0885-3010, 1525-8955. doi: 10.1109/TUFFC.2016.2632707. (*p.* 10)

[11] Ling Ji, Wenzhi Hu, Yonghong Yong, Hongping Wu, Lei Zhou, and Di Xu. Left ventricular energy loss and wall shear stress assessed by vector flow mapping in patients with hypertrophic cardiomyopathy. *The International Journal of Cardiovascular Imaging*, 34(9):1383–1391, 2018. ISSN 1569-5794, 1573-0743. doi: 10.1007/s10554-018-1348-7. (*p.* 11)

[12] L. Agati, S. Cimino, G. Tonti, F. Cicogna, V. Petronilli, L. De Luca, C. Iacoboni, and G. Pedrizzetti. Quantitative analysis of intraventricular blood flow dynamics by echocardiographic particle image velocimetry in patients with acute myocardial infarction at different stages of left ventricular dysfunction. *European Heart Journal - Cardiovascular Imaging*, 15(11):1203–1212, 2014. ISSN 2047-2412, 2047-2404. doi: 10.1093/ehjci/jeu106. (*pp.* 88, 94, and 98)

[13] Florian Vixège, Alain Berod, Pierre-Yves Courand, Simon Mendez, Franck Nicoud, Philippe Blanc-Benon, Didier Vray, and Damien Garcia. Full-volume three-component intraventricular vector flow mapping by triplane color doppler. *Physics in Medicine & Biology*, 67(9):095004, 2022. ISSN 0031-9155, 1361-6560. doi: 10.1088/1361-6560/ac62fe. (*pp.* 10, 81, and 88)

[14] Réka Faludi, Mariola Szulik, Jan D'hooge, Paul Herijgers, Frank Rademakers, Gianni Pedrizzetti, and Jens-Uwe Voigt. Left ventricular flow patterns in healthy subjects and patients with prosthetic mitral valves: An in vivo study using echocardiographic particle image velocimetry. *The Journal of Thoracic and Cardiovascular Surgery*, 139(6):1501–1510, 2010. ISSN 00225223. doi: 10.1016/j.jtcvs.2009.07.060. (*pp.* 10, 58, and 79)

[15] Koichi Akiyama, Naotoshi Nakamura, Keiichi Itatani, Yoshifumi Naito, Mao Kinoshita, Masaru Shimizu, Saeko Hamaoka, Hideya Kato, Hiroaki Yasumoto, Yasufumi Nakajima, Toshiki Mizobe, Satoshi Numata, Hitoshi

Yaku, and Teiji Sawa. Flow-dynamics assessment of mitral-valve surgery by intraoperative vector flow mapping. *Interactive CardioVascular and Thoracic Surgery*, 24(6):869–875, 2017. ISSN 1569-9293, 1569-9285. doi: 10.1093/icvts/ivx033. (*p.* 10)

[16] Pablo Martínez-Legazpi, Javier Bermejo, Yolanda Benito, Raquel Yotti, Candelas Pérez Del Villar, Ana González-Mansilla, Alicia Barrio, Eduardo Villacorta, Pedro L. Sánchez, Francisco Fernández-Avilés, and Juan C. Del Álamo. Contribution of the diastolic vortex ring to left ventricular filling. *Journal of the American College of Cardiology*, 64(16):1711–1721, 2014. ISSN 07351097. doi: 10.1016/j.jacc.2014.06.1205. (*pp.* 11, 62, 81, 83, 88, and 98)

[17] Daniel Rodríguez Muñoz, José Luis Moya Mur, Covadonga Fernández-Golfín, Derly Carlos Becker Filho, Ariana González Gómez, Sara Fernández Santos, Carla Lázaro Rivera, Luis Miguel Rincón Díaz, Eduardo Casas Rojo, and José Luis Zamorano Gómez. Left ventricular vortices as observed by vector flow mapping: Main determinants and their relation to left ventricular filling. *Echocardiography*, 32(1):96–105, 2015. ISSN 0742-2822, 1540-8175. doi: 10.1111/echo.12584. (*p.* 11)

[18] Nobuaki Fukuda, Keiichi Itatani, Koichi Kimura, Aya Ebihara, Kazuaki Negishi, Kansei Uno, Kagami Miyaji, Masahiko Kurabayashi, and Katsu Takenaka. Prolonged vortex formation during the ejection period in the left ventricle with low ejection fraction: a study by vector flow mapping. *Journal of Medical Ultrasonics*, 41(3):301–310, 2014. ISSN 1346-4523, 1613-2254. doi: 10.1007/s10396-014-0530-3. (*p.* 11)

[19] Hang Jung Ling, Salomé Bru, Julia Puig, Florian Vixège, Simon Mendez, Franck Nicoud, Pierre-Yves Courand, Olivier Bernard, and Damien Garcia. Physics-guided neural networks for intraventricular vector flow mapping. *IEEE Transactions on Ultrasonics, Ferroelectrics, and Frequency Control*, 71(11):1377–1388, 2024. ISSN 0885-3010, 1525-8955. doi: 10.1109/TUFFC.2024.3411718. (*p.* 11)

[20] Mohammed S M Elbaz, Emmeline E Calkoen, Jos J M Westenberg, Boudewijn P F Lelieveldt, Arno A W Roest, and Rob J van der Geest. Vortex flow during early and late left ventricular filling in normal subjects: quantitative characterization using retrospectively-gated 4d flow cardiovascular magnetic resonance and three-dimensional vortex core analysis. *Journal of Cardiovascular Magnetic Resonance*, 16(1):78, 2014. ISSN 1532-429X. doi: 10.1186/s12968-014-0078-9. (*pp.* 11 and 65)

[21] Vivian P. Kamphuis, Arno A. W. Roest, Pieter J. Van Den Boogaard, Lucia J. M. Kroft, Hildo J. Lamb, Willem A. Helbing, Nico A. Blom, Jos J. M. Westenberg, and Mohammed S. M. Elbaz. Hemodynamic interplay of vorticity, viscous energy loss, and kinetic energy from 4d flow MRI and link to

cardiac function in healthy subjects and fontan patients. *American Journal of Physiology-Heart and Circulatory Physiology*, 320(4):H1687–H1698, 2021. ISSN 0363-6135, 1522-1539. doi: 10.1152/ajpheart.00806.2020. (*pp.* 11, 94, and 95)

[22] Trung Bao Le, Mohammed S. M. Elbaz, Rob J. Van Der Geest, and Fotis Sotiropoulos. High resolution simulation of diastolic left ventricular hemodynamics guided by four-dimensional flow magnetic resonance imaging data. *Flow, Turbulence and Combustion*, 102(1):3–26, 2019. ISSN 1386-6184, 1573-1987. doi: 10.1007/s10494-018-0003-7. (*pp.* 11, 17, 21, and 26)

[23] Pankaj Garg, Saul Crandon, Peter P. Swoboda, Graham J. Fent, James R. J. Foley, Pei G. Chew, Louise A. E. Brown, Sethumadhavan Vijayan, Mariëlla E. C. J. Hassell, Robin Nijveldt, Malenka Bissell, Mohammed S. M. Elbaz, Abdallah Al-Mohammad, Jos J. M. Westenberg, John P. Greenwood, Rob J. Van Der Geest, Sven Plein, and Erica Dall'Armellina. Left ventricular blood flow kinetic energy after myocardial infarction - insights from 4d flow cardiovascular magnetic resonance. *Journal of Cardiovascular Magnetic Resonance*, 20(1):61, 2018. ISSN 1532-429X. doi: 10.1186/s12968-018-0483-6. (*p.* 11)

[24] James Wong, Radomir Chabiniok, Adelaide deVecchi, Nathalie Dedieu, Eva Sammut, Tobias Schaeffter, and Reza Razavi. Age-related changes in intraventricular kinetic energy: a physiological or pathological adaptation? *American Journal of Physiology-Heart and Circulatory Physiology*, 310(6): H747–H755, 2016. ISSN 0363-6135, 1522-1539. doi: 10.1152/ajpheart.00075. 2015. (*pp.* 11 and 95)

[25] Valentina Meschini, Francesco Viola, and Roberto Verzicco. Heart rate effects on the ventricular hemodynamics and mitral valve kinematics. *Computers & Fluids*, 197:104359, 2020. ISSN 00457930. doi: 10.1016/j.compfluid.2019. 104359. (*pp.* 11, 18, 21, and 26)

[26] Fotis Sotiropoulos, Trung Bao Le, and Anvar Gilmanov. Fluid mechanics of heart valves and their replacements. *Annual Review of Fluid Mechanics*, 48(1):259–283, 2016. ISSN 0066-4189, 1545-4479. doi: 10.1146/ annurev-fluid-122414-034314. (*p.* 12)

[27] Francesco Viola, Elizabeth Jermyn, James Warnock, Giorgio Querzoli, and Roberto Verzicco. Left ventricular hemodynamics with an implanted assist device: An in vitro fluid dynamics study. *Annals of Biomedical Engineering*, 47(8):1799–1814, 2019. ISSN 0090-6964, 1573-9686. doi: 10.1007/s10439-019-02273-6. (*pp.* 12 and 65)

[28] Andrew W. Siefert and Ryan L. Siskey. Bench models for assessing the mechanics of mitral valve repair and percutaneous surgery. *Cardiovascular Engineering and Technology*, 6(2):193–207, 2015. doi: 10.1007/s13239-014-0196-4. (*p.* 12)

[29] Ke-Wei Xu, Qi Gao, Min Wan, and Ke Zhang. Mock circulatory loop applications for testing cardiovascular assist devices and in vitro studies. *Frontiers in Physiology*, 14:1175919, 2023. ISSN 1664-042X. doi: 10.3389/fphys.2023.1175919. (*p.* 12)

[30] Victor K. Tsui and Daniel Ewert. Review of cardiovascular mock circulatory loop designs and applications. *Bioengineering*, 12(8):851, 2025. ISSN 2306-5354. doi: 10.3390/bioengineering12080851.

[31] Morgane Evin. *Caractérisation de la fonction hémodynamique suite au remplacement valvulaire mitral. Etude in-vitro.* Phd thesis, Université d'Aix-Marseille, 2013. (*p.* 12)

[32] Hicham Saaid, Jason Voorneveld, Christiaan Schinkel, Jos Westenberg, Frank Gijsen, Patrick Segers, Pascal Verdonck, Nico De Jong, Johan G. Bosch, Sasa Kenjeres, and Tom Claessens. Tomographic PIV in a model of the left ventricle: 3d flow past biological and mechanical heart valves. *Journal of Biomechanics*, 90:40–49, 2019. ISSN 00219290. doi: 10.1016/j.jbiomech.2019.04.024. (*p.* 12)

[33] Lea Christierson, Petter Frieberg, Tania Lala, Johannes Töger, Petru Liuba, Johan Revstedt, Hanna Isaksson, and Nina Hakacova. Multi-modal in vitro experiments mimicking the flow through a mitral heart valve phantom. *Cardiovascular Engineering and Technology*, 15(5):572–583, 2024. ISSN 1869-408X, 1869-4098. doi: 10.1007/s13239-024-00732-3. (*pp.* 12 and 13)

[34] Xiaolin Wu, Hicham Saaid, Jason Voorneveld, Tom Claessens, Jos J. M. Westenberg, Nico De Jong, Johan G. Bosch, and Saša Kenjereš. 4d flow patterns and relative pressure distribution in a left ventricle model by shake-the-box and proper orthogonal decomposition analysis. *Cardiovascular Engineering and Technology*, 14(6):743–754, 2023. ISSN 1869-408X, 1869-4098. doi: 10.1007/s13239-023-00684-0. (*p.* 12)

[35] Ghassan Maraouch and Lyes Kadem. Flow dynamics in a model of a left ventricle with different mitral valve orientations. *Fluids*, 6(12):428, 2021. ISSN 2311-5521. doi: 10.3390/fluids6120428. (*p.* 12)

[36] John C Westerdale, Ronald Adrian, Kyle Squires, Hari Chaliki, and Marek Belohlavek. Effects of bileaflet mechanical mitral valve rotational orientation on left ventricular flow conditions. *The Open Cardiovascular Medicine Journal*, 9(1):62–68, 2015. ISSN 1874-1924. doi: 10.2174/1874192401509010062. URL https://opencardiovascularmedicinejournal.com/VOLUME/9/PAGE/62/. (*p.* 12)

[37] Morgane Evin, Philippe Pibarot, Carine Guivier-Curien, David Tanné, Lyes Kadem, and Regis Rieu. Localized transvalvular pressure gradients in mitral bileaflet mechanical heart valves and impact on gradient overestimation

by doppler. *Journal of the American Society of Echocardiography*, 26(7): 791–800, 2013. ISSN 08947317. doi: 10.1016/j.echo.2013.03.012. (*p.* 12)

[38] Morgane Evin, Carine Guivier-Curien, Philippe Pibarot, Lyes Kadem, and Régis Rieu. Are the current doppler echocardiography criteria able to discriminate mitral bileaflet mechanical heart valve malfunction? an in vitro study: Current doppler echocardiography criteria. *Artificial Organs*, 40(5): E52–E60, 2016. ISSN 0160564X. doi: 10.1111/aor.12653. (*p.* 12)

[39] Morteza Jeyhani, Shahrokh Shahriari, and Michel Labrosse. Experimental investigation of left ventricular flow patterns after percutaneous edge to edge mitral valve repair. *Artificial Organs*, 42(5):516–524, 2018. ISSN 0160-564X, 1525-1594. doi: 10.1111/aor.13020. (*p.* 13)

[40] Chloé Papolla, Ahmed Darwish, Lyes Kadem, and Régis Rieu. Impact of mitral regurgitation on the flow in a model of a left ventricle. *Cardiovascular Engineering and Technology*, 11(6):708–718, 2020. ISSN 1869-408X, 1869-4098. doi: 10.1007/s13239-020-00490-y. (*p.* 13)

[41] Morgane Evin, Carine Guivier-Curien, Regis Rieu, Josep Rodés-Cabau, and Philippe Pibarot. Mitral valve-in-valve hemodynamic performance: An in vitro study. *The Journal of Thoracic and Cardiovascular Surgery*, 151 (4):1051–1059.e6, 2016. ISSN 00225223. doi: 10.1016/j.jtcvs.2015.11.039. (*p.* 13)

[42] M. Peirlinck, F. Sahli Costabal, J. Yao, J. M. Guccione, S. Tripathy, Y. Wang, D. Ozturk, P. Segars, T. M. Morrison, S. Levine, and E. Kuhl. Precision medicine in human heart modeling: Perspectives, challenges, and opportunities. *Biomechanics and Modeling in Mechanobiology*, 20(3):803–831, 2021. ISSN 1617-7959, 1617-7940. doi: 10.1007/s10237-021-01421-z. (*p.* 13)

[43] Steven A. Niederer, Joost Lumens, and Natalia A. Trayanova. Computational models in cardiology. *Nature Reviews Cardiology*, 16(2):100–111, 2019. ISSN 1759-5002, 1759-5010. doi: 10.1038/s41569-018-0104-y.

[44] Richard A. Gray and Pras Pathmanathan. Patient-specific cardiovascular computational modeling: Diversity of personalization and challenges. *Journal of Cardiovascular Translational Research*, 11(2):80–88, 2018. ISSN 1937-5387, 1937-5395. doi: 10.1007/s12265-018-9792-2. (*p.* 13)

[45] Jung Hee Seo, Vijay Vedula, Theodore Abraham, Albert C Lardo, Fady Dawoud, Hongchang Luo, and Rajat Mittal. Effect of the mitral valve on diastolic flow patterns. *Phys. Fluids*, 2014. (*pp.* 13, 14, 15, 16, 21, and 23)

[46] Vijay Vedula, Richard George, Laurent Younes, and Rajat Mittal. Hemodynamics in the left atrium and its effect on ventricular flow patterns. *Journal of Biomechanical Engineering*, 137(11):111003, 2015. ISSN 0148-0731, 1528-8951. doi: 10.1115/1.4031487. (*pp.* 14, 15, 23, and 88)

[47] C. Chnafa, S. Mendez, and F. Nicoud. Image-based large-eddy simulation in a realistic left heart. *Computers & Fluids*, 94:173–187, 2014. ISSN 00457930. doi: 10.1016/j.compfluid.2014.01.030. (*pp.* 14, 32, 40, 41, 52, 55, 70, and 163)

[48] Lukas Obermeier, Katharina Vellguth, Adriano Schlief, Lennart Tautz, Jan Bruening, Christoph Knosalla, Titus Kuehne, Natalia Solowjowa, and Leonid Goubergrits. CT-based simulation of left ventricular hemodynamics: A pilot study in mitral regurgitation and left ventricle aneurysm patients. *Frontiers in Cardiovascular Medicine*, 9:828556, 2022. ISSN 2297-055X. doi: 10.3389/fcvm.2022.828556. (*pp.* 19, 21, 27, 40, and 109)

[49] Chiara Celotto, Luigino Zovatto, Dario Collia, and Gianni Pedrizzetti. Influence of mitral valve elasticity on flow development in the left ventricle. *European Journal of Mechanics - B/Fluids*, 75:110–118, 2019. ISSN 09977546. doi: 10.1016/j.euromechflu.2018.11.018. (*pp.* 13, 17, 21, 25, and 40)

[50] Vijay Vedula, Jung-Hee Seo, Albert C. Lardo, and Rajat Mittal. Effect of trabeculae and papillary muscles on the hemodynamics of the left ventricle. *Theoretical and Computational Fluid Dynamics*, 30(1):3–21, 2016. ISSN 0935-4964, 1432-2250. doi: 10.1007/s00162-015-0349-6. (*pp.* 15, 21, 23, and 98)

[51] Ivan Fumagalli, Marco Fedele, Christian Vergara, Luca Dede', Sonia Ippolito, Francesca Nicolò, Carlo Antona, Roberto Scrofani, and Alfio Quarteroni. An image-based computational hemodynamics study of the systolic anterior motion of the mitral valve. *Computers in Biology and Medicine*, 123:103922, 2020. ISSN 00104825. doi: 10.1016/j.compbiomed.2020.103922. (*pp.* 17 and 26)

[52] Leonid Goubergrits, Katharina Vellguth, Lukas Obermeier, Adriano Schlief, Lennart Tautz, Jan Bruening, Hans Lamecker, Angelika Szengel, Olena Nemchyna, Christoph Knosalla, Titus Kuehne, and Natalia Solowjowa. CT-based analysis of left ventricular hemodynamics using statistical shape modeling and computational fluid dynamics. *Frontiers in Cardiovascular Medicine*, 9:901902, 2022. ISSN 2297-055X. doi: 10.3389/fcvm.2022.901902. (*pp.* 19, 21, and 27)

[53] Jonas Lantz, Lilian Henriksson, Anders Persson, Matts Karlsson, and Tino Ebbers. Patient-specific simulation of cardiac blood flow from high-resolution computed tomography. *Journal of Biomechanical Engineering*, 138(12): 121004, 2016. ISSN 0148-0731, 1528-8951. doi: 10.1115/1.4034652. (*pp.* 13, 14, 15, 21, and 24)

[54] Federico Domenichini and Gianni Pedrizzetti. Asymptotic model of fluid–tissue interaction for mitral valve dynamics. *Cardiovascular Engineering and Technology*, 6(2):95–104, 2015. ISSN 1869-408X, 1869-4098. doi: 10.1007/s13239-014-0201-y. (*pp.* 13, 14, 15, 17, 19, 23, 42, 57, and 58)

[55] Vamsi Spandan, Valentina Meschini, Rodolfo Ostilla-Monico, Detlef Lohse, Giorgio Querzoli, Marco D. de Tullio, and Roberto Verzicco. A parallel interaction potential approach coupled with the immersed boundary method for fully resolved simulations of deformable interfaces and membranes. *Journal of Computational Physics*, 348:567–590, 2017. ISSN 00219991. doi: 10.1016/j.jcp.2017.07.036. (*pp.* 13, 16, and 24)

[56] Hao Gao, Liuyang Feng, Nan Qi, Colin Berry, Boyce Griffith, and Xiaoyu Luo. A coupled mitral valve – left ventricle model with fluid-structure interaction. *arXiv:1704.01960 [physics]*, 2017. (*pp.* 13, 14, 16, 21, and 24)

[57] Liuyang Feng, Hao Gao, Boyce Griffith, Steven Niederer, and Xiaoyu Luo. Analysis of a coupled fluid-structure interaction model of the left atrium and mitral valve. *International Journal for Numerical Methods in Biomedical Engineering*, 35(11):e3254, 2019. ISSN 2040-7939, 2040-7947. doi: 10.1002/cnm.3254. (*pp.* 13, 14, 17, and 25)

[58] Alberto Zingaro, Ivan Fumagalli, Luca Dede, Marco Fedele, Pasquale C. Africa, Antonio F. Corno, and Alfio Quarteroni. A geometric multiscale model for the numerical simulation of blood flow in the human left heart. *Discrete and Continuous Dynamical Systems - S*, 15(8):2391, 2022. ISSN 1937-1632, 1937-1179. doi: 10.3934/dcdss.2022052. (*pp.* 13, 19, and 28)

[59] Lorenzo Bennati, Vincenzo Giambruno, Francesca Renzi, Venanzio Di Nicola, Caterina Maffeis, Giovanni Puppini, Giovanni Battista Luciani, and Christian Vergara. Turbulent blood dynamics in the left heart in the presence of mitral regurgitation: a computational study based on multi-series cine-MRI. *Biomechanics and Modeling in Mechanobiology*, 22(6):1829–1846, 2023. ISSN 1617-7959, 1617-7940. doi: 10.1007/s10237-023-01735-0. (*pp.* 13, 20, 21, 28, 40, 99, and 109)

[60] F. Levrero-Florencio, F. Margara, E. Zacur, A. Bueno-Orovio, Z.J. Wang, A. Santiago, J. Aguado-Sierra, G. Houzeaux, V. Grau, D. Kay, M. Vázquez, R. Ruiz-Baier, and B. Rodriguez. Sensitivity analysis of a strongly-coupled human-based electromechanical cardiac model: Effect of mechanical parameters on physiologically relevant biomarkers. *Computer Methods in Applied Mechanics and Engineering*, 361:112762, 2020. ISSN 00457825. doi: 10.1016/j.cma.2019.112762. (*pp.* 13, 14, 18, and 26)

[61] Brian Baillargeon, Nuno Rebelo, David D. Fox, Robert L. Taylor, and Ellen Kuhl. The living heart project: A robust and integrative simulator for human heart function. *European Journal of Mechanics - A/Solids*, 48:38–47, 2014. ISSN 09977538. doi: 10.1016/j.euromechsol.2014.04.001. (*pp.* 15 and 23)

[62] Tobias Gerach, Steffen Schuler, Jonathan Fröhlich, Laura Lindner, Ekaterina Kovacheva, Robin Moss, Eike Moritz Wülfers, Gunnar Seemann, Christian

Wieners, and Axel Loewe. Electro-mechanical whole-heart digital twins: A fully coupled multi-physics approach. *Mathematics*, 9(11):1247, 2021. ISSN 2227-7390. doi: 10.3390/math9111247.

[63] Matteo Salvador, Marco Fedele, Pasquale Claudio Africa, Eric Sung, Luca Dede', Adityo Prakosa, Jonathan Chrispin, Natalia Trayanova, and Alfio Quarteroni. Electromechanical modeling of human ventricles with ischemic cardiomyopathy: numerical simulations in sinus rhythm and under arrhythmia. *Computers in Biology and Medicine*, 136:104674, 2021. ISSN 00104825. doi: 10.1016/j.compbiomed.2021.104674. (*pp.* 19 and 27)

[64] Matteo Salvador, Francesco Regazzoni, Stefano Pagani, Luca Dede', Natalia Trayanova, and Alfio Quarteroni. The role of mechano-electric feedbacks and hemodynamic coupling in scar-related ventricular tachycardia. *Computers in Biology and Medicine*, 142:105203, 2022. ISSN 00104825. doi: 10.1016/j.compbiomed.2021.105203. (*pp.* 13, 19, and 27)

[65] Francesco Viola, Valentina Meschini, and Roberto Verzicco. Fluid–structure-electrophysiology interaction (FSEI) in the left-heart: A multi-way coupled computational model. *European Journal of Mechanics - B/Fluids*, 79:212–232, 2020. ISSN 09977546. doi: 10.1016/j.euromechflu.2019.09.006. (*pp.* 13, 18, and 26)

[66] Trung Bao Le and Fotis Sotiropoulos. On the three-dimensional vortical structure of early diastolic flow in a patient-specific left ventricle. *European Journal of Mechanics - B/Fluids*, 35:20–24, 2012. ISSN 09977546. doi: 10.1016/j.euromechflu.2012.01.013. (*pp.* 13, 14, 15, and 23)

[67] Jung Hee Seo and Rajat Mittal. Effect of diastolic flow patterns on the function of the left ventricle. *Physics of Fluids*, 25(11):110801, 2013. ISSN 1070-6631, 1089-7666. doi: 10.1063/1.4819067. (*pp.* 13, 15, 21, 23, 88, 94, and 98)

[68] Boyang Su, Ru San Tan, Ju Le Tan, Kenneth Wei Qiang Guo, Jun Mei Zhang, Shuang Leng, Xiaodan Zhao, John Carson Allen, and Liang Zhong. Cardiac MRI based numerical modeling of left ventricular fluid dynamics with mitral valve incorporated. *Journal of Biomechanics*, 49(7):1199–1205, 2016. ISSN 00219290. doi: 10.1016/j.jbiomech.2016.03.008. (*pp.* 14, 16, 21, and 24)

[69] Valentina Meschini, Marco D. de Tullio, and Roberto Verzicco. Effects of mitral chordae tendineae on the flow in the left heart ventricle. *The European Physical Journal E*, 41(2):27, 2018. ISSN 1292-8941, 1292-895X. doi: 10.1140/epje/i2018-11634-7. (*pp.* 13, 16, 18, 21, and 25)

[70] C. Chnafa, S. Mendez, and F. Nicoud. Image-based simulations show important flow fluctuations in a normal left ventricle: What could be the

implications? *Annals of Biomedical Engineering*, 44(11):3346–3358, 2016. ISSN 0090-6964, 1573-9686. doi: 10.1007/s10439-016-1614-6. (*pp.* 14, 32, 52, 81, 88, and 98)

[71] Mojgan Ghodrati, Thomas Schlöglhofer, Alexander Maurer, Thananya Khienwad, Daniel Zimpfer, Dietrich Beitzke, Francesco Zonta, Francesco Moscato, Heinrich Schima, and Philipp Aigner. Effects of the atrium on intraventricular flow patterns during mechanical circulatory support. *The International Journal of Artificial Organs*, 45(4):421–430, 2022. ISSN 0391-3988, 1724-6040. doi: 10.1177/03913988211056018. (*pp.* 19, 21, 27, and 88)

[72] Lorenzo Bennati, Christian Vergara, Vincenzo Giambruno, Ivan Fumagalli, Antonio Francesco Corno, Alfio Quarteroni, Giovanni Puppini, and Giovanni Battista Luciani. An image-based computational fluid dynamics study of mitral regurgitation in presence of prolapse. *Cardiovascular Engineering and Technology*, 14(3):457–475, 2023. ISSN 1869-408X, 1869-4098. doi: 10.1007/s13239-023-00665-3. (*pp.* 14, 19, 21, 28, 109, and 116)

[73] Jonas Lantz, Sophia Bäck, Carl-Johan Carlhäll, Ann Bolger, Anders Persson, Matts Karlsson, and Tino Ebbers. Impact of prosthetic mitral valve orientation on the ventricular flow field: Comparison using patient-specific computational fluid dynamics. *Journal of Biomechanics*, 116:110209, 2021. ISSN 00219290. doi: 10.1016/j.jbiomech.2020.110209. (*pp.* 14, 18, 21, and 27)

[74] Andrés Caballero, Wenbin Mao, Raymond McKay, Charles Primiano, Sabet Hashim, and Wei Sun. New insights into mitral heart valve prolapse after chordae rupture through fluid–structure interaction computational modeling. *Scientific Reports*, 8:17306, 2018. ISSN 2045-2322. doi: 10.1038/s41598-018-35555-5. (*pp.* 14, 16, 24, 99, and 109)

[75] Hiroshi Watanabe, Seiryo Sugiura, and Toshiaki Hisada. The looped heart does not save energy by maintaining the momentum of blood flowing in the ventricle. *American Journal of Physiology-Heart and Circulatory Physiology*, 294(5):H2191–H2196, 2008. ISSN 0363-6135, 1522-1539. doi: 10.1152/ajpheart.00041.2008. (*pp.* 14, 15, 23, 88, 94, and 98)

[76] R. Mittal, H. Dong, M. Bozkurttas, F.M. Najjar, A. Vargas, and A. Von Loebbecke. A versatile sharp interface immersed boundary method for incompressible flows with complex boundaries. *Journal of Computational Physics*, 227(10):4825–4852, 2008. ISSN 00219991. doi: 10.1016/j.jcp.2008.01.028. (*p.* 15)

[77] Jung Hee Seo, Thura Abd, Richard T. George, and Rajat Mittal. A coupled chemo-fluidic computational model for thrombogenesis in infarcted left ventricles. *American Journal of Physiology-Heart and Circulatory Physiology*,

310(11):H1567–H1582, 2016. ISSN 0363-6135, 1522-1539. doi: 10.1152/ajpheart.00855.2015. (*pp.* 16, 24, and 129)

[78] Seyedvahid Khodaei, Nasser Fatouraee, and Malikeh Nabaei. Numerical simulation of mitral valve prolapse considering the effect of left ventricle. *Mathematical Biosciences*, 285:75–80, 2017. ISSN 00255564. doi: 10.1016/j.mbs.2016.12.008. (*pp.* 16 and 24)

[79] Gianni Pedrizzetti, Per M. Arvidsson, Johannes Töger, Rasmus Borgquist, Federico Domenichini, Håkan Arheden, and Einar Heiberg. On estimating intraventricular hemodynamic forces from endocardial dynamics: A comparative study with 4d flow MRI. *Journal of Biomechanics*, 60:203–210, 2017. ISSN 00219290. doi: 10.1016/j.jbiomech.2017.06.046. (*pp.* 16 and 24)

[80] Vijay Govindarajan, John Mousel, H. S. Udaykumar, Sarah C. Vigmostad, David D. McPherson, Hyunggun Kim, and Krishnan B. Chandran. Synergy between diastolic mitral valve function and left ventricular flow aids in valve closure and blood transport during systole. *Scientific Reports*, 8(1):6187, 2018. ISSN 2045-2322. doi: 10.1038/s41598-018-24469-x. (*pp.* 16 and 24)

[81] V. Meschini, M. D. de Tullio, G. Querzoli, and R. Verzicco. Flow structure in healthy and pathological left ventricles with natural and prosthetic mitral valves. *Journal of Fluid Mechanics*, 834:271–307, 2018. ISSN 0022-1120, 1469-7645. doi: 10.1017/jfm.2017.725. (*pp.* 16, 17, 18, 21, and 25)

[82] Bee Ting Chan, Azam Ahmad Bakir, Amr Al Abed, Socrates Dokos, Chin Neng Leong, Ean Hin Ooi, Renly Lim, and Einly Lim. Impact of myocardial infarction on intraventricular vortex and flow energetics assessed using computational simulations. *International Journal for Numerical Methods in Biomedical Engineering*, 35(6):e3204, 2019. ISSN 2040-7939, 2040-7947. doi: 10.1002/cnm.3204. (*pp.* 17, 21, and 25)

[83] Dario Collia, Luigino Zovatto, and Gianni Pedrizzetti. Analysis of mitral valve regurgitation by computational fluid dynamics. *APL Bioengineering*, 3(3):036105, 2019. ISSN 2473-2877. doi: 10.1063/1.5097245. (*pp.* 17, 21, 25, and 109)

[84] Dario Collia, Marija Vukicevic, Valentina Meschini, Luigino Zovatto, and Gianni Pedrizzetti. Simplified mitral valve modeling for prospective clinical application of left ventricular fluid dynamics. *Journal of Computational Physics*, 398:108895, 2019. ISSN 00219991. doi: 10.1016/j.jcp.2019.108895. (*pp.* 17 and 25)

[85] Valentina Meschini, Francesco Viola, and Roberto Verzicco. Modeling mitral valve stenosis: A parametric study on the stenosis severity level. *Journal of Biomechanics*, 84:218–226, 2019. ISSN 00219290. doi: 10.1016/j.jbiomech.2019.01.002. (*pp.* 17, 21, and 26)

[86] Boyang Su, Xikun Wang, Foad Kabinejadian, Calvin Chin, Thu Thao Le, and Jun-Mei Zhang. Effects of left atrium on intraventricular flow in numerical simulations. *Computers in Biology and Medicine*, 106:46–53, 2019. ISSN 00104825. doi: 10.1016/j.compbiomed.2019.01.011. (*pp.* 17, 21, 26, and 88)

[87] Dario Collia, Luigino Zovatto, Giovanni Tonti, and Gianni Pedrizzetti. Comparative analysis of right ventricle fluid dynamics. *Frontiers in Bioengineering and Biotechnology*, 9:667408, 2021. ISSN 2296-4185. doi: 10.3389/fbioe.2021.667408. (*pp.* 18, 21, and 26)

[88] Dario Collia. Mitral valve asymmetry in healthy, pathological, and repaired cases. *Physics of Fluids*, 33(7):077118, 2021. ISSN 1070-6631, 1089-7666. doi: 10.1063/5.0055485. (*pp.* 18, 26, 58, and 79)

[89] Valentina Meschini, Rajat Mittal, and Roberto Verzicco. Systolic anterior motion in hypertrophic cardiomyopathy: a fluid–structure interaction computational model. *Theoretical and Computational Fluid Dynamics*, 35(3): 381–396, 2021. ISSN 0935-4964, 1432-2250. doi: 10.1007/s00162-021-00564-0. (*pp.* 18 and 27)

[90] Yujia Chang, Yi Jiang, and Rongliang Chen. A parallel domain decomposition algorithm for fluid-structure interaction simulations of the left ventricle with patient-specific shape. *Electronic Research Archive*, 30(9):3377–3396, 2022. ISSN 2688-1594. doi: 10.3934/era.2022172. (*pp.* 19 and 27)

[91] Dario Collia and Gianni Pedrizzetti. The influence of mitral valve asymmetry for an improved choice of valve repair or replacement. *Fluids*, 7(9):293, 2022. ISSN 2311-5521. doi: 10.3390/fluids7090293. (*pp.* 19 and 27)

[92] Jorge Corral-Acero, Francesca Margara, Maciej Marciniak, Cristobal Rodero, Filip Loncaric, Yingjing Feng, Andrew Gilbert, Joao F Fernandes, Hassaan A Bukhari, Ali Wajdan, Manuel Villegas Martinez, Mariana Sousa Santos, Mehrdad Shamohammdi, Hongxing Luo, Philip Westphal, Paul Leeson, Paolo DiAchille, Viatcheslav Gurev, Manuel Mayr, Liesbet Geris, Pras Pathmanathan, Tina Morrison, Richard Cornelussen, Frits Prinzen, Tammo Delhaas, Ada Doltra, Marta Sitges, Edward J Vigmond, Ernesto Zacur, Vicente Grau, Blanca Rodriguez, Espen W Remme, Steven Niederer, Peter Mortier, Kristin McLeod, Mark Potse, Esther Pueyo, Alfonso Bueno-Orovio, and Pablo Lamata. The 'digital twin' to enable the vision of precision cardiology. *European Heart Journal*, 41(48):4556–4564, 2020. ISSN 0195-668X, 1522-9645. doi: 10.1093/eurheartj/ehaa159. (*p.* 22)

[93] Simon Mendez, Alain Bérod, Christophe Chnafa, Morgane Garreau, Etienne Gibaud, Anthony Larroque, Stephanie Lindsey, Marco Martins Afonso, Pascal Mattéoli, Rodrigo Mendez Rojano, Dorian Midou, Thomas Puiseux, Julien Sigüenza, Pierre Taraconat, Vladeta Zmijanovic, and Franck Nicoud.

YALES2BIO: A General Purpose Solver Dedicated to Blood Flows, chapter 7, pages 183–206. John Wiley & Sons, Ltd, 2022. doi: https://doi.org/10.1002/9781119986607.ch7. (*pp.* 32 and 55)

[94] Vincent Moureau, Pascale Domingo, and Luc Vervisch. Design of a massively parallel CFD code for complex geometries. *Comptes Rendus. Mécanique*, 339(2):141–148, 2010. ISSN 1873-7234. doi: 10.1016/j.crme.2010.12.001. (*p.* 32)

[95] Vladeta Zmijanovic, Simon Mendez, Vincent Moureau, and Franck Nicoud. About the numerical robustness of biomedical benchmark cases: Interlaboratory FDA's idealized medical device. *International Journal for Numerical Methods in Biomedical Engineering*, 33(1):e02789, 2017. ISSN 2040-7939, 2040-7947. doi: 10.1002/cnm.2789. (*p.* 32)

[96] Alain Berod, Christophe Chnafa, Simon Mendez, and Franck Nicoud. A heterogeneous model of endovascular devices for the treatment of intracranial aneurysms. *International Journal for Numerical Methods in Biomedical Engineering*, 38(2):e3552, 2022. ISSN 2040-7939, 2040-7947. doi: 10.1002/cnm.3552. (*pp.* 32 and 128)

[97] Julien Sigüenza, Desiree Pott, Simon Mendez, Simon J. Sonntag, Tim A.S. Kaufmann, Ulrich Steinseifer, and Franck Nicoud. Fluid-structure interaction of a pulsatile flow with an aortic valve model: A combined experimental and numerical study. *International Journal for Numerical Methods in Biomedical Engineering*, 34(4):e2945, 2018. ISSN 2040-7939, 2040-7947. doi: 10.1002/cnm.2945. (*p.* 32)

[98] David N Ku. BLOOD FLOW IN ARTERIES. 1996. (*p.* 32)

[99] D. A. Siginer, D. De Kee, and R. P. Chhabra. *Advances in the Flow and Rheology of Non-Newtonian Fluids*, volume 8. Elsevier, 1999. ISBN 9780080540559. (*p.* 32)

[100] Erwin Stein, editor. *Encyclopedia of computational mechanics*. Wiley, 2004. ISBN 978-0-470-84699-5. (*p.* 34)

[101] C W Hirt, A A Amsden, and J L Cook. An arbitrary lagrangian-eulerian computing method for all flow speeds. *Journal of Computational Physics*, 14(3): 227–253, 1974. ISSN 0021-9991. doi: https://doi.org/10.1016/0021-9991(74)90051-5. (*p.* 34)

[102] Christophe Chnafa. *Using image-based large-eddy simulations to investigate the intracardiac fow and its turbulent nature*. Phd thesis, University of Montpellier, 2014. (*pp.* 35 and 46)

[103] Barthélémy Thibaud. *Numerical simulation of fluid-structure interaction in venous valves*. Phd thesis, University of Montpellier, 2024. (*p.* 35)

[104] Morgane Garreau. *Simulations hémodynamiques pour l'IRM: contrôle qualité, optimisation et intégration à la pratique clinique*. Phd thesis, University of Montpellier, 2023. (*pp.* 36 and 163)

[105] Stijn Vantieghem. *Numerical simulations of quasi-static magnetohydrodynamics using an unstructured finite volume solver: development and applications*. Phd thesis, Université Libre de Bruxelles, 2011. (*p.* 36)

[106] J.H Williamson. Low-storage runge-kutta schemes. *Journal of Computational Physics*, 35(1):48–56, 1980. ISSN 0021-9991. doi: https://doi.org/10.1016/0021-9991(80)90033-9. (*p.* 36)

[107] Charbel Farhat, Philippe Geuzaine, and Céline Grandmont. The discrete geometric conservation law and the nonlinear stability of ALE schemes for the solution of flow problems on moving grids. *Journal of Computational Physics*, 174(2):669–694, 2001. ISSN 00219991. doi: 10.1006/jcph.2001.6932. (*p.* 37)

[108] Daniele Boffi and Lucia Gastaldi. Stability and geometric conservation laws for ALE formulations. *Computer Methods in Applied Mechanics and Engineering*, 193(42):4717–4739, 2004. ISSN 00457825. doi: 10.1016/j.cma.2004.02.020. (*p.* 37)

[109] A.J. Chorin. Numerical solution of the navier-stokes equations. *Math. Comp*, 1968. doi: https://doi.org/10.2307/2004575. (*pp.* 38 and 55)

[110] Mathias Malandain, Nicolas Maheu, and Vincent Moureau. Optimization of the deflated conjugate gradient algorithm for the solving of elliptic equations on massively parallel machines. *Journal of Computational Physics*, 238:32–47, 2013. ISSN 0021-9991. doi: https://doi.org/10.1016/j.jcp.2012.11.046. (*p.* 38)

[111] Franck Nicoud, Hubert Baya Toda, Olivier Cabrit, Sanjeeb Bose, and Jungil Lee. Using singular values to build a subgrid-scale model for large eddy simulations. *Physics of Fluids*, 23(8):085106, 2011. ISSN 1070-6631, 1089-7666. doi: 10.1063/1.3623274. (*pp.* 39, 55, and 90)

[112] Gianni Pedrizzetti and Federico Domenichini. Nature optimizes the swirling flow in the human left ventricle. *Physical Review Letters*, 95(10):108101, 2005. ISSN 0031-9007, 1079-7114. doi: 10.1103/PhysRevLett.95.108101. (*pp.* 40 and 94)

[113] Gianni Pedrizzetti, Federico Domenichini, and Giovanni Tonti. On the left ventricular vortex reversal after mitral valve replacement. *Annals of Biomedical Engineering*, 38(3):769–773, 2010. ISSN 0090-6964, 1573-9686. doi: 10.1007/s10439-010-9928-2. (*pp.* 40 and 57)

[114] J. Sigüenza, S. Mendez, D. Ambard, F. Dubois, F. Jourdan, R. Mozul, and F. Nicoud. Validation of an immersed thick boundary method for simulating fluid–structure interactions of deformable membranes. *Journal of Computational Physics*, 322:723–746, 2016. ISSN 00219991. doi: 10.1016/j.jcp.2016.06.041. (*pp.* 44, 45, and 163)

[115] Wing Kam Liu, Sukky Jun, and Yi Fei Zhang. Reproducing kernel particle methods. *International Journal for Numerical Methods in Fluids*, 20(8): 1081–1106, 1995. ISSN 0271-2091, 1097-0363. doi: 10.1002/fld.1650200824. (*p.* 44)

[116] A. Pinelli, I.Z. Naqavi, U. Piomelli, and J. Favier. Immersed-boundary methods for general finite-difference and finite-volume navier–stokes solvers. *Journal of Computational Physics*, 229(24):9073–9091, 2010. ISSN 00219991. doi: 10.1016/j.jcp.2010.08.021. (*p.* 44)

[117] E. Constant, J. Favier, M. Meldi, P. Meliga, and E. Serre. An immersed boundary method in openfoam : Verification and validation. *Computers Fluids*, 157:55–72, 2017. ISSN 0045-7930. doi: https://doi.org/10.1016/j.compfluid.2017.08.001. (*p.* 45)

[118] Yu-Heng Tseng and Joel H. Ferziger. A ghost-cell immersed boundary method for flow in complex geometry. *Journal of Computational Physics*, 192(2):593–623, 2003. ISSN 0021-9991. doi: https://doi.org/10.1016/j.jcp.2003.07.024.

[119] Ming-Chih Lai and Charles S. Peskin. An immersed boundary method with formal second-order accuracy and reduced numerical viscosity. *Journal of Computational Physics*, 160(2):705–719, 2000. ISSN 0021-9991. doi: https://doi.org/10.1006/jcph.2000.6483.

[120] T. Ye, R. Mittal, H.S. Udaykumar, and W. Shyy. An accurate cartesian grid method for viscous incompressible flows with complex immersed boundaries. *Journal of Computational Physics*, 156(2):209–240, 1999. ISSN 0021-9991. doi: https://doi.org/10.1006/jcph.1999.6356.

[121] A.L.F. Lima E Silva, A. Silveira-Neto, and J.J.R. Damasceno. Numerical simulation of two-dimensional flows over a circular cylinder using the immersed boundary method. *Journal of Computational Physics*, 189(2):351–370, 2003. ISSN 0021-9991. doi: https://doi.org/10.1016/S0021-9991(03)00214-6.

[122] M. Coutanceau and R. Bouard. Determination of the main features of the viscous flow in the wake of a circular cylinder in uniform translation. *Journal of Fluid Mechanics*, 79:231–256, 1977. doi: https://doi.org/10.1017/S0022112077000135. (*p.* 46)

[123] A. Pinelli, I.Z. Naqavi, U. Piomelli, and J. Favier. Immersed-boundary methods for general finite-difference and finite-volume navier–stokes solvers.

Journal of Computational Physics, 229(24):9073–9091, 2010. ISSN 0021-9991. doi: https://doi.org/10.1016/j.jcp.2010.08.021. (*pp.* 45 and 46)

[124] Dzung L. Pham, Chenyang Xu, and Jerry L. Prince. Current methods in medical image segmentation. *Annual Review of Biomedical Engineering*, 2 (1):315–337, 2000. ISSN 1523-9829, 1545-4274. doi: 10.1146/annurev.bioeng.2.1.315. (*p.* 52)

[125] J Ashburner, P Neelin, D L Collins, A Evans, and K Friston. Incorporating prior knowledge into image registration. *Neuroimage*, 1997. doi: 10.1006/nimg.1997.0299.PMID:9417976. (*p.* 52)

[126] Stephen B Pope. Ten questions concerning the large-eddy simulation of turbulent flows. *New Journal of Physics*, 6:35–35, 2004. ISSN 1367-2630. doi: 10.1088/1367-2630/6/1/035. (*p.* 55)

[127] Utkarsh Ayachit. *The ParaView Guide: A Parallel Visualization Application*. Kitware, Inc., 2015. (*pp.* 55, 92, and 130)

[128] Gianni Pedrizzetti, Giovanni La Canna, Ottavio Alfieri, and Giovanni Tonti. The vortex—an early predictor of cardiovascular outcome? *Nature Reviews Cardiology*, 11(9):545–553, 2014. ISSN 1759-5002, 1759-5010. doi: 10.1038/nrcardio.2014.75. (*pp.* 57, 81, 88, and 98)

[129] Gianni Pedrizzetti and Federico Domenichini. Left ventricular fluid mechanics: The long way from theoretical models to clinical applications. *Annals of Biomedical Engineering*, 43(1):26–40, 2015. ISSN 0090-6964, 1573-9686. doi: 10.1007/s10439-014-1101-x. (*p.* 58)

[130] Arash Kheradvar, Ramin Assadi, Ahmad Falahatpisheh, and Partho P. Sengupta. Assessment of transmitral vortex formation in patients with diastolic dysfunction. *Journal of the American Society of Echocardiography*, 25(2):220–227, 2012. ISSN 08947317. doi: 10.1016/j.echo.2011.10.003. (*pp.* 62, 81, 83, 88, and 98)

[131] Tobias Günther and Holger Theisel. The state of the art in vortex extraction. *Computer Graphics Forum*, 37(6):149–173, 2018. ISSN 0167-7055, 1467-8659. doi: 10.1111/cgf.13319. (*p.* 65)

[132] Ikechukwu U. Okafor, Arvind Santhanakrishnan, Brandon D. Chaffins, Lucia Mirabella, John N. Oshinski, and Ajit P. Yoganathan. Cardiovascular magnetic resonance compatible physical model of the left ventricle for multimodality characterization of wall motion and hemodynamics. *Journal of Cardiovascular Magnetic Resonance*, 17(1):51, 2015. ISSN 1532-429X. doi: 10.1186/s12968-015-0154-9. (*pp.* 65 and 88)

[133] Shinichi Fujimoto, Kim H. Parker, Han Bin Xiao, and Derek G. Gibson. Detection and localization of early diastolic forces within the left ventricle

from inflow jet dynamics. a comparison between normal subjects and patients with dilated cardiomyopathy. *Heart and Vessels*, 10(4):204–210, 1995. ISSN 0910-8327, 1615-2573. doi: 10.1007/BF01744987. (*p.* 79)

[134] Morteza Gharib, Edmond Rambod, Arash Kheradvar, David J. Sahn, and John O. Dabiri. Optimal vortex formation as an index of cardiac health. *Proceedings of the National Academy of Sciences*, 103(16):6305–6308, 2006. ISSN 0027-8424, 1091-6490. doi: 10.1073/pnas.0600520103. (*p.* 88)

[135] Siamak N. Doost, Dhanjoo Ghista, Boyang Su, Liang Zhong, and Yosry S. Morsi. Heart blood flow simulation: a perspective review. *BioMedical Engineering OnLine*, 15(1):101, 2016. ISSN 1475-925X. doi: 10.1186/s12938-016-0224-8. (*p.* 88)

[136] Jonatan Eriksson, Petter Dyverfeldt, Jan Engvall, Ann F. Bolger, Tino Ebbers, and Carl Johan Carlhäll. Quantification of presystolic blood flow organization and energetics in the human left ventricle. *American Journal of Physiology-Heart and Circulatory Physiology*, 300(6):H2135–H2141, 2011. ISSN 0363-6135, 1522-1539. doi: 10.1152/ajpheart.00993.2010. (*pp.* 88, 95, and 98)

[137] F. Nicoud, C. Chnafa, J. Siguenza, V. Zmijanovic, and S. Mendez. Large-eddy simulation of turbulence in cardiovascular flows. In Peter Wriggers and Thomas Lenarz, editors, *Biomedical Technology*, volume 84, pages 147–167. Springer International Publishing, 2018. ISBN 978-3-319-59547-4 978-3-319-59548-1. doi: 10.1007/978-3-319-59548-1_9. Series Title: Lecture Notes in Applied and Computational Mechanics. (*p.* 88)

[138] Shohei Yoshida, Shigeru Miyagawa, Satsuki Fukushima, Yasushi Yoshikawa, Hiroki Hata, Shunsuke Saito, Daisuke Yoshioka, Satoshi Kainuma, Keitaro Domae, Ryohei Matsuura, Satoshi Nakatani, Koichi Toda, and Yoshiki Sawa. Cardiac function and type of mitral valve surgery affect postoperative blood flow pattern in the left ventricle. *Circulation Journal*, 83(1):130–138, 2018. ISSN 1346-9843, 1347-4820. doi: 10.1253/circj.CJ-18-0625. (*pp.* 88, 94, and 98)

[139] Sarah Frank, Junsung Lee, Jonas Lantz, Tino Ebbers, and Shawn C. Shadden. Cardiac kinetic energy and viscous dissipation rate from radial flow data. *Frontiers in Physiology*, 12:725104, 2021. ISSN 1664-042X. doi: 10.3389/fphys.2021.725104. (*pp.* 88 and 98)

[140] Mohammed S.M. Elbaz, Rob J. Van Der Geest, Emmeline E. Calkoen, Albert De Roos, Boudewijn P.F. Lelieveldt, Arno A.W. Roest, and Jos J.M. Westenberg. Assessment of viscous energy loss and the association with three-dimensional vortex ring formation in left ventricular inflow: In vivo evaluation using four-dimensional flow MRI. *Magnetic Resonance in Medicine*,

77(2):794–805, 2017. ISSN 0740-3194, 1522-2594. doi: 10.1002/mrm.26129. (*pp.* 88, 94, and 95)

[141] Philippe Reymond, Fabrice Merenda, Fabienne Perren, Daniel Rüfenacht, and Nikos Stergiopulos. Validation of a one-dimensional model of the systemic arterial tree. *American Journal of Physiology-Heart and Circulatory Physiology*, 297(1):H208–H222, 2009. ISSN 0363-6135, 1522-1539. doi: 10.1152/ajpheart.00037.2009. (*pp.* 93 and 166)

[142] Y. Morinishi, T.S. Lund, O.V. Vasilyev, and P. Moin. Fully conservative higher order finite difference schemes for incompressible flow. *Journal of Computational Physics*, 143(1):90–124, 1998. ISSN 00219991. doi: 10.1006/jcph.1998.5962. (*p.* 94)

[143] James Wong, Radomir Chabiniok, Shane M. Tibby, Kuberan Pushparajah, Eva Sammut, David Celermajer, Daniel Giese, Tarique Hussain, Gerald F. Greil, Tobias Schaeffter, and Reza Razavi. Exploring kinetic energy as a new marker of cardiac function in the single ventricle circulation. *Journal of Applied Physiology*, 125(3):889–900, 2018. ISSN 8750-7587, 1522-1601. doi: 10.1152/japplphysiol.00580.2017. (*p.* 95)

[144] M. Carlsson, E. Heiberg, J. Toger, and H. Arheden. Quantification of left and right ventricular kinetic energy using four-dimensional intracardiac magnetic resonance imaging flow measurements. *American Journal of Physiology-Heart and Circulatory Physiology*, 302(4):H893–H900, 2012. ISSN 0363-6135, 1522-1539. doi: 10.1152/ajpheart.00942.2011. (*p.* 95)

[145] Philip J Kilner, Guang-Zhong Yang, A John Wilkes, Raad H Mohiaddin, David N Firmin, and Magdi H Yacoub. Asymmetric redirection of flow through the heart. *Nature*, 404, 2000. (*p.* 98)

[146] Harjinder Kaur, Hosamadin Assadi, Samer Alabed, Donnie Cameron, Vassilios S. Vassiliou, Jos J. M. Westenberg, Rob Van Der Geest, Liang Zhong, Amardeep Dastidar, Andrew J. Swift, and Pankaj Garg. Left ventricular blood flow kinetic energy assessment by 4d flow cardiovascular magnetic resonance: A systematic review of the clinical relevance. *Journal of Cardiovascular Development and Disease*, 7(3):37, 2020. ISSN 2308-3425. doi: 10.3390/jcdd7030037. (*p.* 98)

[147] Qiuyu Xiao, Xin Zhao, Rui Yang, Zizhuo Li, Dongmei Li, Yuanyuan Xie, Xinyue Mao, Yi Wang, Lixue Yin, Chunmei Li, Mingliang Zuo, Qingguo Meng, Wenhua Li, Xuebing Liu, Zhaohuan Li, Qingfeng Zhang, and Yan Deng. Assessment of left ventricular energy loss in patients with mild coronary artery stenosis by using vector flow mapping combined with exercise stress echocardiography. *Echocardiography*, 40(6):537–549, 2023. ISSN 0742-2822, 1540-8175. doi: 10.1111/echo.15591. (*p.* 98)

[148] Antonia Delgado-Montero, Pablo Martinez-Legazpi, M Mar Desco, Daniel Rodríguez-Pérez, Fernando Díaz-Otero, Lorenzo Rossini, Candelas Pérez Del Villar, Elena Rodríguez-González, Christian Chazo, Yolanda Benito, et al. Blood stasis imaging predicts cerebral microembolism during acute myocardial infarction. *Journal of the American Society of Echocardiography*, 2020. doi: 10.1016/j.echo.2019.09.020. (*p.* 98)

[149] Michael Broomé, Elira Maksuti, Anna Bjällmark, Björn Frenckner, and Birgitta Janerot-Sjöberg. Closed-loop real-time simulation model of hemodynamics and oxygen transport in the cardiovascular system. *BioMedical Engineering OnLine*, 12(1):69, 2013. ISSN 1475-925X. doi: 10.1186/1475-925X-12-69. (*p.* 99)

[150] Elias Karabelas, Stefano Longobardi, Jana Fuchsberger, Orod Razeghi, Cristobal Rodero, Marina Strocchi, Ronak Rajani, Gundolf Haase, Gernot Plank, and Steven Niederer. Global sensitivity analysis of four chamber heart hemodynamics using surrogate models. *IEEE Transactions on Biomedical Engineering*, 69(10):3216–3223, 2022. ISSN 0018-9294, 1558-2531. doi: 10.1109/TBME.2022.3163428. (*p.* 99)

[151] Bernard Iung, Victoria Delgado, Raphael Rosenhek, Susanna Price, Bernard Prendergast, Olaf Wendler, Michele De Bonis, Christophe Tribouilloy, Arturo Evangelista, Alexander Bogachev-Prokophiev, Astrid Apor, Hüseyin Ince, Cécile Laroche, Bogdan A. Popescu, Luc Piérard, Michael Haude, Gerhard Hindricks, Frank Ruschitzka, Stefan Windecker, Jeroen J. Bax, Aldo Maggioni, Alec Vahanian, And the EORP VHD II Investigators, Artan Goda, Julia Mascherbauer, Fuad Samadov, Agnes Pasquet, Katerina Linhartova, Nikolaj Ihlemann, Magdy Abdelhamid, Antti Saraste, Christophe Tribouilloy, Elizabeta Srbinovska Kostovska, Gani Bajraktari, Erkin Mirrakhimov, Andrejs Erglis, Vaida Mizariene, Daniela Cassar, Victoria Delgado, Lidia Tomkiewicz-Pajak, Regina Ribeiras, Branko Beleslin, Iveta Simkova, Arturo Evangelista, Sait Mesut Dogan, and Shelley Rahman-Haley. Contemporary presentation and management of valvular heart disease: The EURObservational research programme valvular heart disease II survey. *Circulation*, 140(14):1156–1169, 2019. ISSN 0009-7322, 1524-4539. doi: 10.1161/CIRCULATIONAHA.119.041080. (*p.* 106)

[152] Thomas J Cahill, Anthony Prothero, Jo Wilson, Andrew Kennedy, Jacob Brubert, Megan Masters, James D Newton, Sam Dawkins, Maurice Enriquez-Sarano, Bernard D Prendergast, and Saul G Myerson. Community prevalence, mechanisms and outcome of mitral or tricuspid regurgitation. *Heart*, 107(12):1003–1009, 2021. ISSN 1355-6037, 1468-201X. doi: 10.1136/heartjnl-2020-318482. (*p.* 106)

[153] Alec Vahanian, Friedhelm Beyersdorf, Fabien Praz, Milan Milojevic, Stephan Baldus, Johann Bauersachs, Davide Capodanno, Lenard Conradi, Michele

De Bonis, Ruggero De Paulis, Victoria Delgado, Nick Freemantle, Martine Gilard, Kristina H. Haugaa, Anders Jeppsson, Peter Jüni, Luc Pierard, Bernard D. Prendergast, J. Rafael Sádaba, Christophe Tribouilloy, and Wojtek Wojakowski. 2021 ESC/EACTS guidelines for the management of valvular heart disease: Developed by the task force for the management of valvular heart disease of the european society of cardiology (ESC) and the european association for cardio-thoracic surgery (EACTS). *Revista Española de Cardiología (English Edition)*, 75(6):524, 2022. ISSN 18855857. doi: 10.1016/j.rec.2022.05.006. (*pp.* 106 and 109)

[154] Abdallah El Sabbagh, Yogesh N.V. Reddy, and Rick A. Nishimura. Mitral valve regurgitation in the contemporary era. *JACC: Cardiovascular Imaging*, 11(4):628–643, 2018. ISSN 1936878X. doi: 10.1016/j.jcmg.2018.01.009. (*pp.* 107 and 166)

[155] William A. Zoghbi, David Adams, Robert O. Bonow, Maurice Enriquez-Sarano, Elyse Foster, Paul A. Grayburn, Rebecca T. Hahn, Yuchi Han, Judy Hung, Roberto M. Lang, Stephen H. Little, Dipan J. Shah, Stanton Shernan, Paaladinesh Thavendiranathan, James D. Thomas, and Neil J. Weissman. Recommendations for noninvasive evaluation of native valvular regurgitation. *Journal of the American Society of Echocardiography*, 30(4): 303–371, 2017. ISSN 08947317. doi: 10.1016/j.echo.2017.01.007. (*pp.* 108 and 166)

[156] William Katz, Matthew Suffoletto, Jeffrey Fowler, Valentina Jaramillo-Restrepo, Saurabh Sanon, and Conrad Smith. Transesophageal echocardiography guidance during transcatheter mitral valve edge-to-edge repair for severe mitral regurgitation post–mitral annuloplasty: A case series. *CASE*, 8(12):525–534, 2024. ISSN 24686441. doi: 10.1016/j.case.2024.09.006. (*p.* 109)

[157] Rebecca T. Hahn, Theodore Abraham, Mark S. Adams, Charles J. Bruce, Kathryn E. Glas, Roberto M. Lang, Scott T. Reeves, Jack S. Shanewise, Samuel C. Siu, William Stewart, and Michael H. Picard. Guidelines for performing a comprehensive transesophageal echocardiographic examination: Recommendations from the american society of echocardiography and the society of cardiovascular anesthesiologists. *Journal of the American Society of Echocardiography*, 26(9):921–964, 2013. ISSN 08947317. doi: 10.1016/j.echo.2013.07.009.

[158] Frank A. Flachskampf, Patrick F. Wouters, Thor Edvardsen, Artur Evangelista, Gilbert Habib, Piotr Hoffman, Rainer Hoffmann, Patrizio Lancellotti, Mauro Pepi, and for the European Association of Cardiovascular Imaging Document reviewers: Erwan Donal and Fausto Rigo. Recommendations for transoesophageal echocardiography: EACVI update 2014. *European Heart Journal - Cardiovascular Imaging*, 15(4):353–365, 2014. ISSN 2047-2412, 2047-2404. doi: 10.1093/ehjci/jeu015. (*p.* 109)

[159] Benjamin Fidock, Gareth Archer, Natasha Barker, Alaa Elhawaz, Abdallah Al-Mohammad, Alexander Rothman, Rod Hose, Ian R. Hall, Ever Grech, Norman Briffa, Nigel Lewis, Rob J. Van Der Geest, Jun-Mei Zhang, Liang Zhong, Andrew J. Swift, James M. Wild, Estefania De Gárate, Chiara Bucciarelli-Ducci, Jeroen J. Bax, Sven Plein, Saul Myerson, and Pankaj Garg. Standard and emerging CMR methods for mitral regurgitation quantification. *International Journal of Cardiology*, 331:316–321, 2021. ISSN 01675273. doi: 10.1016/j.ijcard.2021.01.066. (*p.* 109)

[160] Seth Uretsky, Edgar Argulian, Jagat Narula, and Steven D. Wolff. Use of cardiac magnetic resonance imaging in assessing mitral regurgitation. *Journal of the American College of Cardiology*, 71(5):547–563, 2018. ISSN 07351097. doi: 10.1016/j.jacc.2017.12.009. (*p.* 109)

[161] Pankaj Garg, Andrew J. Swift, Liang Zhong, Carl-Johan Carlhäll, Tino Ebbers, Jos Westenberg, Michael D. Hope, Chiara Bucciarelli-Ducci, Jeroen J. Bax, and Saul G. Myerson. Assessment of mitral valve regurgitation by cardiovascular magnetic resonance imaging. *Nature Reviews Cardiology*, 17(5):298–312, 2020. ISSN 1759-5002, 1759-5010. doi: 10.1038/s41569-019-0305-z.

[162] Tim Leiner, Jan Bogaert, Matthias G. Friedrich, Raad Mohiaddin, Vivek Muthurangu, Saul Myerson, Andrew J. Powell, Subha V. Raman, and Dudley J. Pennell. SCMR position paper (2020) on clinical indications for cardiovascular magnetic resonance. *Journal of Cardiovascular Magnetic Resonance*, 22(1):76, 2020. ISSN 10976647. doi: 10.1186/s12968-020-00682-4.

[163] Saul G. Myerson, Joanna d'Arcy, Jonathan P. Christiansen, Laura E. Dobson, Raad Mohiaddin, Jane M. Francis, Bernard Prendergast, John P. Greenwood, Theodoros D. Karamitsos, and Stefan Neubauer. Determination of clinical outcome in mitral regurgitation with cardiovascular magnetic resonance quantification. *Circulation*, 133(23):2287–2296, 2016. ISSN 0009-7322, 1524-4539. doi: 10.1161/CIRCULATIONAHA.115.017888. (*p.* 109)

[164] Li Cai, Ying Wang, Hao Gao, Xingshuang Ma, Guangyu Zhu, Ruihang Zhang, Xiaoqin Shen, and Xiaoyu Luo. Some effects of different constitutive laws on FSI simulation for the mitral valve. *Scientific Reports*, 9:12753, 2019. ISSN 2045-2322. doi: 10.1038/s41598-019-49161-6. (*p.* 109)

[165] Akshita Rana, Erik Westein, Be'eri Niego, and Christoph E. Hagemeyer. Shear-dependent platelet aggregation: Mechanisms and therapeutic opportunities. *Frontiers in Cardiovascular Medicine*, 6:141, 2019. doi: 10.3389/fcvm.2019.00141. (*p.* 128)

[166] Rodrigo Méndez Rojano, Mansur Zhussupbekov, and James F. Antaki. Multi-constituent simulation of thrombus formation at LVAD inlet cannula

connection: Importance of virchow's triad. *Artificial Organs*, 45(9):1014–1023, 2021. ISSN 0160-564X, 1525-1594. doi: 10.1111/aor.13949. (*p.* 129)

[167] Mehrdad Khamooshi, Marjan Azimi, and Shaun D. Gregory. Intraventricular flow dynamics and thrombosis risk with a left ventricular assist device using accelerated thrombosis modeling and stress-blended eddy simulation. *Physics of Fluids*, 36(8):081907, 2024. ISSN 1070-6631, 1089-7666. doi: 10.1063/5.0214303. (*p.* 129)

[168] Zhiliang Xu, Malgorzata Kamocka, Mark Alber, and Elliot D. Rosen. Computational approaches to studying thrombus development. *Arteriosclerosis, Thrombosis, and Vascular Biology*, 31(3):500–505, 2011. ISSN 1079-5642, 1524-4636. doi: 10.1161/ATVBAHA.110.213397. (*p.* 129)

[169] Noelia Grande Gutiérrez, Debanjan Mukherjee, and David Bark. Decoding thrombosis through code: a review of computational models. *Journal of Thrombosis and Haemostasis*, 22(1):35–47, 2024. ISSN 15387836. doi: 10.1016/j.jtha.2023.08.021. (*p.* 129)

[170] Junyi Chen. *Modeling, analysis and numerical simulation of the coagulation cascade*. Phd thesis, University of Montpellier, 2025. (*p.* 129)

[171] Alexandre Ranc, Salome Bru, Simon Mendez, Muriel Giansily-Blaizot, Franck Nicoud, and Rodrigo Méndez Rojano. Critical evaluation of kinetic schemes for coagulation. *PLOS ONE*, 18(8):e0290531, 2023. doi: 10.1371/journal.pone.0290531. (*p.* 130)